Observations and Characterisation of Rapid Variations in the Earth's Internal Magnetic Field

William James Brown

Submitted in accordance with the requirements for the degree of Doctor of Philosophy

The University of Leeds
School of Earth and Environment

April, 2015

Intellectual Property and Publication Statement

The candidate confirms that the work submitted is his own, except where work which has formed part of jointly-authored publications has been included. The contribution of the candidate and the other authors to this work has been explicitly indicated below. The candidate confirms that appropriate credit has been given within the thesis where reference has been made to the work of others.

Chapter 1 contains a figure that was published in:

> Cox, G.A., & W.J. Brown, (2013), Rapid dynamics of the Earth's core, *Astronomy & Geophysics*, 54(5), 5-32, doi:10.1093/astrogeo/att167.

This figure, along with the caption and all associated discussion in the main text were produced by the candidate.

Chapters 2 and 3 contain material from the publication:

> Brown, W.J., J.E. Mound & P.W. Livermore, (2013), Jerks abound: An analysis of geomagnetic observatory data from 1957 to 2008, *Physics of the Earth and Planetary Interiors*, 223, 62-67, doi:10.1016/j.pepi.2013.06.001.

This publication, and all the work it constitutes, was produced by the candidate with advice and consultation on the work and writing provided by J.E. Mound and P.W. Livermore.

ACKNOWLEDGEMENTS

I must first thank my supervisors Jon Mound and Phil Livermore for their help, guidance and tuition, in Jon's case pre-dating this PhD. It has been a pleasure to work with you and I am thankful for the opportunity you gave me. Sorry I still haven't managed to adopt a more concise style, you did your best. I would additionally like to thank Richard Holme, Ingo Wardinski, Nicolas Gillet and Chris Finlay for valuable comments during the development of this work and Richard Rigby for unparallelled and unassuming technical support no matter the issue and without regard to sensible working hours.

The results presented here rely on data collected at geomagnetic observatories. I thank the national institutes that support them, *INTERMAGNET*[1] for promoting high standards of magnetic observatory practice and the *World Data Centre* (WDC) *for Geomagnetism*[2] at the *British Geological Survey*, Edinburgh. Geomagnetic indices were provided by the *WDC for Geomagnetism*[3], Kyoto and the *Dcx Server*[4] of the *University of Oulu*, Finland. I also thank the authors of numerous geomagnetic field models made available online.

Throughout my PhD I have benefited from the efforts of other researchers in making their work reproducible by providing open access to their software. This has allowed me to develop both my scientific goals and my own programming skills beyond the level they would have achieved otherwise and I highly recommend use of such resources and continuation of these practises. Special mention goes to: Frederik J. Simons' extensive repository for useful spherical harmonic tools[5]; Jason McEwan's routines for the rotation of spherical harmonic functions[6]; and Anna Kalbert's adaptation[7] of parts of Mark Wieczorek's spherical harmonics toolbox[8].

This PhD was funded by *Natural Environment Research Council* grant NE/I012052/1 and I have been fortunate to receive additional funding from the *Royal Astronomical Society* and the *Study of Earth's Deep Interior* consortium, making it possible for me to present and discuss my work at conferences across the globe.

Thank you to everyone in Leeds for making this a wonderful place to live and work. Thanks to the members of the *School of Earth and Environment* and those in *Applied Mathematics* for the camaraderie, be it in the department, on fieldwork or at conferences

worldwide. Thanks especially to the many occupants of 8.152 for every bit of help, hindrance, biscuit and beer that has made the time fly faster than I wish.

Finally thank you to my family for assuming I've known what I was doing and supporting me regardless and most of all to my newest family, Sherry, for putting up with me through five years, seven timezones, two nationalities, 7400 km, innumerable bad jokes and a thesis write-up for good measure.

[1] www.intermagnet.org
[2] http://www.wdc.bgs.ac.uk
[3] http://wdc.kugi.kyoto-u.ac.jp/wdc/
[4] http://dcx.oulu.fi
[5] http://geoweb.princeton.edu/people/simons/software.html
[6] http://www.jasonmcewen.org/index.html
[7] MATLAB File Exchange #15279 "shtools".
[8] http://shtools.ipgp.fr/

"The function of an expert is not to be more right than other people, but to be wrong for more sophisticated reasons."

– Dr David Butler

ABSTRACT

The internal magnetic field of Earth is generated by dynamo processes in the fluid outer core, variations in flow resulting in the constantly changing form of the magnetic field. The rapid dynamics of the core are largely unknown; the mantle and crust filter and mask small-scale spatial and temporal features and field sources external to the Earth contaminate the limited observations. Geomagnetic jerks represent the most rapid observed variations of the internal field, on the scale of months, and are poorly understood. Jerks are sharp changes between periods of an otherwise linear rate of change of the field. The main aims of this thesis are: to systematically catalogue observations of jerks, focussing on 1957–2008, and to quantify their characteristics; to assess how representative observations of jerks are through synthetic field modelling; and to evaluate what the results of these analyses inform us about the nature of the source of jerks in the core.

I identify jerks in observations via a two-step method, removing contaminating external signal before identifying possible times at which a simple jerk model produces a good fit to data. I quantify the properties of the model and fit, providing uncertainty estimates, all with minimal prior information on the occurrences of jerks. Jerks are found to be frequent, regional and not globally contemporaneous. Jerks are identified every year but with relative abundance in 1968–71, 1973–74, 1977–79, 1983–85, 1989–93, 1995–98 and 2002–03. The amplitudes of jerks in Europe are seen to vary periodically, suggesting a regular generation mechanism. Limited observations preclude a global assessment of this.

I create stochastic synthetic field models to assess the significance of observations and to infer compatible jerk characteristics. These models reinforce the view that jerks occur in localised patches at the Earth's surface without a consistent temporal or spatial distribution. Spherical harmonic (SH) analysis of the synthetic and observed jerks suggests that despite the localised nature of jerk signals, they can be represented by a potential field with most power below SH degree 4.

A lag time of 6 months between variations in Earth's rotation and geomagnetic jerks suggests that sufficiently electrically conductive material must be present in the lower

$\sim$130 km of the mantle. At the core-mantle boundary, the power spectrum of the SH jerk models and the demonstrated ability to model jerks with a stochastic process, indicates a chaotic, turbulent core-surface flow regime is a likely generation mechanism.

CONTENTS

List of Figures

List of Tables

NOMENCLATURE

ABBREVIATIONS, ACRONYMS AND NAMES

aa-index	Antipodal activity index
AE-index	Auroral electrojet index
AK135	Seismic velocity model
BCMT	Bureau Central de Magnétisme Terrestre
BGS	British Geological Survey
CALSjk	Continuous Archaeomagnetic and Lake Sediment Geomagnetic Model, field model series over j ka
C^{3}FM(j)	Continuous Covariance Constrained-end-points Field Model, field model series
CHAMP	CHAllenging Mini-satellite Payload
CHAOS-(j)	*CHAMP Ørsted SAC-C*, field model series
CMj	Comprehensive Model, field model series
CMB	Core-Mantle Boundary
COV-OBS	Geomagnetic field model
jD	j-Dimensional
DE-2	Dynamics Explorer, satellite
D_{st}-, D_{xt}-, D_{cx}-index	Storm-time disturbance index
E	Geographic East
ESA	European Space Agency
$F_{10.7}$-index	Solar radio flux at 10.7 cm wavelength index
gufm1	Geomagnetic field model
gufm-sat-E3	Geomagnetic field model
GRIMM-(j)	*GFZ* Reference Internal Magnetic Model, field model series
IAGA	International Association of Geomagnetism and Aeronomy
IGRF-(j)	International Geomagnetic Reference Field, field model series
INTERMAGNET	International Real-time Magnetic Observatory Network
IQ	Geomagnetic International Quiet days
IMF	Interplanetary Magnetic Field

K-index	Characteristic storm index
LOD	Length-Of-Day, rotation period of Earth
LS	Least-Squares
MAC	Magneto-Archimedes-Coriolis
Magsat	Magnetic field Satellite
MF	Main (core) Field
N	Geographic North
NASA	National Aeronautics and Space Administration
Ørsted	Magnetic field satellite
PDF	Probability Density Function
(P)OGO-j	(Polar) Orbiting Geophysical Observatory, satellite series
R_z-index	Wolf relative sunspot number index
RC-index	Ring current index
RMS	Root-Mean-Square
S	Geographic South
SA	Secular Acceleration
SAC-C	Satélite de Aplicaciones Científicas-C, satellite
SC	Solar Cycle
SH(A)	Spherical Harmonic (Analysis)
SIFM	Swarm Initial Field Model
SMC	Solar-Magnetic Cycle
STT	Spherical Triangular Tessellation
SV	Secular Variation
THEMIS	Time History of Events and Macroscale Interactions during Substorms, satellite constellation
W	Geographic West
WDC	World Data Centre
WMM	World Magnetic Model series

SYMBOLS AND NOTATION

#	Number
$\hat{\mathbf{j}}$	Coordinate direction of j
$\mathbf{j}$	Vector or matrix j
$^\top$	Matrix transpose
$\partial/\partial j$	Partial derivative with respect to j
$\partial/\partial t$ or $\dot{}$	First time derivative
$\partial^2/\partial t^2$ or $\ddot{}$	Second time derivative
$\mathrm{d}/\mathrm{d}j$	Derivative with respect to j
i	$\sqrt{-1}$

Δ	Change
Γ	Gamma function
∇	Gradient
∇^2	Laplacian
$\nabla\cdot$	Divergence
$\nabla\times$	Curl
$\mathcal{O}(j)$	Order or magnitude j
cov	Covariance
diag	Matrix diagonal
$\exp$	Exponential
E	Expected value
Tr	Matrix trace
α	Statistical significance or first Euler angle for spherical rotation
β	Second Euler angle for spherical rotation
γ	Third Euler angle for spherical rotation
ζ	Wiener process
η	Magnetic diffusivity
θ	Co-latitude, spherical coordinate direction
θ_{North}	Co-latitude of magnetic North pole
λ	Damping parameter
Λ_{clean}	Eigenvalue of clean-component covariance
$\Lambda_{\mathrm{intermediate}}$	Eigenvalue of intermediate-component covariance
Λ_{noisy}	Eigenvalue of noisy-component covariance
μ	Mean
μ_0	Permeability of free space ($4\pi\times10^{-7}$ Vs/Am)
ν	Kinematic viscosity or correlation function smoothness parameter
π	Ratio of circle circumference to diameter
$\rho_{(n)}$	Correlation function (of degree n)
ρ_0	Hydrostatic density
ρ'	Hydrostatic density perturbation
σ	Standard deviation
σ_a	Standard deviation of slope
σ_b	Standard deviation of intercept
σ_g^2, $\sigma_{\dot{g}}^2$, $\sigma_{\ddot{g}}^2$	Variance of first three time derivatives of Gauss coefficients
$\tilde{\sigma}$	Estimated standard deviation
τ	Timescale of variation
τ_c	Characteristic timescale of variation
ϕ	Longitude, spherical coordinate direction
ϕ_{North}	Longitude of magnetic North pole
$\tilde{\phi}_{\mathrm{North}}$	Uncorrected longitude of magnetic North pole

$\bar{\phi}_{\mathrm{North}}$	Temporal mean longitude of magnetic North pole
$\mathbf{\Phi}$	Minimisation function
φ	Stochastic process
φ'	Perturbation of stochastic process
$\bar{\varphi}$	Mean of stochastic process
$\mathbf{\Omega}$	Earth rotation vector
a	Slope
a_1, a_2	Gradients of secular variation before and after a jerk
A, A_j or A^j	Jerk amplitude, j component of jerk amplitude
b	Intercept
$\mathbf{B}$, B_j	Magnetic field, j component of magnetic field
$\bar{\mathcal{B}}^2$	Global mean temporal magnetic power
$c_{1,2}$	Correlation coefficient between Gauss coefficient sets 1 and 2
$\dot{C}$	Reference noisy-component unmodelled secular variation residual
$\mathbf{C}$	Covariance matrix
$\mathbf{C}_{\mathrm{annual}}$	Covariance matrix of annual unmodelled secular variation
$\mathbf{C}_{\mathrm{corrected}}$	Covariance matrix of corrected monthly unmodelled secular variation
$\mathbf{C}_d$	Data covariance matrix
$\mathbf{C}_{\mathrm{est}}$	Estimated covariance matrix of model parameters
$\mathbf{C}_m$	Model covariance matrix
$\mathbf{C}_n$	Covariance matrix of Gauss coefficient for degree n
$\mathbf{C}_{\mathrm{monthly}}$	Covariance matrix of monthly unmodelled secular variation
d	Dimension of stochastic process
$\mathbf{d}$	Data vector
$\mathbf{d}^n_{m,l}$	Real polar rotation matrix
D	Magnetic declination
$\mathbf{D}^n_{m,l}$	Wigner function matrix
$\mathbf{e}$, e_i	Misfit, element of misfit
$\mathbf{E}$	Electric field
f	Frequency
$\mathbf{g}$	Gravitational acceleration
g^m_n	Gauss cosine coefficient for internal field of degree n, order m
G	Electrical conductance
$\mathbf{G}$	Inversion matrix operator
h	Height above CMB
h^m_n	Gauss sine coefficient for internal field of degree n, order m
$\mathbf{H}$, H	Horizontal field component
H_0	Fit to horizontal field component of International Quiet days
H_{obs}	Observed horizontal field
I	Magnetic inclination

$\mathbf{J}$	Electric current density
K_ν	Modified Bessel function of the second kind, order ν
$\mathbf{L}$, L_{ii}	Leverage matrix, diagonal elements of leverage matrix
n	Spherical harmonic degree
$n_{\max}$	Maximum spherical harmonic degree
N	Number of data points
$N_{\text{detections}}$	Number of jerks detected in a histogram time bin
N_{active}	Number of active observatories during a histogram time bin
N_{total}	Total number of observatories
m, (l)	Spherical harmonic order (when two are required simultaneously)
$\mathbf{m}$	Model vector
$\bar{\mathbf{m}}$	Temporal mean model vector
$\tilde{\mathbf{m}}$	Perturbation from mean model vector
p	Non-hydrostatic pressure
$\mathbf{P}$	Matrix operator of power law inversion
P_n^m	Schmidt semi-normalised associated Legendre function of degree n, order m
q_n^m	Gauss cosine coefficient for external field of degree n, order m
r	Spherical radius, spherical coordinate direction
r_c	Radius to core-mantle boundary, 3485 km
r_E	Radius to surface of Earth, 6,371 km
$\dot{r}_{\text{cor}}$	Corrected noisy component residual
$\dot{r}_{\text{noisy}}$	Noisy-component unmodelled secular variation residual
$\mathbf{R}$	Resolution matrix
R_n	Spatial power spectrum at spherical harmonic degree, n
s	Cylindrical radius
s_n^m	Gauss sine coefficient for external field of degree n, order m
S	Spectral density
S_q	Solar quiet-time geomagnetic variation
t	Time
t_0	Jerk time
T	Lag time between jerk and LOD
$\mathbf{u}$	Core surface flow velocity
$\mathbf{U}_C$	Upper triangle of covariance matrix
$\mathbf{v}_{\text{clean}}$	Eigenvector of clean-component covariance
$\mathbf{v}_{\text{intermediate}}$	Eigenvector of intermediate-component covariance
$\mathbf{v}_{\text{noisy}}$	Eigenvector of noisy-component covariance
V	Magnetic potential
W_{bin}	Histogram bin weighting
X, X	Northward component of geomagnetic field

$\mathcal{X}(f)$	Fourier transform of $X(t)$
$\mathcal{X}$	First horizontal axis for spherical rotation
Y, Y	Eastward component of geomagnetic field
$\mathcal{Y}$	Second horizontal axis for spherical rotation
Z, Z	Vertically downward (centre) component of geomagnetic field
$\mathcal{Z}$	Vertical axis for spherical rotation

UNITS AND PREFIXES

$^\circ$	Degrees
$^\circ$C	Degrees Celsius
a	Annum, years before present
G	Giga, 1×10^9
k	Kilo, 1×10^3
kg	Kilogram
m	Meter or as prefix milli, 1×10^{-3}
M	Mega, 1×10^6
month	Calendar month or 1/12 year
n	Nano, 1×10^{-9}
s	Second
S	Siemens, SI base: s^3A^2/kgm^2
T	Tesla, SI base: kg/As^2
yr	Calendar year

CHAPTER 1

INTRODUCTION

1.1 OVERVIEW

The internal magnetic field of the Earth is generated by dynamo processes in the fluid outer core, the variations in flow resulting in the constantly changing form of the geomagnetic field. The magnetic field therefore acts as an indicator of the processes in the core and observation of the field leads to the ability to extract information about the fluid motion responsible for generating the field. Observations of the magnetic field made both at the surface and in satellite orbit provide an ever expanding and improving dataset documenting the variations of the field both spatially and temporally. There is a lack of knowledge on the rapid dynamics of the core, the Earth's mantle and crust filter or mask short spatial and temporal scales of the internal magnetic field and externally sourced magnetic fields, influenced primarily by the Sun, contaminate the observations of the internal signal. While theory suggests certain forms for the core's rapid fluid motions, evidence is either poorly resolved or unobserved so far.

The most rapid variations of the internal magnetic field observed are known as geomagnetic jerks, rapid changes in the otherwise linear rate of change of the magnetic field. Jerks are a poorly defined phenomenon: better cataloguing the observations of jerks to quantify their characteristics is the first step to a better understanding of the phenomena and their source in the dynamics of the core. This is the primary aim of this thesis. If rapid internally-generated magnetic variations are to be studied, the externally generated magnetic fields that contaminate observations must be accounted for, as this thesis also investigates.

We must however realise that our observations of geomagnetic jerks are not comprehensive and therefore may not be truly representative. As such, suitable synthetic models may allow a means to test how representative we might expect existing observations to be. If shown to be a good analogy for real data, these synthetic data may then allow more detailed study of the generic character of features which resemble observed jerks. Here lies the second main task of this thesis.

With knowledge of the observed occurrences of geomagnetic jerks and the backing of synthetic models to validate my interpretations I aim to make better grounded assumptions about the nature of the dynamical source of jerks in the Earth's core.

In this chapter I first introduce some necessary background about the structure of the Earth in Section 1.2, and the details of the geomagnetic field in Section 1.3. Next in Section 1.4 observations of the field are described. This leads to an overview of the process of geomagnetic field modelling in Section 1.5 and the derived ability to infer the motions of the outer core responsible for generating the field in Section 1.6. With the scene set I introduce geomagnetic jerks in detail in Section 1.7. This chapter concludes with a statement of the motivation and aims for this work and a summary of the structure of the thesis, in Section 1.8.

1.2 STRUCTURE OF THE EARTH AND NEAR-EARTH ENVIRONMENT

INSIDE THE EARTH

Seismology has provided a wealth of information regarding the internal structure of the Earth. Studies such as Dziewonski and Anderson [1981] and Kennett et al. [1995] have produced 1D models (Figure 1.1a) to describe the average velocity (and subsequently density) structure with depth observed in the Earth by the travel times of seismic waves. While there is much complexity and heterogeneity in the real Earth, for the purposes of this study a very basic understanding will suffice and a model of concentric spherical shells is sufficient, as depicted in Figure 1.1b.

Beginning at the surface of the Earth, there is the rigid rind of the lithosphere containing magnetically susceptible and electrically conducting elements such as iron, above a silicate mantle that generally becomes increasingly viscous with depth. The mantle is divided by the seismic discontinuities of mineralogical phase changes in the transition zone into upper and lower portions (Figure 1.1b). The primary component of mantle composition is olivine, the iron content of this and other mantle materials causes the mantle to be

electrically conductive and magnetically susceptible. Below the mantle, seismological observations first identified a shadow zone of shear waves, an observation attributed to the presence of a liquid outer core through which only pressure waves can propagate. The overall density of the Earth compared to the density of the surface materials, along with modelling of the pressures and temperatures within the Earth, suggest that this outer core consists predominantly of iron alloyed with lighter elements such as nickel. The outer core is thus an electrically conductive fluid. It is this property that is key to the generation of the geomagnetic field through the dynamo action of the fluid motion. Below the fluid region of the outer core, the pressure and temperature conditions are such that iron crystallises to form a solid inner core, releasing buoyant light elements which, in combination with thermal gradients, act to drive convection of the fluid outer core.

Of particular relevance for calculations in this thesis are the radius of the outer core, $r_c = 3485$ km, which defines the core-mantle boundary (CMB), and the radius of the Earth's surface, taken to be the mean radius, $r_E = 6371.2$ km.

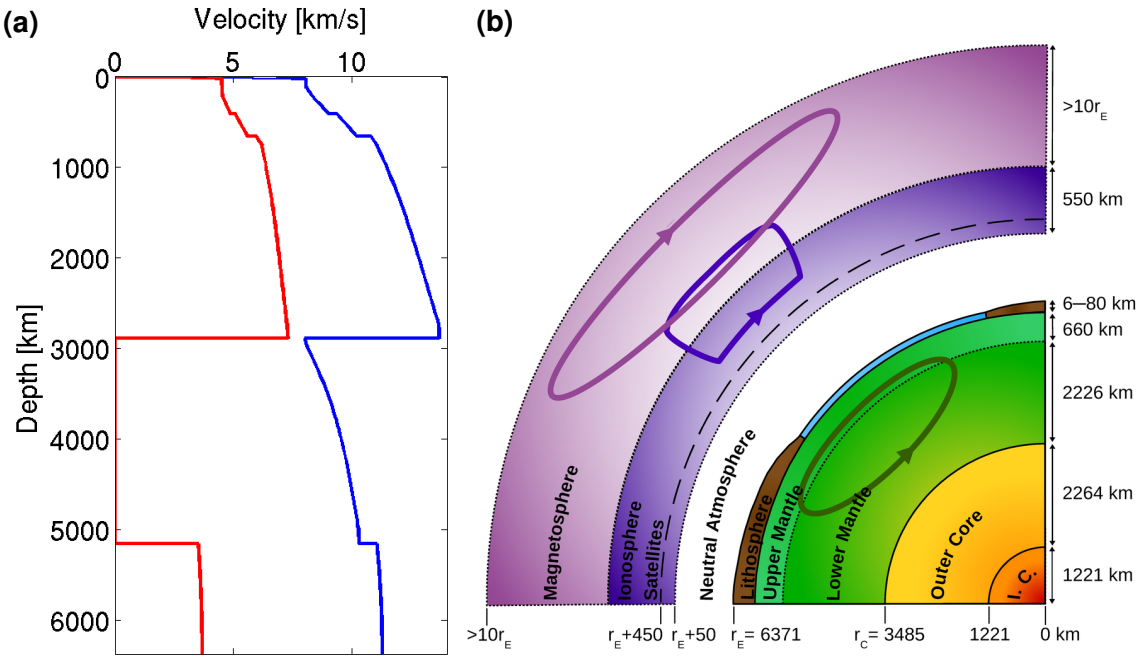

Figure 1.1: The structure of the Earth as described by the *AK135* seismic velocity model of Kennett et al. [1995] (a), and a cartoon of the rough dimensions of the layered structure within and surrounding the Earth (b). In (a) the red curve shows the average shear wave velocity through the Earth while the blue curve shows the pressure wave velocity; zero shear wave velocity indicates the fluid outer core. In (b) electrical current systems in magnetosphere, field aligned currents connecting the magnetosphere to the ionosphere and induced currents in the electrically conducting mantle are depicted as looped arrows. "I.C." denotes inner core.

OUTSIDE THE EARTH

Outside of the Earth the regions of particular interest to this study are those comprised of plasmas, the motions of whose charged particles produce electrical currents and subsequently magnetic fields, as will be described in the next section. These regions stretch from the ionosphere, just above the neutral atmosphere, through the plasmasphere (inner magnetosphere) to the outer edge of the magnetosphere (Figure 1.1b). The ionosphere is defined as the region in which matter is ionised by incident Solar radiation and includes, moving radially outward, part of the mesosphere, the thermosphere and part of the exosphere. The plasmasphere is defined as the region beyond the ionosphere in which low energy (or cold) plasma is present, making way with an order of magnitude drop in plasma density for the magnetosphere which encompasses the furthest region in which charged particles are controlled by the geomagnetic field. All three of these regions are controlled by a combination of geomagnetic and Solar effects and thus vary in size, shape and structure with fluctuations of the Solar wind which carries the interplanetary magnetic field (IMF) produced in the Sun. The Solar wind is a continuous but variable eminence of plasma at supersonic speeds from the Sun [Isenberg, 1991].

1.3 THE GEOMAGNETIC FIELD

The magnetic field of Earth, or geomagnetic field, acts as a shield, protecting the planet, its atmosphere and its life from much of the damaging radiation and particles which emanate from the Sun. The field has operated for at least 3.45 Ga [e.g. McElhinny and Senanayake, 1980; Tarduno et al., 2010] of the Earth's 4.55 Ga lifespan so far [Manhes et al., 1980]. Indeed the presence of a strong and long-lived magnetic field is one of the characteristics which distinguishes Earth from its barren terrestrial neighbours, Venus and Mars. The geomagnetic field is a combination of fields from several sources and extends from the depths of the Earth's core to the magnetopause. The magnetopause represents the boundary between the region dominated by the geomagnetic field and that of the IMF (Figure 1.2), which has a strength of approximately 5–10 nT at Earth's orbit [Baumjohann and Nakamura, 2007]. Within this region, stretching from the bow shock some 10–15 r_E from Earth to the magnetotail which extends well past the Moon's orbit to $\mathcal{O}(100)\, r_E$, exists a complicated array of interacting magnetic and electric fields (Figure 1.2) which result in a magnetic field which varies on a wide range of spatial and temporal scales about the Earth.

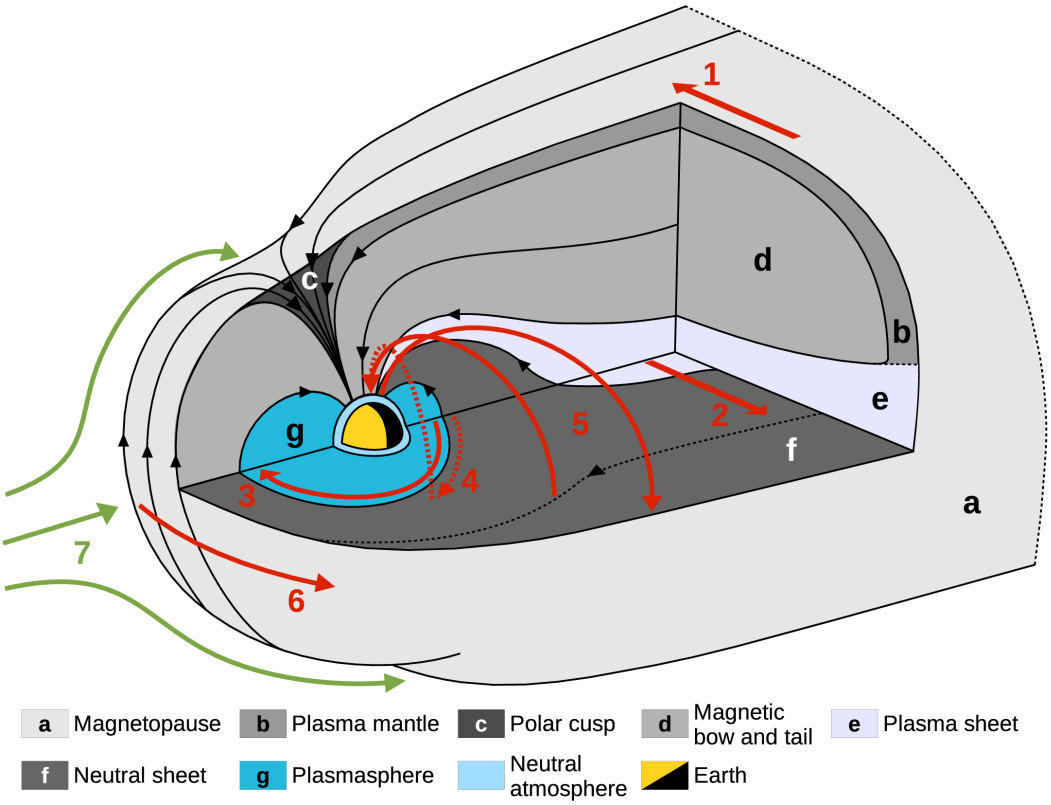

Figure 1.2: The structure of the magnetosphere of the Earth. The morphology of the magnetosphere is formed by a balance between the geomagnetic field and the Solar wind. Diagram is cut away to show magnetic field lines (black arrows) about the magnetic Southern (geographic Northern) polar cusp. Labels represent examples of: 1. tail current; 2. neutral sheet current; 3. ring current; 4. partial ring current; 5. Birkeland/field-aligned current; 6. Chapman-Ferraro current; 7. Solar wind particles. Adapted from Kivelson and Russell [1995].

1.3.1 Magnetic Field Sources

The sources of the geomagnetic field can be broken down into those produced by previously magnetised materials and those generated by electrical currents as described by the Maxwell-Faraday equation,

$$\nabla \times \mathbf{E} = -\frac{\partial \mathbf{B}}{\partial t}, \tag{1.3.1}$$

where $\mathbf{E}$ is the electric field and $\mathbf{B}$ the magnetic field. The solid rocks of the lithosphere can be magnetised when below the Curie temperature of the predominantly iron based magnetic minerals they contain (500–700°C or typical depths of 6–30 km [Thébault et al., 2010]). Electromagnetic induction sources include the electrical currents which flow in the Earth's fluid outer core, in the mantle and lithosphere, in the saline oceans and outside the body of the Earth in the ionosphere and magnetosphere.

A second distinction can be made between those sources which are internal to the body of the Earth and those which are external to the Earth.

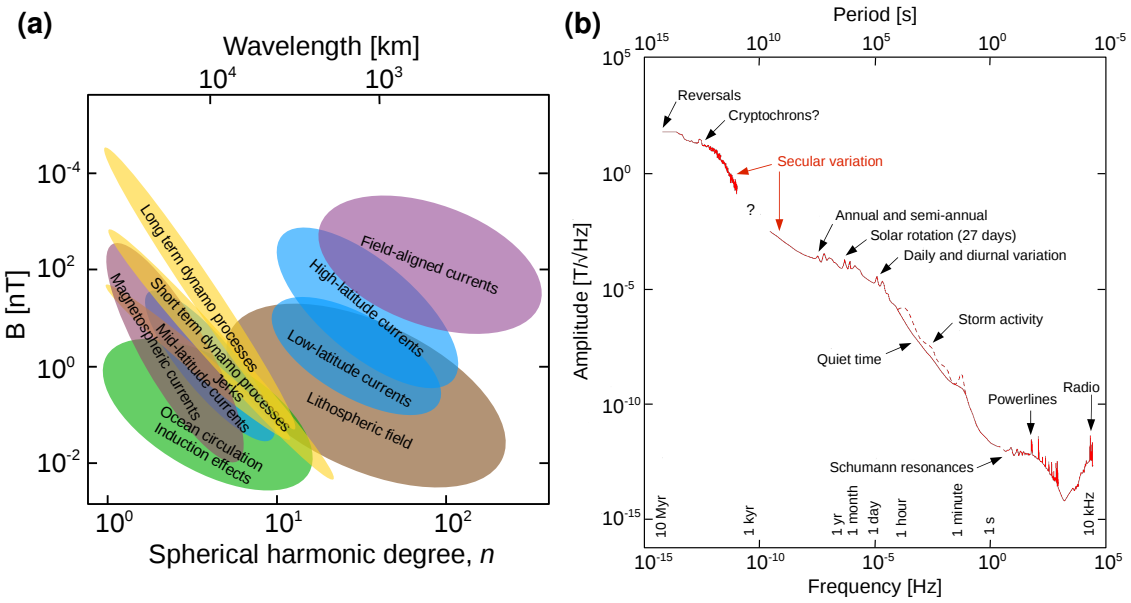

Figure 1.3: Cartoon of spatial scales (a) and observed temporal scales (b) of the geomagnetic field. The complex overlapping spatial scales of magnetic fields generated by different sources makes separation of these sources difficult in the spatial domain (a). Similarly, there is no clear partition in the "grand spectrum" of temporal geomagnetic activity, rather a continuum of overlapping effects. Adapted from Haagmans and Plank, *ESA*[1] (a) and Constable and Constable [2013] (b).

INTERNAL SOURCES

Of the internal field the most intense component comes from the dynamo effect of the flow of electrically conducting outer core fluid, varying between approximately 30,000 nT at the magnetic equator to 60,000 nT at the magnetic poles at Earth's surface [Olsen et al., 2007]. It is this component which is of interest for this study and it will be referred to as the "core field" or "main field" (MF), all other field sources will be considered noise sources, hampering the study of the MF. The MF is considered to vary on timescales from several months (geomagnetic jerks) to millions of years (polarity reversals) (Figure 1.3), reflecting the timescales of the responsible dynamo process. Often, as is the case here, it is the variations of the MF represented by its time derivatives that are of interest. The first time derivative is known as the secular variation (SV) while the second time derivative is known as the secular acceleration (SA). The term "secular" here implies non-periodic variations altough this is primarily a question of relative timescales.

The lithospheric field, which with the core field makes up what is generally known as the "internal field", is much less intense than that of the core at approximately ± 200 nT at the Earth's surface [Maus et al., 2008]. The innate magnetic susceptibility of the lithosphere

[1] http://pcwww.liv.ac.uk/~holme/RAS/haagmans.pdf, 2015-03.

varies only on geological timescales. Since the internal field is dominated by the core field at large-scales, the crustal field is seen to describe features below length scales of approximately 2,500 km at the Earth's surface.

Of the other internal sources; electric currents in the mantle, crust and ocean are induced by the time varying magnetic fields generated both internally and externally. The internally induced fields vary with the respective source of the MF thus the effects can be difficult to separate; conversely, since the externally induced fields vary with the externally sourced fields, some of their effects can be distinguished from internal sources more readily [Olsen et al., 2007]. The oceans also host their own dynamo effects ($<$10 nT at Earth's surface [Manoj et al., 2006]) as the electrically conductive salt-water circulates in the presence of the MF. While still a dynamo, this magnetoconvection effect differs from the magnetohydrodynamic effect present in the Earth's core.

External Sources

Sources external to the body of the Earth are located in the magnetosphere and ionosphere, combining to form what is generally termed the "external field". The ionospheric field takes its name from its inducing source in the moving ions of Earth's ionosphere while the magnetospheric field is generated by charged particles flowing through the magnetosphere. These two regions are coupled by Birkeland electrical currents (field-aligned currents) (Figure 1.2) which are aligned with magnetic field lines. Much like the MF, the magnetospheric field has a largely dipolar nature but with a magnitude of approximately $\pm$20 nT [Olsen et al., 2007] at Earth's surface although this can be much enhanced by the impacts of Solar activity and thus varies on much shorter time scales than the large-scale core field (Figure 1.3). The ionospheric field is also highly variable in local time due to the Sun's influence, it fluctuates on the order of $\pm$50 nT [Olsen et al., 2007] at Earth's surface between its day-side maximum and night-side minimum. The external field can vary quite dramatically between magnetic (i.e. Solar) "quiet" and "disturbed" times with variations up to $\mathcal{O}(1000)$ nT recorded as the effects of the Solar cycle (SC) and various forms of space weather bombard the Earth's magnetic field. The various sources and relationships between external fields are not discussed here in detail except where relevant in Chapter 2, a thorough summary can be found in Baumjohann and Nakamura [2007].

One of the major issues in the study of Earth's field is the separation of field sources. In both the temporal and spatial domain this can be a difficult task due to the overlap of the scales on which many of the sources operate, as illustrated in Figure 1.3. Generally

internal features are seen to vary more slowly than external features with the internal field varying on monthly to geological timescales and external fields varying on seconds to decadal timescales. The overlap of different sources is a particular problem when studying the MF as at small spatial scales the lithospheric field is dominant and at short periods the external fields have a significant effect. This rapid end of the MF variation is the regime in which geomagnetic jerks lie and thus one has to contend with such factors, as will be discussed at length later in this thesis.

1.4 GEOMAGNETIC OBSERVATIONS

The magnetic field of the Earth is a vector quantity and as such will be described throughout this work in either a local Cartesian vector form or in a spherical coordinate system. The definitions of each are illustrated in Figure 1.4.

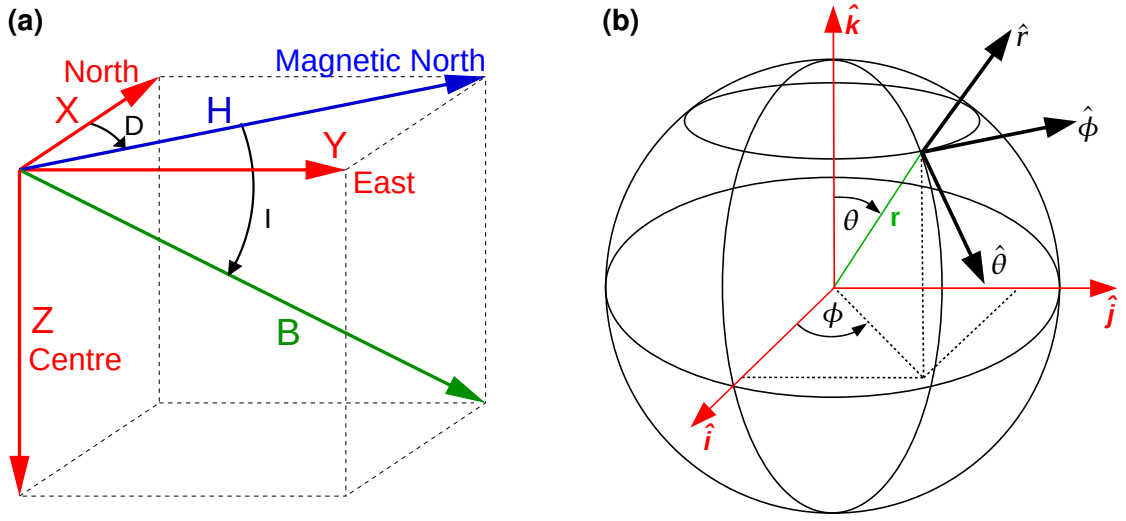

Figure 1.4: The magnetic field vector components in a local Cartesian coordinate system (a) and in a geocentric spherical system (b). In (a) the X-, Y- and Z-components relate to the geographic North, East and vertically downward (centre) directions respectively. They can be related to the field intensity, $\mathbf{B}$, and the horizontal intensity, $\mathbf{H}$, by the angle between magnetic and geographic North, declination D, and the angle between the horizontal plane and the field intensity, inclination I. In (b) the position is defined by the angles of co-latitude, θ, and longitude ϕ and the radius, r. The local system can be related to the spherical system as follows: $\hat{\theta} = -\hat{\mathbf{x}}$, $\hat{\phi} = \hat{\mathbf{y}}$ and $\hat{\mathbf{r}} = -\hat{\mathbf{z}}$.

Since the 16th century, mariners recorded magnetic declination (see Figure 1.4), and later inclination, for navigational purposes; however, measurements of horizontal and total field intensity were not possible until Gauss' work of 1832 [Jackson et al., 2000]. Modern observations are generally recorded in X-, Y- and Z-components at designated magnetic observatories spread across the globe as well as on satellites in orbit around Earth.

The *INTERMAGNET* programme was established in 1987 to oversee the provision of near real-time data from a global network of observatories operated by various organisations, adhering to high recording standards (accuracy of 1 nT). Data are channelled to *Geomagnetic Information Nodes* within 72 hours and stored centrally by the *World Data Centre for Geomagnetism*, currently operated by the *British Geological Survey* (*BGS*) in Edinburgh, United Kingdom. The locations of all *INTERMAGNET* associated observatories are displayed in Figure 1.5 (and details are in Appendix A). It can be seen that observatory locations are biased towards locations on land (and hence the Northen Hemisphere), particularly to Europe. While not used in this study, data are available from many other observatory locations which do not meet the *INTERMAGNET* standards and also from temporary repeat station networks, periodically rolled out across a particular territory for the purpose of studying the regional magnetic variations over longer periods. On a finer spatial scale, generally for the purpose of crustal field or industrial economic applications, aeromagnetic and oceanic based surveys can be carried out.

In addition to the spatial bias, there is also a variation of observatory distribution through time as observatories open and close (or meet the *INTERMAGNET* standards) as illustrated in Figure 1.6. Generally there has been an increase in the number of observatories operating and an improvement in the spatial distribution through time. A marked increase in the numbers of observatories appears after the *International Geophysical Year* in 1957–1958 and in recent years efforts have been made to establish observatories in the sparsely sampled Pacific, South Atlantic and Southern Indian Oceans. Regardless of the spatial coverage at a given point in time, the longevity of the recorded data series about that point must also be considered. Studies of the SV or SA need the perspective of several years of continuous data. As such both the temporal and spatial distribution biases play a strong role in the interpretation of results from observatory based studies.

The development of satellite measurements has greatly altered the temporal and spatial distribution of available data, with a great abundance recorded for relatively short durations (Figure 1.7). Satellites designed to measure the geomagnetic field typically fly in a close to polar orbit, passing through all latitudes at roughly the same local time of the day or night side while sweeping across longitudes with each orbit, at altitudes between 300 km and 800 km. Thus they circle the Earth in around 90 minutes, completing roughly 15 orbits per day. This leads to a very dense temporal sampling and a full surface coverage at roughly 24° longitudinal intervals each day. Scalar measurements can be made to an accuracy of <0.5 nT while vector data can have an accuracy of <4 nT root-mean-square

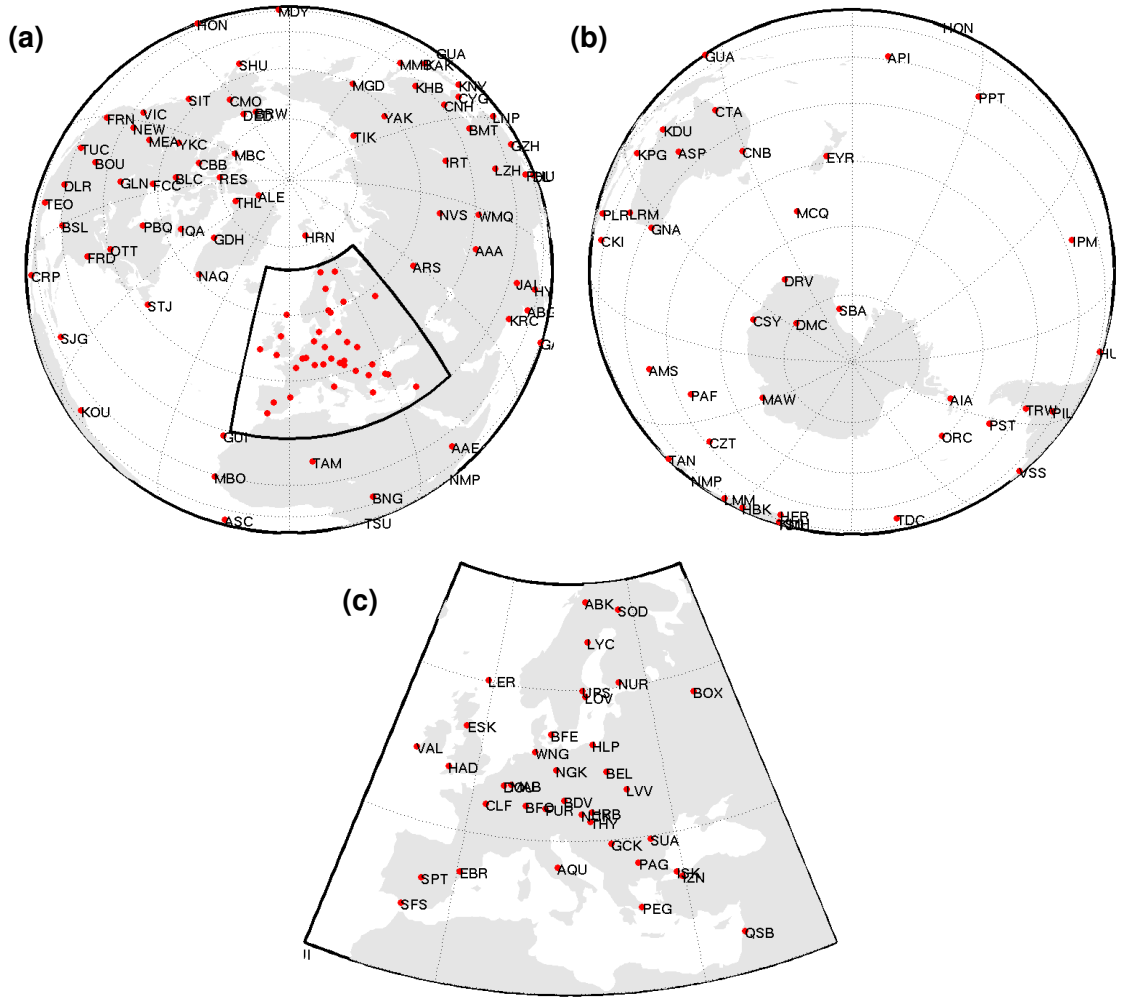

Figure 1.5: Maps of all *INTERMAGNET* observatory locations as of 2014, maps show observatories in the Northern Hemisphere (a), the Southern Hemisphere (b) and the dense network in Europe (c). The area of the zoom in (c) is marked as a black box in (a). Observatories are marked with their *International Association of Geomagnetism and Aeronomy (IAGA)* code, details of which can be found in Appendix A.

(RMS), limited predominantly by attitude (instrument orientation) errors [Olsen et al., 2007]. Measurements accuracy is expected to improve during the *ESA Swarm* mission, launched in November 2013, with initial results for 2014 indicating accuracy of <2 nT and as low as 0.2 nT for gradient data (made possible by the three satellite constellation) [Olsen et al., 2015]. Generally these data are used to create magnetic field models which can represent the magnetic field at any point in space and time during the duration of the model (see Section 1.5). Models of the late 20th century are constructed primarily from observatory data, with the inclusion of brief spans of *POGO* (*OGO-2/POGO-1*[1] 1965–1967,

[1] http://nssdc.gsfc.nasa.gov/nmc/spacecraftDisplay.do?id=1965-081A, 2015-03.

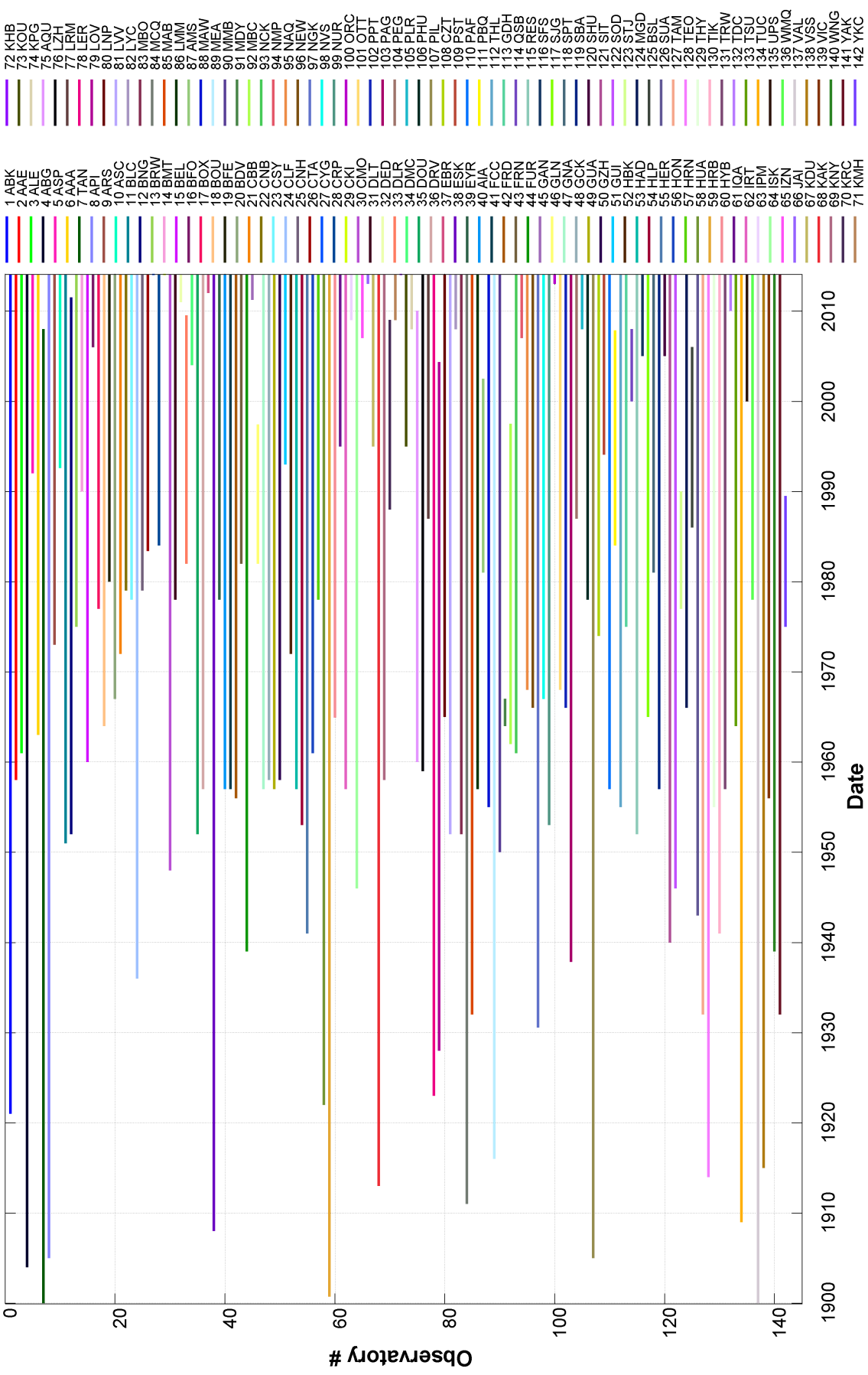

Figure 1.6: Operational timespans of *INTERMAGNET* affiliated observatories from 1900 to 2014 corresponding to maps in Figure 1.5. Observatories are marked with their *IAGA* code, details of which can be found in Appendix A.

OGO-4/POGO-2[1] 1967–1969, *OGO-6/POGO-3*[2] 1969–1971) [Langel and Hinze, 1998], *Magsat*[3] (1979–1980) [Langel and Estes, 1985] and *DE-2*[4] (1981–83) [Langel et al., 1988] satellite data. In the early 21st century, ever improving and more abundant satellite data from the *Ørsted*[5] (1999–present) [Neubert et al., 2001], *CHAMP*[6] (2000–2010) [Reigber et al., 2002], *SAC-C*[7] (2001–2004) [Olsen et al., 2006] and *Swarm*[8] (2013–present) [Olsen et al., 2015] missions provides a strong basis for many field models.

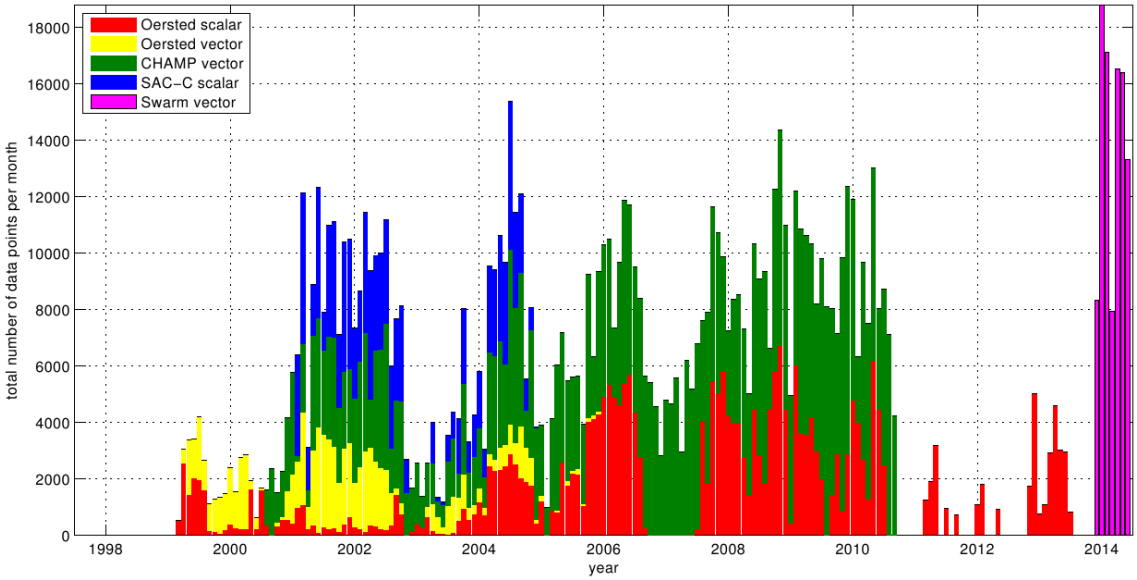

Figure 1.7: Histogram of geomagnetic satellite data coverage through time [from Finlay et al., 2014]. Pre-*Ørsted* satellite missions are not shown.

Since modern observations are made of the MF, the SV must be derived for each of the X-, Y- and Z-components. The SV can be calculated in many ways from MF data, throughout this work SV will be calculated as the annual difference of monthly means. Annual differences of monthly means are chosen as it reduces the great variability seen in monthly first differences allowing longer term trends to be seen while limiting the smoothing effect which results from methods involving longer period averages. Annual differences of monthly means implies the difference between monthly time samples 12 months apart so that the SV $(\dot{X}, \dot{Y}, \dot{Z})$ at 6 months between the two measurements is, in the X-component

[1] http://nssdc.gsfc.nasa.gov/nmc/spacecraftDisplay.do?id=1967-073A, 2015-03.
[2] http://nssdc.gsfc.nasa.gov/nmc/spacecraftDisplay.do?id=1969-051A, 2015-03.
[3] http://nssdc.gsfc.nasa.gov/nmc/spacecraftDisplay.do?id=1979-094A, 2015-03.
[4] http://nssdc.gsfc.nasa.gov/nmc/spacecraftDisplay.do?id=1981-070B, 2015-03.
[5] http://www.space.dtu.dk/english/Research/Projects/Oersted, 2015-03.
[6] http://op.gfz-potsdam.de/champ/, 2015-03.
[7] http://www.conae.gov.ar/satelites/sac-c.html, 2015-03.
[8] http://www.esa.int/Swarm, 2015-03.

for example,

$$\dot{X}(t_{k+6}) = X(t_{k+12}) - X(t_k), \tag{1.4.1}$$

with a sampling rate of $\Delta t_k = 1$ month. Where annual means are referenced, the SV as first differences of annual means is implied and refers to the difference between a given annual time sample and the next sample so that the SV at 6 months between the two measurements is,

$$\dot{X}(t_{k+0.5}) = X(t_{k+1}) - X(t_k), \tag{1.4.2}$$

with a sampling rate of $\Delta t_k = 1$ yr.

1.5 Field Modelling

While there are several ways in which the geomagnetic field can be modelled [see e.g. Langel, 1989, for a summary], the most relevant to this work is the spherical harmonic (SH) representation. This approach takes advantage of the spherical geometry of the Earth system and the wide spatial distribution of measurements and provides the ability to distinguish spatially distinct field sources. Models are produced to represent many parts of the field for a variety of purposes. For example, the *World Magnetic Model*[1] (*WMM*) defines the standard reference field for global navigation, attitude and headings as used by organisations such as the *North Atlantic Treaty Organisation* (*NATO*) [Chulliat et al., 2015], the *International Geomagnetic Reference Field* (*IGRF*) [Thébault et al., 2015] gives a definitive reference core field for many geomagnetic studies and high resolution models of satellite based measurements such as the recent *Swarm Initial Field Model* (*SIFM*) of Olsen et al. [2015] detail the temporal and spatial variations of the core field and the static lithospheric field. There are many categories of field modelling and there is of course overlap, some prominent approaches are those which attempt to simultaneously parameterise each source of magnetic field [e.g. the comprehensive models of Sabaka et al., 2002, 2004, 2015] and those which primarily model single magnetic sources, separating sources by data selection and sequential modelling and removal of field sources [e.g. Maus et al., 2007] or by treating remaining signal statistically as noise [e.g. Wardinski and Holme, 2006]. For the purposes of this thesis, models of the core field are of primary interest.

Outside of the source region, a magnetic field $\mathbf{B}$ can be considered to be the gradient

[1] http://www.ngdc.noaa.gov/geomag/WMM/DoDWMM.shtml, 2015-03.

of a scalar potential V,

$$\mathbf{B} = -\nabla V, \tag{1.5.1}$$

which satisfies a Laplace equation, following from Maxwell's equations, and describing the non-existence of magnetic monopoles such that,

$$\nabla^2 V = \nabla \cdot \mathbf{B} = 0. \tag{1.5.2}$$

This Laplace equation can be solved in terms of SH for the potential as,

$$\begin{aligned} V = \; r_E \sum_{n=1}^{\infty} \sum_{m=0}^{n} \Bigg\{ & \left(\frac{r_E}{r}\right)^{n+1} \left[g_n^m \cos m\phi + h_n^m \sin m\phi \right] \\ & + \left(\frac{r}{r_E}\right)^{n} \left[q_n^m \cos m\phi + s_n^m \sin m\phi \right] \Bigg\} P_n^m \left(\cos\theta\right), \end{aligned} \tag{1.5.3}$$

where θ and ϕ are co-latitude and longitude respectively, n and m are SH degree and order respectively, r is the location radius, r_E is the radius of the Earth, g_n^m and h_n^m are the Gauss coefficients for internal sources ($r \leq r_E$), q_n^m and s_n^m are the Gauss coefficients for external sources ($r > r_E$) and P_n^m denotes Schmidt semi-normalised associated Legendre functions. The dependence of the internal sources on the term (r_E/r) implies that these effects diminish as distance from the centre of the Earth increases while the dependence of the external sources on the term (r/r_E) implies that these effects increase with increasing radius. This allows the potential governing internal sources as measured outside of the Earth (away from the source region in the core) to be approximated by,

$$V = \; r_E \sum_{n=1}^{\infty} \sum_{m=0}^{n} \left\{ \left(\frac{r_E}{r}\right)^{n+1} \left[g_n^m \cos m\phi + h_n^m \sin m\phi \right] \right\} P_n^m \left(\cos\theta\right). \tag{1.5.4}$$

Following from Equations (1.5.1) and (1.5.4), the internally generated magnetic field can be approximated by the SH expansion, in spherical coordinates of,

$$\begin{aligned} \mathbf{B} = \sum_{n=1}^{\infty} \sum_{m=0}^{n} \left(\frac{r_E}{r}\right)^{n+2} \Bigg\{ & (n+1) \left[g_n^m \cos m\phi + h_n^m \sin m\phi \right] P_n^m \left(\cos\theta\right) \; \hat{\mathbf{r}} \\ & - \left[g_n^m \cos m\phi + h_n^m \sin m\phi \right] \frac{\partial P_n^m \left(\cos\theta\right)}{\partial \theta} \; \hat{\theta} \\ & + \frac{1}{\sin\theta} m \left[g_n^m \sin m\phi - h_n^m \cos m\phi \right] P_n^m \left(\cos\theta\right) \; \hat{\phi} \Bigg\}. \end{aligned} \tag{1.5.5}$$

Representing the field in this manner allows the downward or upward continuation of the field observed at one radius to any other radius, outside of the source region. These equations can be used to model the field by minimising the misfit of the modelled field to

the observed field, based on observatory and/or satellite measurements. Often this minimisation or objective function is weighted and regularised to account for data uncertainties, incomplete knowledge of the field in terms of sampling and ignorance of small spatial scales obscured by the crustal field as well as the desire to force the model to describe the core field only, despite observations including crustal and external fields. Generally such an objective function takes the form,

$$\Phi = \mathbf{e}^\top \mathbf{C}_d^{-1} \mathbf{e} + \lambda \mathbf{m}^\top \mathbf{C}_m^{-1} \mathbf{m}, \tag{1.5.6}$$

where $\mathbf{e}$ is the misfit between the modelled field and observations, $\mathbf{C}_d^{-1}$ is the data weighting matrix, $\mathbf{m}$ is the modelled Gauss coefficients, $\mathbf{C}_m^{-1}$ is the model weighting matrix and λ is a trade-off or damping parameter which balances the two terms of the minimisation function.

The modelling procedure above allows representation of the spatial structure of the field at a single snapshot in time. It is of interest to extend this description to also allow the modelling of the temporal variation of this structure. A time dependence of V and $\mathbf{B}$ can be described by the partial differentials of Equations (1.5.4) and (1.5.5) with respect to time. The results take the same form as Equations (1.5.4) and (1.5.5) but now with the coefficients $\dot{g}_n^m$ and $\dot{h}_n^m$ replacing g_n^m and h_n^m to describe the SV rather than the MF. Differentiating again with respect to time gives the SA coefficients, $\ddot{g}_n^m$ and $\ddot{h}_n^m$. Although the Gauss coefficients and each of their time derivatives describe the potential V and its time derivatives not the magnetic field $\mathbf{B}$, they will be referred to as MF, SV and SA coefficients here for simplicity. Exactly how the time evolution of the field is parametrised varies between models, the most common being B-splines [De Boor, 2001] of an order, in combination with a knot spacing, sufficient to describe the detail of the data [e.g. Jackson et al., 2000; Lesur et al., 2008; Maus et al., 2006; Olsen et al., 2014; Wardinski and Holme, 2006]. Common choices are cubic (order 4) B-splines [e.g. Jackson et al., 2000] which correspond to a minimisation of the SA squared over the core's surface, or order 6 B-splines [e.g. Lesur et al., 2010] which similarly correspond to a minimisation of the third time derivative. These temporal parameterisations, along with other additional constraints, are added to the minimisation function (Equation (1.5.6)) in the same manner as the spatial regularisation term and controlled by additional damping parameters.

Recently, an alternative to such an approach was described by Gillet et al. [2013] and Hellio et al. [2014] termed "stochastic field modelling" (not to be confused with field models from the "stochastic inversion" method of Gubbins [1983]). This approach employs an

ensemble of models, built from realisations of a stochastic process which describe the possible time evolution of the Gauss coefficients as constrained by their assumed mean values and covariances. By choosing a stochastic process which is not twice differentiable, so as to allow the occurrence of rapid jerk-like changes, Gillet et al. [2013] create a field model with markedly sharper time changes compared to the more traditional temporal regularisations. The details of the modelling process as applicable to the work of this thesis are discussed in Chapter 4 while applications of such a technique are then covered in Chapter 5.

Further separation of the internally generated field into core and lithospheric contributions can be made by the assumption that deep sources produce longer wavelength signals than shallow sources. This is illustrated by the Mauersberger-Lowes power spectrum [Lowes, 1966; Mauersberger, 1956] (Figure 1.8) which plots the power (averaged magnetic field, squared) of the magnetic field over a sphere of radius r given by,

$$R_n = (n+1)\sum_{m=0}^{n}\left(\frac{r_E}{r}\right)^{2n+4}\left[(g_n^m)^2 + (h_n^m)^2\right]. \tag{1.5.7}$$

It can be seen in Figure 1.8 that the spectrum resembles two intersecting linear trends with one dominating below approximately SH degree 14 and one above. Although the core and lithospheric fields have power at all degrees, it is assumed that the approximate cut off at degree 14 divides the regions dominated by the large-scale core field and the small-scale lithospheric field. The degree 1 component is particularly strong indicating the common first order approximation of a dipolar core field at the Earth's surface..

Throughout this thesis there will be many references to geomagnetic field models, the key details of relevant models are summarised in Table 1.1 and I refer the reader to the associated publications for full details.

1.6 CORE FLOW INVERSION

In order to discuss work on the generation of geomagnetic jerks and the implications of results later in the thesis it is necessary to have a basic understanding of how the flow at the surface of the outer core can be inferred from observations of the magnetic field.

The MF of Earth is generated by the movement of electrically conducting outer core fluid below the CMB. Knowledge of the resulting field and its time derivatives at Earth's surface or at satellite altitude can be used to infer the generating motions, under a series

Table 1.1: Overview of the geomagnetic core field models used or discussed in this thesis. Any regularisation of the core field is detailed in the notes column.

Model	Author	Era	Source [degree,order]	Data	Notes
gufm1	Jackson et al. [2000]	1590–1990	Core [14]	Maritime, land, observatory	Temporal cubic B-splines with 2.5 yr knots (SA penalised), spatial minimum Ohmic heating norm
CM4	Sabaka et al. [2004]	1960–2002	Core [13], lithospheric [65], ionospheric/induced [60,12], magnetospheric/induced [1], toroidal [60,12]	Observatory, *POGO*, *Magsat*, *Ørsted*, *CHAMP*, D_{st}-index, $F_{10.7}$-index	Temporal cubic B-splines with 2.5 yr knots (SA penalised)
C³FM	Wardinski and Holme [2006]	1980–2000	Core [15]	Observatory, *Magsat* 1980, *Ørsted* 2000	Temporal cubic B-splines with 2 yr knots (SA penalised), spatial minimum Ohmic heating norm, satellite snapshot end model constraints
xCHAOS	Olsen and Mandea [2008][a]	1997–2006	Core [20], lithospheric [50], external [2]	*Ørsted*, *CHAMP*, *SAC-C*, observatory, D_{st}-index	Extended version of *CHAOS*, temporal cubic B-splines with 1 yr knots (SA penalised)
GRIMM-2	Lesur et al. [2010]	2001.0–2009.5	Core [16], lithospheric [30], external [2]	*CHAMP*, observatory	Temporal order 6 B-splines with 1 yr knots (third time derivative penalised), minimised SA at end points
CALS3k.4	Korte and Constable [2011]	1000BC–1990AD	Core [10]	Archaeomagnetic, lake sediment	Temporal cubic B-splines with 10 yr knots, minimise radial SA at CMB, spatial minimum Ohmic heating norm, penalise departure from *gufm1*
C³FM2	Wardinski and Lesur [2012]	1957–2008	Core [14]	Observatory, *Magsat* 1980, *GRIMM* from *CHAMP* 2004	Temporal order 6 B-splines with 1.5 yr knots (third time derivative penalised), spatial minimum Ohmic heating norm, satellite snapshot model constraints, co-estimated frozen flux toroidal core flow
COV-OBS	Gillet et al. [2013]	1840–2010	Core [14], external [1]	Maritime, land, observatory, *POGO*, *DE-2*, *Magsat*, *Ørsted*, *CHAMP*, *SAC-C*	Temporal cubic B-splines with 2 yr knots (SA penalised), ensemble stochastic field modelling approach
CHAOS-4α	Olsen et al. [2014][b]	1997–2011	Core [20], lithospheric [100], external [2]	*Ørsted*, *CHAMP*, *SAC-C*, observatory, D_{st}-index	Preliminary version of *CHAOS-4*, temporal order 6 B-splines with 0.5 yr knots (third time derivative penalised)
IGRF-12	Thébault et al. [2015]	1900–2015, 2015–2020 prediction	Core [13]	Observatory, satellites	MF snapshots at 5 yr interval, linear SV prediction, average of various candidate models

[a] Time extended version of *CHAOS* [Olsen et al., 2006].

[b] Preliminary *CHAOS-4α* from http://www.spacecenter.dk/files/magnetic-models/CHAOS-4/CHAOS-4alpha/, 2015-03, updated version published in Olsen et al. [2014].

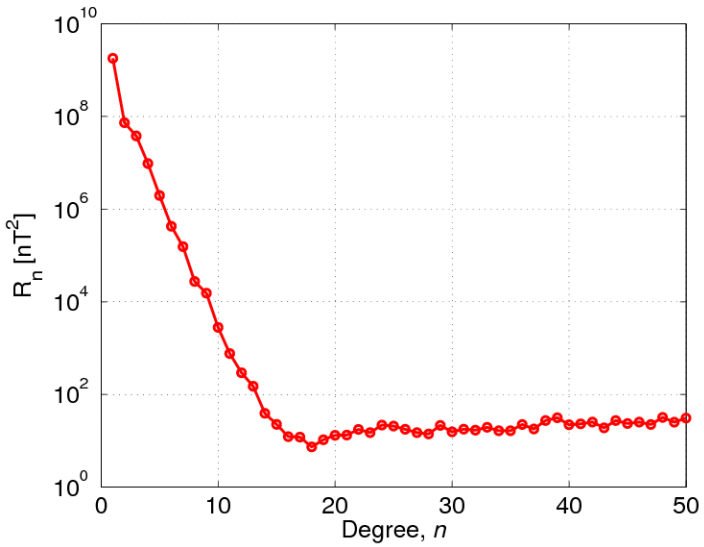

Figure 1.8: The Mauersberger-Lowes spectrum for the *CHAOS-4* field model of Olsen et al. [2014] at 2005.0 at the Earth's surface. The core field dominates below approximately SH degree 14 while the lithospheric field dominates above this point.

of assumptions and approximations. The theoretical basis for this procedure is briefly described here, more detailed accounts can be found in, for example, Holme [2007] and Finlay et al. [2010]. The following two equations and Equation (1.5.5) act as a starting point for the development of the ability to probe core flows. The evolution of flow, $\mathbf{u}$, is described as part of the conservation of momentum by the Navier-Stokes equation,

$$\rho_0 \left(\frac{\partial \mathbf{u}}{\partial t} + \mathbf{u} \cdot \nabla \mathbf{u} + 2\boldsymbol{\Omega} \times \mathbf{u} \right) = -\nabla p + \rho' \mathbf{g} + \mathbf{J} \times \mathbf{B} + \rho_0 \nu \nabla^2 \mathbf{u}, \tag{1.6.1}$$

where ρ_0 is the hydrostatic density with ρ' the departure from this, $\boldsymbol{\Omega}$ is Earth's rotation vector, p is the non-hydrostatic pressure, $\mathbf{g}$ is gravitational acceleration, $\mathbf{J}$ is electrical current density, $\mathbf{B}$ is the magnetic field and ν is the kinematic viscosity. The evolution of the magnetic field due to the effects of magnetic advection and diffusion is described by the induction equation,

$$\frac{\partial \mathbf{B}}{\partial t} = \nabla \times (\mathbf{u} \times \mathbf{B}) + \eta \nabla^2 \mathbf{B}, \tag{1.6.2}$$

where η is the uniform magnetic diffusivity.

Roberts and Scott [1965] showed that if the outer core is considered to be a perfectly conducting fluid beneath an electrically insulating mantle, a boundary layer at the top of the free flow in the outer core is necessary for the magnetic field to be continuous across the CMB. They consider that the material boundary which the CMB represents requires the radial component of flow to be zero as no material, only magnetic field lines, cross

into the mantle. Roberts and Scott [1965] argue that with the core being a good conductor (hydromagnetically) the diffusion timescale for creation and destruction of magnetic flux tubes in the core ($\sim$200,000 yrs for a length scale of the outer core shell using the electrical conductivity estimate of Pozzo et al. [2012]) is much greater than the advection timescale for fluid motion to redistribute field lines (SV operates at less than $\sim$1000 yr timescales), therefore advection can be assumed to dominate over diffusion. This leads to the frozen-flux approximation, whereby magnetic field lines are considered to be frozen into a moving flow of conducting material. While the toroidal components of the field must vanish at the CMB, the radial component is unaffected by any boundary layers, thus knowledge of the radial field (B_r) and its time variations ($\partial B_r/\partial t$) provides a direct link to the horizontal motion of the flow advecting the field lines. The simplification of Equation (1.6.2) is now,

$$\frac{\partial B_r}{\partial t} = -\nabla_H \cdot (\mathbf{u} B_r), \tag{1.6.3}$$

where ∇_H represents the horizontal component of the divergence operator. The factor of (r_E/r) in Equation (1.5.5) means that observations at the Earth's surface can be downward continued to the outer core to give estimates of the flow. The problem is in fact not solved at the CMB but for the top of the free stream, that is the top of the flow below the Ekman-Hartmann and magnetic diffusion boundary layers at the top of the outer core. This approximation is a common starting point for flow modelling but is also a topic of some debate as to whether length and time scale estimates are accurate and whether diffusion in the induction equation is truly negligible [see e.g. Bloxham and Gubbins, 1985; Bloxham and Jackson, 1991]. Recent reevaluation of the presence of a stably stratified layer at the top of the outer core [e.g. Buffett, 2014] may alter the length scale significantly and bring magnetic diffusion on par with the scale of the SV.

Further assumptions must still be made since a single equation (Equation (1.6.3)) cannot uniquely constrain the two dimensional horizontal flow. As well as the non-uniqueness of Equation (1.6.3) [see Backus, 1968], the downward continuation of a potential field whose spatial complexity is greatly dependent on distance from source and the limited knowledge of the small scale core field invoke additional non-uniqueness issues [see e.g. Eymin and Hulot, 2005; Gillet et al., 2009; Hagedoorn and Martinec, 2015]. It is necessary to make further simplifying assumptions as to the geometry or dynamics of the flow in order to reduce the number of parameters to be solved or to provide additional equations to constrain the problem [see e.g. Holme, 2007, for a summary of common dynamical

parameterisations]. Some authors also make assumptions regarding the extension of the core field spectrum to higher spatial degrees and attempt to assess the contributions of the un-observed small scale field to the large-scale flow [e.g. Gillet et al., 2009].

It is possible to relate a portion of a calculated core flow to independent measurements of the Earth's rotation rate, length-of-day (LOD), in order to verify the flow estimate. A core flow can be decomposed into poloidal and toroidal components with each then expanded in terms of SH. Jault [1988] demonstrated that when considering the timescales of Earth's rotational variations, rotation must be avoided on decadal timescales. Variations are accommodated by the oscillation of concentric cylinders of fluid aligned with the Earth's rotation axis (torsional oscillations), only two toroidal-zonal harmonics of the core surface flow are necessary to describe the angular momentum change of the entire core as a result of such a flow structure. Hence for any calculated core-surface flow, a prediction of LOD and change in LOD ($\triangle$LOD) contributions can be made and compared to measured values. This work was reinforced by Jackson et al. [1993] who assessed core flows inverted from observatory data between 1840 and 1990 and found that they could provide sufficient force to conserve angular momentum between the core and mantle, explaining decadal LOD observations.

1.7 GEOMAGNETIC JERKS

Geomagnetic jerks are a conspicuous yet poorly understood phenomena of Earth's magnetic field, motivating investigations of their morphology and the theory behind their origins. Jerks are most commonly defined by their observed form at a single observatory as "$\vee$" or "$\wedge$" shapes in a single component of the SV. The times of the gradient changes, which separate linear trends of several years, have associated step changes in the SA and impulses in the third time derivative (Figure 1.9).

Jerks have occasionally been termed "geomagnetic impulses" or "rapid secular variations/changes" but should not be confused with "rapid secular variation fluctuations" or "archaeomagnetic jerks". Mandea and Olsen [2009] suggested distinguishing: *geomagnetic jerks* as the result of torsional oscillations, fluid motion in the outer core on concentric cylinders aligned with the Earth's rotation axis; *rapid secular variation fluctuations* as field changes associated with core flow on monthly timescales; and *archaeomagnetic jerks* as millennial scale SV associated with convective motion and large-scale zonal flow in the core, although the term is more commonly used to describe changes of field direction or

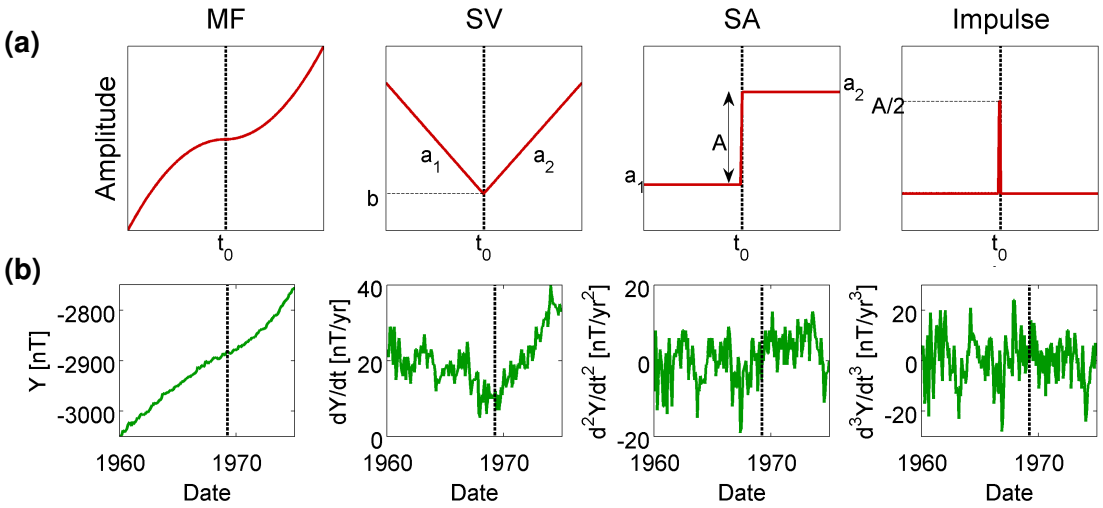

Figure 1.9: The idealised (a) and observed (b) morphology of a geomagnetic jerk in the MF and its first three time derivatives. A jerk at t_0 in (a) can be characterised by the SV gradients a_1 and a_2 and intercept b, the jerk amplitude (ΔSA) is $A = a_2 - a_1$. Observatory monthly mean Eastward-component data at Eskdalemuir, Scotland are depicted in (b) for the 1969 jerk for comparison. Plot (a) is adapted from Cox and Brown [2013].

intensity in centennial and millennial scale data. Since the source of jerks is still debated, I will simply use *geomagnetic jerk* to describe the gradient changes which separate periods of assumed linear SV on the scale of years.

The "$\vee$" shape SV definition of jerks includes an implicit expectation of a "large" magnitude step change in the gradient without definition of this scale or its threshold value other than the basic need for it to be observable in the data above the highly variable background noise. The impact of high frequency noise and rapid external field contamination on the ability to identify jerks is highlighted when the SA and third time derivative of observations in Figure 1.9b are compared to the theoretical case in Figure 1.9a. Such a comparison also illustrates why the SV is often the most straightforward data in which to detect jerks. Jerks can be described by their amplitude, that is, the difference in the gradients of the two linear SV segments about a jerk, $A = a_2 - a_1$, where a_2 is the gradient after the jerk and a_1 is the gradient before the jerk. This measure is essentially the best fit SA change (ΔSA) across a jerk. Jerk amplitude is thus positive for a positive step in SA and negative for a negative step. Here I do not consider spatial extent in the definition and refer to individual features in one field component of a given observatory time series as a single jerk.

The phenomenon of a geomagnetic jerk was first reported by Courtillot et al. [1978] as an abrupt turning point separating the otherwise linear trends of the Y-component of SV prior to and after 1970 at several Northern Hemisphere observatories. The authors

also suggested that jerks occurred in 1840 and 1910, all corresponding to minima in Earth's rotation rate. The range of jerks detected since this work are noted in Chapter 2. The origins of these phenomena were debated primarily by Malin and Hodder [1982] who suggested internal origins, and Alldredge [1984] who suggested some external component was present in the observatory records. Nevanlinna [1985] showed that external signal contributions to the 1969 jerk were present but small compared to the internal contribution. A large span of observations were similarly considered by Nagao et al. [2002a], who investigated possible external origins and concluded that the X- and Z-component features of jerks cannot be explained consistently by external sources. Spherical harmonic analysis (SHA) by Le Huy et al. [1998] and wavelet analysis by Alexandrescu et al. [1995] corroborated the generally accepted view of the internal origin of jerks as a feature of large-scale SV. The debate has again been broached by Demetrescu and Dobrica [2014] who argue that the sharp SV change associated with jerks is in fact an external effect linked to the 11 yr SC and that the internally produced component of the SV merits a different jerk definition than that used in this work.

The specifics of internal origins are still debated: variations in outer core flow near the CMB and mechanisms such as wave oscillations have been investigated in numerous ways. Pinheiro and Jackson [2008] showed that jerks can be viewed as simultaneous events across the CMB, influenced by variations in mantle electrical conductivity, after the mantle filter theory of Backus [1983], to produce the observed variation in occurrence times by location. The possibility of negligible mantle effects and a spatially complex, non-simultaneous origin at the CMB were not ruled out however. It has been demonstrated that steady flows [Waddington et al., 1995] and steady flows in an azimuthally drifting reference frame [Holme and Whaler, 2001] cannot explain jerks suggesting flow acceleration is a key part of the phenomena [Bloxham et al., 2002; Olsen and Mandea, 2008]. Bloxham et al. [2002] investigated a combination of steady flow and torsional oscillations and concluded that this can explain some features of jerks and the SV in general but failed to explain, in particular, features involving a component of axially symmetric field. Zonal flows have been found to partially explain jerks [Wardinski et al., 2008] while tangentially geostrophic and quasi-geostrophic flows [Gillet et al., 2009] have been shown to explain jerk features. Silva and Hulot [2012] conclude that while torsional oscillations are too simple to explain the observed SV and SA, quasi-geostrophic flows comply with the core flow accelerations that observations imply. Chulliat et al. [2010] demonstrated that a core field acceleration pulse is a likely cause of the 2003 and 2007 jerks. Extending this suggestion with a potential

step towards a more formal definition for jerks at the CMB, Chulliat and Maus [2014] show that SA pulses centered on 2006 and 2009 form part of a 6 yr period standing wave which can be related to the successive 2003, 2007, 2011 jerks. This standing wave could not be explained by the toroidal zonal flow of torsional oscillations [Chulliat and Maus, 2014]. Recently Qamili et al. [2013] suggested jerks are expressions of more chaotic and unpredictable field behaviour, this may allude to jerks being at the more rapid end of a poorly understood spectrum of core dynamics.

Numerous links have been made between geomagnetic jerk occurrences and other observables [see Mandea et al., 2010, for a review], particularly those related to Earth's rotation such as ΔLOD [e.g. Holme and de Viron, 2005, 2013], Chandler wobble [e.g. Gibert and Le Mouël, 2008] and the wander of Earth's rotation pole [e.g. Golovkov et al., 2003] suggesting there may be significant angular momentum exchange between the core and mantle as a result of the core flows related to jerks. The computation of high resolution core related LOD time series by Holme and de Viron [2005, 2013] showed instances of sub-decadal oscillations resulting in a poor fit to a smooth (decadal) profile. These sub-decadal oscillations appear to correlate with jerk occurrences; Holme and de Viron [2005] went on to predict the identification of the 2003 geomagnetic jerk based on this correlation. While these links are not certain, some headway has been made to show that core flows relating to observations of jerks may be able to produce variations in Earth's rotation [e.g. Nakada, 2009, 2011].

The details of previously published jerk detection methods are discussed in Chapter 2, setting up the original work on this topic, documented in the remaining parts of Chapter 2 and Chapter 3.

1.7.1 Smoothing of Geomagnetic Jerks in SV Calculation

It should be noted that by calculating the SV as the annual differences of monthly mean data by Equation (1.4.1), a smoothing effect is applied to the data. This smoothing is equivalent to a twelve month running average and results in the monthly SV data possessing a two-fold, and not twelve-fold, increase in temporal resolution over first differences of annual mean data (calculated by Equation (1.4.2)). The impact of the smoothing is illustrated in Figure 1.10 where the significance of this effect, particularly for the consideration of the second and third time derivatives of the magnetic field, is evident. Jerks which occur instantaneously in time will no longer appear to do so when any level of smoothing is applied to the data and thus a jerk duration, T, is introduced.

The smoothing effect can be seen to have limited impact on the SV timeseries; while a jerk can no longer truly appear instantaneous and an increased occurrence time uncertainty would likely be identified, the effect would likely be indistinguishable given the expected level of noise in observatory data. The use of annual mean data would introduce a greater smoothing, and thus greater jerk time uncertainty. In the SA and the third time derivative the smoothing effect on monthly mean data is more noticeable. A detection method designed to identify jerks in these higher derivatives would need to consider the apparent morphology of jerks in each case and not assume that jerks are instantaneous [as in e.g. Nagao et al., 2003]. Whether the physical process which generates jerks is or indeed can be instantaneous in time remains to be conclusively proved. I will maintain the working assumption of jerks as 'v' shapes in this thesis.

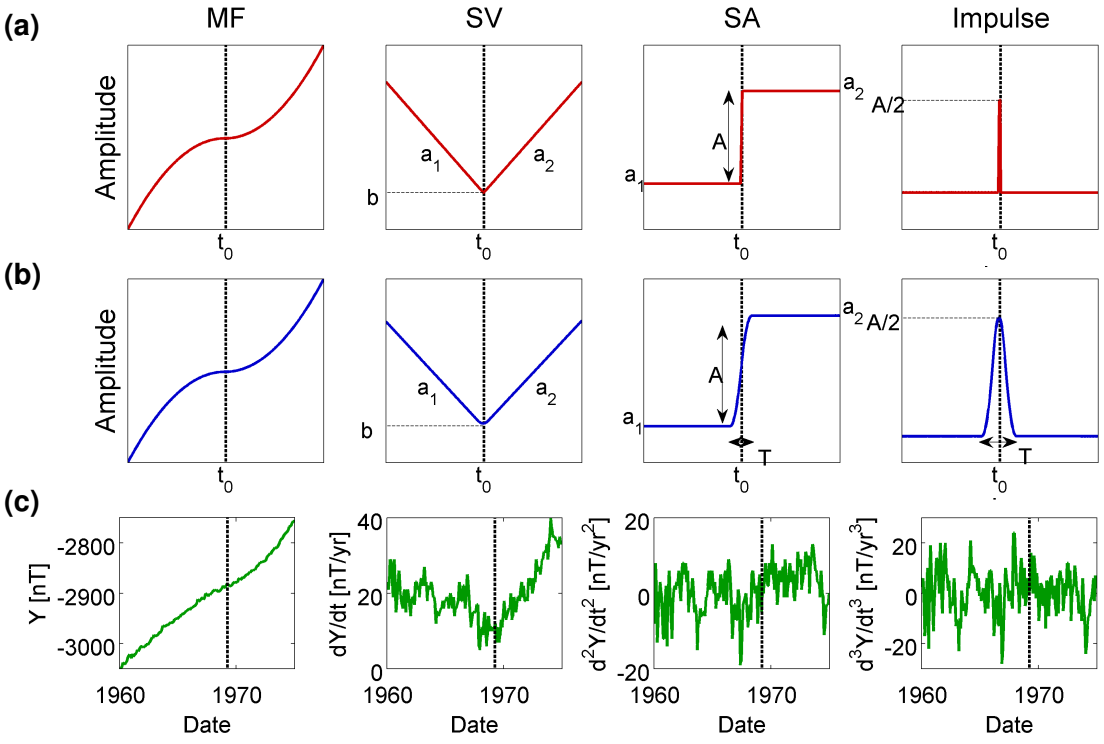

Figure 1.10: As Figure 1.9 but with the jerk shown in (a) smoothed to produce (b) by taking annual differences of the monthly samples, leading to a jerk duration, T. Plots (a) and (b) are scaled to give the same number of time samples and amplitude range as the real data in shown (c). Plot (a) is adapted from Cox and Brown [2013].

1.8 Motivation, Aims and Thesis Structure

1.8.1 Motivation

Knowledge of rapid geomagnetic variations — jerks — gives a view of the effects of the core's internal behaviour at the most rapid timescales observable. An obvious question is, why do we wish to understand the rapid dynamics of the core at all? Aside from the intrigue of one of the fundamental and defining workings of our planet, ultimately, understanding jerks and the generation of the geomagnetic field in general could lead to the improved ability to predict the future behaviour of the internal field. Since this field protects Earth, and particularly our modern technologically reliant lifestyle, from Solar radiation it is important to understand, monitor and prepare for the consequences of variations of the magnetic field and the related impacts from Solar activity.

An aspect where understanding jerks could directly benefit is in magnetic field modelling. Currently the *IGRF* assumes linear SV over 5 yr periods and is quickly made obsolete by the occurrence of jerks, that is, non-linear SV. The SV can be modelled retrospectively but prediction of variations, even over short timescales (a few years), is challenging and requires a reliable technique and the necessary observation and data management infrastructure. One approach being developed is to observe and model the internal field, invert this model for the responsible core flow and assuming the dynamics of this flow or through a trained numerical geodynamo model, propagate it forward in time to predict the future field variations [e.g. Beggan and Whaler, 2009; Kuang et al., 2008]. So-called "data assimilation" techniques are prevalent in the fields of weather and ocean dynamic forecasting and are being developed for geomagnetic purposes [see review in Fournier et al., 2010] but fundamentally, the core dynamics need to be understood for such a procedure to be implemented effectively. A stepping stone to this more complex solution might be to clarify the relation between non-linear SV such as jerks and other observables of core dynamics such as LOD, which may allow limited prediction of future variations.

If we are to understand the source mechanisms which could generate jerks, we must first understand the observational evidence. Since observations of internal variations at rapid timescales are masked by external fields, accounting for such noise must be considered. Furthermore, because our observations are sparse it is wise to assess what effects this could have on our interpretation of jerks.

1.8.2 AIMS

The aims of this thesis are as follows:

- To catalogue systematically the observations of jerks and quantify their characteristics.
- To assess how representative our observations of jerks are through synthetic models and to infer likely characteristics of jerks.
- To evaluate what the results of these analyses inform us about the nature of the source of jerks in the Earth's core.

1.8.3 THESIS STRUCTURE

Chapter 2 reviews and discusses the removal of external field signal from observatory data and methods for identifying geomagnetic jerks. This leads to the development of a new two-part data cleaning and jerk identification method which is then applied to monthly mean observatory data to address the first main aim of this thesis. This method considers how well a simple jerk model can be fit to data with minimal prior constraints on the timing and form of jerks. The results of this study are presented in Chapter 3. I find that jerks are frequent occurrences in all field components with complex and irregular global temporal and spatial patterns and are not globally contemporaneous. While jerks are observed in all years over the time period studied, there are relative peaks in the number of jerk occurrences globally which correspond to previously suggested global and local jerk times. Jerks are observed as localised patches of high SA and jerk amplitudes in Europe show periodic variations which may indicate a regularity in the source mechanism.

The sparse spatial distribution of observations raises the question of how reliable these results and their subsequent interpretations can be and so with the second main aim in mind, Chapter 4 describes the theory and methodology of building stochastic synthetic field models with which to investigate the influence of sampling. The synthetic models are shown to have statistically similar temporal and spatial content to observations. When the jerk detection algorithm of Chapter 2 is applied to the synthetic models, jerks are observed with similar properties to those in observatory data. The results of the identification of jerks in the synthetic field models are presented in Chapter 5 and comparison to the results from observatory data are drawn. I use SHA to investigate the spatial scales and patterns of jerks. The synthetic models suggest that observatory distributions are sufficient to resolve

an underlying large-scale structure to jerks and close parallels can be seen between the synthetic and observed jerk distributions, in time and space. Comparison of densely and sparsely sampled synthetic models to observations reinforce my interpretation that jerks are manifested at the Earth's surface as localised patches of intense SA which can occur in all field components in an irregular manner and are not globally contemporaneous. I also find that the observation of periodicity in jerk amplitudes and the variation of this property spatially as suggested by observations can be recreated by the synthetic models and are likely robust observations. Inferences about the characteristics of jerks at the CMB are made from the downward continuation of the analyses at the Earth's surface. I suggest that results are consistent with a chaotic turbulent regime in the core being responsible for the observed properties of jerks.

Chapter 6 draws the thesis to an end with a summary of the work and discussion of outstanding questions and future directions of work.

CHAPTER 2

GEOMAGNETIC JERK DETECTION

2.1 OVERVIEW

This chapter begins the investigation of geomagnetic jerks recorded in observatory data. A variety of methods and data have been used in the past to study the occurrences and characteristics of jerks, these will be reviewed and built upon to develop a new method for jerk identification. I describe and test a method to tackle two of the greatest challenges for such studies: firstly to reduce the contamination of observatory data by externally sourced fields and secondly, to identify all features which fit a given definition of a jerk in a robust and quantifiable manner with minimal *a priori* information. The aim of this is to systematically catalogue the observations of jerks in order to be able to better quantify their characteristics. Such knowledge is the first step towards a better understanding of the phenomena and their source in the dynamics of the core.

This study is structured in the following manner. Section 2.2 reviews the existing literature regarding externally sourced magnetic signals, in particular their contamination of and removal from observatory measurements. Next, in Section 2.3, works concerned with geomagnetic jerks are discussed, focussing on methods for the identification of jerks in timeseries. Following from this background I introduce and validate through testing, a two-step method to remove external field noise and to identify jerks in the data, in Section 2.4. The observatory data to be used is described in Section 2.5 and the applicability of monthly means is discussed. This chapter is then summarised in Section 2.6 to lead into Chapter 3 where the results of this study are presented and subsequently interpreted.

2.2 EXTERNAL SIGNALS IN OBSERVATORY DATA

Externally generated magnetic signals overlap the periods at which rapid internal field variations occur and thus are a significant noise source for studies of the internal field of the Earth, particularly at sub-decadal periods. This overlap means that internal and external fields cannot be separated in the frequency domain [Stewart and Whaler, 1992]. A major source of external signals are electrical currents present in the ionosphere and magnetosphere of the Earth. The secondary magnetic fields which are induced by external signals in the solid Earth can be particularly problematic since they cannot be distinguished by source separation (e.g. by spherical harmonic analysis) from internally produced fields [Wardinski and Holme, 2011]. It has long been known that observatory data are contaminated by externally sourced fields, particularly through the prevalence of 11 yr period variations (and their shorter period harmonics [Courtillot and Le Mouël, 1976]), related to the SC, which remain in the residuals when smoothed trends are removed from the MF or SV [see e.g. Ducruix et al., 1980, and references therein]. External field variations are generally seen in the X- and Z-components, related to the orientation of the magnetospheric ring current at mid- to low-latitudes and the auroral electrojets which circle the poles at high-latitudes [see e.g. Stewart and Whaler, 1992]. Thus the Y-component is often least contaminated and shows rapid internal features such as jerks most clearly, hence why many studies focus only on this component (see references in Table 2.1). Such geometric effects can be emphasised by the use of geomagnetic dipole coordinates — rotating geographic North (X) and East (Y) to magnetic North and East as in, for example, Pinheiro et al. [2011]. With the knowledge that observatory measurements include external signals it is possible to design ways in which to process this data to produce measures of that external content, namely geomagnetic indices.

2.2.1 GEOMAGNETIC INDICES AND EXTERNAL FIELD FEATURES

At any given time the observed geomagnetic field is a combination of regular (from permanent sources) and transient (from temporary sources) variations [Mayaud, 1980]. A geomagnetic index is a set of discrete values through time which aims to summarise the measurements of a particular geomagnetic phenomenon. This follows the notion that the field can be thought of as “quiet” when only regular variations are observed, e.g. the MF, or “active” (“disturbed”) when variations from transient sources, e.g. geomagnetic storms, are observed. Through complex and varied construction, indices provide the means to analyse

the variations of a phenomenon and to draw comparison to other phenomena which may be related. This has lead to the use of indices which quantify external field activity for the selection of data or the removal of correlated signals in observatory records. The D_{st}-index has historically been used to remove a major component of external field signals, the equatorial ring current, from observatory data and is introduced in the following section, as well as the geomagnetic phenomena it attempts to chronicle. Given the spatial distribution of observatories (Figure 1.5) and since observatory data are generally averaged over monthly or annual periods, the effects of short lived auroral phenomena are generally less prevalent than those of the ring current, in part because there are few observatories at high latitudes. A thorough review of geomagnetic indices and their applications can be found in Mayaud [1980] and Rangarajan [1987].

THE RING CURRENT AND D_{ST}-INDEX

The storm time disturbance index or D_{st}-index is a measure of the enhancement of the symmetrical (Westward) magnetospheric equatorial ring current, generally seen as a depression of the H-component of the magnetic field [Love and Remick, 2007]. The ring current is the electrical current which manifests due to motion of charged particles present in the plasmasphere of the Earth. No clear distinction between ring current particles and those of the Van Allen belts (trapped radiation belts) is made; most of the ring current is carried by trapped particles and all trapped particles contribute to the ring current [Kivelson and Russell, 1995]. The term ring current emphasises contribution to total current density while the term Van Allen belt emphasises penetrating radiation [Kivelson and Russell, 1995]. Trapped particles gyrate in a helical manner about magnetic field lines as a result of the Lorentz force, but are repelled from the dense concentrations of field lines in the polar regions and accelerated back towards the field minimum at the magnetic equator. As the particles are repeatedly turned back towards the magnetic equator, the gradient of the magnetic field causes a longitudinal drift to occur [Baumjohann and Nakamura, 2007; Daglis et al., 1999] (Figure 2.1). The direction of this drift is dependent on the charge after the principle of Guiding center motion. Thus positive particles (primarily protons but also α-particles and an abundance of ionospheric oxygen (O^+) during storm times) drift Westward, negative particles (electrons) drift Eastward at altitudes of approximately 2–9 r_E [Kivelson and Russell, 1995]. This net movement of charge Westward results in a current which circles the low latitudes. This circulating current generates a magnetic disturbance field predominantly aligned to the Earth's dipole axis, the X-component, orientated in a

Southward direction. This depression of the field occurs only within the ring of current, the magnetosphere outside the ring is strengthened. During magnetic storms, enhanced Solar activity causes an increase in incident particles, enhances the ring current and depresses the magnetic field to a greater degree. It should be noted that depression of the H-component of the magnetic field during storms is predominantly, but not solely, due to the ring current; other ionospheric and magnetospheric currents are also enhanced, hence why the H-component and not simply the X-component is considered Mayaud [1980].

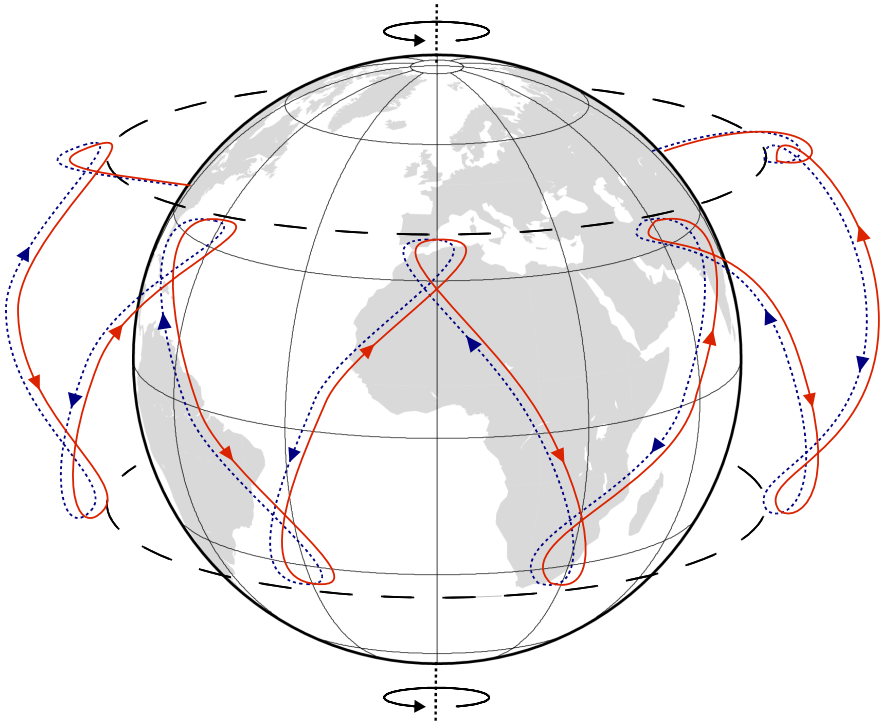

Figure 2.1: Particle drift of the equatorial ring current. Particles gyrate along helical paths following the approximately South–North dipolar field lines. The high density of field lines in the polar regions repels the particles causing them to be accelerated towards the magnetic equator, leading to a North–South bouncing path across low latitudes. Negative particles drift Eastward (red line), positive particles drift Westward (blue dashed line). Adapted from Kivelson and Russell [1995].

The D_{st}-index is calculated as the residual variation seen when the trends of quiet Solar activity days and mean horizontal field values are subtracted from the observed horizontal field,

$$D_{\mathrm{st}} = H_{\mathrm{obs}} - S_q - H_0, \tag{2.2.1}$$

where H_{obs} is the observed horizontal field value, S_q is the value of linear midnight-to-midnight trends in the Solar quiet variation of the five International Quiet[1] (IQ) days each month and H_0 is the value of a parabola fitted to the mean horizontal field values of the

[1] IQ days are the globally determined, five most geomagnetically quiet days each month [Mayaud, 1980].

IQ days. Equation (2.2.1) is then normalised to values on the magnetic equator [Mayaud, 1980]. Due to the large-scale nature of the spatial and temporal variation of the ring current, wide observatory coverage is acceptable to calculate the index [Rangarajan, 1987]. Historically four observatories (HER, HON, KAK, SJG) at roughly even longitudinal spacing and angular distance from the magnetic equator were used to calculate the index [Rangarajan, 1987]. These observatories must be located in the lower-mid latitudes to best observe the ring current while minimising the effects of the auroral zone. In recent years observatory records have been used to extend the timespan of the index back in time and to introduce a more dense array of observatories included in the calculation of the index to better observe local variation in partial ring current activity [Karinen and Mursula, 2005; Mursula and Karinen, 2005; Mursula et al., 2011].

The original index as recorded from 1957–present is termed the D_{st}-index[1]. An extended index covering 1932–present and correcting known issues in the original D_{st}-index calculation is termed the D_{xt}-index and includes the observatory CTO as a precursor to the HER record prior to 1957 [Karinen and Mursula, 2005, 2006; Love and Gannon, 2009; Mursula and Karinen, 2005]. A third version of the index termed the D_{cx}-index is also available for the period 1932–present and represents the D_{xt}-index with a new treatment of semi-annual and quiet Solar variations [Mursula and Karinen, 2005][2]. Hereafter when referring to the D_{st}-index in calculations it is the D_{cx}-index version which was used unless explicitly stated. Theory [e.g. Mursula and Karinen, 2005] and testing carried out during the work in Section 2.4 show that this version represents the most reliable form, with greatest signal content, and thus removes the greatest proportion of unwanted external signal across the longest timespan of data.

Regarding the use of the the D_{st}-index, Mayaud [1980] summarises well: "[The D_{st}-index] is essential for geomagneticians studying the regular variation of the MF because ring current effects are probably the main external source contributing to annual or monthly averages of the field elements." It is however accepted that not only the variations of the ring current are recorded in the index [Wardinski and Holme, 2011] and that while the ring current is predominantly symmetrical and independent of local time, there can be a significant asymmetrical local time dependent contribution to the ring current, often termed a partial ring current [Rangarajan, 1987]. This occurs especially during disturbed times; however, this component is likely to never be completely null [Langel, 1989].

[1] Available from the *WDC for Geomagnetism*, Kyoto (http://wdc.kugi.kyoto-u.ac.jp/wdc/, 2015-03).
[2] D_{xt}- and D_{cx}-index available from the *Dcx Server* of the *University of Oulu*, Finland (http://dcx.oulu.fi, 2015-03).

2.2.2 CLEANING OF OBSERVATORY DATA

A major source of external signals are electrical currents present in the ionosphere and magnetosphere of the Earth. The applicability of geomagnetic indices as a proxy for the strength of such external signals in observations has been investigated by numerous authors.

Gubbins and Tomlinson [1986] used various data selection criteria based on external field activity indices for generating monthly means to study jerks. Gubbins and Tomlinson [1986] note the problems of external signal contamination are aggravated by considering shorter sampling periods such as monthly means over annual means (averaging over annual periods will limit sub-annual variations), but that such use is necessary to study rapid features such as jerks. Comparing means composed of all daily values in a month, only the five IQ days (based on the K-index which quantifies the intensity of irregular currents at Earth produced by Solar radiation [see Mayaud, 1980; Rangarajan, 1987]), and only the days deemed quiet by the AE-index (describing auroral electrojet activity [see Mayaud, 1980; Rangarajan, 1987]) and D_{st}-index, they concluded that monthly data could be suitably cleaned of many external signals by averaging local midnight values on IQ days before removing annual and semi-annual period variations.

The aa-index (derived from the mean of scaled K-index values at two roughly antipodal observatories [see Mayaud, 1980; Rangarajan, 1987]) has been used by several authors to model external fields in the form of the residuals to smooth trends fitted to observed variations of the MF. Gavoret et al. [1986] and De Michelis et al. [1998] used the aa-index in conjunction with the Wolf relative sunspot number (R_z). The aa-index was also used by Stewart and Whaler [1992], who combined it with synthetic six- and twelve-month periodic signals to remove such content, believed to be Solar related, from observatory data. Gavoret et al. [1986] suggested that using the AE-index for high-latitude observatories and D_{st}-index for low-latitude observatories might best account for both ring current and auroral fields. From this De Michelis et al. [1998] assumed that the aa-index could thus generally account for the average levels of external fields globally. Subsequently, however, De Michelis et al. [2000] altered the approach to additionally include the D_{st}-index in their model parameterisation, pointing out that, as they mentioned in De Michelis et al. [1998], the aa-index only effectively improves the Y-component.

The D_{st}-index allows significant corrections to the X- and Z-components to be made. Stewart and Whaler [1992] found that their modelled disturbance fields took the form

of a predominantly dipolar field, aligned with the MF dipole but opposite in polarity, and additionally enhanced in the auroral zones. These corrections were employed later by Stewart and Whaler [1995] to allow the investigation of jerks in annual first difference data. The unsatisfactory correlation between the D_{st}-index and other indices as noted by De Michelis et al. [1998] and Gavoret et al. [1986] may well be a reflection of the corrections necessary to improve the calculation of the D_{st}-index described by for example Karinen and Mursula [2005].

Verbanac et al. [2007] proposed a method for removing external signals in observatory annual means using a combination of field models and magnetic indices. Detailed attempts to parameterise the external field sources as part of field models are documented by e.g. Sabaka et al. [2002, 2004, 2015] and Olsen et al. [2009], allowing modelled corrections for primary and induced ionospheric, magnetospheric and toroidal fields to be applied to observatory data. The third and fourth iterations of the comprehensive model series [Sabaka et al., 2002, 2004] for example parameterise external fields by the D_{st}-index and Solar radio flux index ($F_{10.7}$) amongst other conditions. The D_{st}-index parameterisation for magnetospheric sources is dropped by the fifth comprehensive model iteration [Sabaka et al., 2015] in favour of a static internal and external source SHA of data in discretised time bins. An alternative to the complex source parameterisations of such models is the statistical approach suggested by Wardinski and Holme [2011]. While source parameterisations are effective for those sources which are understood, they are complex and computationally expensive compared to methods such as that of Wardinski and Holme [2011] which will be discussed further in Section 2.4.

A relatively recently proposed index for quantifying ring current activity is the RC-index [initially Olsen, 2002], applied as part of the field modelling procedure of the *CHAOS* models [most recently Olsen et al., 2014]. The RC-index intends to describe ring current activity, including accounting for night-side, quiet-time variations of the symmetric and asymmetric ring current and is aimed at benefitting field modelling of satellite data. It was developed to enable asymmetric ring current activity to be accounted for and to address issues of a questionably stable baseline for the D_{st}-index as well as allowing much faster production of definitive values [Olsen, 2002].

The RC-index may indeed provide an improved ring current description over the D_{st}-index, however as it was not fully realised until 2014 [Olsen et al., 2014] and currently applies only to the satellite era, an in depth study of its application to external signal removal from observatory data was not conducted for this thesis. Some preliminary

results (see Appendix B) suggest that this may be a worthwhile venture in the future as cleaning with the RC-index accounts for a greater proportion ring current signal at a wider distribution of observatories and allows for smaller scale variations of partial ring currents than cleaning with the D_{st}-index.

Further progress in quantifying of external field signals may come with the overlap of the the multi-satellite missions *Swarm*, *Cluster*[1] and *THEMIS*[2] and attempts at direct assessment of current systems at various radii in the ionosphere and magnetosphere as well as during concurrent overpasses of these missions [see e.g. Shen et al., 2012; Shore et al., 2013].

2.3 JERK IDENTIFICATION TECHNIQUES

The majority of documented jerk occurrences are considered to be during the latter half of the 20th century as this period is covered by a widely established network of observatories. Since 1999, near continuous satellite measurements have also been available. Pre- and early-20th century jerks have been discussed, generally in historical declination and inclination records as compiled by Malin and Bullard [1981], Cafarella et al. [1992], Barraclough [1995], Alexandrescu et al. [1996a], Soare et al. [1998], Korte et al. [2009] for London, Rome, Edinburgh, Paris, Bucharest and Munich, respectively. These measurements are limited in terms of spatial and temporal resolution, and require much temporal smoothing due to limited measurement accuracy, making estimates of jerk occurrences unreliable. In the early 21st century, jerks have begun to be identified in satellite data that, while temporally limited at present, provide excellent spatial coverage.

The various field derivatives in which jerks can be observed (e.g. MF, SV, SA) mean that a wide variety of detection methods can be employed. A detection method must contend with several factors, for example: noise content in the data, which may be of several origins; the temporal, amplitude and spatial scales at which an event becomes significant enough to be a jerk; the proximity of consecutive jerks; and the asynchronous form of a jerk in each field component. An overview of events detected and the various techniques used are presented in Table 2.1. A broad summary of studies concerning geomagnetic jerks can be found in Mandea et al. [2010]. I will limit discussion here to addressing the strengths of past techniques to build upon and the deficiencies that remain

[1] http://www.esa.int/cluster/, 2015-03.
[2] http://www.nasa.gov/mission_pages/themis/, 2015-03.

to be overcome.

An idealised detection method for jerks might require no *a priori* information about the number, locations or form of jerks in a timeseries, and would robustly identify all jerks while providing quantitative uncertainties and errors on each of the parameters identified. In a realistic case one may wish these uncertainties to come in part from some measure of data quality or suitability.

Qualitative visual inspection clearly does not provide a sufficiently reliable basis on which to analyse and compare jerks. The most commonly used method is the original suggested, single event, linear regression of SV trends either side of a jerk [e.g. De Michelis et al., 2000; Le Huy et al., 1998; Le Mouël et al., 1982; Olsen and Mandea, 2007]. The main drawback lies in the requirement to pre-screen data for jerks — that is, to manually identify windows of data which are perceived to contain a single jerk and further analyse only this data. This selectiveness can lead to biased interpretations.

The issue of data pre-screening was addressed first by Whaler [1987] and Stewart and Whaler [1995] who utilised entire timeseries without *a priori* knowledge of jerk numbers or locations. Whaler [1987] assumed jerks occur simultaneously in all field components but the optimal piecewise regression algorithm of Stewart and Whaler [1995] was performed on individual components of MF timeseries, assuming quadratic forms which would lead to piecewise linear trends in the SV. While allowing the number and locations of jerks in a series to be determined more objectively, quadratic segments were allowed to overlap or be discontinuous and the trade-off between the number of quadratic sections and the misfit to the data was complex and required some subjective analysis.

Another method which addresses the issue of allowing the detection algorithm itself to define numbers and location of jerks, is based on wavelet analysis. Alexandrescu et al. [1995] initially described this technique, considering the MF as a combination of internal signal containing jerks as singularities, external long period signal and noise. The European Y-component application of Alexandrescu et al. [1995] was extended globally to both horizontal components by Alexandrescu et al. [1996b]. De Michelis and Tozzi [2005] adapted this analysis further with their local intermittency measure which aimed to improve the identification of only internally sourced discontinuities over those coming from external or other noise sources. While such techniques readily provided occurrence times of jerks without *a priori* knowledge, parameters such as jerk amplitudes were not defined and uncertainties were not calculated.

Nagao et al. [2002a,b] developed a third approach which considered whole timeseries

Table 2.1: Overview of key geomagnetic jerk detection works detailing data used, detection technique and events identified (adapted from Pinheiro et al. [2011] and Brown et al. [2013]).

Work	Data	Method	Jerks	Form
Le Mouël et al. [1982]	Annual means (X, Y, Z) 130 observatories	Least-squares (LS) fit two straight lines	1969	Global; amplitudes roughly zonal in X and Z, meridional in Y
Alexandrescu et al. [1996b]	Monthly means, combination of X and Y 74 observatories	Wavelet analysis	1901, 1913, 1925, 1932, 1949, 1969, 1978	'69, '78 global with N–S 2 yr delay; '01, '13, '25 possibly global; '32, '45 local
Alexandrescu et al. [1997]; Korte et al. [2009]	Various smoothed annual means declination, inclination 1–2 locations	Wavelet analysis, SA zero crossings	Various events 1410–1932	N/A insufficient coverage
Le Huy et al. [1998]	Smoothed annual means (X, Y, Z) 160 observatories	LS fit two straight lines	1969, 1978, 1992	All global; alternating sign; similar distribution of amplitudes
De Michelis et al. [1998, 2000]	Annual means (Y), 74 observatories; (X, Y, Z) 109 observatories	LS fit two straight lines	1991	Global; Y amplitude distribution similar to '69, '78
Mandea et al. [2000]	9 European observatories, monthly means (Y) 12 month running average	Visual	1999	Local
Nagao et al. [2003]	Monthly means (Y) ∼50 observatories	Statistical model LS fit two straight lines	1969, 1978, 1991	Global; N–S delay few yrs; '69, '78 show longer duration in South Africa
Chambodut and Mandea [2005]	Monthly means (Y), 12 month running average, 39 observatories, synthetic data from CM4 (Y)	Wavelet analysis/LS fit two straight lines	1971, 1980, 1991	Global but not simultaneous about '71, '80, '91; '91 most complicated structure
De Michelis and Tozzi [2005]	Monthly means (Y), 44 observatories	Wavelet analysis Local Intermittency Measure, LS fit two straight lines	1978, 1986, 1991, 1999	'86 local S Africa and S Pacific, '78, '91, '99 global; '78, '91 show N–S delay
Chambodut et al. [2007]	*CM4*	Rapid move of SA zero isoline, dynamic pressure local max	1968, 1978, 1985, 1990, 1999	1985 local Pacific, rest global
Olsen and Mandea [2007]	*CHAMP* monthly means (virtual observatories at 400 km altitude)	Spherical Harmonic Expansion/LS fit two straight lines	2003	Simultaneous but local around 90°E
Olsen and Mandea [2008]	*xCHAOS*	Visual	2005	Local, S Africa
Olsen et al. [2009]	*CHAOS-2* monthly means (virtual observatories at 400 km altitude)	Visual	2007	Local, W of Africa
Chulliat et al. [2010]	Monthly means (Y, Z) 5 observatories, *CHAOS-2*	Visual	2007	Local, Africa; jerks form in pairs from global acceleration pulse at CMB
Pinheiro et al. [2011]	Annual and monthly means and synthetic data from *CM4*	LS fit two straight lines	1969, 1978, 1991, 1999	'99 local, rest global; no consistency in component pattern; no consistency in global pattern; various regional delays
Qamili et al. [2013]	Synthetic annual Gauss coefficients from *gufm1*	Non-linear forecasting	Various events 1600–1980	Chaotic, unpredictable field behaviour
Chulliat and Maus [2014]	*CHAMP* SA models, monthly means (X, Y, Z)	SA modelling, visual	2003, 2007, 2011	Localised SA pulses (2006, 2009) from standing wave at CMB

of a single component of MF data without *a priori* knowledge of jerk occurrences. The method was based on a statistical time series model of MF data fit with a second order spline function, the optimal knot points of which represent jerk occurrences and were determined by maximum likeliness as judged by an Akaike Information Criterion. The method was extended by Nagao et al. [2003] to determine not just jerk occurrences but also jerk durations, the time span of the SA step associated with a jerk. While the jerk duration provides a form of uncertainty in occurrence time, by approximating the data with a smooth spline model initially, it is difficult to say how the parameters determined might hence relate to uncertainties induced by, for example, the noise level of the data.

Pinheiro et al. [2011] improved on the rigour of the single event analysis significantly by developing a technique to compute error bars in occurrence times and amplitudes based on the misfit of a two-part linear regression to annual means of SV either side of a jerk. This method provides a measure of likeliness, for all possible configurations of two joined linear trends, to determine the optimal jerk time and amplitude combination. Despite this improvement, data still required pre-screening.

There have been several works which utilise geomagnetic field models to overcome the spatial limitations of observatory data when studying jerks [see e.g. Chambodut et al., 2007; Chulliat et al., 2010; Olsen and Mandea, 2007, 2008; Olsen et al., 2009; Qamili et al., 2013]. While such models provide a much improved ability to analyse spatial distributions by generating timeseries at any location, they are inherently constructed to smooth variations both spatially and temporally. Despite the improving coverage and quality of both observatory and satellite data, field models cannot surpass the quality and extent of the original data used to construct them. I choose to avoid the additional uncertainty introduced by temporally and spatially smoothed field models and to investigate the extent to which direct measurements in the form of observatory data constrain the detection and thus justify the interpretation of jerks.

A key point illustrated by previous investigations is that in order to be more objective in the identification of jerks, a definition of the phenomenon is required. The catalogue of work shows that jerks must ideally be considered in entire timeseries, at unknown times, and not constrained to be simultaneous between field components or locations. In allowing such variation, it should become clear whether the data justifies conclusions of simultaneity or particular occurrence patterns. With no exact definition agreed upon I must suggest my own and try to soften this subjective aspect by searching for features in the observatory records which fit variations of this definition, explicitly and quantitatively assessing how

well this definition is met. This will allow all identified jerks and their associated properties to be attributed some uncertainty, adding weight to any interpretations made. The ability to associate uncertainties with jerk occurrence parameters makes the method of Pinheiro et al. [2011] attractive, in Section 2.4 I adapt the premise of this method to allow entire timeseries to be processed without the assumption *a priori* of known jerk occurrences.

2.4 METHOD

Here I describe a method comprising a combination of two primary components: the removal of external field signals from observatory monthly means after Wardinski and Holme [2011] (Section 2.4.1), and the identification of jerk events in the observatory data based on the premise described by Pinheiro et al. [2011] (Section 2.4.2). Finally in Section 2.4.3 the developed method is validated through testing with both synthetic and real data in order to inform the choice of parameters for the application to the observatory data.

2.4.1 EXTERNAL SIGNAL REMOVAL

Wardinski and Holme [2011] document a method to remove SV signals which correlate with the first time derivative of the D_{st}-index, representing primarily the activity of the magnetospheric ring current. Furthermore, Wardinski and Holme [2011] showed that the residual between observatory data and a magnetic field model can replace the D_{st}-index in their calculations as a proxy for unmodelled external signals. Removal of such signals was shown to reduce the standard deviation of the SV and thus improve the resolution of rapid internal features such as jerks. A full description of the method can be found in Wardinski and Holme [2011], a summary of which is given here.

The premise of Wardinski and Holme [2011] is that information regarding external field signals is contained in the unmodelled SV residual between observatory data and the internal magnetic field approximated by a field model. Coherent signal between the residuals to the SV of the X-, Y-, and Z-components can be described by a 3×3 covariance matrix, assumed to be constant through time at each given observatory location. The eigenvectors of this residual covariance matrix can then be used to rotate the observed and modelled field components into the directions of least-, intermediate- and most-coherent signal; these directions will be referred to as the ‘clean’, ‘intermediate’, and ‘noisy’ field components and correspond to the eigenvectors with the smallest to largest

magnitude eigenvalues, respectively. Two example sets of these rotated field components are depicted in Figure 2.2. The plots depict the three field vector components through time for the period 1957 to 2008, projected in the directions of the component axes, either X, Y, Z (Figure 2.2a,c) or clean, intermediate and noisy (Figure 2.2b,d). The projections are calculated such that if, for example, the clean-component was found to be exactly parallel to the Y-component, both component axes would be plotted parallel and the signal content would be identical.

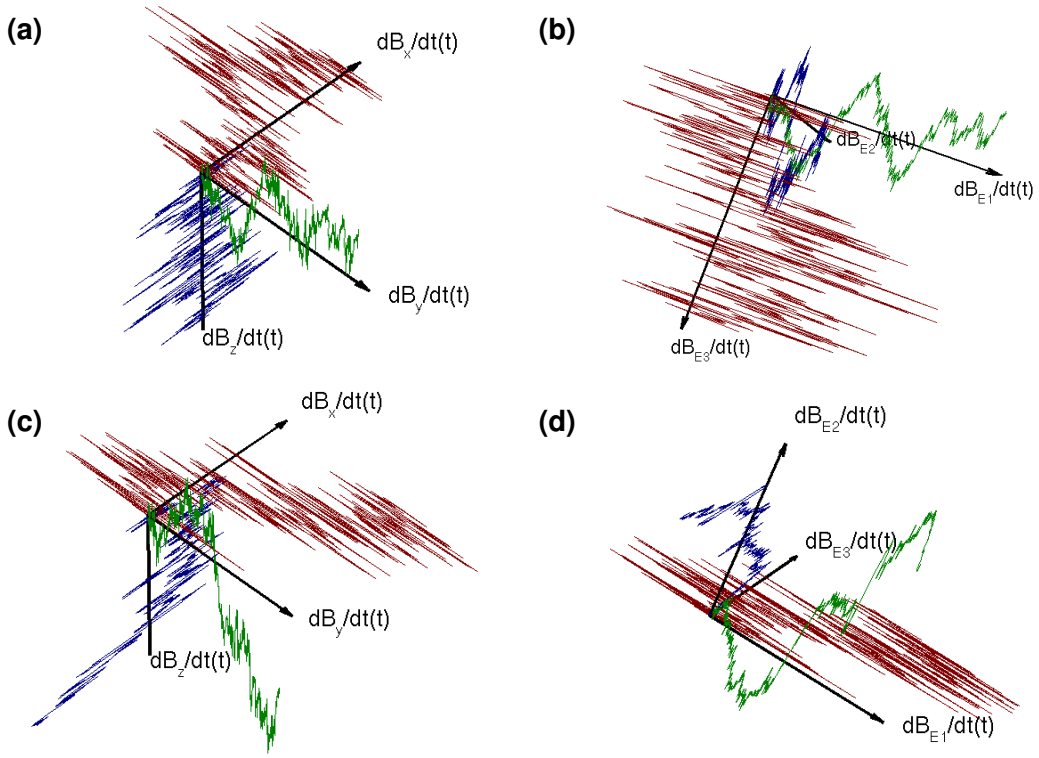

Figure 2.2: The magnetic field at NGK (Northern Hemisphere) for the period 1957 (base of arrows) to 2008 (tip of arrows) in (a) X- (red), Y- (green), Z-component (blue) directions and (b) in eigenvector directions corresponding to clean (E1, green), intermediate (E2, blue) and noisy (E3, red). Both are projected in the same local coordinate space, an eigenvector direction in (b) which points in the direction of either X, Y or Z in (a) would thus be parallel to that component geographically. The cleanest eigenvector component is most similar in direction and thus content to the Y-component while the noisy-component is predominantly made up of X-component signal. Plots (c) and (d) show the equivalent at HER in the Southern Hemisphere.

Wardinski and Holme [2011] showed that the noisy-components, at the 50 observatories used in their study over the period of 1980 to 2000, are approximately in the North-South plane, this orientation is shared by the 102 observatories used in this study (Figure 2.3). This North-South alignment and a strong zero-lag correlation of the unmodelled residuals in the noisy-component with $\dot{D}_{st}$, is consistent with external field signals generated by the equatorial ring current. However, Wardinski and Holme [2011] noted

a stronger correlation between the noisy-component residuals at different observatories than to $\dot{D}_{st}$, signifying that the index does not fully explain all the unmodelled residual in the noisy-component.

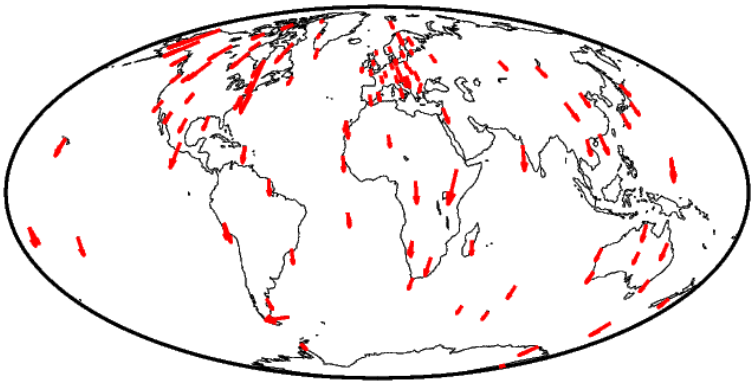

Figure 2.3: The eigenvector directions corresponding to the noisy-component at the 102 observatories used in this study. A common North-South alignment is seen, illustrating that the strongest coherent signal in the unmodelled residuals is likely an effect of the equatorial ring current.

It was proposed by Wardinski and Holme [2011] that a zero-lag correlation based weighting function can be used to remove signal which is coherent between the noisy-component residuals at different observatories, to produce SV time series with reduced external signal content:

$$\dot{r}_{\mathrm{cor}}(t_k) = \dot{r}_{\mathrm{noisy}}(t_k) - \frac{\sum_j \dot{C}(t_j)\, \dot{r}_{\mathrm{noisy}}(t_j)}{\sum_j \dot{C}(t_j)^2}\, \dot{C}(t_k), \tag{2.4.1}$$

where $\dot{r}_{\mathrm{cor}}$ is the corrected noisy-component SV residual, $\dot{r}_{\mathrm{noisy}}$ is the noisy-component unmodelled SV residual, $\dot{C}$ is the noisy-component unmodelled SV residual from an alternative observatory and subscripts j and k run over the number of time samples. This correction is applied only to the noisy-component residual before reforming the modelled and unmodelled residual component parts and rotating back to the original X-, Y-, and Z-component directions. This procedure therefore removes signal from the noisy-component residual, which when rotated back to geographic coordinates, results in a removal of signal from each component based on the strength of the correlation to the external signal proxy in each component.

An advantage of this statistical approach over source parameterisation is that it helps to account for localised induced fields that result from heterogeneity in subsurface electrical conductivity [Wardinski and Holme, 2011]. Wardinski and Holme [2011] state that parameterising the unmodelled SV residuals as a uniform external field and the resultant

induced effects does not adequately represent the variations observed. By treating the external field contamination statistically, more of this noise can be accounted for, at the expense of knowledge of the source. As in Wardinski and Holme [2011], I correct for external signal using the residual from the observatory at Niemegk (NGK), Germany, since it provides coverage of the entire timespan of interest with a well-documented and reliable record (Niemegk itself is corrected using data from Chambon-la-Forêt (CLF) observatory, France). No other reference observatory was found to produce a significant improvement on the overall results, likely due to the reliable record and location of Niemegk in central Europe, close to roughly 30% of the observatories used in this study. An example of the improvement made by applying the method to the data is shown in Figure 2.4. As expected the greatest signal variation is removed from the X- and Z-components, with limited improvement to the Y-component (Figure 2.5). As can be seen in Figure 2.5, the greatest

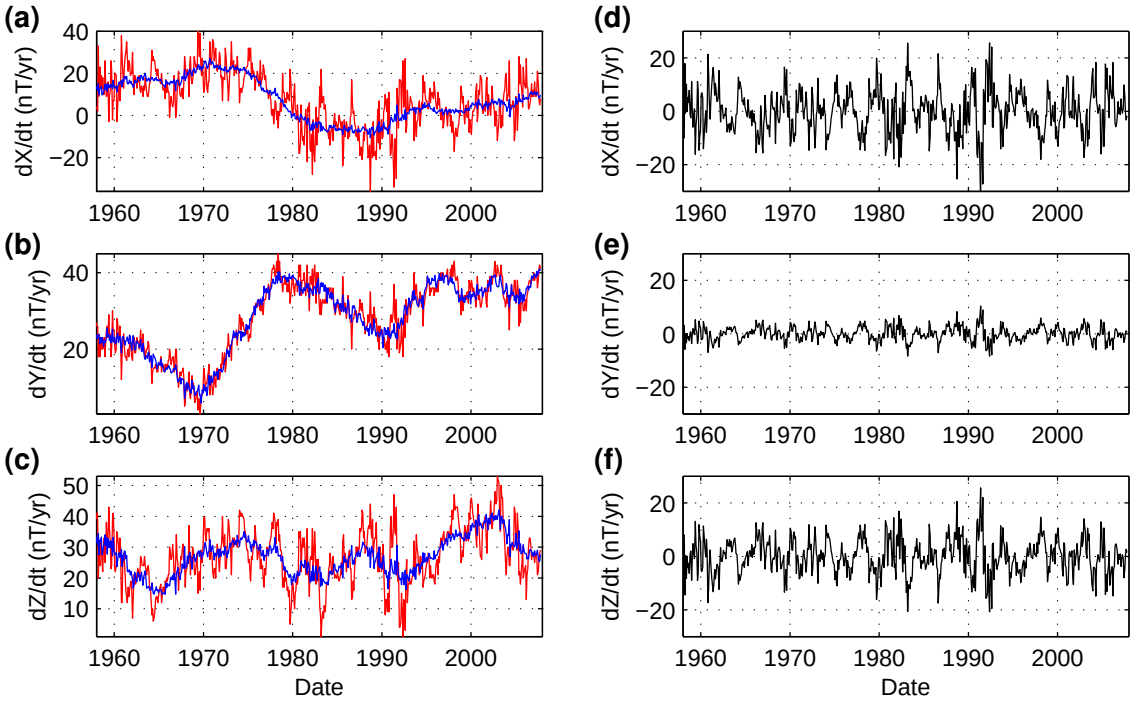

Figure 2.4: Original and external field corrected monthly mean SV (a–c) from the observatory at Niemegk (NGK), Germany. Original signal in red and corrected signal in blue. Also shown is the external signal SV removed (d–f) from the original data to produce the corrected signal for the X-, Y- and Z-components (top to bottom). From Brown et al. [2013].

reductions in variations are found in the X-component of observatories at low latitudes. The choice of NGK as the reference observatory for corrections at other observatories is likely responsible for the greater effectiveness of the cleaning in the Y- (subtle) and Z-components in Europe (Figure 2.5). This trend is best correlated to magnetic latitude, rather than proximity to the reference observatory, since North American and Australasian

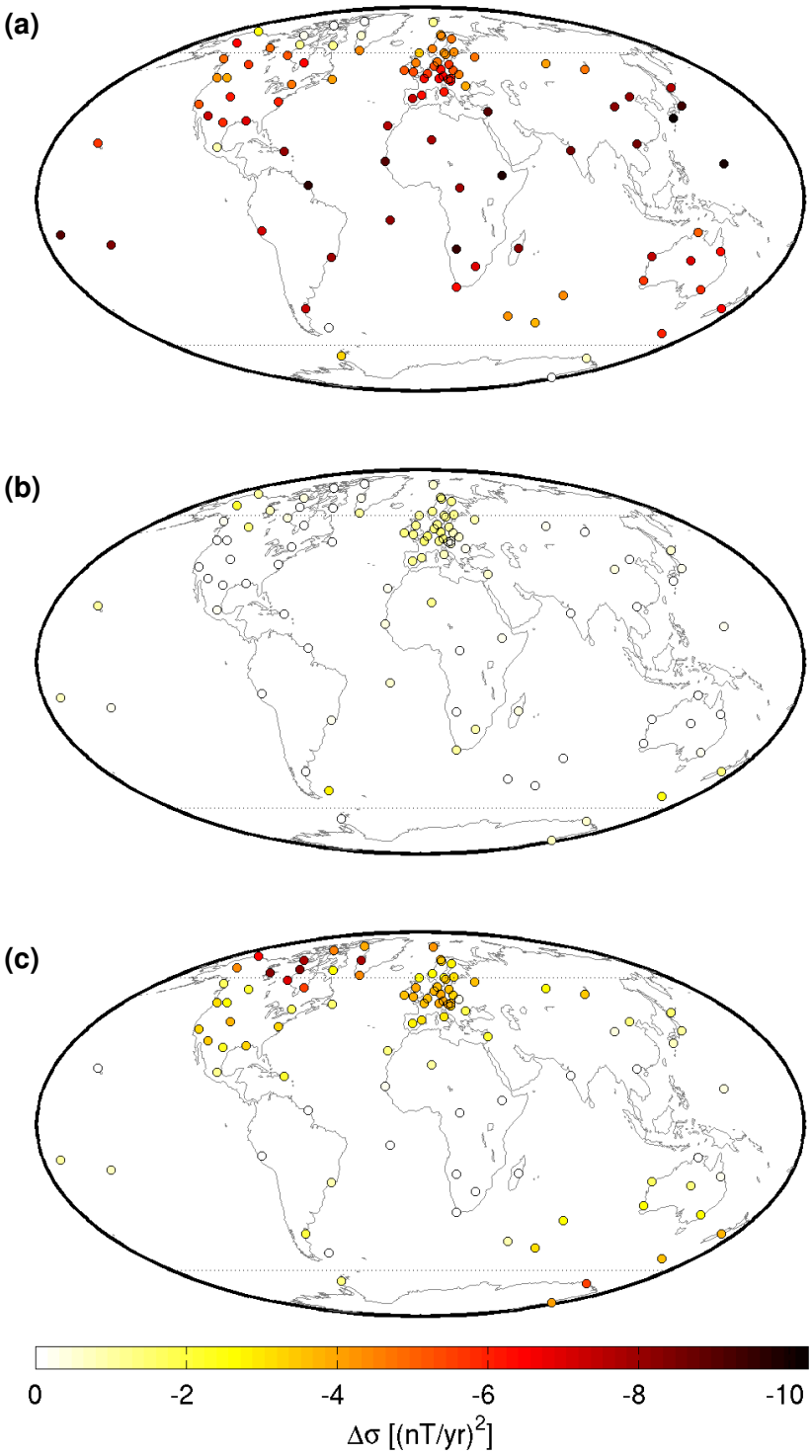

Figure 2.5: Change in standard deviation ($\Delta\sigma$) of observatory SV timeseries with external field correction applied. The change in the X- (a), Y- (b) and Z-component (c) are shown for each observatory between 1957 and 2008. Negative change signifies a smaller standard deviation after cleaning and thus a reduced noise content. Parallels are marked at $\pm 60^\circ$.

observatories also show greater improvement in the Y- and Z-components than is seen at the equator (Figure 2.5b,c). This adds weight to the choice of the NGK record as a correction reference since it lies at a latitude that is central to the distribution of the other observatories. It also enforces the point that the signals being removed are correlated on a large scale and not localised features introduced by the choice of reference observatory. The noise removed from each component is a scaled version of the noisy-direction SV residual, in the case of Figure 2.4, the residual from the relatively nearby CLF observatory. It was found that, on average the standard deviations of the removed noise were 7 nT/yr, 2 nT/yr and 5 nT/yr for the X-, Y- and Z-components respectively. The mean peak-to-peak amplitude ranges of these removed signals were 59 nT/yr, 13 nT/yr and 41 nT/yr for the X-, Y- and Z-components respectively.

2.4.2 JERK IDENTIFICATION

Pinheiro et al. [2011] described a method for applying a two-part linear regression to the SV of observatory annual means, generating a probability density function (PDF) of the likeliness of potential jerk occurrence times. A window of a single component of SV data was selected and the two-part linear regression iterated across the window, considering a potential jerk occurrence at each time step of 0.001 yrs. The inverse problem to find the best fitting linear regression, in a least-squares sense, can be formulated as follows,

$$\mathbf{m}(t_0) = (\mathbf{G}^\top(t_0)\mathbf{G}(t_0))^{-1}\mathbf{G}^\top(t_0)\mathbf{d}(t_0), \tag{2.4.2a}$$

$$\mathbf{m}(t_0) = \begin{bmatrix} a_1 & a_2 & b \end{bmatrix}, \tag{2.4.2b}$$

$$\mathbf{d}(t_0) = \begin{bmatrix} \dot{X}(t_i) \\ \vdots \\ \dot{X}(t_N) \end{bmatrix}, \tag{2.4.2c}$$

$$\mathbf{G}(t_0) = \begin{bmatrix} t_1 - t_0 & 0 & 1 \\ \vdots & \vdots & \vdots \\ t_i - t_0 & 0 & 1 \\ 0 & t_i - t_0 & 1 \\ \vdots & \vdots & \vdots \\ 0 & t_N - t_0 & 1 \end{bmatrix} \begin{matrix} \\ \\ \\ \\ \\ \\ \end{matrix} \begin{matrix} \\ \\ \text{for } t_i \le t_0 \\ \\ \\ \text{for } t_i > t_0 \end{matrix}, \tag{2.4.2d}$$

where $\mathbf{m}(t_0)$ is the model vector with a_1 the gradient of the first linear trend, a_2 the gradient of the second linear trend and b the amplitude of the intercept of the trends at the proposed jerk time t_0. The data vector $\mathbf{d}(t_0)$ contains the amplitudes of the SV of the given

component in the window. The matrix $\mathbf{G}(t_0)$ is split about t_0 and contains the sampling time of each corresponding SV measurement in $\mathbf{d}(t_0)$, shifted by a factor of t_0 to give two trends about a relative origin of t_0.

For each value of t_0, the least-squares misfit of the regression to the data was calculated by,

$$\mathbf{e}(t_0) = (\mathbf{d}(t_0) - \mathbf{G}(t_0)\mathbf{m}(t_0))^\top (\mathbf{d}(t_0) - \mathbf{G}(t_0)\mathbf{m}(t_0)). \tag{2.4.3}$$

Pinheiro et al. [2011] tested both L_1- and L_2-norms (least-squares), deciding that the assumed Gaussian error distribution of the least-squares approach was preferable to the Laplacian distribution assumed for the L_1-norm approach. Following the notation and reasoning of Pinheiro et al. [2011], the PDF for a Gaussian distribution of errors in variable x is of the form,

$$PDF = \frac{1}{\sigma\sqrt{2\pi}} \exp\left(-\frac{(x-\mu)^2}{2\sigma^2}\right), \tag{2.4.4}$$

where σ is the standard deviation, and μ is the mean or expected (most likely) value of x. The term $(x-\mu)^2$ can be considered to be the difference between the observed and modelled values, $\mathbf{e}$ and the standard deviation can be an inferred estimate from the data,

$$\tilde{\sigma} = \sqrt{\frac{\mathbf{e}_{\min}(t_0)}{N - \mathrm{Tr}(\mathbf{R})}}, \tag{2.4.5}$$

[Sivia and Skilling, 2006] where $\mathbf{e}_{\min}$ is the minimum value of $\mathbf{e}$ and $\mathrm{Tr}(\mathbf{R})$ is the trace of the resolution matrix $\mathbf{R} = \mathbf{G}(\mathbf{G}^\top\mathbf{G})^{-1}\mathbf{G}^\top$ giving $\mathrm{Tr}(\mathbf{R}) = 3$. Substitution of these two terms into Equation (2.4.4) leads to a PDF function where,

$$PDF(t_0) \propto \exp\left(-\frac{\mathbf{e}(t_0)(N-3)}{2\mathbf{e}_{\min}(t_0)}\right). \tag{2.4.6}$$

The function in Equation (2.4.6) must, by definition, be normalised by its integral to be a PDF. The peak value of this function, $PDF_{\max}$, represents the most likely jerk occurrence time. The uncertainty in this measurement is given by the bounds of the 68% confidence interval as determined by the times at which the probability falls to $\exp(-1/2)PDF_{\max}$, or one standard deviation of the assumed Gaussian error distribution. Pinheiro et al. [2011] applied this procedure to selected 11–15 yr time windows of data roughly centred about the previously identified jerk occurrences of 1969, 1978, 1991 and 1999 in the X-, Y- and Z-components of 123 observatories worldwide.

Possible events were considered an identified jerk if the PDF function in the time window allowed a 68% confidence window ($\pm 1\sigma$) to be defined about the most likely

occurrence time. Other potential jerks were excluded if a peak in likeliness was seen but the confidence interval could not be contained in the window chosen. If no likeliness peak was found at any occurrence time in a given data window, no jerk was identified.

SLIDING WINDOW REGRESSION

I propose that the use of a static window of data may bias the identification by severely limiting the extent and time of potential jerk events considered. Methods which utilise complete time series rather than requiring *a priori* data selection [e.g. Alexandrescu et al., 1996b; De Michelis and Tozzi, 2005; Stewart and Whaler, 1995] can be seen as more robust in this respect. I thus propose a sliding window, acting initially as described by Pinheiro et al. [2011], but with the window shifting, one time step per iteration, along the series being considered and the PDF calculation repeated. A summation of the resulting overlapping functions produced can then be normalised (to an integral of 1) to give a continuous PDF for the entire series which has considered each possible jerk time at every relative time in all possible data windows (Figure 2.6). This removes the bias towards events centred in the window and also removes any potential bias arising from manually selected window times.

The time uncertainty estimation procedure of Pinheiro et al. [2011], assuming $\pm 1\sigma$ from the estimated jerk time to be when the probability becomes $\exp(-1/2)PDF_{\max}$ (equivalent to the 68% area under a Gaussian peak), can still be applied to peaks in the PDF provided the Gaussian assumption still holds, as is discussed in Section 2.5.1 and will be analysed in the results of Chapter 3.

This method moves towards identification of jerk-like trends in SV with minimal *a priori* information required; nevertheless some assumptions are made and limiting parameters imposed. It is assumed that: a jerk takes the form of an instantaneous change in the gradient of SV (a step in SA); that the linear SV trends either side of a jerk have a set minimum length and can be contained within a particular time window; that there is a minimum jerk amplitude below which events are not considered likely to be jerks; and that the misfit of the jerk model to the data can be related to the probability of that model representing the data by Equation (2.4.6) both for sections of data in which jerks are present or absent. All input parameter values were chosen after testing using both synthetic and real data, this testing and the chosen parameter values are described in Section 2.4.3.

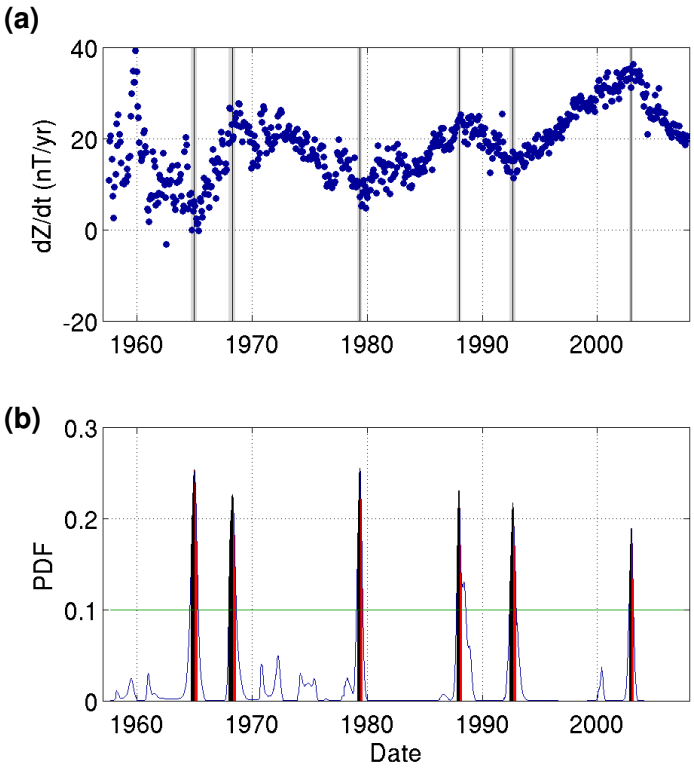

Figure 2.6: Example of jerk identification using the sliding window method for the Z-component of SV (a) at Chambon-la-Forêt (CLF), France. PDF function (b) used to identify the most likely jerk times, marked by positive (red) and negative (black) time uncertainties. Jerks are judged to be distinct peaks in the PDF above the cut off value (green line). Identified jerks are marked in (a) as black lines with grey areas representing the uncertainty. Adapted from Brown et al. [2013].

2.4.3 METHOD TESTING

It is important to validate the effectiveness of the sliding window method and ultimately to justify the parameter choices used when the method is applied to the observatory data for the main study. The sensitivity of the detection method to noise levels inherent in the data, the jerk amplitude and the proximity in time of successive jerks were deemed key behavioural features to understand.

SENSITIVITY TO NOISE, TIME IN WINDOW AND JERK AMPLITUDE

A test was designed to gauge the sensitivity of the two-part linear regression algorithm to the level of noise present in the data, the time of a jerk within a data window and to variations of jerk amplitude. A series of windows of 15 yrs worth of synthetic monthly SV data, containing two linear trends about a single jerk time, were created with a range of 25 evenly spaced jerk amplitude values between 1 nT/yr^2 and 25 nT/yr^2. Ten iterations of randomly generated Gaussian noise at each of a range of 11 standard deviations between

1 nT/yr and 20 nT/yr were added to the linear trends before the jerk detection algorithm was applied. A set of example synthetics is illustrated in Figure 2.7. The errors between the known jerk times and the most likely occurrence times identified were calculated along with the time uncertainties gauged by the generated PDF functions. Additionally, the timing of the jerk within the window was varied to see if this would bias the error distribution.

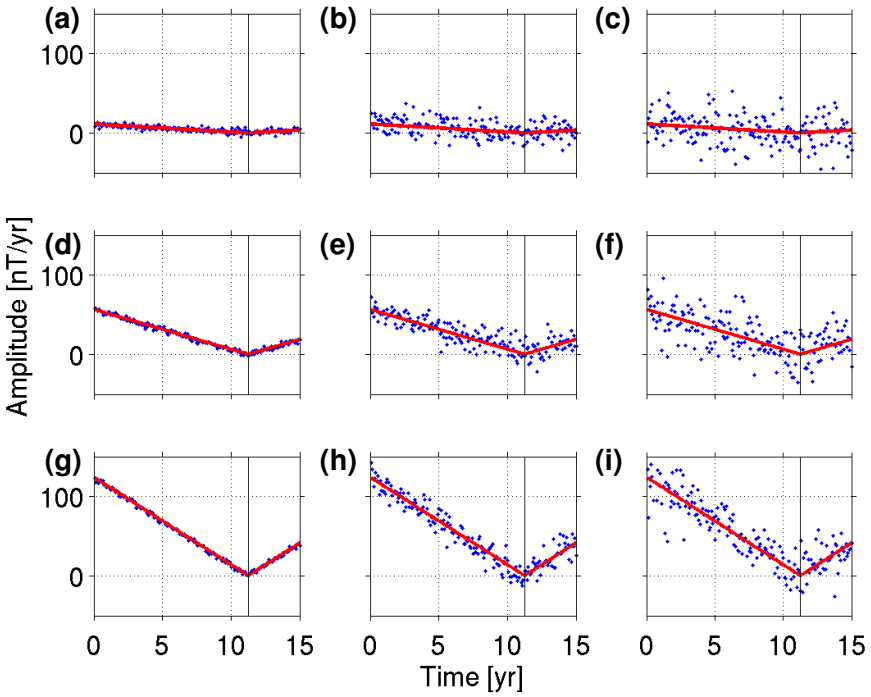

Figure 2.7: Examples of synthetic series used for jerk amplitude and noise level sensitivity test with a single jerk in a static detection window. Clean jerk synthetics (red) are shown overlaid with a Gaussian noise (blue), known jerk times are indicated by vertical black lines. Increasing noise levels are shown from left to right with increasing jerk amplitude shown from top to bottom.

Example results for the case of a jerk in the centre (7.5 yrs), in the left (3.75 yrs), and in the right (11.25 yrs) of the detection window are illustrated in Figure 2.8. It was found that the mean error in identified jerk times increased as the amplitude of the noise increased, as may be expected. A maximum error in the identified jerk times of $\sim$4 months was seen with noise levels up to a standard deviation of 20 nT, a noise level higher than expected in observatory data[1].

The variation of the jerk amplitude was seen to be a more dominant factor in controlling the errors with errors increasing rapidly for low values of jerk amplitude, while at higher jerk amplitudes, errors are smaller (Figure 2.8). For jerk amplitudes greater than $\sim$10 nT/yr^2,

[1] Stewart and Whaler [1992] found that disturbance fields contributed $\sim$10 nT (amplitude, not standard deviation) variations to monthly mean data.

regardless of noise level, the time errors are found to be smaller than the temporal resolution of the test data (1 month).

The mean error in identification time can be seen to be unaffected by the offset of the jerk away from the centre of the detection window by comparing Figure 2.8a,d,g. The individual lower and upper error bars however show that there is a bias in a static detection window towards larger error bars on side of the shorter linear SV trend on one side of the jerk (maximum 2 months versus 1.5 months). This can be seen by comparing the magnitudes of the lower and upper error bars of the jerk offset to the left of the data window (Figure 2.8b,c), the central jerk (Figure 2.8e,f) and the right offset jerk (Figure 2.7 and Figure 2.8h,i). While the central jerk has roughly even magnitude lower and upper error bars, the left offset jerk has a larger magnitude lower error bar and the right offset jerk a larger magnitude upper error bar. This effect drops off at higher jerk amplitudes as does the identification time error and is averaged out when a sliding window detection is applied to give symmetrical error bars, compliant with the assumption of Gaussian error distributions about the PDF peaks.

The robustness of the identification method to variations in noise level, time in window and jerk amplitude is judged to be sufficient to deal with observatory monthly mean data. The maximum error in identified jerk time in the range of values tested is 4 months and the error bars are appropriate in magnitude (maximum $\pm$2.5 months), in the majority of cases covering the correct jerk time.

SENSITIVITY TO JERK PROXIMITY

The response of the sliding detection window method to jerks which lie in close proximity to each other is an important characteristics to consider. The detection method will have some resolution below which closely spaced features do not provide long enough linear SV trends to be distinguished, or the noise level in the data becomes high enough that the two features cannot be easily distinguished. This characteristic was tested by applying the sliding window algorithm to a series of synthetic data cases in which jerk-like features were spaced at systematically increasing separations. Additionally the noise level in the synthetic data, represented as Gaussian random noise added to the linear trends, was varied in the same manner as in the previous section. An example of the results of this testing can be seen in Figure 2.9.

Overall it was found that, as in the jerk amplitude sensitivity tests, the algorithm is capable of handling noise levels above those expected in observatory data. The limiting

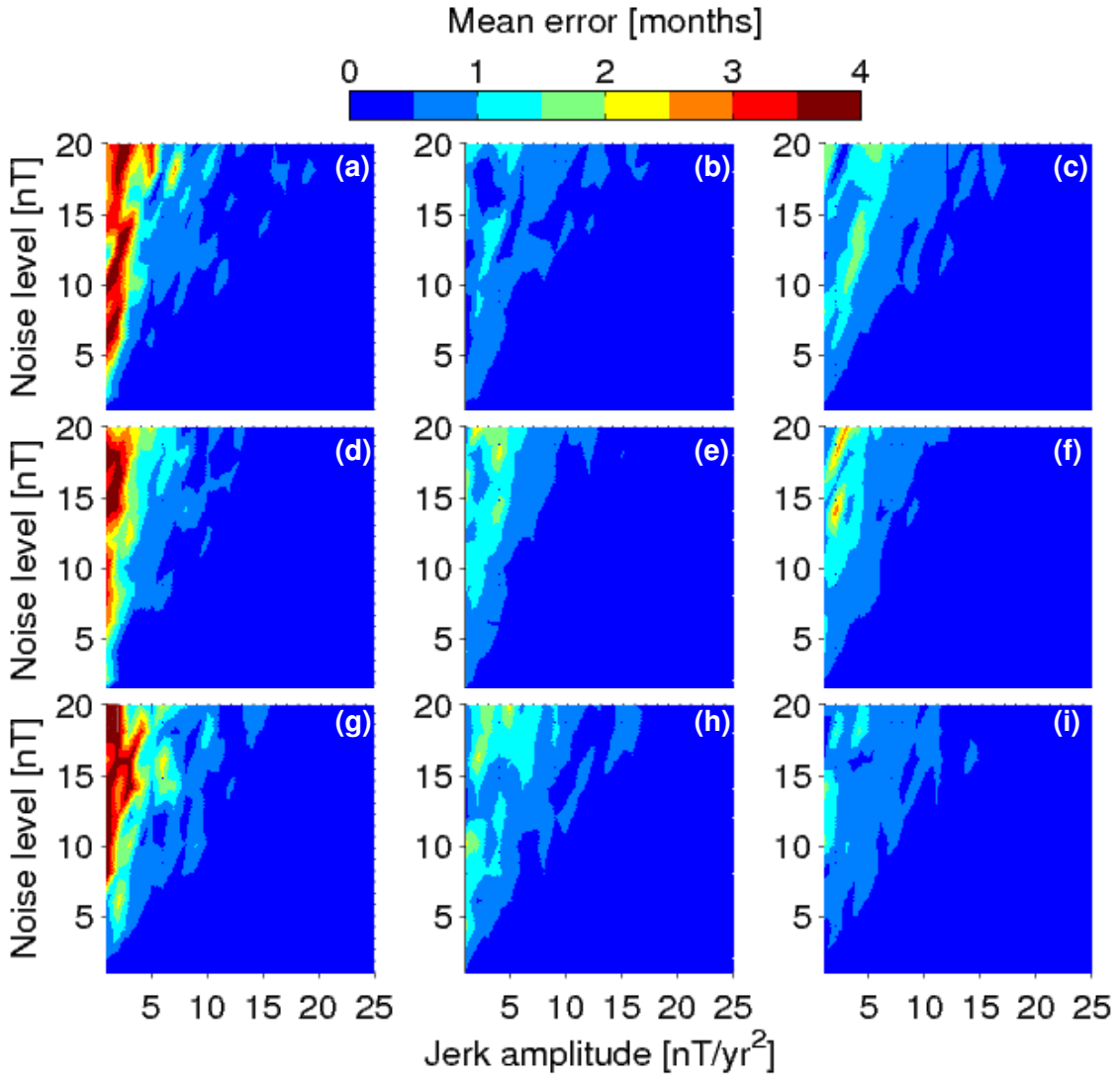

Figure 2.8: Results of synthetic jerk amplitude sensitivity test with a single jerk at various times in a static detection window. For a jerk offset to the left (3.75 yrs), mean jerk time errors (a) with mean upper (b) and lower (c) error bar values for a range of jerk amplitude and noise level combinations are shown. Plots (d,e,f) show the equivalent for a jerk in the centre of the window (7.5 yrs) while plots (g,h,i) show the errors for a jerk offset to the right (11.25 yrs). Each error value is an average over 10 iterations of random noise at each given noise level and jerk amplitude.

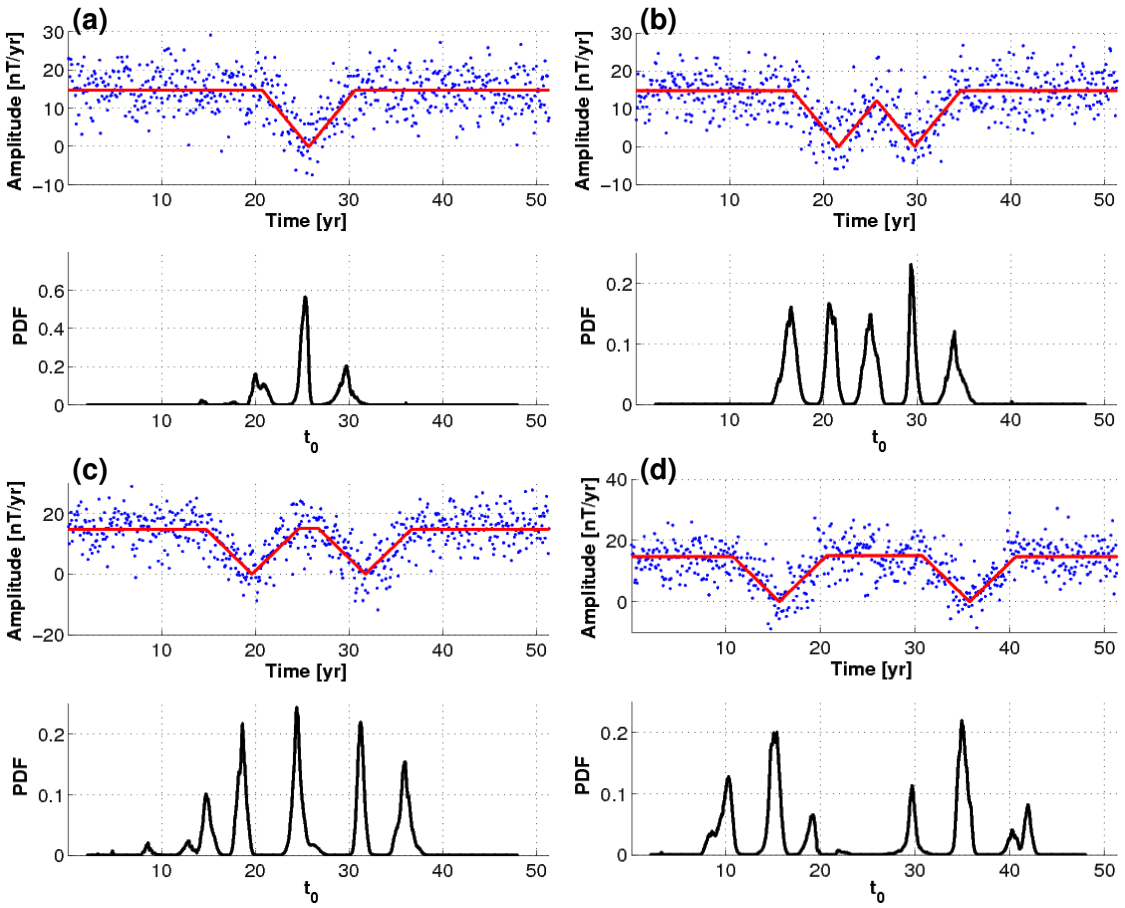

Figure 2.9: Examples of four stages of a jerk proximity test. The sliding window detection algorithm is applied to a series of synthetic SV trends (red lines) with added noise (blue points) to produce a PDF of jerk likeliness (black lines). Subplots (a) through (d) show the separation of a feature with three gradient changes (representing jerks), into two such overlapping features which are gradually moved apart. A 10 yr identification window was used with noise of a 5 nT standard deviation. The detection can be seen to fail in resolving the two proximal gradient changes at ∼24 yrs and ∼27 yrs in (c).

factor in resolving successive jerks is the length of the detection window (Figure 2.10) (and of course the time resolution of the data). The tests indicate that jerks can be resolved when the length of the linear SV trends from both sides of a jerk are contained within the detection window (Figure 2.10). That is, somewhat predictably, the limit where only a single gradient change (jerk) is found in any one detection window. With shorter detection windows comes a reduced number of data points in the regression and an increased sensitivity to noise. It is key in this case to distinguish a minimum jerk amplitude threshold so that long, linear SV segments with higher noise levels do not lead to numerous false positives when using a relatively shorter identification window. It was found to be helpful in such situations to also restrict the minimum length of each of the linear SV trends in the jerk model. Requiring, for example, a buffer of at least 2 yrs of data to be present in each

linear trend limits the detection to only the central area of the window, but greatly reduces the likelihood of false positives in noisy, roughly linear data sections.

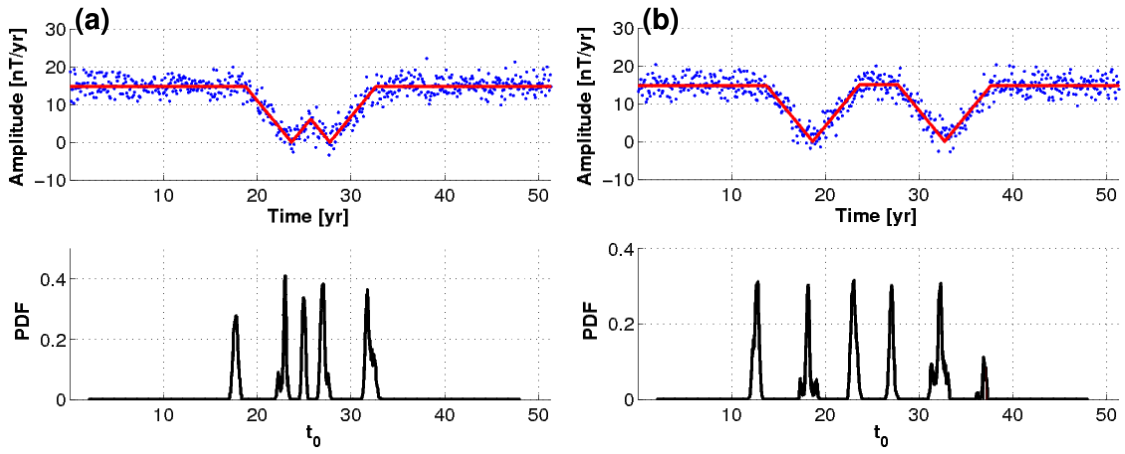

Figure 2.10: Examples of two stages of a jerk proximity test, as Figure 2.9 but with a 5 yr identification window with noise of a 3 nT standard deviation. The shorter detection window leads to better resolution of gradient changes (jerks) separated by roughly the length scale of the window. Compare (a) and (b) to results of a 10 yr window in Figure 2.9c.

Realistic Synthetic Data

With the method tested against variations in noise levels, jerk amplitudes and the proximity in time of consecutive jerks, a final test bringing all these aspects together in controlled circumstances was designed. Synthetic series constructed of several linear segments, overlaid with Gaussian random noise were created to allow the direct comparison of identified jerk parameters with those initially input to create the synthetic series. A representative example of such a test case and the results are displayed in Figure 2.11 and Table 2.2. It can be seen that the identification method correctly locates the six jerks present in the example and the absolute time errors are found to be $<$4 months with error bars estimated to be $<$7 months, spanning the actual jerk time in all but one case. Generally it was found that where noise levels were higher or jerk amplitudes lower, the error bars were estimated to be larger. Similar trends were seen for the jerk amplitudes although they have in general greater relative error and error bar estimates. The jerk amplitude estimates were found to always have the correct sign, even where jerk amplitudes were low and error bars large. Overall the method performs well, struggling most where either two jerks or a jerk and an end of the data series were contained within a single detection window. In terms of eliminating false positives it was found to be beneficial to apply a minimum threshold of probability, below which PDF peaks were ignored, so as to keep only the most likely jerk occurrences.

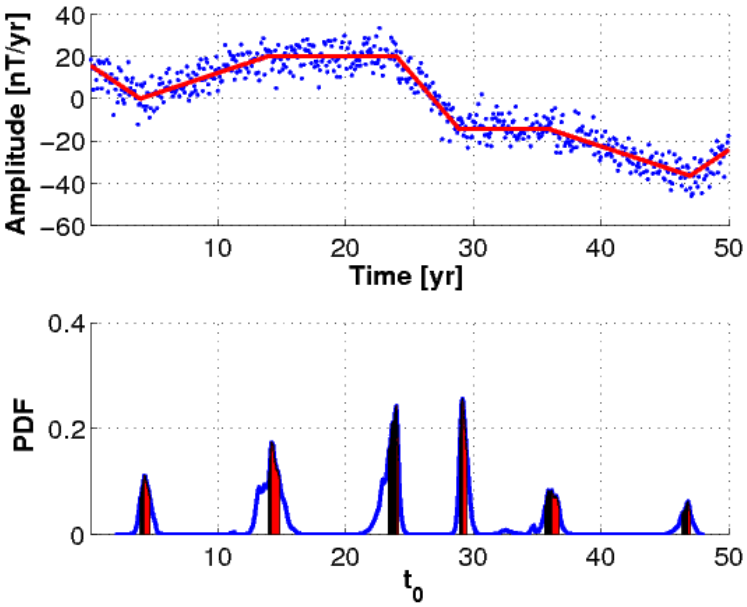

Figure 2.11: Example of the sliding window algorithm applied to a synthetic series with a 10 yr detection window. Original linear SV trends (red line) are overlaid with 5 nT Gaussian noise (blue points), the detection produced the PDF shown in the lower plot (blue line) with identified jerks shown as peaks with positive (red areas) and negative (black areas) time error bars. Associated errors are listed in Table 2.2

Table 2.2: Errors associated with jerk detection test shown in Figure 2.11. The uncertainties predicted by the identification method based on the fit to the noisy synthetic data can be compared to the actual values of jerk times and amplitudes used to construct the synthetic data.

Jerk times [yrs]				
Actual time	Identified time	Error	Lower error bar	Upper error bar
4.0	4.3	+0.3	−0.3	0.5
14.0	14.2	+0.3	−0.2	0.6
24.0	24.0	0.0	−0.6	0.2
29.0	29.2	+0.2	−0.2	0.3
36.0	36.2	+0.2	−0.6	0.6
47.0	46.8	−0.1	−0.4	0.2
Jerk amplitudes [nT/yr^2]				
Actual amplitude	Identified amplitude	Error	Lower error bar	Upper error bar
6	4.6	−1.4	−0.3	1.3
−2	−3.5	−1.5	−1.0	0.5
−7	−5.3	+1.7	−5.3	2.2
7	7.4	+0.4	−2.9	0.3
−2	−3.8	−1.8	−1.0	0.7
6	6.1	+0.1	−1.0	0.2

Parameter Choices

As a result of the method testing the following conditions were applied to parameterise the detection algorithm.

I introduce a threshold probability above which events are deemed significantly likely compared to the background level of likeliness which results from the misfit to the variability in the data. A threshold of 0.2 was chosen based on a trade-off curve of the number of jerks identified versus the probability threshold when using the monthly mean observatory data (Figure 2.12). This threshold assumes that the relatively high peaks in the jerk time PDFs are the most sound estimates of jerk times and was set slightly to the right of the knee of the trade-off curve (Figure 2.12) to reduce the likelihood of false positives.

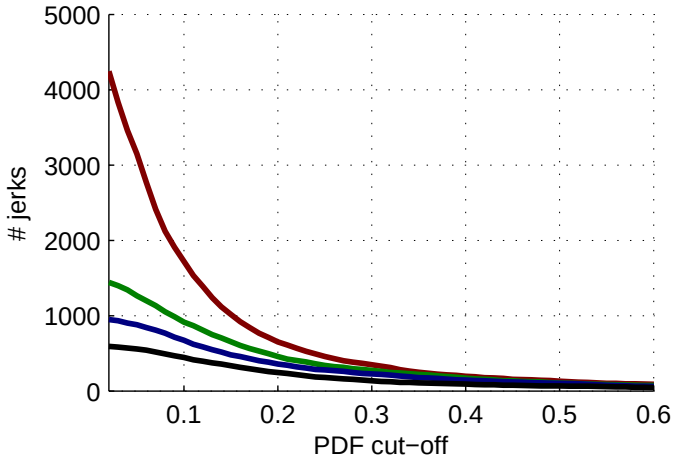

Figure 2.12: Trade-off curve of the number of jerks detected versus the probability cut-off threshold above which peaks in probability are to be considered jerks. Curves for jerk detections in all components with a 5 yr (red), 10 yr (green), 15 yr (blue) and 20 yr window (black) are shown. For all window lengths and all individual components a threshold of 0.2 was chosen. From Brown et al. [2013].

A magnitude of 3 nT/yr^2 was chosen as the minimum jerk amplitude recognised as a significant trend above the variability of the background noise level. Since it is not assumed that a jerk is present in each window, this limit is required to impose zero probability on features such as long linear sections of data, which otherwise show a low misfit when both sections of the linear regression align approximately parallel to each other. Amplitude best estimates are taken to be the value which produces the lowest misfit to the data when considering the range of amplitude estimates from all time windows which identify a given time as a potential jerk. The uncertainties on amplitude estimates are then calculated as the differences between the best estimate and the maximum and minimum values of the range of amplitude estimates. This gives an upper bound to the amplitude uncertainties

and does not explicitly assume a Gaussian error distribution as is the case for the jerk time uncertainties. Whether such an assumption is valid will be discussed in the results of Chapter 3.

The length of the time window in which data is considered during each linear regression must also be imposed. It was decided to utilise a variety of window lengths as a reassurance of the robustness of identified events due to the limiting role the window length plays in the resolution of consecutive events. Consecutive jerks which occur within a single window length are less likely to be resolved individually. Thus jerks were identified with window lengths of 5 yrs, 10 yrs, 15 yrs and 20 yrs. Additionally a limit was placed on how short each side of the two-part linear recursion could be. A value of 2 yrs was imposed to prevent jerks from being identified in noisy linear data sections which are longer than the detection window.

The time instances at which possible events are considered must be defined, this was chosen to be at steps of 0.01 yr since this sampling rate is higher than the monthly (0.08 yr) data sampling, allows fast computation times, and produces smooth PDFs.

This method thus provides a means of consistently identifying features which statistically fit the definition of a jerk in the SV as the abrupt change in gradient between two linear trends. It allows a quantitative estimate of the uncertainties in times and in jerk amplitudes and is also able to provide a relative probability weighting with which to consider the identified events.

2.5 DATA

Monthly mean MF data were obtained from the *Bureau Central de Magnétisme Terrestre (*BCMT*), World Monthly Means Database Project*. This database comprises full monthly averages of X-, Y-, and Z-components at 118 *INTERMAGNET* observatories worldwide and was compiled by Chulliat and Telali [2007] from hourly means, initially obtained from the *World Data Centre for Geomagnetism* at the *BGS*, Edinburgh. Further to the consistency checks of Chulliat and Telali [2007], all documented baseline corrections have been applied and gaps of unrecorded data have been accounted for in one of two ways. Gaps shorter than 6 months were interpolated using a linear fit to the field component in question. A minimum of 12 months of data either side of a gap was required for interpolation to be performed. For gaps longer than 6 months the records were split into separate time series on either side of the gap and will be considered as individual records

from here on.

When considering analysis of observatory data it is important to consider the dependence of any interpretation on the spatial and temporal distribution of the data upon which it is founded. It is well known that observatory data provide spatial sampling biased heavily towards continental regions, particularly Europe and North America, and that the density of observations varies through time, generally increasing towards the present day as more observatories have been established (see Figure 2.13).

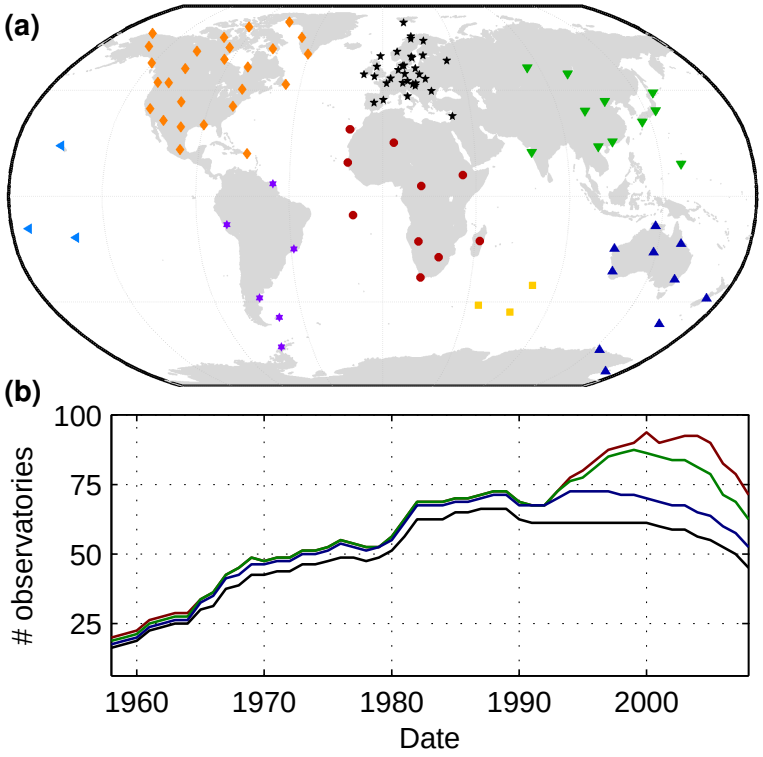

Figure 2.13: Map showing observatory locations used in this study (a). The 8 groups of symbols show regions of observatories as described in Section 3.2. While all the observatories highlighted above were used in this study, not all were operating throughout the entire period of interest, (b) shows the number of observatories operating in any given six month period between 1957 and 2008. The number of observatories providing minimum length time series of 5 yrs (red), 10 yrs (green), 15 yrs (blue) and 20 yrs (black) are shown. From Brown et al. [2013].

The procedure described in detail in Section 2.4.1 requires use of a magnetic field model. For this purpose *C*^{3}*FM2* of Wardinski and Lesur [2012] was used. The model is a fit to observatory SV over the period of 1957.0 to 2008.4, further constrained by satellite field models in 1980 and 2004 and was expanded to SH degree 14. As such it provides coverage specifically tailored to SV across the period in which observatory data is most widely available. The data timespan of this study was thus constrained by the model length. While observatory data are available extending back to the late 1800s, the spatial

coverage is too limited for this study. While *C³FM2* was chosen for this study, the methods described in Section 2.4 are, in principle, applicable to any period for which observations and models are available. Comparable results (not shown here) were achieved using the *CM4* model of Sabaka et al. [2004] in the period 1960 to 2000.

2.5.1 DATA SAMPLING

I suggest that when investigating rapid features such as jerks it is preferable to utilise monthly sampling of observatory data with as little smoothing as possible to achieve the best time resolution. Annual mean observatory data were used by Pinheiro et al. [2011] in preference to monthly means due to the greater availability of observatories and the view that monthly means, in the form of 12 month running means of first differences in dipole coordinates (X- and Y-components rotated to be parallel and perpendicular to the dipole axis, respectively), contain correlated external noise which may break the assumption of Gaussian error distributions, as well as having much greater variability. In Section 2.4.3 it was shown that the two-part linear regression method is suitably robust to handle noise levels above those expected from observatory data. It was also noted by Pinheiro et al. [2011] that jerks appeared to be more contemporaneous between field components when considering annual means.

The spatial coverage of observatory data is not greatly reduced by considering monthly means over annual means. In this study 96 observatories were used when considering an 11–15 year window length as used by Pinheiro et al. [2011] who utilised 123 observatories. Of the 27 additional observatories used by Pinheiro et al. [2011], the majority are short Northern Hemisphere records in the late-20th to early-21st century and do not greatly influence the spatial or temporal distributions of data used. For window lengths of 5 yrs, 102 observatory locations were found to be suitable whilst for windows of 20 yrs, 76 observatory records were available (Figure 2.13).

The assumption that monthly means contain too much correlated signal which is not present in annual means [Pinheiro et al., 2011] can be addressed via an example. Considering the observatory record from Niemegk (NGK), Germany, during the period of the *C³FM* model, the 3×3 covariance matrix ($\mathbf{C}_{\mathrm{annual}}$) of annual means unmodelled SV residuals (X-, Y-, Z-components) and its corresponding normalised eigenvectors ($\mathbf{v}$) and

eigenvalues (Λ) are found to be,

$$\mathbf{C}_{\text{annual}} = \begin{bmatrix} 17.2 & -5.5 & -14.7 \\ -5.5 & 2.1 & 4.0 \\ -14.7 & 4.0 & 28.7 \end{bmatrix} (\text{nT/yr})^2, \tag{2.5.1a}$$

$$\mathbf{v}_{\text{clean}} = \begin{bmatrix} 0.4 \\ 0.9 \\ 0.0 \end{bmatrix}, \ \Lambda_{\text{clean}} = 0.3\,(\text{nT/yr})^2, \tag{2.5.1b}$$

$$\mathbf{v}_{\text{intermediate}} = \begin{bmatrix} -0.8 \\ 0.3 \\ -0.6 \end{bmatrix}, \ \Lambda_{\text{intermediate}} = 7.9\,(\text{nT/yr})^2, \tag{2.5.1c}$$

$$\mathbf{v}_{\text{noisy}} = \begin{bmatrix} -0.6 \\ 0.2 \\ 0.8 \end{bmatrix}, \ \Lambda_{\text{noisy}} = 39.8\,(\text{nT/yr})^2, \tag{2.5.1d}$$

while for monthly means unmodelled SV residuals the covariance matrix ($\mathbf{C}_{\text{monthly}}$), eigenvectors and eigenvalues are found to be,

$$\mathbf{C}_{\text{monthly}} = \begin{bmatrix} 79.8 & -25.5 & -58.0 \\ -25.5 & 10.0 & 18.0 \\ -58.0 & 18.0 & 66.4 \end{bmatrix} (\text{nT/yr})^2, \tag{2.5.2a}$$

$$\mathbf{v}_{\text{clean}} = \begin{bmatrix} 0.3 \\ 0.9 \\ 0.0 \end{bmatrix}, \ \Lambda_{\text{clean}} = 1.6\,(\text{nT/yr})^2, \tag{2.5.2b}$$

$$\mathbf{v}_{\text{intermediate}} = \begin{bmatrix} -0.6 \\ 0.2 \\ -0.8 \end{bmatrix}, \ \Lambda_{\text{intermediate}} = 15.6\,(\text{nT/yr})^2, \tag{2.5.2c}$$

$$\mathbf{v}_{\text{noisy}} = \begin{bmatrix} -0.7 \\ 0.2 \\ 0.6 \end{bmatrix}, \ \Lambda_{\text{noisy}} = 139.0\,(\text{nT/yr})^2. \tag{2.5.2d}$$

The covariance matrices describe the coherency of signal between the X-, Y-, and Z-components and have associated eigenvectors and eigenvalues which describe respectively the directions and magnitudes of these signals. Comparing Equations (2.5.1) and (2.5.2) it can be seen that the eigenvalues are of greater magnitude and thus the coherency of signal is greater for monthly means while the eigenvectors are in similar directions for both annual and monthly data. This shows that while reduced in magnitude, the coherent signal is not removed by calculating annual means. As expected, the reduced covariance seen with annual means is only from the reduction in variability of the signal

overall. These two cases can be compared to the covariance matrix ($\mathbf{C}_{\text{corrected}}$), eigenvectors and eigenvalues of monthly means unmodelled residuals once external signal is reduced as described in Section 2.4.1,

$$\mathbf{C}_{\text{corrected}} = \begin{bmatrix} 2.0 & -0.2 & 2.6 \\ -0.2 & 2.6 & -1.4 \\ 2.6 & -1.4 & 3.7 \end{bmatrix} (\text{nT/yr})^2, \tag{2.5.3a}$$

$$\mathbf{v}_{\text{clean}} = \begin{bmatrix} -0.7 \\ 0.3 \\ 0.6 \end{bmatrix}, \ \Lambda_{\text{clean}} = 0.0(1)\,(\text{nT/yr})^2, \tag{2.5.3b}$$

$$\mathbf{v}_{\text{intermediate}} = \begin{bmatrix} 0.4 \\ 0.9 \\ 0.1 \end{bmatrix}, \ \Lambda_{\text{intermediate}} = 2.3\,(\text{nT/yr})^2, \tag{2.5.3c}$$

$$\mathbf{v}_{\text{noisy}} = \begin{bmatrix} 0.5 \\ -0.3 \\ 0.8 \end{bmatrix}, \ \Lambda_{\text{noisy}} = 6.0\,(\text{nT/yr})^2. \tag{2.5.3d}$$

It is clear that there is much improvement with the removal of coherent unmodelled signal: smaller eigenvalues imply less coherent signal than for untreated annual or monthly data. The eigenvectors, the direction of the dominant coherent signal, are also altered and no longer show the same contaminating ring current effects with the cleanest component direction now close to that of the original noisy-component. With little covariance between the field components, the assumption of Gaussian errors made by Pinheiro et al. [2011] can hold for monthly data, making them suitable for this study. This is demonstrated with an example of a PDF fit with a series of Gaussian distributions in Figure 2.14, corresponding to the case shown in Figure 2.6. The dense monthly sampling leads to greater accuracy in time identification of jerks since the process of calculating annual means from monthly means introduces a smoothing to the data, rounding off the sharp features of jerks to create a broader apex in the SV.

2.6 SUMMARY

This chapter aimed to assess the current state of work on the cleaning of external fields and identification of geomagnetic jerks in observatory data, building on this to develop a new method to perform these tasks.

In order to assess the occurrences and characteristics of geomagnetic jerks in detail, it is necessary to consider all field components, not just the relatively clean Y-component.

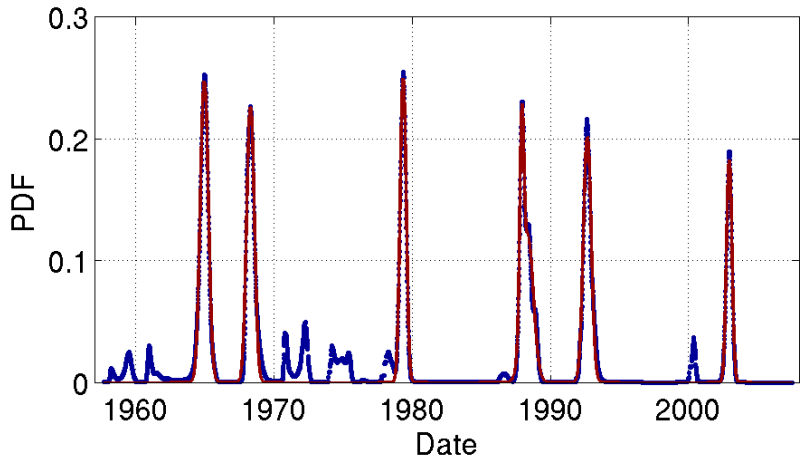

Figure 2.14: A series of Gaussian distributions (red) fit to a PDF (blue) from jerk identification using the sliding window method for the Z-component of SV at CLF (see Figure 2.6). The main peaks in the PDF can be closely approximated by a series of Gaussian distributions, where there are closely spaced SV features which fit the jerk model, the PDFs often show a main peak with secondary shoulders e.g. at ∼1988. In such instances the PDF can be best fit by multiple overlapping Gaussian distributions however this is not required to assess the uncertainty associated with the main peak which will be assumed to be the best fit jerk in such instances.

The presence of external signals, predominantly ionospheric and magnetospheric in origin, hampers the resolution of such rapid features. This is especially true when monthly data are considered since there is no reduction of rapid external field content simply through annual or longer period averaging. Several previous studies have utilised correlation of observatory data with geomagnetic indices to account for contaminating rapid external variations in a simple and practical manner. The approach described by Wardinski and Holme [2011] provides an improvement on the use of indices by considering correlation of observatory data to the unmodelled SV (that not attributed to the core). The primary component of the unmodelled SV is shown to be aligned North-South, consistent with the ring current but not entirely explained by such a single large-scale source. Indeed an advantage of this technique is in its simplicity to account for a greater proportion of unmodelled signals which are difficult to parameterise as a uniform source. Application of this technique is limited by the requirement for an internal field model contemporary to the observatory data timespan rather than in the case of some previous works where the span of geomagnetic indices was a limiting factor. The model C^3FM2 limits this study practically although the dearth of observatory data prior to 1957 certainly makes global jerk analysis difficult at earlier epochs.

Such external field cleaning is pertinent when the findings of previous works on jerk detection are considered. To best resolve rapid SV, the temporal resolution of monthly data

is preferred over annual means for the same reason that observatory data is preferred over modelled timeseries: smoothing SV in time limits the ability to determine rapid changes. With field models there is also the additional effect of regularisation of models in areas of low data constraint acting to increase uncertainty in jerk times [Wardinski and Holme, 2011]. Satellite data do provide excellent temporal and spatial resolution of jerks but currently do not provide the extensive catalogue of events to analyse as observatory data do.

I propose that considering complete observatory timeseries is favourable to pre-selecting time windows of data, removing bias towards any particular occurrence times for jerks and helping to keep time error distributions approximately Gaussian. The quantitative uncertainty analysis of Pinheiro et al. [2011] is a highly desirable quality for a jerk detection method and so is adapted to the case of monthly data and the sliding window analysis to consider entire observatory timeseries. By employing the sliding window procedure to test all possible jerk times and varying window lengths to account for different scales of SV features, a less biased and more flexible approach is achieved.

In tests, the jerk identification method developed here proves to be a useful tool in the assessment of jerks. Applying the specified detection criteria, requiring minimal *a priori* information, leads to the robust identification of all events which exhibit the characteristic form of a jerk in the SV. The technique also allows the variation of the selection criteria to assess the effects of the scale and definition of a jerk that is imposed. With relative probabilities for each event identified, the method also provides a means to gauge the certainty of each jerk detected to assess how well the model is constrained by the data. The results of the application of the technique described here are presented in Chapter 3.

CHAPTER 3

JERKS IN OBSERVATORY DATA

3.1 OVERVIEW

In this chapter the results of the application of the jerk detection method described in Chapter 2 are presented. The algorithm is applied to the X-, Y- and Z- components of monthly mean observatory data spanning 1957 to 2008 at a total of 118 observatory locations. These data have been cleaned of external signals primarily attributed to the equatorial ring current following the method of Wardinski and Holme [2011]. The designed detection method aims to identify all features which fit a given definition of a jerk in a robust and quantifiable manner with minimal *a priori* information. The aim of this is to systematically catalogue the observations of jerks and quantify their characteristics to improve our understanding of the phenomena.

This chapter is arranged as follows: Section 3.2 presents the results and their subsequent analysis and interpretation in four categories. First Section 3.2.1 covers temporal distributions of the identified jerks, second Section 3.2.2 discusses the spatial distributions of the jerks, third Section 3.2.3 discusses combined spatiotemporal trends in jerk occurrences and finally Section 3.2.4 investigates whether jerk amplitudes show periodic variations. Conclusions from this analysis are then summarised in Section 3.3.

3.2 RESULTS

Due to the large number of data involved and the wide extent of results generated, only the key results are summarised here. For brevity, results from the 10 yr detection

window are depicted in subsequent figures, except where stated, as they are deemed representative of the major features in the data. Additional information of interest, surplus to the presentation and discussion of results here is included in Appendix C and is referenced where appropriate.

Across window lengths the numbers of jerks detected was found to be 25% greater on average in the Y-component than in the X- and Z- components (Table 3.1). This is likely a reflection of the cleaner Y-component signal, despite the external field cleaning applied, leading to more jerks being detected at a higher probability level in the Y-component, rather than a true disparity in the numbers of jerks in each field component. While the mean event probability increased with the window length due to lower numbers of jerks being detected, the median probability was found to be independent of window length and equal in all components at a value of $\sim$0.3 (Table 3.2). Overall the number of individual events identified varied depending on the window length used with a maximum of 651 detected with the 5 yr window and 244 detected with the 20 yr window (Table 3.1).

The uncertainty estimates on the identified jerk times were found to increase with window length from $\pm$0.2 yr with a 5 yr window to $\pm$0.4 yr with a 20 yr window in all components (Table 3.3). These values nevertheless show that the use of monthly mean data has indeed increased the time resolution of jerk events compared to previous studies (mean uncertainties of $\pm$1.4 yr were found by Pinheiro et al. [2011]). The positive and negative time uncertainties were found to be symmetrical and therefore consistent with the assumption of Gaussian error distributions. The uncertainty estimates for the jerk amplitude values also show an increasing trend with window length, ranging from $\pm$1.2 nT/yr^2 with a 5 yr window to $\pm$3.6 nT/yr^2 with a 20 yr window (Table 3.4). The amplitude uncertainties are not equal in all components, being consistently largest in the Z-component at any given window length. The mean uncertainty estimate of jerk amplitude across all window length was found to be $\pm$2.1 nT/yr^2. As noted by Pinheiro et al. [2011] jerk amplitudes are a robust measure of jerk identification and it is found here that the sign of contemporary jerk amplitudes at nearby observatories is consistent.

The assumption of Gaussian errors is only explicitly made for the uncertainties in jerk times since, unlike Pinheiro et al. [2011] I must impose a minimum amplitude threshold due to the consideration of all possible time windows of data, not just those preselected to contain only one jerk. Despite this, the positive and negative amplitude error bars are found to be broadly symmetric and can be approximated by a Gaussian distribution, except in the case of the Z-component when a 20 yr window is used. The minimum amplitude

threshold has the effect of clipping the tails of the uncertainty distribution but does not alter the favoured most likely value. The uncertainty estimates for both jerk times and amplitudes were found to be approximately constant through the time period studied.

Table 3.1: Numbers of jerks detected by field component and window length in observatory data.

Window	Component	# Jerks	Total
5	X	194	651
	Y	264	
	Z	193	
10	X	147	457
	Y	174	
	Z	136	
15	X	107	357
	Y	133	
	Z	117	
20	X	70	244
	Y	92	
	Z	82	

Table 3.2: Mean and median probability values for jerks detected in observatory data by field component and window length.

Stat.	Window [yr]	X	Y	Z	Overall
Mean probability	5	0.40	0.44	0.44	0.43
	10	0.46	0.49	0.46	0.47
	15	0.58	0.49	0.37	0.48
	20	0.50	0.61	0.51	0.55
Median probability	5	0.33	0.30	0.31	0.31
	10	0.33	0.36	0.32	0.34
	15	0.38	0.38	0.32	0.35
	20	0.31	0.34	0.30	0.32

Table 3.3: Mean time uncertainty values for jerks detected in observatory data by field component and window length. The negative and positive error bar values are given as well as the mean and mean magnitude of the error bar pairs.

Comp.	Window [yr]	−error [yr]	+error [yr]	Mean error [yr]	Mean |error| [yr]
X	5	−0.21	0.24	0.01	0.23
	10	−0.31	0.30	0.00	0.31
	15	−0.33	0.37	0.02	0.35
	20	−0.40	0.45	0.03	0.43
Y	5	−0.19	0.20	0.00	0.20
	10	−0.26	0.30	0.02	0.28
	15	−0.35	0.41	0.03	0.38
	20	−0.30	0.34	0.02	0.32
Z	5	−0.21	0.21	0.00	0.21
	10	−0.28	0.34	0.03	0.31
	15	−0.36	0.40	0.02	0.38
	20	−0.37	0.50	0.06	0.44

Table 3.4: Mean jerk amplitude uncertainty values for jerks detected in observatory data by field component and window length. The negative and positive error bar values are given as well as the mean and mean magnitude of the error bar pairs.

Comp.	Window [yr]	−error [nT/yr^2]	+error [nT/yr^2]	Mean error [nT/yr^2]	Mean |error| [nT/yr^2]
X	5	−1.49	1.27	−0.11	1.38
	10	−1.78	1.44	−0.17	1.61
	15	−1.73	1.78	0.02	1.76
	20	−2.67	2.48	−0.09	2.58
Y	5	−1.12	1.21	0.04	1.17
	10	−1.61	1.78	0.08	1.70
	15	−1.84	1.70	−0.07	1.77
	20	−2.15	2.33	0.09	2.24
Z	5	−1.49	1.56	0.03	1.52
	10	−2.24	3.04	0.04	2.64
	15	−3.31	2.84	−0.24	3.08
	20	−4.47	2.76	−0.86	3.61

3.2.1 TEMPORAL DISTRIBUTION

The timing of jerks is here assessed by histograms of occurrences through time for a variety of spatial regions to assess the robustness of the idea of specific global or local events. A series of straight histogram counts and of equivalent weighted histograms were calculated. The weighted count (Equation (3.2.1)) is calculated as the number of identified jerks in a time bin ($N_{\mathrm{detections}}$) multiplied by the ratio of the number of active observatories in a given time bin (N_{active}) to the maximum number of observatory locations in the study (N_{total}):

$$W_{\mathrm{bin}} = N_{\mathrm{detections}} \frac{N_{\mathrm{active}}}{N_{\mathrm{total}}}. \tag{3.2.1}$$

Whilst it may seem contradictory to down-weight the significance of high proportions of detections at low numbers of active observatories, the weighting is designed to favour observations at the greatest number of observatories to assess whether identifying global events is a justified conclusion. The uncertainty in the time occurrence of each identified event is assumed to be inconsequential for the histograms provided the time bins are wider than the magnitude of the uncertainty estimates, thus a minimum bin width of 12 months is used.

Since the different window lengths used in the identification procedure resolve features at different time scales, a combined histogram of results from all window lengths is shown (Figure 3.1a). The results for the 10 yr detection window are shown in Figure 3.1b and the majority of figures in this chapter, equivalent histograms for the 5, 15 and 20 yr window results are shown in Figures C.1–C.3 for comparison. Figure 3.1a was used to identify the periods of most frequent jerk activity. Relative peaks can be seen in 1968–71, 1973–74,

1977–79, 1983–85, 1989–93, 1995–98 and 2002–03 with additional suggestions of events in the early 1960s and the late 2000s. The latter periods fall at the ends of the data set and thus suffer a lack of resolution from edge effects of the identification procedure. Additionally, the early 1960s are poorly resolved spatially due to this period having the lowest coverage of observatories in this study. The histograms in Figures 3.1–3.4 show that in general the proportion of observatories at which events are identified at a given time is low. Considering all components at all observatories included in the study worldwide, the most widespread jerk identified is seen in 1989–93 at ∼30% of the observatories (Figure 3.1b). The predominant peaks in the global histogram (Figure 3.1a, combined component histogram) represent both a combination of events from all field components e.g. in the 1990s, and also exceptionally high counts from a single component e.g. 1977–79 in the Y-component. These peaks can also be the result of contributions from various regions at overlapping times to produce a peak in the global histogram. When only observatories which are located in the Northern or Southern Hemisphere are considered (Figure 3.2) it can be seen that events in the Northern Hemisphere dominate the global distribution due to the contribution from 73 observatories compared to 21. While the Northern Hemisphere (and thus global) results can in places be described as showing individual peaks of high numbers of jerks detected in a short period of time, the Southern Hemisphere results do not mirror this pattern. This is potentially due to the lack of data rather than the absence of events. A point of interest is that a peak is seen around 1968–1971 in both Hemispheres which does appear to fit the reported observation of an event occurring in the Northern Hemisphere 1–3 yrs before the Southern Hemisphere [Alexandrescu et al., 1996b]. This trend of short North-South delay is not seen for any other distinct peaks and does not appear to be a consistent feature of jerks although the events in 1989–93 and 1995–98 are observed to be largely hemispheric. It is likely that these periods represent two or more regional events overlapping in time, a common feature of the peaks in the global histograms.

The global time distribution of jerks can be broken down further into jerks occurring in spatially distinct regions of observatories (shown on Figure 2.13a). The regional histograms for observatories in Europe, Africa, North America and South America (Figure 3.3) and Asia, Australasia, the Southern Indian Ocean and the Pacific Ocean (Figure 3.4) show which particular components in which regions contribute to the globally observed trends. For example, the distinct global peak around 1969 is predominantly a feature of the X- and Y-components in Europe, the only other significant contributions coming from the

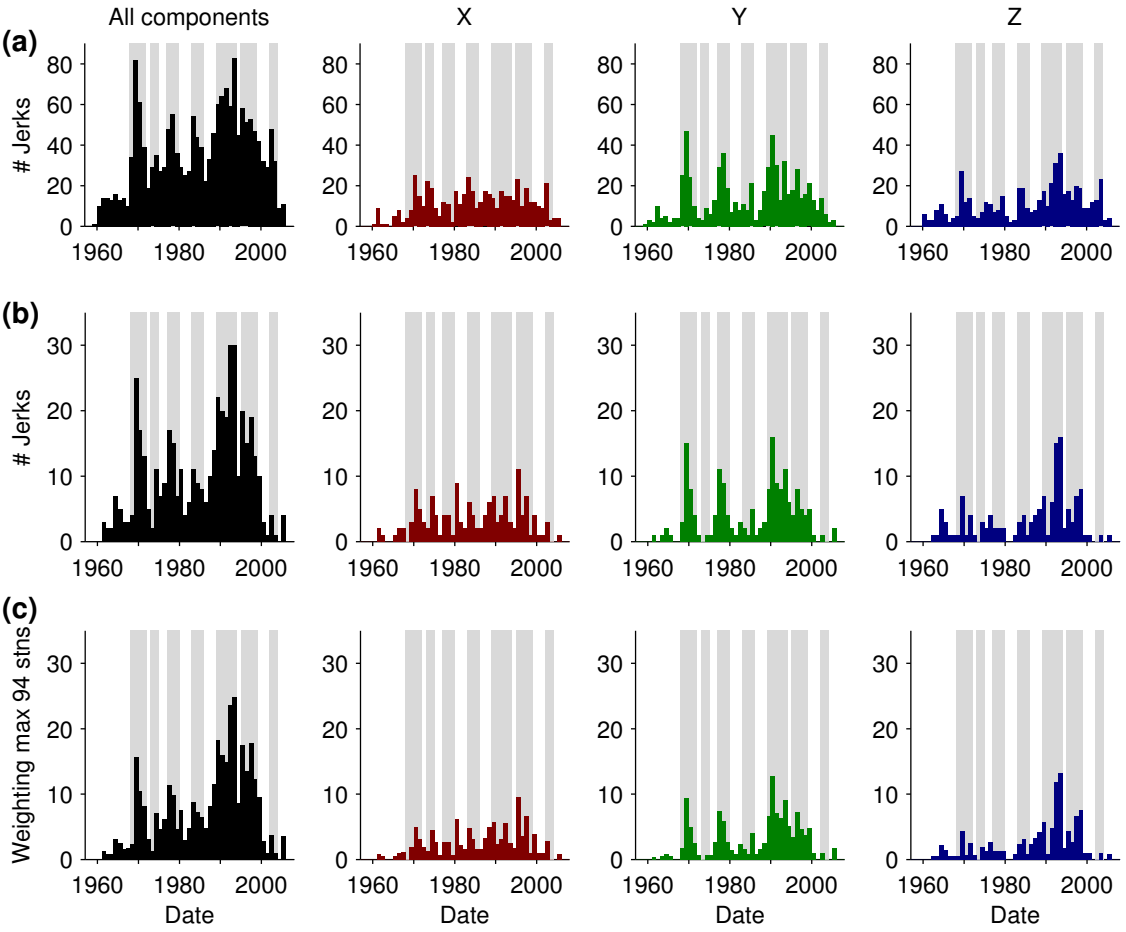

Figure 3.1: Histograms of detected jerks in 12 month time bins between 1957 and 2008, (a) shows straight counts when results from 5 yr, 10 yr, 15 yr and 20 yr windows are combined, (b) shows straight counts for a 10 yr window, (c) shows 10 yr window counts weighted by the number of operating observatories during any given time bin. Columns represent from left to right: the collation of all components, X-component only, Y-component only, Z-component only. The maximum possible weighting value is indicated by the maximum number of observatories (stns) on the y-axis label; this maximum represents a jerk detected at every observatory. Detections at all observatories worldwide are included, grey bands indicate times of peaks in combined (black) histogram for all window lengths (a). From Brown et al. [2013].

Y-components in North America and Asia. This event is very poorly constrained in the Southern Hemisphere.

The global peak around 2003 (Figure 3.1a) appears only weakly in the results for the 10 yr window (Figures3.1b, 3.2–3.4), due to the short time scale of the features in the SV post-2000 and the proximity to the end of the data set. As such, detections are limited with windows of 10 yr and longer but frequent with the 5 yr window (Figure C.1). Proximity to the end of the data set is likely also the reason the 2005 [Olsen and Mandea, 2008] and 2007 [Chulliat et al., 2010; Olsen et al., 2009] events are not resolved. Visual inspection of timeseries suggests that events on a similar scale to those post 2000 may also occur in

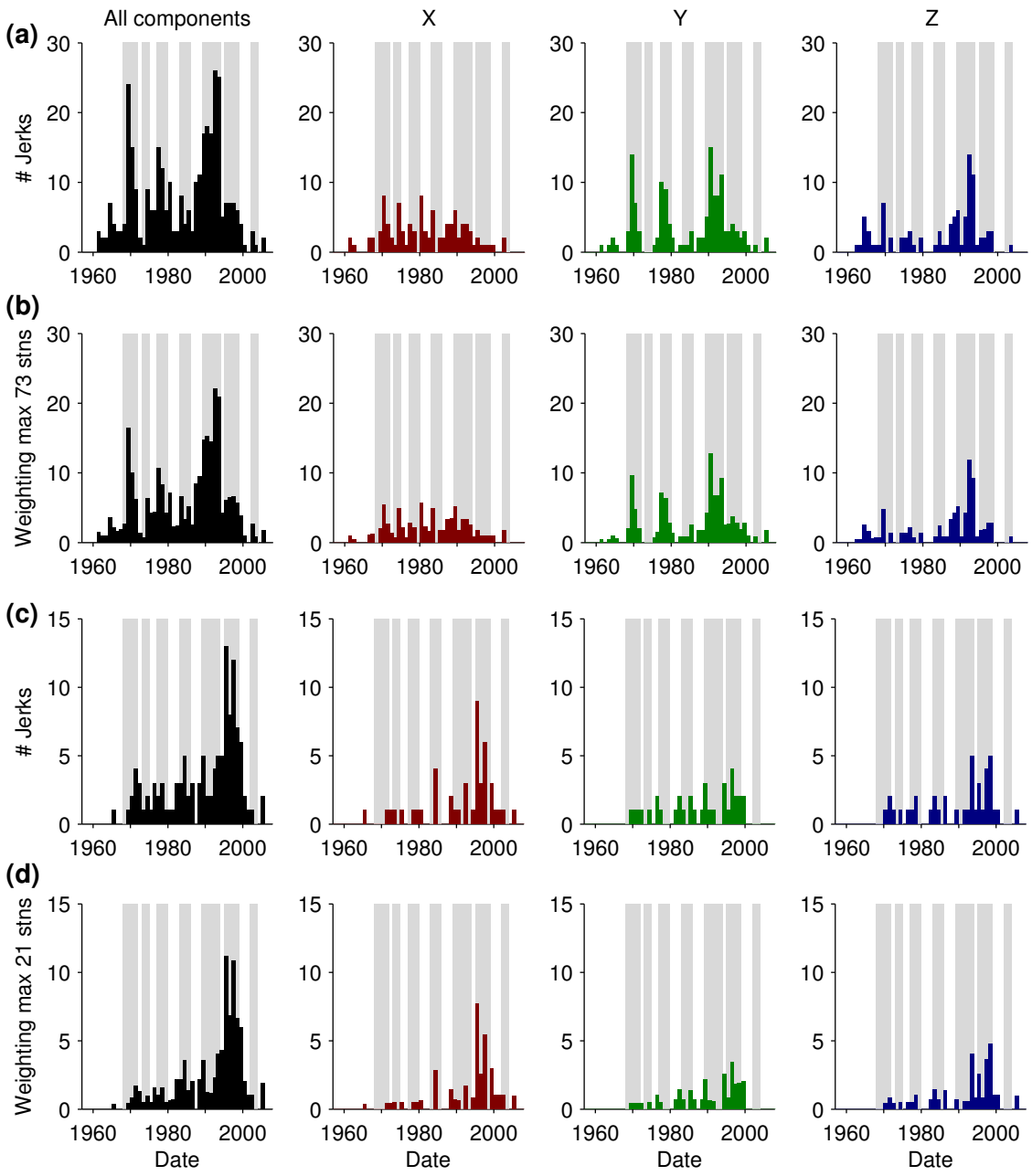

Figure 3.2: As Figure 3.1 but for observatories in the Northern Hemisphere ((a) count, (b) weighted) and Southern Hemisphere ((c) count, (d) weighted) only. From Brown et al. [2013].

the early 1960s, producing small peaks in the histograms (Figure 3.1). These time periods may benefit from a more focused study.

The 1990s show a high incidence of identified events across all regions, focused in the Y- and Z-components in the Northern Hemisphere in 1989–93 and the X- and Z-components in the Southern Hemisphere in 1995–98. These periods may host several events, the overlapping durations of which prevent the definition of a sharp peak. The focus of the latter of these two peaks in the poorly sampled Southern Hemisphere may

explain the previous uncertainty over the extent of the mooted 1999 jerk [e.g. De Michelis and Tozzi, 2005; Pinheiro et al., 2011].

Further distinct events are difficult to trace between regions, being detected in various components in various regions with the dominant signal coming from European observatories.

In order to further check the apparent lack of simultaneity in jerk occurrences worldwide I devised a simple test — the centre times of the global histogram peaks were used as fixed jerk times and a series of piecewise linear trends between these points was fit to each observatory series, minimising the misfit of the piecewise trends sets to all data simultaneously. This was compared to the misfit when a randomly selected number jerks at randomly selected times was used in the same calculation. It was possible to produce the same magnitude of misfit with random jerk times as achieved with the jerk times suggested by the peaks of the global jerk histograms. This implies that global simultaneity of jerks is not supported for the jerk times identified as most common in this study or for any of the combinations of times tested.

3.2.2 SPATIAL DISTRIBUTION AND MORPHOLOGY

Despite the fact that only a small proportion of observatories identify jerks in a given time period, it is still informative to look at the spatial distributions of these events. As noted by Pinheiro et al. [2011], the jerk amplitudes prove to be a reliable measure, showing that even where low probability events are identified, the amplitude uncertainty estimates are small and the amplitudes of events detected at observatories in close proximity show the same polarity and similar magnitude.

Examples of the amplitude distributions for three characteristically different peaks in the histograms seen in Section 3.2.1 are depicted here: a well documented global peak whose precise occurrence time varies by region (1968–71, Figure 3.5); a broad period of the highest incidence of events in all components in all regions (1989–93, Figure 3.6); and a period which contains an event whose extent is debated in various studies (1995–98, Figure 3.7). Equivalent figures of the remaining periods of relative peaks in jerk occurrences are presented in Figures C.4–C.7.

The jerk amplitudes of 1968–71 (Figure 3.5) are seen to be dominated by Northern Hemisphere, particularly European, observations in the X- and Y-components. The X- and Y-components show similar spatial and magnitude patterns but with opposite polarity. There is no definitive evidence of the zonal patterns in X- and Z-components or the sectoral

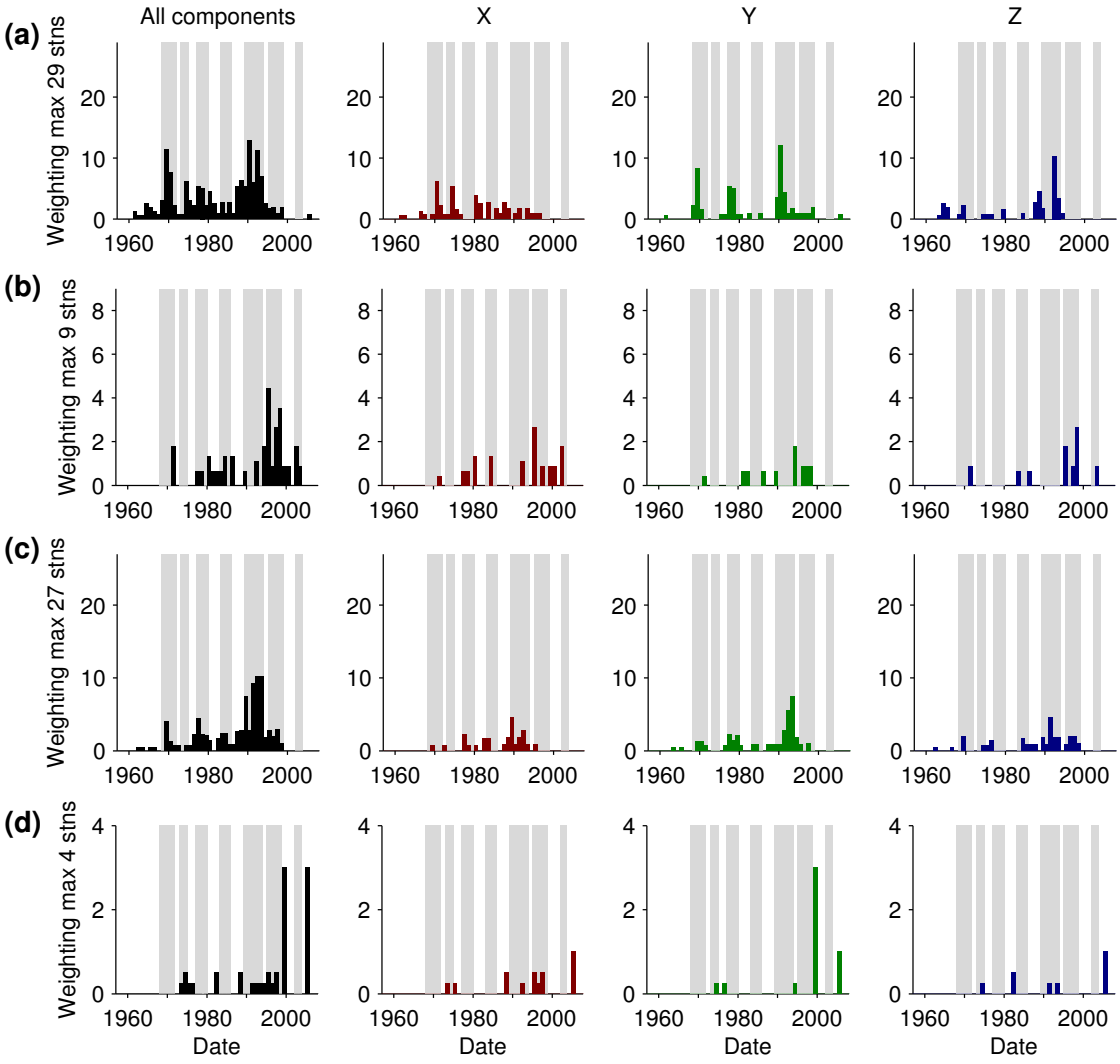

Figure 3.3: Weighted histograms as Figure 3.1 but for observatories in (a) Europe, (b) Africa, (c) North America and (d) South America only. From Brown et al. [2013].

pattern in the Y-component as described by early works such as Le Mouël et al. [1982]. The Z-component is largely unconstrained over Europe and shows a much less significant event than those in the X- and Y-components. The amplitude results fit well with those calculated for the 1969 jerk by Le Huy et al. [1998], De Michelis et al. [2000] and Pinheiro et al. [2011] and disagree with those of Le Mouël et al. [1982] in so doing. Little can be determined conclusively about the morphology in the Southern Hemisphere.

The jerk amplitudes in the period of 1989–93 (Figure 3.6) show a different style from those of 1968–71. Jerks are seen more consistently across wider regions in all three components. There is a very high incidence of jerks in all three components at overlapping times during the 5 yr period of 1989–93. Twin peaks of 1–3 yrs in jerk occurrences are seen in the X-, Y- and Z-components in an asynchronous manner, leading to an

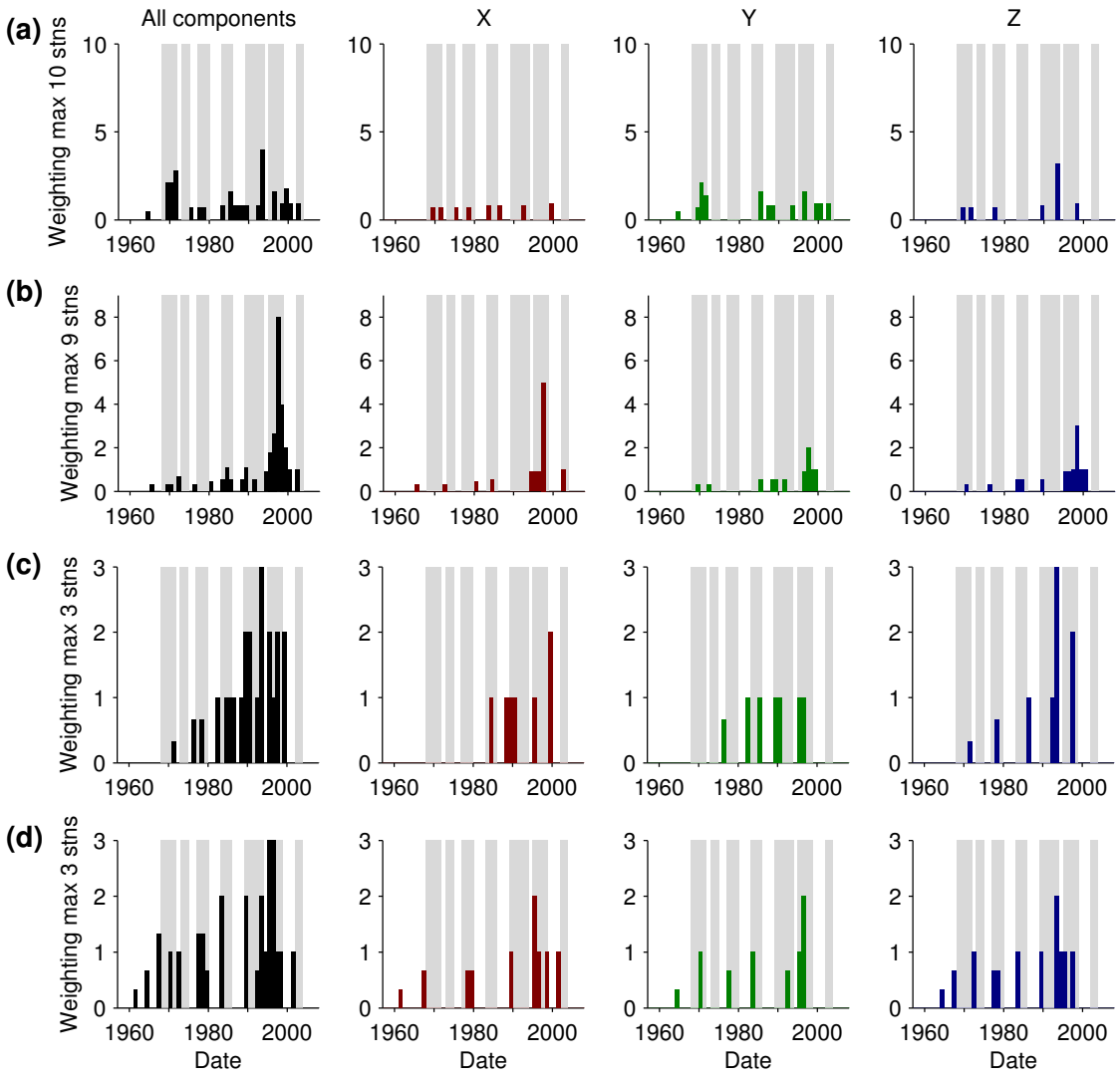

Figure 3.4: Weighted histograms as Figure 3.1 but for observatories in (a) Asia, (b) Australasia, (c) Southern Indian Ocean and (d) Pacific Ocean only. From Brown et al. [2013].

overall peak spanning 1989–93 (Figures 3.1–3.4). The resulting pattern of amplitudes is more complicated than that of 1968–71, with localised variations in polarity. The jerks in the Y-component in Europe appear to transition from positive to negative polarity through time while the X- and Z-component occurrences peak twice with the same polarity. Observations in X- and Y-components in North America appear to transition between positive and negative amplitudes spatially with all jerks occurring in a single span of 2–3 yrs. These results suggest the complicated structure and varying descriptions of the reported 1991 jerk [see Chambodut and Mandea, 2005; De Michelis and Tozzi, 2005; Le Huy et al., 1998] can be explained by a double peak in the occurrences of jerks seen in this study in the period of 1989–93 (Figures 3.1–3.4). The amplitude results from the latter half of the 1989–93 peak best agree with the 1991 jerk amplitudes of Le Huy et al. [1998],

De Michelis et al. [2000] and Pinheiro et al. [2011].

Jerk amplitudes in the period of 1995–98 (Figure 3.7) are unusual with respect to other periods of frequent jerk occurrences in that most of the detections are in the Southern Hemisphere. These amplitude results are consistent with those of De Michelis and Tozzi [2005]; Mandea et al. [2000] but not those of Pinheiro et al. [2011]. Minimal evidence of jerks in Europe can be seen with more widespread occurrences in the rest of the world, whilst Pinheiro et al. [2011] found very limited local evidence, largely in Europe. This discrepancy may be a result of the limited data window of 11–15 yrs of annual means selected by Pinheiro et al. [2011] which was centred around 1999 and thus possible overlap of events in the early to mid 1990s and 2000s, which I define as temporally close but distinct periods of frequent jerk occurrences.

A peak in the occurrences of jerks is seen in the period of 1977–79 (Figures 3.1–3.4), corresponding to the 1978 jerk amplitudes observed by De Michelis et al. [1998], Le Huy et al. [1998] and Pinheiro et al. [2011] in all components. The observations of this period bear much similarity to those of 1968–71 including providing few constraints of events in the Southern Hemisphere.

The jerks in the period of 2002–03 (Figure 3.1a and Figure C.7) are seen in all three components. As mentioned in Section 3.2.1, the proximity to the end of the data set means that few events are seen with a window of 10 yrs or longer and jerks are more readily identified with the 5 yr window (Figure C.1 and Figure C.8). A unique characteristic of this time period is that all the observations of the Z-component suggest a hemispheric dichotomy in polarity (see Figure C.8), a feature not seen in any other period investigated. The amplitude results here agree with the observations of Olsen and Mandea [2007] in all three components.

The reported 2005 [Olsen and Mandea, 2008] and 2007 [Chulliat et al., 2010; Olsen et al., 2009] jerks are not prominent in these results; this is likely due to the reduced effectiveness of the identification method with proximity to the end of the data set.

Observed amplitude patterns do not appear to be consistent in form between events although regional polarity does seem to show an alternating pattern. This will be discussed in Section 3.2.4.

3.2.3 Spatiotemporal Relationship

The relationship between the temporal and spatial patterns of jerk occurrences could hold information as to their source mechanism. For example jerks generated by torsional

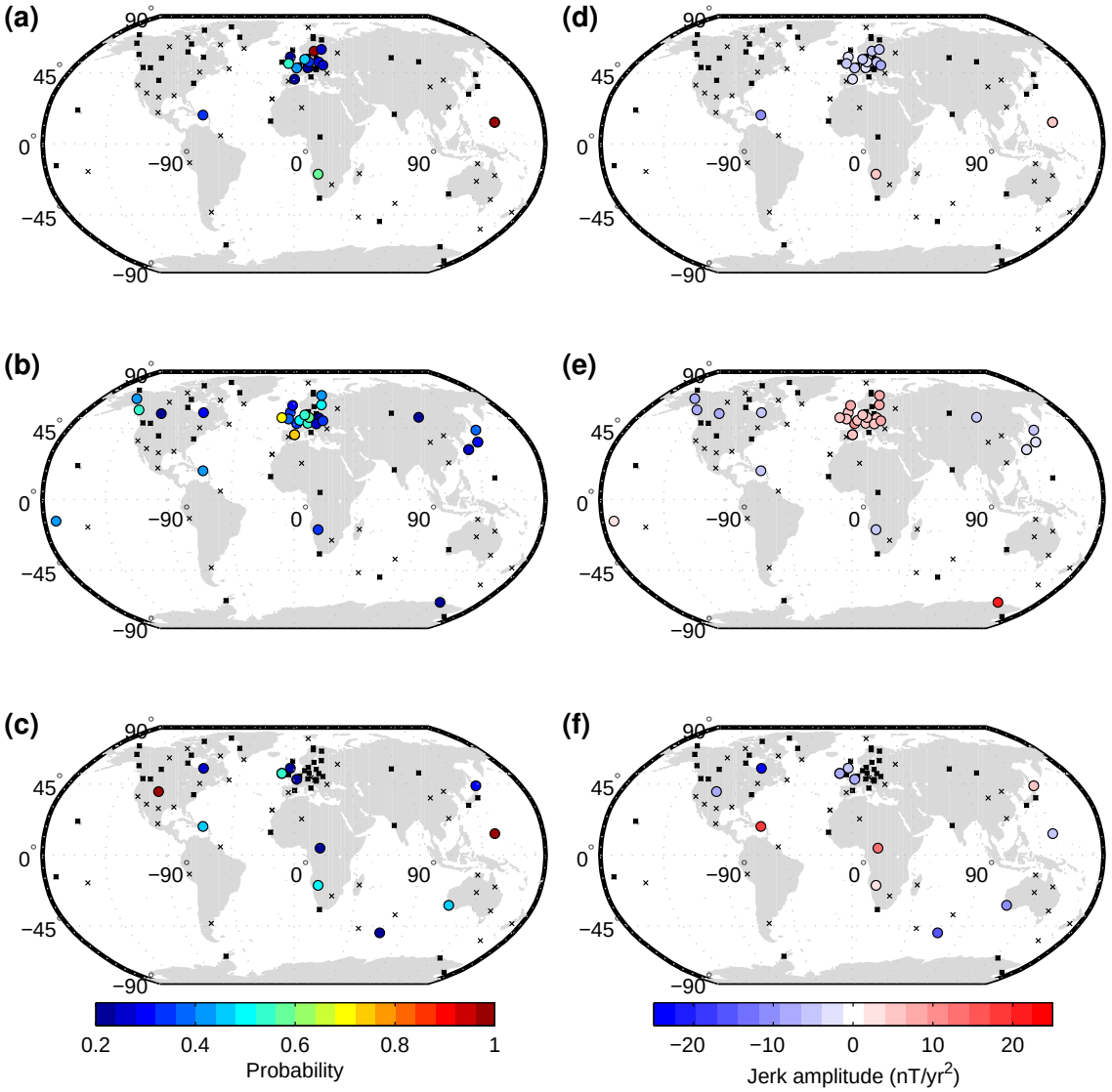

Figure 3.5: Jerk probability (a–c) and amplitudes (d–f) for the period of 1968–71. Top to bottom are the X-, Y- and Z-components respectively. Black crosses represent inactive observatory locations, black squares represent active observatory locations which did not detect a jerk and coloured circles represent identified jerks. Results from 10 yr window. From Brown et al. [2013].

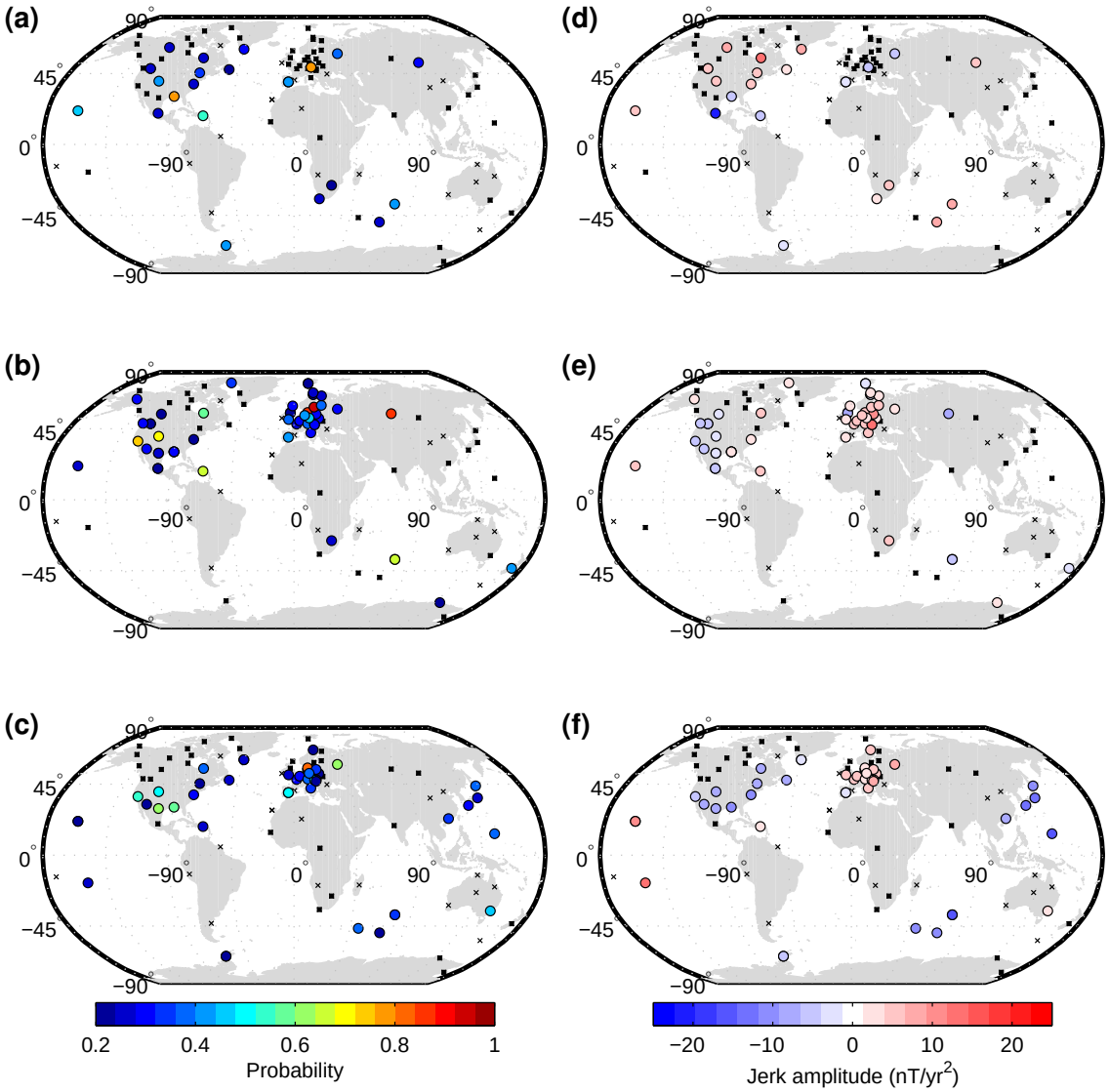

Figure 3.6: As Figure 3.5 but for the period of 1989–93. From Brown et al. [2013].

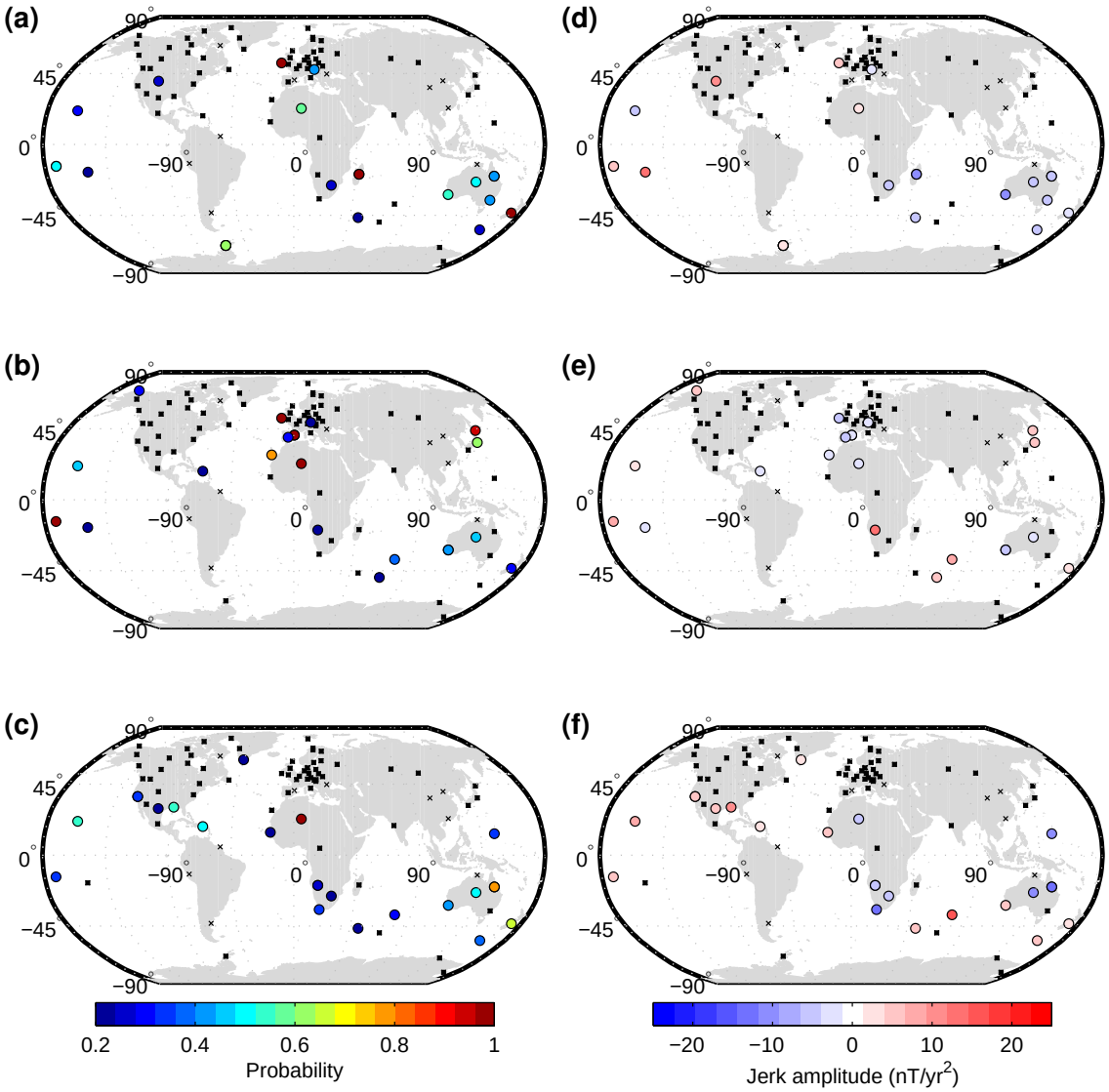

Figure 3.7: As Figure 3.5 but for the period of 1995–98. From Brown et al. [2013].

oscillations [e.g. Bloxham et al., 2002] may show evidence of wave propagation in the cylindrically radial direction. The presence of trends in identified jerk times with cylindrical radius (or latitude) and longitude were investigated. No clear relationships were found in any combination of these variables. It was found that accounting for the concentration of observatory locations in certain regions, jerk times appear to be distributed evenly through latitude, longitude or cylindrical radius and concentrated only about certain time periods as Figures 3.1–3.4 show. It can be seen in Figure 3.8 that while some epochs, e.g. around 1970 in the Y-component, show a more dense clustering in time of jerks at a range of cylindrical radii, there is no consistent pattern between the events which correspond to relative peaks in the histograms in Figures 3.1–3.4.

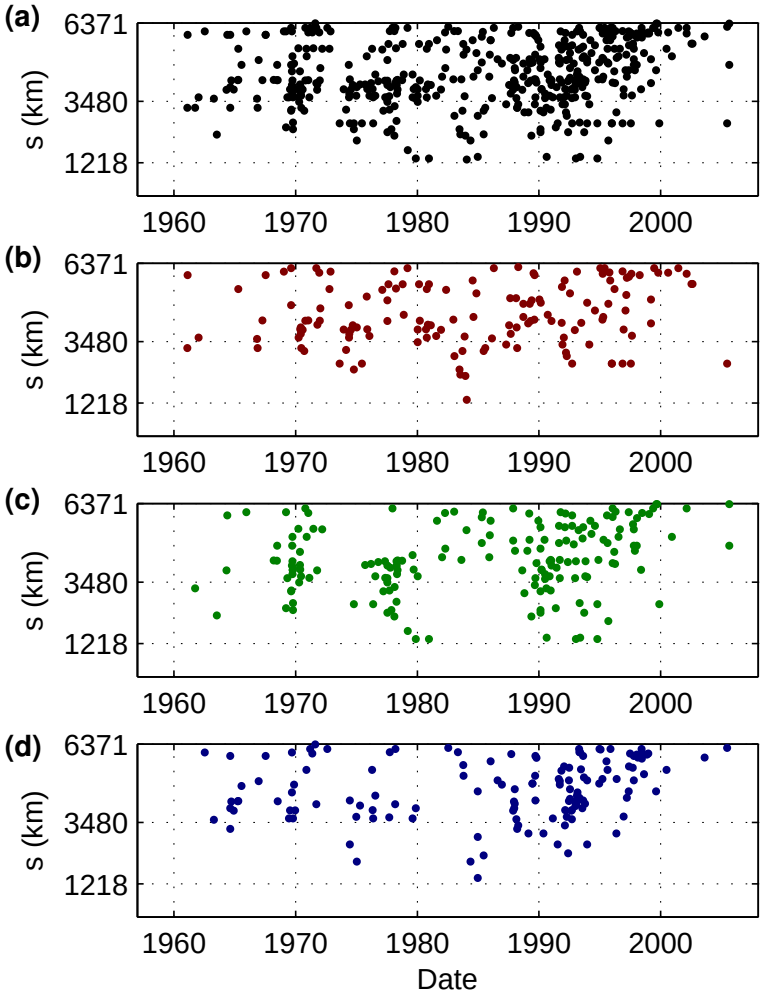

Figure 3.8: All identified jerk occurrences using a 10 yr window plotted against cylindrical radius (s). Plots show jerks in all three components (a) and in the individual X- (b), Y- (c) and Z-components (d). From Brown et al. [2013].

3.2.4 PERIODICITY OF JERK AMPLITUDE

It has been observed [e.g. Chulliat et al., 2010; Le Huy et al., 1998] that the series of jerks at approximately 1969, 1978 and 1991 show a trend of alternating polarity of jerk amplitude. It has been suggested this is a feature of long term memory in the source mechanism of jerks [e.g. Alexandrescu et al., 1996b; Le Huy et al., 1998]. With regard to analysing this trend in my results three questions arise: Are successive jerks seen to change amplitude polarity through time? Is this trend zero mean? Is this polarity change periodic? The amplitude maps in Figures 3.5–3.7 show that at a given time the polarity of the jerk amplitude varies across the globe, thus trends must be considered in smaller regions of observatories where the same polarity signal would be expected. I focus on Europe and North America since these two regions provide the greatest coverage both in terms of numbers of observatories (29 and 27 respectively) and time spans of data. Global patterns of alternating polarity amplitudes are discussed further in Chapter 5.

It is found that for both Europe and North America, in all three components, the jerk amplitude polarity can be seen to vary through time (Figures 3.9(a–c), 3.10(a–c)). In both regions, for all components these variations are zero mean to within a tolerance of ± 1 nT/yr^2 although distinct clustering of events in time and amplitude is stronger in Europe than in North America as the histograms in Figure 3.3(a,c) show.

To assess the possible periodicity in jerk amplitudes the power spectra of the jerk amplitudes is estimated via the Lomb-Scargle method of least-squares spectral analysis [see Lomb, 1976; Scargle, 1982]. It can be seen that there are predominant peaks in the spectra (Figures 3.9(d–f), 3.10(d–f)). Since it is unknown what effect the irregular time sampling of jerk occurrences may have on the estimated spectra, synthetic tests were conducted. These tests began with the basic case of generating a single frequency sinusoid timeseries of equivalent time span to the jerk amplitude series and then re-sampling this synthetic at the estimated jerk occurrence times, before calculating the spectrum. This spectrum could be compared with the known spectrum of the original sine function. More strenuous tests with multiple combined sine functions of different periodicities and phases and an additional Gaussian noise (comparable to those used in Chapter 2 Section 2.4.3) were then conducted. The testing showed that for realistic noise levels it was possible to recover the input synthetic periodicities with the irregular sampling of estimated jerk times at European and North American observatories and thus the estimated periodicities in jerk amplitudes are likely not artefacts of the irregular time

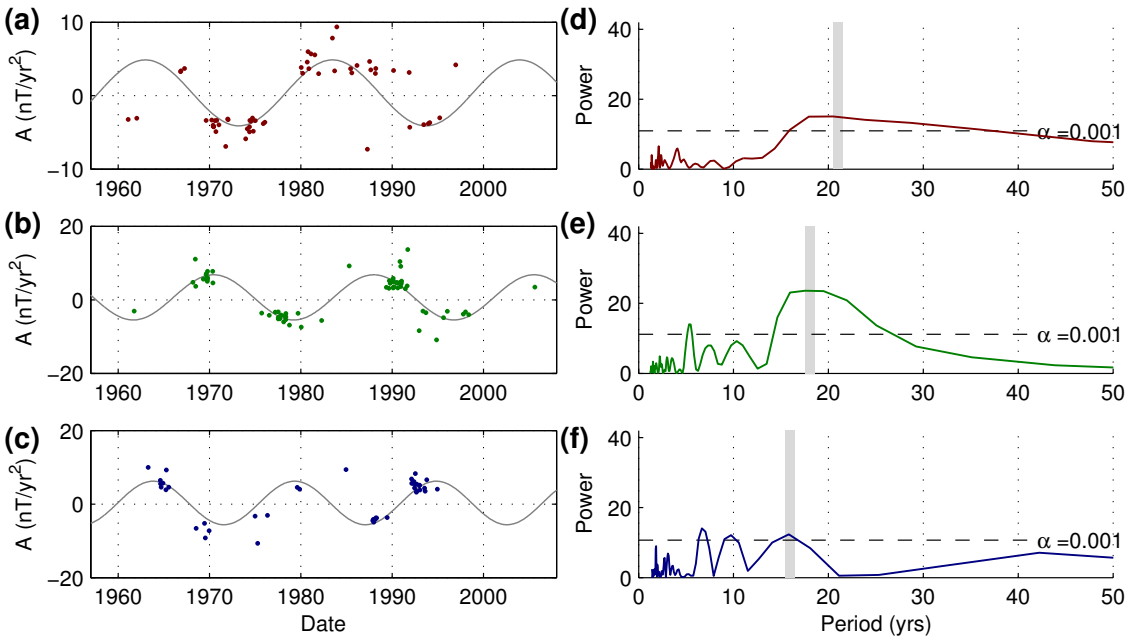

Figure 3.9: Time series of jerk amplitudes for all European observatories (a–c) and corresponding power spectra calculated as Lomb-Scargle periodograms (d–f). Plot rows show X-, Y- and Z-components from top to bottom. Symbol α represents the statistical certainty level as a function of power with higher power more certain. Jerks were detected using the 10 yr window. The highlighted periods in (d–f) are plotted as least-squares fit sinusoids over the data in (a–c). From Brown et al. [2013].

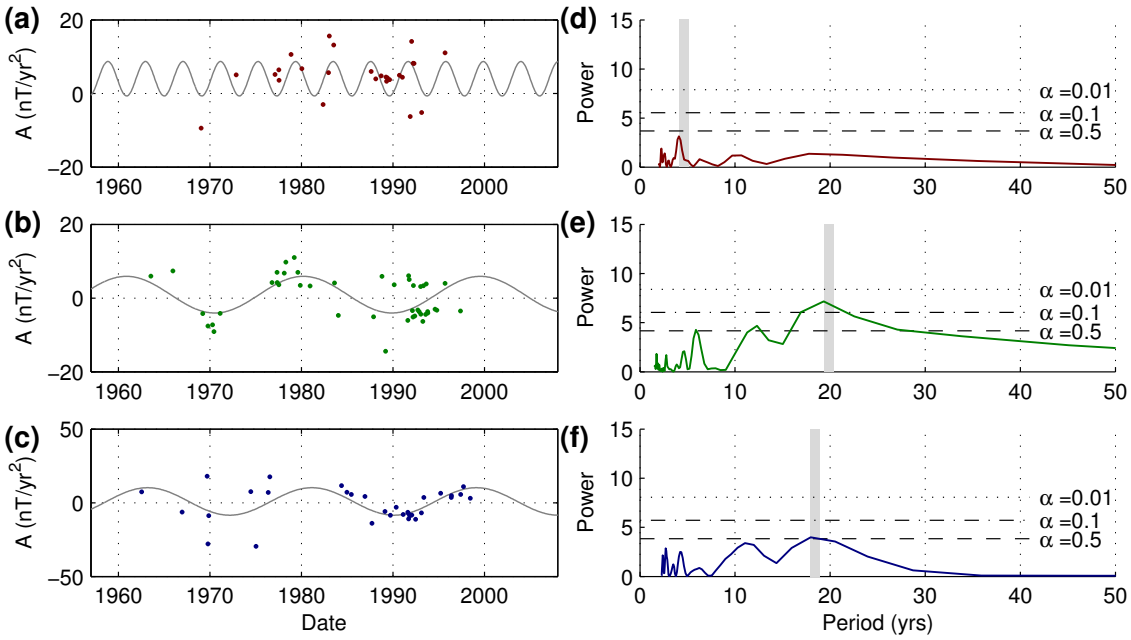

Figure 3.10: As Figure 3.9 but for all North American observatories. From Brown et al. [2013].

sampling.

The statistical significance (false alarm probability of the null hypothesis test, α) of peaks in the spectra was judged as a function of power derived from the exponential

probability distribution of the spectrum and the number of frequencies tested (taken to be evenly spaced up to the equivalent Nyquist frequency for the same number of evenly spaced data points) [see Press et al., 2007]. An oversampling factor of 4 was used to ensure that spectra peaks can be resolved [Press et al., 2007]. Thus higher power, and lower values of α, represent more certain results. Generally the spectra for Europe were found to hold more significant peaks than those for North America. It is possible that the length of the identification window used to calculate the linear regression creates artefacts in the periodicity of the identified jerk events. While no spectral peaks appear at aliased window periods, only signals which appear consistently in results from the 5 yr, 10 yr, 15 yr and 20 yr windows are considered robust observations.

European observatories were found to show significant, consistent signals for all detection window lengths at periods of ∼18–20 yrs in the Y-component. Significant signals for three of the four window lengths were seen at ∼17–20 yrs in the X-component, ∼7–8 yrs in the Y-component, and ∼7 yrs and ∼15–16 yrs in the Z-component. North American observatories were not found to show consistent signals at all detection window lengths but moderately significant signals were seen for three of four window lengths at ∼11–12 yrs and ∼19–21 yrs in the Y-component and ∼18–22 yrs in the Z-component. The greater uncertainty of results for North America may be attributed to the greater spatial extent of the observatories (and thus greater variation of signal) compared to the dense network in Europe.

With the limited data available it is hard to be conclusive as to the presence of periodic signals worldwide. However, the premise is an interesting one, perhaps complementary to the ∼6 yr magnetic and LOD signals (or higher harmonics of) reported by Abarco del Rio et al. [2000]; Gillet et al. [2010]; Holme and de Viron [2013]; Silva et al. [2012]. These periodic signals are likely to be internal since corrections for external fields have been applied to the data but also considering that geographic variation of the periodicity is observed and periodic external signals would be expected to be consistant globally [Langel, 1989]. Globally observed periodicities attributed to the Solar-magnetic cycle (SMC) and/or SC and their harmonics have been found at for example 22.9, 11.5, 6.9, 5.6, 4.4, 3.8, 3.0, 2.8, 2.4, 2.3 and 2.1 yrs by Currie [1976] or for only the SC at 11.1, 5.3, 4.3, 2.7, 2.1 yrs by Prestes et al. [2006]. While periodic jerk amplitude trends are observed close to the dominant 22 yr (SMC) and 11 yr (SC) periods in the X- and Y-components in Europe, and the Y-component in North America, they are not consistently seen at these periods across all components in all regions as might be expected. The higher harmonics

of the SMC and SC periods are not observed in any component to a significant degree.

Periodicity in the polarity of jerk amplitudes implies that the observed step changes in the SA associated with jerks regularly oscillate between a similar maximum and minimum magnitude. This suggests that the source mechanism for the jerk signal is periodic and shows a relatively consistent magnitude effect in the observed magnetic field in a given region. It has yet to be determined if the disparities in the periodicity observed between European and North American observatories persist to the CMB as a feature of the source mechanism or are an effect resulting from interaction with a conducting mantle [e.g. Pinheiro and Jackson, 2008].

3.3 SUMMARY

Using monthly mean data and removing external field signals produces increased time resolution and reduced uncertainty estimates on jerk occurrence times and amplitudes compared to the results of Pinheiro et al. [2011]. The results presented here suggest that the established global and local jerk times reported in previous studies do not fully characterise the observations as a whole but rather describe select portions of a much larger data set. It should be noted that observatory data provide a sparse data set for even the best observed events and that this should be taken into consideration when assessing the potential occurrence of global events. Nevertheless these observations suggest that between the epochs of 1957 and 2008 there are periods when jerks occur more frequently in particular regions of the world (Figure 3.11). These can be summarised as 1968–71, 1973–74, 1977–79, 1983–85, 1989–93, 1995–98 and 2002–03 with the suggestion of further poorly sampled events in the early 1960s and late 2000s. It should be noted that none of these events were detected at more than 30% of observatories in a given year. These peaks in jerk occurrences do not appear to manifest as consistent forms in the distribution of amplitudes and are seen to occur in various combinations of components. Jerks are not seen to occur simultaneously across all regions of the globe and the bias of the data set to the Northern Hemisphere, particularly Europe, is evident in the composition of global jerk occurrences. Neither do jerks show a consistent relationship in patterns of occurrence between regions, which suggests that the relationship between so called jerk delay times and properties such as mantle electrical conductivity do not follow a simple or constant rule if at all. Better understanding of the cause of jerks may be needed to explain the variations in occurrence times observed.

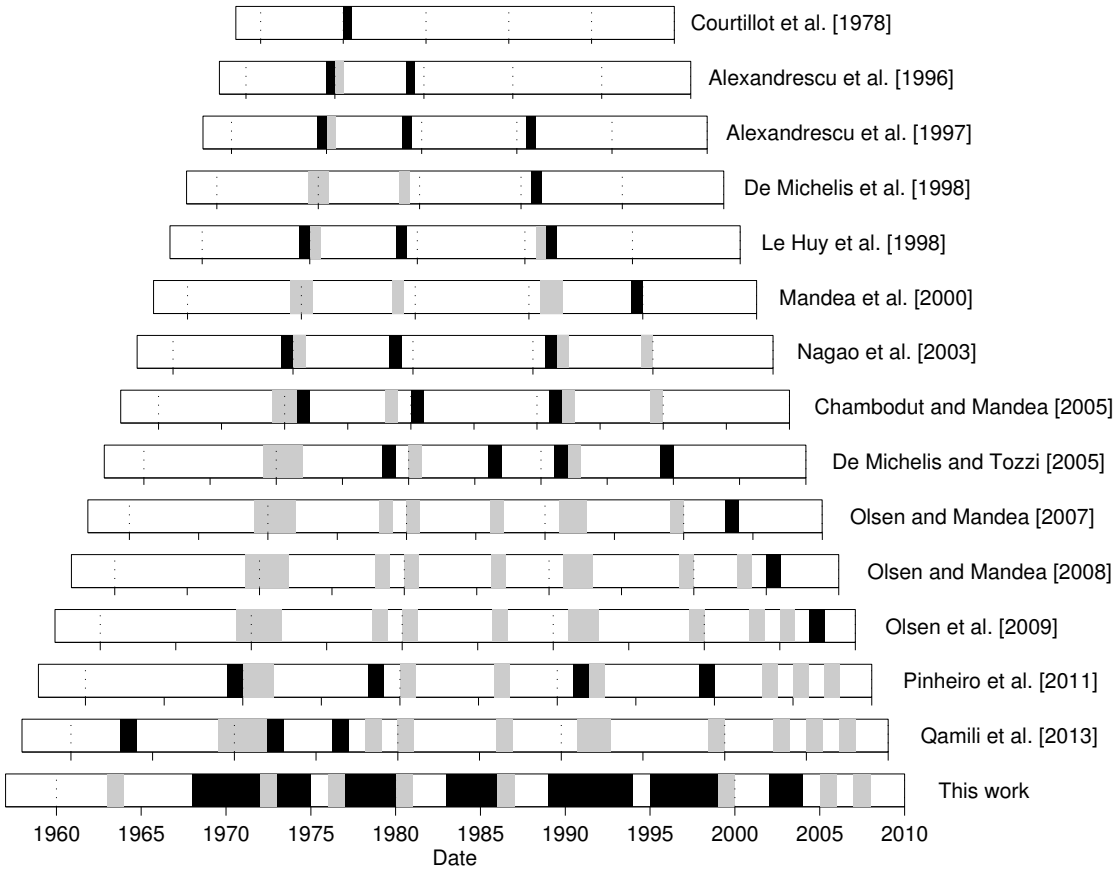

Figure 3.11: Summary of identified jerks in selected publications. Black boxes represent jerks discussed in each particular publication, grey boxes show an amalgamation of the events from all works prior to a given publication. For the results of this work, the black boxes represent relative peaks in numbers of global jerk identifications while for all previous studies the boxes indicate the quoted mean year of identified jerks. From Brown et al. [2013].

The results presented here suggest that previously reported observations of jerk times are largely consistent with my findings, but restricted to those events of greatest magnitude and isolation in time. I show that event occurrences are frequent and occurrence patterns vary but that there are times when many events are seen in several components across large portions of the Earth's surface. The jerks detected around 1968–1971 stand out as being of significantly greater magnitude and the most isolated in time making their identification more robust and consistent. The general trend of increased numbers of identified jerks toward the end of the 20th century and start of the 21st century makes defining individual events more complicated as the distinction between 'early' and 'late' events blurs considerably. Again, analysis of the resulting magnetic field without comprehension of the source mechanism can only lead so far.

The analysis of the spatial distributions of jerk amplitudes fits well with the observations of previous studies [e.g. De Michelis et al., 2000; Le Huy et al., 1998; Pinheiro et al., 2011]

and suggests that the observations of less commonly reported events may help to expand the catalogue of features which must be explained by works addressing core dynamics.

To this end I present the final result, the possibility of periodicity in jerk amplitudes. The periodicities in time and magnitude of jerks observed in Europe and North America suggest potential links to other observed periods in the magnetic field, LOD and potential generation mechanisms [Gillet et al., 2010; Silva et al., 2012]. Observing the jerk amplitude polarity and magnitude through time also provides a means of defining peaks in jerk occurrences and separating events which appear to overlap in time. The presence of several signals with varying periods in each component suggests that the source is internal but the mechanism is far from simple. Additionally, there may be superposition of many signals and, potentially, interaction with mantle electrical conductivity variations to create the complicated spatial and temporal observations.

Without complete global coverage and far longer temporal spans of high quality observatory data it is hard to be sure of how much of the preceding analysis provides a true assessment of the phenomena of jerks. Since the alternative is to wait several more years for more data to accumulate, it seems appropriate to investigate what corroboration synthetic data, where temporal and spatial coverage are all but unlimited, can provide. This topic is pursued in Chapters 4 and 5.

ADDENDUM

The smoothing effect of calculating SV as annual differences of monthly means, as noted in Section 1.7.1, has inference on the results and subsequent conclusions of Chapters 2 and 3. If jerks are smoothed in the data to the extent where the 'v' shaped SV assumption no longer holds and a 'u' shape is more appropriate, my identification method may yield less accurate results — certainly higher uncertainties would be expected. Given the limited degree of SV smoothing introduced by taking annual differences of monthly means compared to noise levels in the data (see Figure 1.10), I do not credit this effect with suggesting a significant impact on the result presented here. Various authors have previously used the 'v' shaped assumption to fit smoother annual mean data [e.g. Pinheiro et al., 2011] or regularised model timeseries [e.g. Chambodut and Mandea, 2005] and also found it to be a suitable assumption. The reduced uncertainties in jerk occurrence times estimated in this Chapter compared to the work of Pinheiro et al. [2011] are due to the external field cleaning process in combination with the improved temporal resolution of the data, not solely the data resolution. If study was to focus on jerk identification in the

SA or third time derivative, the smoothing effect of the SV calculation would likely have a much greater impact and the 'v' shaped SV assumption of instantaneous jerks would likely no longer be suitable.

CHAPTER 4

STOCHASTIC SYNTHETIC FIELD MODELS

4.1 OVERVIEW

This chapter, and the following, address some of the issues raised by the analysis of observatory data in Chapter 3 regarding the impact of the limited spatial and temporal coverage of geomagnetic measurements. Of particular interest is how these factors might influence or bias our interpretations of the extent and patterns of jerks.

One approach to this problem is to analyse existing magnetic field models, searching for representations of the jerks detected in observatory data as in works such as Chambodut et al. [2007]. By using the flexible spatial sampling offered by spherical harmonic models to assess how the temporal and spatial interpretation of jerks might vary with sampling density, one could attempt to validate the conclusions drawn in Chapter 2. There are, however, some issues with this approach. First, as discussed in the previous chapter, many field models apply a temporal regularisation which smooths features such as jerks. By deferring to analysis of such models, one may inadvertently have lost some of the signal sought after. Secondly it is probable, as suggested in the previous chapter and by, for example, Alexandrescu et al. [1996b], De Michelis and Tozzi [2005] and Olsen et al. [2009], that jerks are regional features. Thus their spatial intricacies will be best captured in field models built from densely sampled satellite observations. This limits us to analysing only the short period from 1999 to present and the few jerks it contains and which may not be representative of the longer term trends.

Instead I propose to use suitable synthetic models, containing features which mimic jerks, not constrained by a set time period or source of data but instead constrained to

behave in a statistically realistic manner. With freedom to vary the temporal and spatial sampling, the impact of these factors on the analysis of jerks can be investigated. By choosing a synthetic model, the ability to generate many random realisations allows the possibility to separate (low) chance features from those which are consistently displayed.

By doing so I aim to validate the interpretation of jerks as regional and not global scale events at the Earth's surface, as made from observatory data, and to quantify their spatial extent, taking into account the sparse distribution of observatories.

Section 4.2 describes the design of the synthetic models chosen while Section 4.3 compares the synthetic data with observatory data and field models to prove they provide a suitable substitute in this study. Next, Section 4.4 details first the procedure I will use to generate the synthetic data, and second the subsequent analysis applied to it, along with the justification for these steps. Section 4.5 concludes this chapter with a summary of the modelling and analysis procedures to be applied in Chapter 5.

4.2 SYNTHETIC STOCHASTIC FIELD MODELLING

The key to any model used for the purpose of investigating jerks is simple in principle; the model must realistically portray jerks and the SV of the field. Many existing field models fail to do this, principally because observations are not of solely the internal field and because they are regularised in space and time so as to smooth the effects of uneven spatial sampling, noise and variable measurement precision. The modelling procedure to be used here is derived from the stochastic field modelling procedure of Gillet et al. [2013] and Hellio et al. [2014][1]. Such models can account for the described drawbacks of observations but still allow sharp time variations. By utilising synthetic models the ability to sample in space and time arbitrarily is now possible, and many realisations can be calculated to infer general characteristics as well as to quantify variability.

Gillet et al. [2013] and Hellio et al. [2014] applied the stochastic modelling technique to two different eras and timespans of observations. Global observations took the form of land survey and maritime observations (collated by Jackson et al. [2000] for *gufm1*), observatory and satellite measurements spanning 1840.0 to 2010.0 in the case of Gillet et al. [2013], while localised archaeomagnetic intensity and directional observations from Mari, Syria and Paris, France were used in the case of Hellio et al. [2014]. In essence the procedure used in this thesis applies the theoretical concept and statistical prior

[1] I would like to thank Nicolas Gillet for providing the basic code which made this study possible.

constraints used by Gillet et al. [2013] and Hellio et al. [2014], but without the constraints of observations, to produce solely synthetic field models. Here I will predominantly follow the notation of Hellio et al. [2014] but the procedure of Gillet et al. [2013] for application of the modelling technique to the observatory era, noting that there are some known discrepancies between the equivalent descriptions in the two reports.

Gillet et al. [2013] state that to attain reliable estimates of the core dynamics which generate SV, knowledge of the SV at the CMB (a downward continued model of surface or satellite observations) and the related model statistics are necessary. In particular the second order statistics, namely the autocorrelation and autocovariance, of the field model coefficients through time are needed, especially when considering epochs with greater measurement errors prior to the introduction of scalar proton magnetometers (circa 1960) and with poor spatial coverage prior to the continuous, dense coverage of satellite data (1999). By using estimates of the means and covariances of the modelled Gauss coefficients, the variable precision and spatial distribution of measurements through time can be accounted for without strong regularisation being applied. The issue with regularisation is taken to be that use of common temporal smoothing methods does not realistically capture the abruptness of jerks (see Figure 4.1 in Section 4.3), while spatial regularisation often provides visually appealing, but not physically justified smoothing. For example, a norm defining the bound on the Ohmic heating at the CMB [Gubbins and Bloxham, 1985] is often used although the quantity is poorly known [Jackson and Livermore, 2009; Jackson et al., 2011]. Moreover, it is general practice [see e.g. Jackson et al., 2000] to apply a damping parameter to trade-off this norm against the misfit of the model to observations, thus altering the scale of what is in principle a set physical bound, albeit a loosely constrained one, to give the desired level of smoothing [see Backus, 1988, for such criticism].

The concept of using the statistical properties of the well observed large-scale magnetic field to produce ensemble models was used by Gillet et al. [2009]. An ensemble of magnetic field models at the CMB was used to produce estimates of the core flow which could explain the known parts of the field and an extrapolated small scale component, governed by the typical correlation timescale of the observed part of field. Applying such a principle to the magnetic field during the observatory era (1840–2010), Gillet et al. [2013] proposed that the timeseries of model Gauss coefficients could be represented by realisations of a continuous time process φ that is Gaussian, stationary and stochastic. It is assumed the values of the coefficients have zero mean, that there is zero covariance

between different coefficients, only covariance in time of the same coefficient, and that the autocovariance function for all coefficients of the same degree is equal. The process can be defined as the sum of its mean value $\bar{\varphi}$ and a perturbation $\varphi'(t)$,

$$\varphi(t) = \bar{\varphi} + \varphi'(t), \tag{4.2.1}$$

with a covariance function of,

$$\operatorname{cov}\left[\varphi(t), \varphi(t+\tau)\right] = \mathrm{E}\left[\varphi'(t), \varphi'(t+\tau)\right] = \sigma^2 \rho(\tau), \tag{4.2.2}$$

where $\mathrm{E}\left[\dots\right]$ is the statistically expected value, σ^2 is the variance, ρ is the autocorrelation function of φ with the timescale of the variation $\tau = |t - t_0|$, t defining the timesteps at which the process is sampled. Here ρ contains the *a priori* information about the model parameters — the Gauss coefficients that describe the magnetic field. This information can be captured in an *a priori* covariance matrix. Calculations with the covariance matrix $\mathbf{C}$ can be efficiently performed by utilising Cholesky factorisation, $\mathbf{C} = {\mathbf{U}_\mathrm{C}}^\top \mathbf{U}_\mathrm{C}$ where $\mathbf{U}_\mathrm{C}$ is an upper triangular matrix (a similar expression with the lower triangle is also possible).

With this *a priori* information, a realisation of model coefficients $\mathbf{m}$ can be calculated after Equation (4.2.1) as,

$$\mathbf{m} = \bar{\mathbf{m}} + {\mathbf{U}_\mathrm{C}}^\top \tilde{\mathbf{m}}, \tag{4.2.3}$$

where $\bar{\mathbf{m}}$ is the mean model and $\tilde{\mathbf{m}}$ an equivalent vector that describes the variations from that mean.

Gillet et al. [2013] chose a function for the autocorrelation ρ from the Matérn family [so named by Stein, 1999 after the work of Matérn, 1960],

$$\rho_n(\tau) = \frac{2^{1-\nu}}{\Gamma(\nu)} \left[\sqrt{2\nu}\frac{\tau}{\tau_c(n)}\right]^\nu K_\nu \left(\sqrt{2\nu}\frac{\tau}{\tau_c(n)}\right), \tag{4.2.4}$$

where τ_c is the characteristic correlation time of the process φ' at a particular spherical harmonic degree n, essentially defining the time scale on which τ is expected to show significant change. K_ν is a modified Bessel function of the second kind, order ν. Here ν is a smoothness parameter, with low values representing rougher processes, tending toward a smooth process with a squared exponential covariance function as $\nu \to \infty$ [Stein, 1999]. The special case when $\nu = {}^3/_2$ was chosen as the best approximation of the roughness of

the variation of Gauss coefficients through time [Gillet et al., 2013], giving,

$$\rho_n(\tau) = \left[1 + \sqrt{3}\frac{\tau}{\tau_c(n)}\right] \exp\left(-\sqrt{3}\frac{\tau}{\tau_c(n)}\right). \tag{4.2.5}$$

The correlation function, Equation (4.2.5), is a solution to the stochastic differential equation,

$$\mathrm{d}\frac{\mathrm{d}\varphi'}{\mathrm{d}t} + \frac{2\sqrt{3}}{\tau_c^2}\mathrm{d}\varphi' + \frac{3}{\tau_c^2}\varphi'\mathrm{d}t = \mathrm{d}\zeta(t), \tag{4.2.6}$$

[from Yaglom, 1962, and as in Hellio et al., 2014, not as given in Gillet et al., 2013] which corresponds to an autoregressive process or order 2 where ζ is a process corresponding to Brownian motion (a Wiener process), the integral of a process with a white spectrum. From Equation (4.2.6), realisations of the SV of the Gauss coefficients $\mathrm{d}\varphi'/\mathrm{d}t$ are thus continuous but not differentiable. This allows rapid slope changes, i.e. jerks, in the SV. Additionally through the choice of $\nu = {}^3/_2$, the spectral density of Equation (4.2.5),

$$S(f) = \frac{2^d\pi^{d/2}\Gamma(\nu + d/2)(2\nu)^\nu}{\Gamma(\nu)\tau_c^{2\nu}}\left(\frac{2\nu}{\tau_c^2} + 4\pi^2 f^2\right)^{-(\nu+d/2)}, \tag{4.2.7}$$

[Rasmussen and Williams, 2006] where f is frequency and d the dimension of the process (here $d = 1$), becomes,

$$S(f) = \frac{12\sqrt{3}}{\tau_c^3}\left(\frac{3}{\tau_c^2} + 4\pi^2 f^2\right)^{-2}. \tag{4.2.8}$$

Hence the spectral density $S(f) \propto |f|^{-4}$, approximates the frequency spectra for observatory series on annual to decadal timescales. De Santis et al. [2003] measured a power law slope of $-3.8\pm0.2\,\mathrm{nT}^2/\mathrm{yr}$ (and proposed a theoretical prediction of $-3.6\pm0.4\,\mathrm{nT}^2/\mathrm{yr}$) at periods of 7–64 yrs. Currie [1968] measured a measured power law slope of $-2.9\pm0.1\,\mathrm{nT}^2/\mathrm{yr}$ for the Z-component and $-3.4\pm0.1\,\mathrm{nT}^2/\mathrm{yr}$ for the H-component over periods of 4–33 yrs.

The characteristic correlation time τ_c as in Equations (4.2.4) and (4.2.5) is part of the *a priori* information on the behaviour of the stochastic processes and is calculated from observations, albeit indirectly, in the form of field model coefficients. Equations (4.2.2) and (4.2.5) give,

$$\tau_c(n) = \sqrt{3}\sqrt{\frac{\sigma_g^2(n)}{\dot{\sigma}_g^2(n)}}, \tag{4.2.9}$$

where $\sigma_g^2(n)$ represents the variance of the MF coefficients by,

$$\sigma_g^2(n) = \frac{1}{2n+1}\sum_{m=0}^{n}\left[g_n^m(t)^2 + h_n^m(t)^2\right]_{t=2005.0}, \tag{4.2.10}$$

while $\sigma_{\dot{g}}^2(n)$ similarly describes the variance of the SV coefficients,

$$\sigma_{\dot{g}}^2(n) = \frac{1}{2n+1} \sum_{m=0}^{n} \left[\dot{g}_n^m(t)^2 + \dot{h}_n^m(t)^2 \right]_{t=2005.0}. \tag{4.2.11}$$

The property $\sqrt{\sigma_g^2(n)/\sigma_{\dot{g}}^2(n)}$ is defined as the instantaneous correlation time by Hulot and Le Mouël [1994]. In both of these cases the coefficients are taken from the model *GRIMM-2* of Lesur et al. [2010] for degrees $n \leq 13$ at $t = 2005.0$ signifying the mid-point of the model, furthest from any end effects which may result from the smoothing splines. This model was selected as it is based on *(*CHAMP) satellite data and thus should well represent the spatial variations of the field. Gillet et al. [2013] used coefficients from the model *gufm-sat-E3* of Finlay et al. [2012] but note that other satellite models provide similar constraints. This is to be expected since although different satellite models are based on measurements from different satellites and/or data selection criteria with differing regularisation applied, the differences are generally minimal. They do not constitute order of magnitude differences in the values of low degree coefficients and therefore will not greatly alter the variances that result. The synthetic models used in this thesis will all be truncated at degree 13 to be consistent with the limit of the direct *a priori* information and the best resolved internal field spectrum from surface and satellite observations.

Bringing together Equations (4.2.2), (4.2.5) and (4.2.9)-(4.2.11) gives a covariance of Gauss coefficients such that,

$$\mathrm{cov}\left[g_n^m(t), g_n^m(t+\tau)\right] = \mathrm{cov}\left[h_n^m(t), h_n^m(t+\tau)\right] = \sigma_g^2(n)\rho_n(\tau) = \mathbf{C}_n(\tau), \tag{4.2.12}$$

where $\mathbf{C}_n(\tau)$ contains the prior covariance information for the degree n. To solve for realisations of the synthetic model coefficients one has to make two final assumptions as in Gillet et al. [2013]: first that all Gauss coefficients have a mean value of zero ($\bar{\mathbf{m}} = 0$); and second that their deviations from this mean state ($\tilde{\mathbf{m}}$) are governed by Gaussian distributed random variables of unit variance. Then, utilising Cholesky factorisation of $\mathbf{C}_n(\tau)$ and returning to Equation (4.2.3), one can solve for realisations of coefficients, degree by degree. Even if the prior information is not varied between realisations, this generation process can be iterated through many realisations of models by calculating a new $\tilde{\mathbf{m}}$ vector for every degree of every realisation. In practice this can be accomplished with a random number generator and a variable seed value, based for example, on the time of calculation.

A key difference between the documented methods of Gillet et al. [2013] and Hellio et al. [2014] is that while Gillet et al. [2013] assume the variances of a satellite field model for all degrees and that the dipole coefficient g_1^0 has a mean value of zero, Hellio et al. [2014] fix a lower variance for degree 1 terms and a non-zero mean value for g_1^0. These changes act to force an Earth-like orientation for the dipole (approximately axial, positive flux in the Southern Hemisphere) and to limit the temporal variations of degree 1 coefficients. The analysis in this thesis was carried out prior to the publication of Hellio et al. [2014] and adopted an alternative approach to ensure all synthetic model realisations possessed an Earth-like dipole orientation. Without this, each model realisation may have a dipole component in any orientation, making spatial comparisons of timeseries difficult although spectral analysis would be unaffected. The Gauss coefficients for the MF of each realisation were rotated to give a temporal mean (magnetic North) dipole position at the South geographic pole. Coefficients for the SV and subsequently, via Equation (1.5.5), X-, Y- and Z-component timeseries were then generated from the rotated MF coefficients. Such a procedure was not necessary in the work of Gillet et al. [2013] as the constraints of data ensured consistent dipole orientation was enforced. The appropriateness of the approach adopted in this thesis is discussed in Section 4.3 while the significance of the difference in *a priori* variance assumptions to the results, as well as in the wider context of the analysis of global field models, is discussed in Section 5.4.

4.3 Comparison of Synthetics to Data and Models

4.3.1 Temporal Comparison

The temporal properties of the synthetic models can be assessed to validate their Earth-like quality. Observatory timeseries as well as those derived from geomagnetic models will be considered. In Figure 4.1 observatory data from Hermanus (HER), South Africa are displayed along with series derived from *COV-OBS* and *C*^{3}*FM2* for that location and a synthetic timeseries. Since there is no observational data constraining the synthetic realisation, the synthetic timeseries does not resemble the other series (and should not be expected to).

The issue of temporal smoothing is apparent, while *COV-OBS* can be seen to improve on models such as *C*^{3}*FM2* in capturing the SV, much of the more rapid (higher frequency content) of observatory data is not represented. Partly this can be attributed to attempts in modelling to eradicate such behaviour, attributing it to external fields, partly it is due to

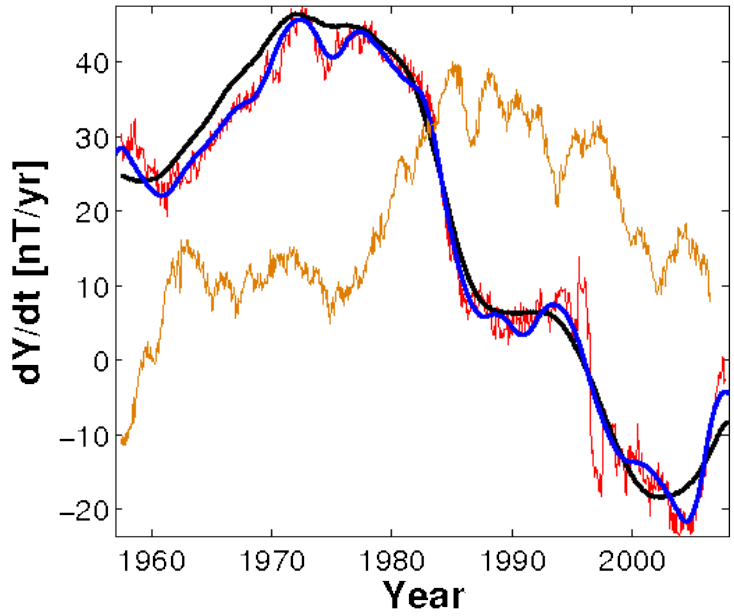

Figure 4.1: Comparison of annual differences of monthly SV Y-component of observatory timeseries (HER, red), *C*^{3}*FM2* (at HER, black), *COV-OBS* (at HER, blue) and stochastic synthetic model timeseries with an added 2 nT standard deviation Gaussian noise (yellow). The smooth nature of regularised models such as *C*^{3}*FM2* compared to observations is stark. While the *COV-OBS* model can be seen to better capture the more rapid temporal trends, the synthetic model shows significantly more rapid variations.

the nature of smoothing splines applied to regularise the time variations of the models. The SV displayed in this figure is the cleaned SV produced in Chapter 2 and thus has had much of the external field content removed as well as a temporal smoothing from taking the annual difference of monthly means. It is worth noting that *C*^{3}*FM2* is built from observatory monthly means to best capture the SV and yet *COV-OBS*, which is built from more sparsely sampled observatory annual means, does a better job of representing the rapid SV. The SV character of the synthetic timeseries, by visual comparison at least, is remarkably similar to the observatory data. Of greatest significance to this thesis is the fact that the synthetic timeseries have sharp changes in slope of SV in a manner very reminiscent of the observatory data. This is the basic premise for which these synthetic models were chosen.

A quantitative comparison can be made via the frequency spectra of the synthetic timeseries and the observatory data. For this, the observatory data from Chapter 2 was culled into a subset that consisted of all the locations with a continuous record from 1957 to 2008, a span of 51 yrs. The cleaned SV was integrated back to give a cleaned MF record by reversing the calculation procedure of Equation (1.4.1), using the first time sample of

the original MF record as a starting value. Records from the following observatories were used: ABG, CLF, ESK, FRD, HAD, HER, HRB, KAK, LER, MBO, MEA, NGK, NUR, RES, SIT, SOD, THL, THY (see Appendix A for interpretation of IAGA codes and Figure 2.13 for locations). Similarly a set of one hundred realisations of synthetic models was generated, over spans of 50 yrs at monthly sampling. Synthetic timeseries were generated at the center of cells of a spherical triangular tessellation (STT) grid of 1620 points, giving roughly even spatial coverage of approximately one observation point per 315,000 km^2 of the Earth's surface, or every 500 km (Figure 4.2). Since the synthetic models will be expanded up to spherical harmonic degree 13, a spatial sampling of 500 km is sufficient to resolve the smallest modelled features which are on the order of 2000 km.

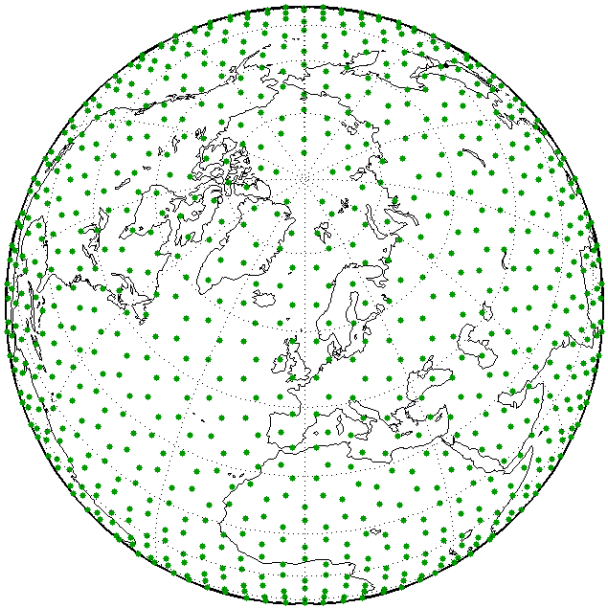

Figure 4.2: Map of the global STT grid used for synthetic timeseries generation. Grid consists of 1620 approximately evenly distributed points across the globe.

Following the analysis of De Santis et al. [2003] the mean vector power spectrum was calculated by summing the Fourier transforms, of the MF X-, Y- and Z-component timeseries at each observatory or synthetic timeseries location. Assuming representative spatial coverage, the global mean power spectrum was then calculated by averaging the mean spectra across the observatory locations. The fast Fourier transform $\mathcal{X}(f)$ of timeseries $X(t_{1,\ldots,N})$ is given by,

$$\mathcal{X}(f) = \sum_{t=1}^{N} X(t) \exp^{-2\pi i(t-1)(f-1)/N}, \tag{4.3.1}$$

and the spectra that result are displayed in Figure 4.3.

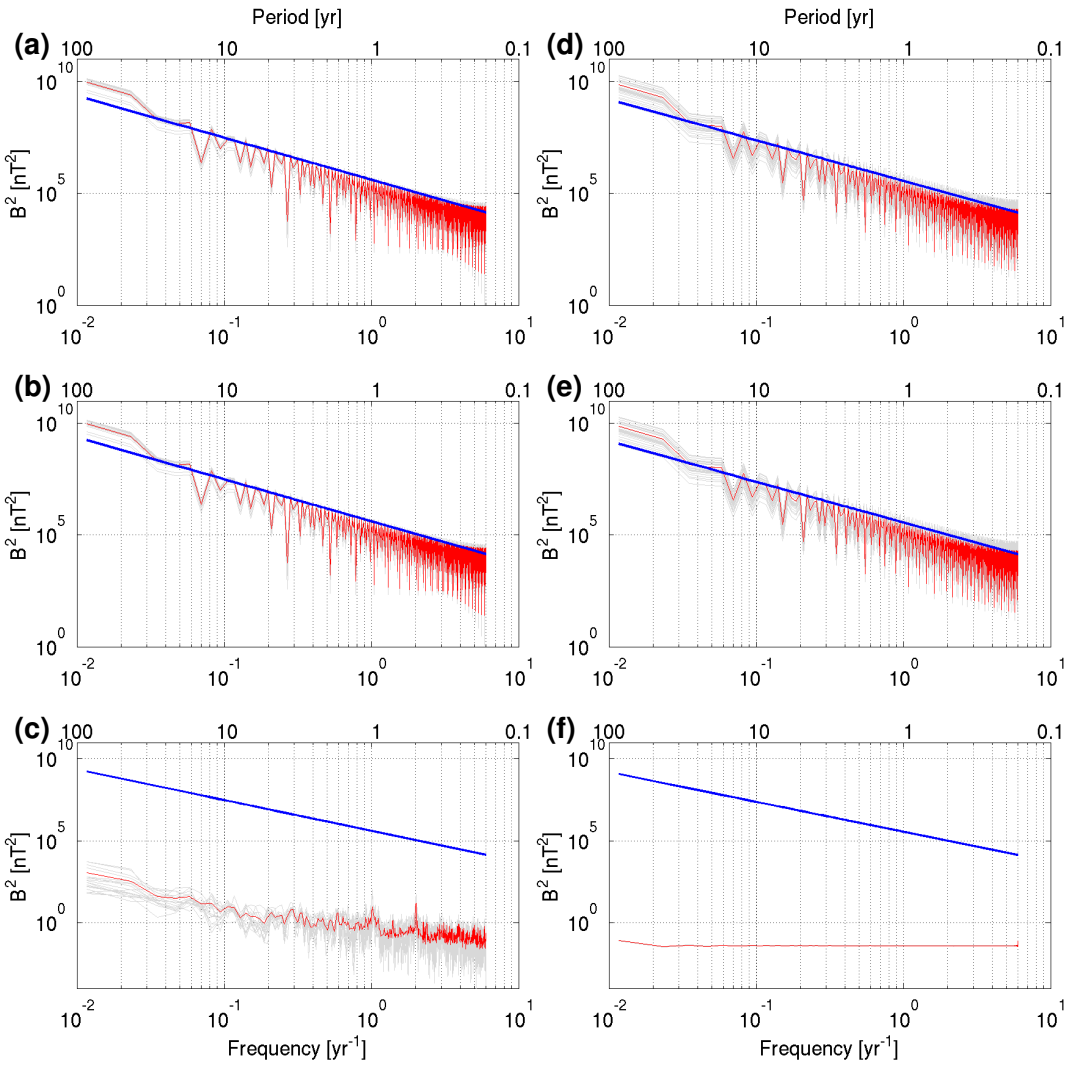

Figure 4.3: Global mean temporal power spectra from observatory MF data and synthetic timeseries. Shown are spectra of observatory monthly mean series (a–c, grey) with global mean (a–c, red) and global means of one hundred realisations of 50 yrs of monthly sampled synthetic MF series (d–f, grey) with realisations mean (d–f, red). Top "clean" row for cleaned observatory data (a) and raw synthetic series (b). Middle "noisy" row for raw observatory data (b) and synthetics with added ± 2 nT Gaussian noise (e). Bottom row for differences between "clean" and "noisy" rows. Best fit power law in frequency shown on each plot (blue, see Table 4.1), for (c,f) this is the fit to plots (a,d), respectively.

Each of the mean spectra in Figure 4.3 is fit with a power law in frequency of the form,

$$\log(\bar{\mathcal{B}}^2(f)) = b + a\log(f), \tag{4.3.2}$$

as suggested by Currie [1968] and formulated here after De Santis et al. [2003] where $\bar{\mathcal{B}}^2$ is the global mean temporal power spectrum, a and b are the slope (exponent in power law) and intercept, respectively and f is frequency. Such a law fit to surface observations corresponds to the assumption of a spectrum which obeys a power law with an exponent of $-0.5\,\mathrm{nT}^2/\mathrm{yr}$ at the CMB [De Santis et al., 2003]. These power law fits aim to confirm that the spectral content of the synthetic data scales as a $-4\,\mathrm{nT}^2/\mathrm{yr}$ power slope as it theoretically should and, perhaps of more relevance, attest to whether it is reasonable to assume that the spectral content of the synthetic timeseries approximates that of observatory data. The power law fits were optimised for the parameters a and b using a Nelder-Mead simplex direct search method [Lagarias et al., 1998] and standard errors were calculated following the heteroskedastically-robust approach to parameter variance calculation, as documented by Horn et al. [1975], as follows.

The misfit of the estimated power law to the calculated spectrum is given by,

$$\mathbf{e} = \bar{B}^2(f) - \mathbf{P}\begin{bmatrix} a \\ b \end{bmatrix}, \tag{4.3.3}$$

where $\mathbf{P}$ is the Jacobian of the power law function for $\bar{\mathcal{B}}^2$ from Equation (4.3.2),

$$\mathbf{P} = \begin{bmatrix} \dfrac{\partial}{\partial a}\bar{B}^2(f) & \dfrac{\partial}{\partial b}\bar{B}^2(f) \end{bmatrix}. \tag{4.3.4}$$

The leverage of each sampling point is then given by the trace of the matrix $\mathbf{L}$,

$$\mathbf{L} = \mathbf{P}^\top(\mathbf{P}^\top\mathbf{P})^{-1}\mathbf{P}, \tag{4.3.5}$$

to enable an estimate of the covariance matrix of the model parameters, a and b, regardless of any bias in the variance of the spectrum as a function of frequency [Horn et al., 1975], to be given by,

$$\mathbf{C}_{\mathrm{est}} = (\mathbf{P}^\top\mathbf{P})^{-1}\left(\sum_{i=1}^{N}(1-L_{ii})^{-1}f_i f_i^\top e_i^2\right)(\mathbf{P}^\top\mathbf{P})^{-1}. \tag{4.3.6}$$

where N denotes the numbers of frequency samples. The standard errors of the model

Table 4.1: Parameters and errors for power law fit to temporal power spectrum of MF (see Figure 4.3). Global mean spectra from 18 observatories, 1957–2008 and one hundred realisations of 50 yr synthetic time series were used. Observatory MF data before and after external field cleaning and synthetic data with and without a ± 2 nT Gaussian noise are considered.

MF data	Slope [nT^2/yr]	Slope error [nT^2/yr]	Intercept [nT^2]	Intercept Error [nT^2]
raw observatory	-3.8	0.6	25.8	2.1
clean observatory	-3.8	0.6	25.8	2.1
synthetic + noise	-3.6	0.7	25.6	2.0
raw synthetic	-3.6	0.7	25.6	2.0

parameters can then be calculated from the diagonal of the covariance matrix as

$$\begin{bmatrix} \sigma_a \\ \sigma_b \end{bmatrix} = \sqrt{\mathrm{diag}(\mathbf{C}_{est})}. \tag{4.3.7}$$

The results for the power law fit to the calculated spectra can be seen in Table 4.1.

Periods between 6 months and 28.5 yrs were considered when calculating the parameters of the power law fits and only periods longer than $\sim$2 months (equivalent to the Nyquist frequency) and shorter than 85.5 yrs are presented in Figure 4.3. It can be seen in Table 4.1 that for the cases of both "noisy" and "clean" observatory and synthetic timeseries, there is good agreement in the estimated parameters of the power law fit. Observatory data show a slope of -3.8 ± 0.6 nT^2/yr while the synthetic data suggest a shallower slope of -3.6 ± 0.7 nT^2/yr. Both mean estimates are within error of each other and the expected value of -4 nT^2/yr, this is taken as indication my requirement that the synthetic timeseries be a good approximation of the observatory timeseries is met for the timespans and frequency ranges to be used. Currie [1968] found values of -2 nT^2/yr to -5 nT^2/yr while De Santis et al. [2003] found values between -3.6 nT^2/yr and -3.8 nT^2/yr although it should be noted that different data sets, sampling rates, temporal spans, frequency bands, field components and analysis methods have been used in each case. While the calculation uncertainty can explain the discrepancy between my estimated value of -3.6 ± 0.7 nT^2/yr for the synthetic data and the theoretical construction of the synthetic model to have a slope of -4 nT^2/yr, this is also likely due to the truncated frequency range used in this test. The -4 nT^2/yr slope estimated by Currie [1968] and De Santis et al. [2003] and hence the design of the synthetic models is predicted to be relevant on decadal to centennial timescales, I truncate my timeseries at 50 yrs to mimic the observatory data I use as this seems the most appropriate comparison.

A Gaussian noise was added to the synthetic data to show that the original spectral content is robust and to test the validity of adding additional noise to the SV series before

implementing the jerk identification process of Chapter 2. It can be seen that the residual from the noise (Figure 4.3f) is a white spectrum, as expected, and the predicted slope of the power law fit is in both cases the same (Table 4.1). By adding Gaussian noise to the SV, the assumption of a Gaussian distribution of errors from which to calculate uncertainty bounds on the identified jerk properties can again be used. In all cases in this thesis, noise was added after calculation of any time integrals or derivatives, for example deriving SA from SV, so as not to alter the frequency spectrum of the noise away from the desired properties.

While not discussed in detail in this thesis, the content of the residuals between the raw and external field cleaned SV (and the integrated MF and SA derivative timeseries that can be derived from this) show some content of interest (Appendix B). Of note is that the removal of external field signal with some evident complexity makes minimal difference to the overall spectral slope, this is an indication that the slope is indeed characteristic of the internal field as Currie [1968] aimed to show. Additionally the spectral slopes determined from the observational data deserve more in-depth analysis as they appear to be quite dependent on the periods considered. This may simply be a reflection of timeseries length and sampling rate (and thus the frequency band considered). Currie [1968] used 50 yrs of observatory annual means while De Santis et al. [2003] used series of annual means of at least 100 yrs span; here I have used 51 yrs of monthly MF data but from a greater number of more widely distributed observatories. Nevertheless, the appropriateness of a power law (or other function) to represent the spectrum and the slope of such a law as fit to the data has some considerable importance to this work and also to works concerning chaotic and turbulent dynamo processes [De Santis et al., 2003]. The statistical basis of the synthetic models, for example, is derived from the assumption that frequency scales as $S(f) \propto |f|^{-4}$. There is a divergence at the higher frequency end away from the linear fits to the spectra which may be better represented by use of a different law. Such analysis is beyond the scope of this thesis but some (limited) preliminary material can be found in Appendix D.

4.3.2 Spatial Comparison

As well as considering whether the temporal character and variations are appropriate, the spatial properties of the synthetic models must also be assessed. The synthetic models are intended to represent the geomagnetic field in the observatory era, I therefore compare the temporally averaged spatial power spectra of synthetic realisations to those of the

models *COV-OBS* and *GRIMM-2* (Figure 4.4). The spectra of the MF, SV and SA are considered to assess whether the synthetic models not only hold the characteristic spatial shape of the geomagnetic field, but also match our estimates of its variations in time. One hundred realisations of synthetic models were generated, sampled at monthly intervals for 100 yrs each. The spectrum of the synthetic models was calculated at each timestep and averaged over the 100 yr span before these mean values were averaged across the one hundred realisations to produce an overall mean synthetic spectrum with bounds constrained by the variation across realisations.

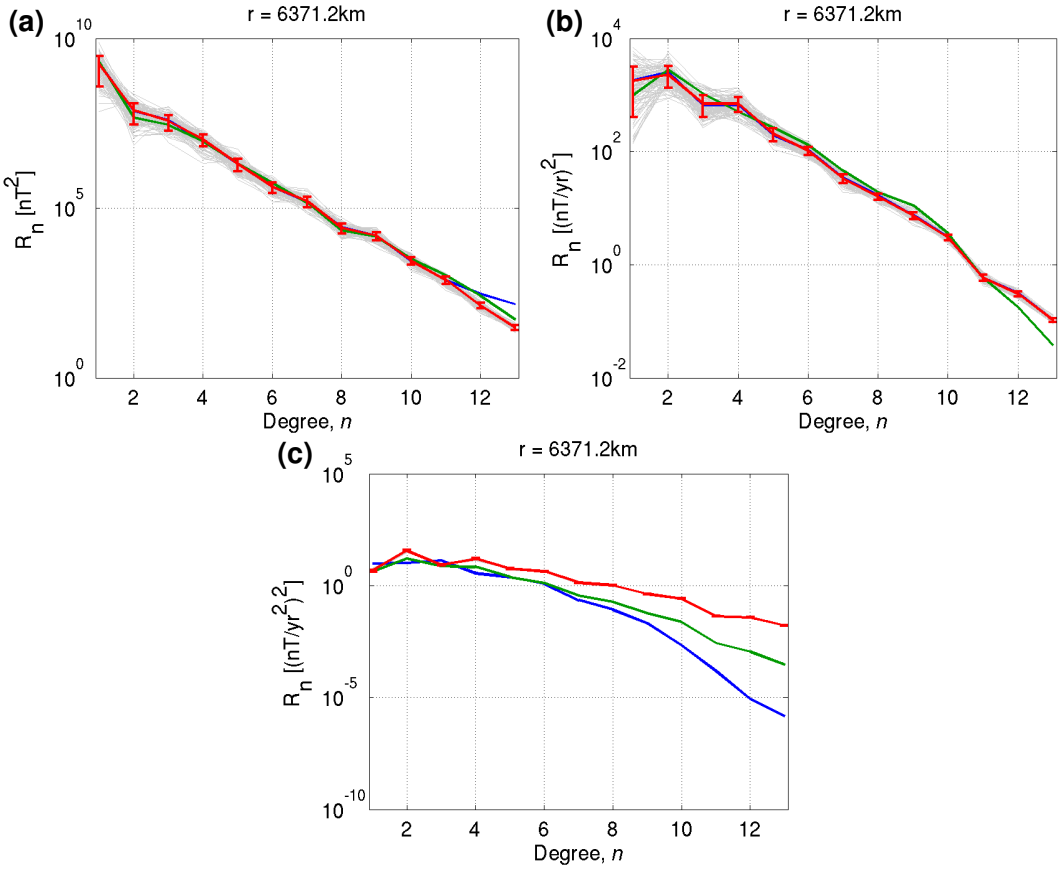

Figure 4.4: Comparison of temporal mean spatial spectra of synthetic models and field models. Temporal mean spectra of one hundred realisations over 100 yrs of monthly sampled synthetic models (grey), overlaid with the overall mean (red with one standard deviation error bars), as well as temporal mean spectra for the *GRIMM-2* (2001.0–2009.5) (blue) and *COV-OBS* (1840–2010) (green) field models, calculated at monthly intervals. The spectra for the MF (a), SV (b) and SA (c) are shown. *GRIMM-2* and *COV-OBS* spectra are hidden underneath mean synthetic spectra when not visible, in the case of the SA, all synthetic realisations lie beneath the mean synthetic spectrum line since the error bars are smaller than the line width.

The two additional geomagnetic field models plotted in Figure 4.4 were chosen for the following reasons; since *COV-OBS* is built from observations spanning the observatory era (1840–2010) and designed to fit the SV closely, it should capture the spatial variations

required by observatory data well. It should be noted that since such data are sparsely distributed in space and time, particularly towards the beginning of the *COV-OBS* model, the spectrum is less well constrained at such times. Hence as well as taking the temporal average of the model, sampled at monthly intervals through its time span, comparison can also be made to a satellite based field model. Recent satellite based models are built from densely sampled data, both temporally and spatially and therefore constrain the shape of the geomagnetic field and its variations tightly. The *GRIMM-2* model was chosen since the variances used to constrain the synthetic models were calculated from the coefficients for this model and so the synthetic models should resemble the behaviour of *GRIMM-2*. As Gillet et al. [2013] note and I again reiterate, other satellite models display very similar behaviour.

As Figure 4.4 shows, the mean MF and SV spectra of the synthetic models very closely track that of *GRIMM-2* and *COV-OBS*. The exceptions to this agreement are above degree 11 in the MF where *GRIMM-2* has higher power and above degree 11 in the SV where *COV-OBS* has lower power. The mean SA spectra are seen to be far more different, with *COV-OBS* then *GRIMM-2* displaying progressively lower power at all degrees except 1 and 3. Generally the SA spectra can be seen to diverge towards higher degrees as the higher derivatives of temporal variations (2^{nd} and 3^{rd}) of each of the models are regularised in different manners (or not at all in the case of the synthetic models) and these regularisation effects increase as a function of degree. This behaviour is expected given the construction of the three models compared as will be discussed in the following subsection. The other behaviour to note is that the variation between realisations, seen as error bars in Figure 4.4, is large for degree 1 in both the MF and SV. This is a result of the assumed variance for the degree 1 coefficients, discussed in Section 4.2, and will be assessed in the second subsection below.

Differences in Secular Acceleration Spectra

The *GRIMM-2* model penalises the third time derivative of the radial magnetic field at the surface of the core to smooth the model in time and requires the SA to be zero at the beginning and end of the model [Lesur et al., 2010]. This acts to subdue the SA, particularly at higher degrees, bringing it towards a constant value which is guided towards low values by the zero end point constraints [Finlay et al., 2012; Gillet et al., 2013]. Sixth-order B-splines are used to represent the smoothed time variations of the coefficients of *GRIMM-2* and *COV-OBS* (although with *COV-OBS* Gillet et al. [2013] discuss alternative

approaches).

Gillet et al. [2013] tested the impact of regularisation of the third time derivative, SA end point constraints and sixth-order B-spline on the resulting SV and SA spectrum of a model compared to the original observations. Synthetic realisations, generated as described in Section 4.2, were used by Gillet et al. [2013] to produce "noise free" synthetic internal field data in the style of satellite observations. These were then inverted for an internal field model while varying the damping parameters that weighted the regularisation procedures and varying the temporal knot spacing of the splines. It was found that while the timescale of changes in the MF ($\tau_c(n)$, Equation (4.2.9)) is well defined, the timescale for changes in the SV, $\sqrt{\sigma_{\dot{g}}^2(n)/\sigma_{\ddot{g}}^2(n)}$ where the SA variance $\sigma_{\ddot{g}}^2(n)$ is defined in a similar manner to Equations (4.2.10) and (4.2.11), is not. Gillet et al. [2013] argue that since the synthetic models have no external field contamination, no end effects from inversion procedures and no effects of poor temporal or spatial data sampling, they can resolve variations in the SV timescale that are otherwise introduced by regularisation procedures. The SV timescale recovered from the inverted field models was found to be dependent on the choice of regularisation damping parameter and spline knot spacing [Gillet et al., 2013] while the true starting models had higher SA power, particularly at high degrees, than the recovered models. The high degree SA in the synthetic input models was deemed to not be captured by the regularised recovered models, designed to filter out external signals of such nature.

Despite the seemingly high degree SA power, once annual differences of monthly mean SV are calculated from the synthetic models, much of the high degree SA energy is filtered out and SV that closely resembles real observations can still be achieved as can be seen in Figure 4.4b and as was seen in Section 4.3.1. Overall the spatial characteristics of the synthetic models are deemed to be representative of the SV that are to be studied in this thesis.

FORCING OF AN AXIAL DIPOLE

In order to rectify the lack of *a priori* or observational constraints on the orientation of the dipole, the synthetic model MF coefficients were rotated to give a temporal mean North magnetic pole position at the South geographic pole. The calculations used are detailed in the methods of Section 4.4. Deviation from an axisymmetric field is a key aspect of the dynamo process [Cowling, 1933] and observations from the last century, in the form of the latest *IGRF* update [*IGRF-12*, Thébault et al., 2015], show that the mean dipole location from 1900 to 2015 is at (78.9°S,110.2°E). However since it is only desired to produce

synthetic models which resemble geomagnetic SV and I do not intend to draw direct spatial comparisons to locations on Earth, the working assumption of a dipole located at a mean latitude of 89.0°S will suffice. A value of 89.0°S was chosen over the exact geographic pole to prevent mathematical errors when dealing with undefined values of the tangent function at 90° when rotating the coefficients. Of more importance is the potentially high variation of the dipole through time as indicated by the spectra in Figure 4.4. In order to assess the impact of this variation across realisations, I compare the path of the dipole through 100 yr spans of synthetic realisations and compare to the *IGRF-12* values as a measure of realism.

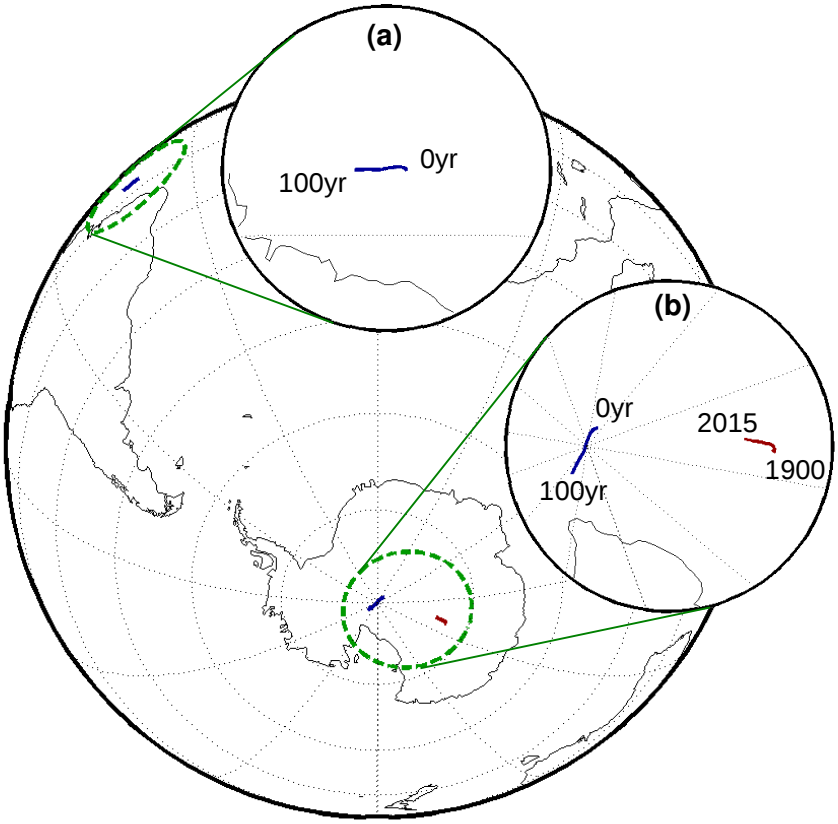

Figure 4.5: Dipole location through a 100 yr synthetic realisation (blue) before (zoom (a)) and after (zoom (b)) the rotation of the model Gauss coefficients to give a temporal mean axial dipole. The dipole location for *IGRF-12* [Thébault et al., 2015] from 1900 to 2015 (red) is shown for comparison in (b). Corresponding dipole drift rates are given in Table 4.2.

It can be seen in Figure 4.5 that a realisation of the synthetic model can have a non-Earth-like dipole location and that after the coefficients are rotated to the pole, the original longitudinal orientation of the dipole motion path is retained. It should also be noted that proper account for the quadrant of calculated angles was anticipated and included so that paths that cross the pole continue in the same direction and are not

rotated by 180° in longitude. Since any one synthetic realisation does not fully represent the mean characteristics of the synthetic models and an average dipole motion path across realisations has no clear meaning, the average distance travelled by the synthetic dipoles in 100 yrs is compared to similar figures calculated from *IGRF-12* (Table 4.2). Dipole motion paths were taken to be piecewise great circle segments between model time samples with synthetic models sampled every month for 100 yrs and *IGRF-12* sampled every 5 yrs from 1900 to 2015.

Table 4.2: Comparison of synthetic model dipole motion averaged across one hundred realisations of 100yrs span sampled at monthly intervals and *IGRF-12* model which covers 1900–2015. Uncertainty on synthetic model estimates taken to be one standard deviation as given by variation across realisations.

Model	Mean dipole latitude [°]	Mean dipole annual drift [°/yr]
IGRF-12	78.9 S	0.02
synthetic	89.1 S	0.05±0.03

It can be seen in Table 4.2 that the mean drift of the dipole in the synthetic models is approximately double that of *IGRF-12* although the high uncertainty, in this case due to significant variation across realisations, means that the synthetic model value range does overlap the *IGRF-12* estimate. A method to reduce the variation of the dipole and to fix its position to be Earth-like is given by Hellio et al. [2014] in an update to the procedure detailed in Gillet et al. [2013]. Simply imposing a mean value, similar to that found in field models, for the g_0^1 coefficient *a priori* acts in the same manner as rotating the coefficients to a consistent orientation. It is the variance of the degree 1 coefficients, not the mean, that controls the significant behavioural aspect in this case. Results with the updated Hellio et al. [2014] method are presented and discussed in Section 5.4. Otherwise, for the remainder of the analysis in this chapter I will assume that since the distribution of likely dipole movements shown by the synthetic models encompasses observationally constrained values, the motion will be treated as representative of the Earth. It will be seen that enhanced SV of degree 1 is not apparent in the results of numerous realisations and that variations commonly abide by the mean spectra shown in Figure 4.4 as is to be expected when variations from the mean are governed by a Gaussian distribution.

4.4 METHOD

Having demonstrated that the synthetic models suitably mimic the spatial and temporal properties of observatory data on a global scale and that visually SV timeseries contain

Table 4.3: MF and SV variances from *GRIMM-2* used as *a priori* constraints.

SH degree, n	$\sigma_g^2(n)$ [nT^2]	$\sigma_{\dot{g}}^2(n)$ [nT^2]
1	3.00×10^{8}	2.93×10^{2}
2	4.90×10^{6}	1.60×10^{2}
3	1.36×10^{6}	2.60×10^{1}
4	2.14×10^{5}	1.57×10^{1}
5	2.99×10^{4}	3.19×10^{0}
6	4.69×10^{3}	1.16×10^{0}
7	1.30×10^{3}	2.88×10^{-1}
8	1.80×10^{2}	1.07×10^{-1}
9	8.11×10^{1}	3.92×10^{-2}
10	1.21×10^{1}	1.33×10^{-2}
11	2.73×10^{0}	2.15×10^{-3}
12	4.15×10^{-1}	9.48×10^{-4}
13	8.17×10^{-2}	2.91×10^{-4}

features that resemble jerks, comparison to observations can be drawn. In order to investigate the spatial and temporal properties of jerks in the stochastic synthetic field models, to draw parallel to those identified in observatory data (Chapter 3), the following procedure was used. It can be subdivided into two parts: first to generate suitable synthetic models (Section 4.4.1); second to identify and analyse the features that resemble jerks (Section 4.4.2).

4.4.1 Generation of Synthetic Models

Realisations of MF Coefficients

First the calculations described in Section 4.2 were followed to calculate realisations of MF coefficients up to spherical harmonic degree and order 13. The MF and SV coefficient variances calculated from *GRIMM-2* up to degree 13 were applied as *a priori* constraints on the distributions of the realisations of coefficients (Table 4.3). MF coefficients were generated at intervals of one month for 102 yr time spans to ensure that after annual differences of monthly values were calculated to produce the SV, and subsequently again to give the SA, there remained a centered period of 100 yrs where all three time derivatives were obtained at the same time instances. This centered 100 yr span, although initially covering 1 yr to 101 yr in the initial MF realisation was nominally denoted to be from 0 yr to 100 yr as will be marked in all subsequent plots. It should here be noted that calculating the annual differences of monthly samples of each individual Gauss coefficient is equivalent to the same procedure applied to each field component timeseries. Such a procedure results in 195 non-zero coefficients (all except h_n^0 terms) per time step, with 1201 monthly samples spanning the 100 yrs of each realisation.

ROTATE MF TO AXIAL DIPOLE

Next, the dipole location was calculated from the degree 1 MF coefficients at each time step by the following formulae. The co-latitude of the positive flux pole of the dipole (equivalent to Earth's Northern geomagnetic pole) is given by,

$$\theta_{\text{North}}(t) = \cos^{-1}\left(\frac{g_1^0(t)}{\sqrt{(g_1^0(t))^2 + (g_1^1(t))^2 + (h_1^1(t))^2}}\right), \tag{4.4.1}$$

while the corresponding longitude (positive East) is given by,

$$\tilde{\phi}_{\text{North}}(t) = \tan^{-1}\left(\frac{h_1^1(t)}{g_1^1(t)}\right), \tag{4.4.2}$$

after Olson and Amit [2006]. Practically, the $\tan^{-1}$ function must be treated with care, accounting for all four quadrants the resulting angle may lie in. Many computation languages provide an *atan2* function for such eventualities which can be adopted for our purposes here and adapted to a range of longitudes of $-\pi/2 \leq \phi_{\text{North}} \leq \pi/2$ by performing the following,

$$\phi_{\text{North}}(t) = \begin{cases} \tilde{\phi}_{\text{North}}(t) - \pi, & h_1^1(t) > 0 \\ \tilde{\phi}_{\text{North}}(t) + \pi, & h_1^1(t) \leq 0 \end{cases}. \tag{4.4.3}$$

Once the dipole locations are known at each time step, the temporal mean location can be calculated, again employing the *atan2* function, as,

$$\bar{\phi}_{\text{North}}(t) = \text{atan2}(\overline{\sin(\phi_{\text{North}}(t))}, \overline{\cos(\phi_{\text{North}}(t))}), \tag{4.4.4}$$

where the over-bar signifies the arithmetic mean across the time samples, t, taking into account that the spherical nature of Earth causes circular statistics to be necessary.

A rotation is then applied in spectral space, directly to the MF coefficients at each time step so as to move the temporal mean dipole location to a latitude of 89°S (to prevent mathematical errors when dealing with undefined values of the tangent function at 90°), the rotation is thus an identical transformation at each time step. This rotation of the sphere acts as though in a fixed coordinate frame $(\mathcal{X}, \mathcal{Y}, \mathcal{Z})$ and applies rotations sequentially about the $\mathcal{Z}$, $\mathcal{Y}$ then $\mathcal{Z}$ axes via three Euler angles α, β, γ [McEwen et al., 2006]. As Figure 4.6 illustrates, the angle α represents longitudinal rotation about the Earth's rotation axis ($\mathcal{Z}$), β rotates about $\mathcal{Y}$ to bring the dipole to an axial position and γ rotates about $\mathcal{Z}$ once more to restore the original longitudinal orientation.

The rotated matrix $\mathbf{R}_n^l(\alpha, \beta, \gamma)$ and relationship between the original g_n^m, h_n^m and rotated

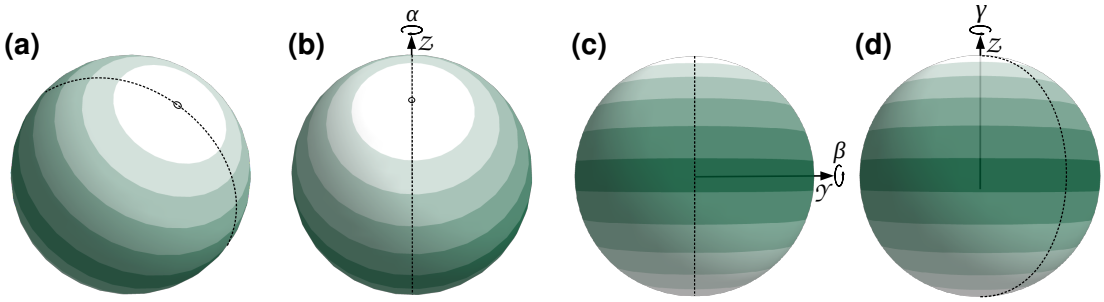

Figure 4.6: Illustrative example of rotation of SH coefficients to align the dipole with the rotation axis. The original SH function (a) is rotated first about $\mathcal{Z}$ by angle α (b), then about $\mathcal{Y}$ by angle β (c) and finally about $\mathcal{Z}$ by angle $\gamma = -\alpha$ (d). The (0,π) meridian is marked for reference.

coefficients g_n^l, h_n^l (note the change in order subscript) can be described as a weighted sum of coefficients of the same degree. This is given, after the notation of McEwen et al. [2006] adapted for real spherical harmonics,

$$\mathbf{R}_n^l(\alpha,\beta,\gamma)[g_n^l, h_n^l] = \sum_{l=0}^{n} \mathbf{D}_{m,l}^n(\alpha,\beta,\gamma)[g_n^m, h_n^m], \tag{4.4.5}$$

where $\mathbf{D}_{m,l}^n(\alpha,\beta,\gamma)$ represents the Wigner functions given by,

$$\mathbf{D}_{m,l}^n(\alpha,\beta,\gamma) = \exp(-im\alpha)\mathbf{d}_{m,l}^n(\beta)\exp(-il\gamma). \tag{4.4.6}$$

Here the terms of the real polar matrix, $\mathbf{d}_{m,l}^n(\beta)$, are described by a long and complex (and tedious) sum over a combination of degrees and the two sets of orders with these integers weighting $\sin(\beta/2)$ and $\cos(\beta/2)$ terms to ensure the rotation limit of β in co-latitude is between 0 and π radians. In essence the Wigner matrices are formed of a large block sparse structure since coefficients of each degree only affect the rotated coefficients of the same degree due to the rotational invariance of SH basis functions. The full definitions can be found in McEwen et al. [2006] while Blanco et al. [1997] give some useful and efficient recursion formulae to compute Wigner functions for real SH.

For my purpose here this procedure[1] involves a rotation at each timestep of ϕ_{North} in longitude, a rotation of $(179^\circ - \theta_{\text{North}})$ to bring the dipole to 89°S, and then a rotation of $-\phi_{\text{North}}$ in longitude to restore the original longitudinal orientation.

[1] Calculations were performed using the `SHRotateVec` function by Frederik J. Simons (available from `http://geoweb.princeton.edu/people/simons/software.html`, 2015-03) which is an adaptation of a routine produced by the authors of Masters and Richards-Dinger [1998].

DERIVE SV AND SA

With final sets of rotated MF coefficients, all possessing axial dipolar fields with positive flux in the Southern Hemisphere, the SV and SA coefficients are derived as annual differences of monthly values. These coefficients are then used in Equation (1.5.5) and its next two time derivatives, given the co-latitude and longitude coordinates of both the 1620 STT cells described in Section 4.3 and the 102 observatory locations displayed in Figure 2.13, to derive timeseries values for the X-, Y- and Z-components and time derivatives, for each realisation at each location. Since each spatial sampling of timeseries is derived from the same Gauss coefficients, the jerk analysis of each is directly comparable. This amounts to 17,510,580 timeseries data points for the STT cell locations, 1,102,518 timeseries data points for the observatory locations and an additional 936,780 Gauss coefficient values ($h_n^0 = 0$ values are not stored) per realisation: enough to ensure considerable effort was required devising efficient calculation and storage procedures.

4.4.2 ANALYSIS OF SYNTHETIC MODELS

IDENTIFICATION OF JERKS

With a range of synthetic model realisations to hand, the analysis of jerks begins with the application of the jerk detection algorithm from Chapter 2 to the SV of the X-, Y- and Z-components. Using monthly time samples and 100 yr timeseries, the analysis was applied at both the 1620 STT cells and 102 observatory locations. The algorithm parameters used previously (see Section 2.4.3) were again applied with the following exceptions.

The sampling interval at which to perform the two-part linear regression was increased from 0.01 yrs to 0.04 yrs to decrease the number of computations, and therefore computation time by an approximate factor of four while still oversampling the timeseries (1 month is $\sim$0.08 yr).

The window lengths considered were altered from 5, 10 and 15 yrs with variable 5–50 yr spans of observatory data, to 5, 15 and 25 yrs with consistent 100 yr spans of synthetic timeseries. This alteration was made for two reasons; firstly to account for the variations in timescale of jerk-like features seen in observatory and synthetic timeseries and the dependence of resolvable features on window length, and second to account for the longer time series used in the synthetic case. The range of window lengths allows consistency of jerk identifications and properties to be checked as well as separating features on different timescales. The window buffer lengths were also adjusted to be 20% of the window length

at either end: 12, 36 and 60 months for 5, 15 and 25 yr windows, respectively.

A trade-off curve was plotted for the number of jerks detected versus the probability cut-off level below which features were deemed unlikely to be jerks (Figure 4.7). Since the knee of the trade-off curve for each detection window length varied more than in the case of observatory data, a compromise was needed. A PDF trade-off level of 0.07 was chosen since it was deemed more stable to invert a greater number of jerk amplitudes for a SH model and rely on jerk amplitude uncertainty estimates to weight data, rather than relying more heavily on the spatial regularisation with fewer data points (see next section). The value is lower than for the case of observatory data since there is no normalisation for the length of timeseries used, 100 yrs here as opposed to the previous 5 yr to 50 yr length. This cut-off was applied to all window lengths.

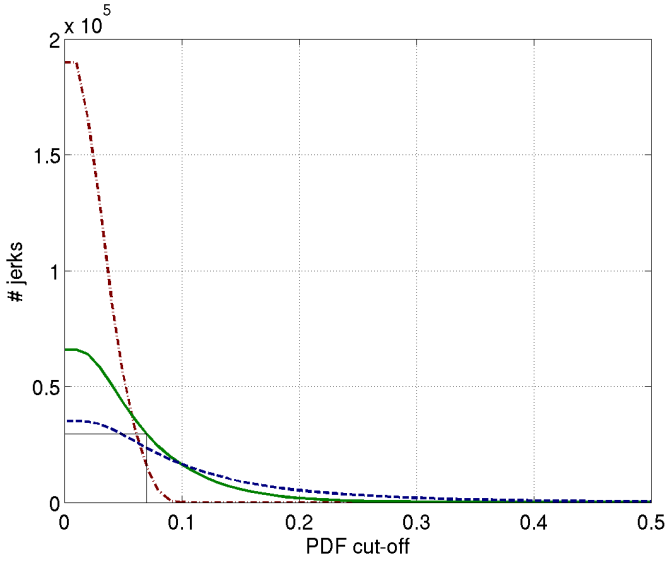

Figure 4.7: Trade-off curve for the number of synthetic jerks detected versus the probability cut-off threshold above which peaks in probability are considered jerks. Curves for detection windows of 5 yr (red), 15 yr (green) and 25 yr (blue) are shown with the applied value of 0.07 highlighted by black lines. The numbers of jerks detected are notably higher than was seen with observatory data (Figure 2.12) as longer timeseries (double the length) and more spatial locations (roughly 16 times more) are used.

The final update to the procedure was to add a Gaussian random noise of standard deviation ± 2 nT to the synthetic SV series before the jerk identification procedure in order to stabilise the regression and allow the calculation of uncertainties on jerk properties under an assumption of Gaussian noise distributions. Whilst the same basic algorithm as in Chapter 2 was applied, the computation procedure was upgraded to run in parallel to handle the large amount of synthetic data more efficiently.

With output of identified jerks and their properties from the jerk identification program,

histograms of jerk occurrences through time were calculated and analysed as well as other temporal properties such as jerk amplitude periodicity.

MODELLING OF JERK AMPLITUDES

Analysis and comparison of the spatial properties and their observed variations with sampling density were performed through the process of spherical harmonic modelling of jerk amplitudes. The synthetic jerk amplitudes identified in time periods of interest were used as input constraints for a SH inversion to model the component of SA at the Earth's surface attributable to the jerk. Positive and negative jerk identifications were both included in the input, counting no detected jerk at any time as a zero value of SA at that spatial location. Inversions were performed for the results with both the densely sampled STT cell locations and the sparse locations of observatories. It is because of this desired comparison to observatory spatial distributions (and to models of the observatory data themselves later) that I choose to invert for a SH model in the following manner rather than apply a spherical harmonic transform directly to evenly gridded synthetic data as Olsen and Mandea [2007] demonstrated in their virtual observatory study.

A minimisation function, as described in Section 1.5 and reiterated here, was applied:

$$\Phi = (\mathbf{d} - \mathbf{G}\mathbf{m})^{\top} \mathbf{C}_d^{-1} (\mathbf{d} - \mathbf{G}\mathbf{m}) + \lambda \mathbf{m}^{\top} \mathbf{C}_m^{-1} \mathbf{m}, \tag{4.4.7}$$

where $(\mathbf{d} - \mathbf{G}\mathbf{m})$ is the misfit between identified jerk amplitudes $\mathbf{d}$ and the modelled amplitude values given by the model coefficients $\mathbf{m}$ multiplied by the Jacobian matrix of Equation (1.5.5) $\mathbf{G}$, $\mathbf{C}_d^{-1}$ is the data covariance matrix, $\mathbf{m}$ is a vector of the modelled coefficients, $\mathbf{C}_m^{-1}$ is the model covariance matrix and λ is a damping parameter to trade-off the data and model terms of the function. The matrix $\mathbf{C}_d^{-1}$ was chosen, assuming independent errors, to be zero everywhere except along the diagonal where values corresponding to the inverse of the variance of each jerk amplitude estimate were entered. For times and locations where no jerk was detected, I used the equivalent variance of allowed amplitudes as governed by the amplitude threshold used during jerk detection. Assuming that no jerk being detected lies in the 99.7% confidence $\pm 3\sigma$ range, the amplitude threshold of 3 nT/yr equates to a variance of 1 nT^2. These values thus give greater weight to jerk amplitude estimates with smaller uncertainty bounds, and linear segments of timeseries in which no jerk was detected. The matrix $\mathbf{C}_m^{-1}$ was chosen to apply the Ohmic heating norm[1] of

[1]The Ohmic heating norm limits the spatial complexity of a field model through restricting the energy in the modelled magnetic field to abide by a decay proportional to SH degree n^{-2}. It is derived from the

Gubbins [1975] [although see e.g. Gubbins and Bloxham, 1985; Jackson et al., 2000, for correct formulation] with the diagonal terms of $\mathbf{C}_m^{-1}$ given by,

$$\operatorname{diag}\left(\mathbf{C}_m^{-1}\right) = 4\pi \sum_{n=1}^{n_{\max}} \frac{(n+1)(2n+1)(2n+3)}{n} \left(\frac{r_E}{r_c}\right)^{2n+4}, \tag{4.4.8}$$

where c is the radius to the CMB. By choosing such a spatial regularisation it is implicitly assumed that the modelled phenomenon is best approximated by a SH function in which large-scales are dominant. I make this assumption under the supposition that if well fitting SH models cannot be made in this manner and the resultant misfit to jerk amplitudes is high, then jerks cannot be modelled as large-scale phenomena at the Earth's surface. It would be equally valid to assume other spatial regularisation designed to act in a similar manner, for example that of Gubbins and Bloxham [1985][1] (the use of which produces very similar results in the small number of cases tested). The impacts of the spatial regularisation are quite obvious and are to be closely monitored, as will be seen later in this section, to ensure that features are not spuriously attributed to data requirements as opposed to the regularisation.

Minimisation of Equation (4.4.7) can be achieved by solving,

$$\mathbf{m} = \left(\mathbf{G}^\top \mathbf{C}_d^{-1} \mathbf{G} + \lambda \mathbf{C}_m^{-1}\right)^{-1} \mathbf{G}^\top \mathbf{C}_d^{-1} \mathbf{d}, \tag{4.4.9}$$

where the terms of $\mathbf{d}$, $\mathbf{m}$ and $\mathbf{G}$ are arranged in the following manner (remembering that $\ddot{g}_n^m$ and $\ddot{h}_n^m$ here may represent only a portion of the SA attributed to the jerk signal),

$$\mathbf{m} = \left[\begin{array}{ccccccccc} \ddot{g}_1^0 & \ddot{g}_1^1 & \cdots & \ddot{g}_n^m & \ddot{h}_1^0 & \ddot{h}_1^1 & \cdots & \ddot{h}_n^m \end{array} \right]^\top, \tag{4.4.10}$$

$$\mathbf{d} = \left[\begin{array}{ccccccccc} A_1^x & \cdots & A_N^x & A_1^y & \cdots & A_N^y & A_1^z & \cdots & A_N^z \end{array} \right]^\top, \tag{4.4.11}$$

assumed physical lower bound that the work of fluid motion in the core against the magnetic field must at least equal the energy lost through electrical resistive heating (known as Ohmic or Joule heating).

[1] Gubbins and Bloxham [1985] design a norm to limit the energy present in short wavelengths of a field model based on the neglect of diffusion in the frozen-flux approximation of core flow estimation (Section 1.6). If diffusion is indeed negligible, then for consistency a field model at the CMB cannot be allowed to possess sufficient energy at short wavelengths to contradict this assumption. Gubbins and Bloxham [1985] assess that a stronger energy decay proportional to SH degree n^{-3} is suggested but from a less physical bound than in the case of the Ohmic heating norm.

where A_i^x is the X-component amplitude of a jerk at location i of a total N and so on, and

$$\mathbf{G} = \begin{bmatrix} \frac{\partial \ddot{B}_x(r,\theta_1,\phi_1)}{\partial \ddot{g}_1^0} & \cdots & \frac{\partial \ddot{B}_x(r,\theta_1,\phi_1)}{\partial \ddot{g}_n^m} & \frac{\partial \ddot{B}_x(r,\theta_1,\phi_1)}{\partial \ddot{h}_1^0} & \cdots & \frac{\partial \ddot{B}_x(r,\theta_1,\phi_1)}{\partial \ddot{h}_n^m} \\ \vdots & & \vdots & \vdots & & \vdots \\ \frac{\partial \ddot{B}_x(r,\theta_N,\phi_N)}{\partial \ddot{g}_1^0} & \cdots & \frac{\partial \ddot{B}_x(r,\theta_N,\phi_N)}{\partial \ddot{g}_n^m} & \frac{\partial \ddot{B}_x(r,\theta_N,\phi_N)}{\partial \ddot{h}_1^0} & \cdots & \frac{\partial \ddot{B}_x(r,\theta_N,\phi_N)}{\partial \ddot{h}_n^m} \\ \frac{\partial \ddot{B}_y(r,\theta_1,\phi_1)}{\partial \ddot{g}_1^0} & \cdots & \frac{\partial \ddot{B}_y(r,\theta_1,\phi_1)}{\partial \ddot{g}_n^m} & \frac{\partial \ddot{B}_y(r,\theta_1,\phi_1)}{\partial \ddot{h}_1^0} & \cdots & \frac{\partial \ddot{B}_y(r,\theta_1,\phi_1)}{\partial \ddot{h}_n^m} \\ \vdots & & \vdots & \vdots & & \vdots \\ \frac{\partial \ddot{B}_y(r,\theta_N,\phi_N)}{\partial \ddot{g}_1^0} & \cdots & \frac{\partial \ddot{B}_y(r,\theta_N,\phi_N)}{\partial \ddot{g}_n^m} & \frac{\partial \ddot{B}_y(r,\theta_N,\phi_N)}{\partial \ddot{h}_1^0} & \cdots & \frac{\partial \ddot{B}_y(r,\theta_N,\phi_N)}{\partial \ddot{h}_n^m} \\ \frac{\partial \ddot{B}_z(r,\theta_1,\phi_1)}{\partial \ddot{g}_1^0} & \cdots & \frac{\partial \ddot{B}_z(r,\theta_1,\phi_1)}{\partial \ddot{g}_n^m} & \frac{\partial \ddot{B}_z(r,\theta_1,\phi_1)}{\partial \ddot{h}_1^0} & \cdots & \frac{\partial \ddot{B}_z(r,\theta_1,\phi_1)}{\partial \ddot{h}_n^m} \\ \vdots & & \vdots & \vdots & & \vdots \\ \frac{\partial \ddot{B}_z(r,\theta_N,\phi_N)}{\partial \ddot{g}_1^0} & \cdots & \frac{\partial \ddot{B}_z(r,\theta_N,\phi_N)}{\partial \ddot{g}_n^m} & \frac{\partial \ddot{B}_z(r,\theta_N,\phi_N)}{\partial \ddot{h}_1^0} & \cdots & \frac{\partial \ddot{B}_z(r,\theta_N,\phi_N)}{\partial \ddot{h}_n^m} \end{bmatrix}, \tag{4.4.12}$$

where, for example, $\ddot{B}_x$ is the X-component ($\hat{\mathbf{x}} = -\hat{\theta}$) of the second time derivative of Equation (1.5.5). Evaluating the partial derivatives with respect to each model parameter (Gauss coefficient), Equation (4.4.12) becomes,

$$\mathbf{G} = \underbrace{\begin{bmatrix} \frac{\partial P_1^0}{\partial \theta}\cos(m\phi_1) & \cdots & \frac{\partial P_n^m}{\partial \theta}\cos(m\phi_1) \\ \vdots & & \vdots \\ \frac{\partial P_1^0}{\partial \theta}\cos(m\phi_N) & \cdots & \frac{\partial P_n^m}{\partial \theta}\cos(m\phi_N) \\ \frac{m}{\sin\theta_1}P_1^0\sin(m\phi_1) & \cdots & \frac{m}{\sin\theta_1}P_n^m\sin(m\phi_1) \\ \vdots & & \vdots \\ \frac{m}{\sin\theta_N}P_1^0\sin(m\phi_N) & \cdots & \frac{m}{\sin\theta_N}P_n^m\sin(m\phi_N) \\ -(n+1)P_1^0\cos(m\phi_1) & \cdots & -(n+1)P_n^m\cos(m\phi_1) \\ \vdots & & \vdots \\ -(n+1)P_1^0\cos(m\phi_1) & \cdots & -(n+1)P_n^m\cos(m\phi_1) \end{bmatrix}}_{(n=1,m=0)\ ,\ \ldots\ ,\ (n=n_{\max},m=n_{\max})} \tag{4.4.13}$$

$$\underbrace{\begin{bmatrix} \frac{\partial P_1^0}{\partial \theta}\sin(m\phi_1) & \cdots & \frac{\partial P_n^m}{\partial \theta}\sin(m\phi_1) \\ \vdots & & \vdots \\ \frac{\partial P_1^0}{\partial \theta}\sin(m\phi_N) & \cdots & \frac{\partial P_n^m}{\partial \theta}\sin(m\phi_N) \\ -\frac{m}{\sin\theta_1}P_1^0\cos(m\phi_1) & \cdots & -\frac{m}{\sin\theta_1}P_n^m\cos(m\phi_1) \\ \vdots & & \vdots \\ -\frac{m}{\sin\theta_N}P_1^0\cos(m\phi_N) & \cdots & -\frac{m}{\sin\theta_N}P_n^m\cos(m\phi_N) \\ -(n+1)P_1^0\sin(m\phi_1) & \cdots & -(n+1)P_n^m\sin(m\phi_1) \\ \vdots & & \vdots \\ -(n+1)P_1^0\sin(m\phi_N) & \cdots & -(n+1)P_n^m\sin(m\phi_N) \end{bmatrix}}_{(n=1,m=0)\ ,\ \ldots\ ,\ (n=n_{\max},m=n_{\max})} \begin{matrix} \} X(\theta_i,\phi_i) \\ \\ \} Y(\theta_i,\phi_i) \\ \\ \} Z(\theta_i,\phi_i) \end{matrix},$$

where the horizontal term order follows the coefficient order of terms in $\mathbf{m}$, the vertical term order follows the data order of terms in $\mathbf{d}$, and P_n^m are Schmidt semi-normalised associated Legendre functions of argument $\cos\theta_i$. The derivatives $\partial P_n^m/\partial\theta$ are related to P_n^m by the recursion,

$$\frac{\partial P_n^m}{\partial\theta} = \frac{1}{\sin\theta_i}\left[-(n+1)\cos\theta_i P_n^m + (n-m+1)\sqrt{\frac{n+m+1}{n-m+1}}P_{n+1}^m\right]. \tag{4.4.14}$$

Since it is not apparent whether the portion of the modelled SA that the jerk amplitudes respresent is required to be a potential field or not [it has been assumed to be by e.g. Le Huy et al., 1998; Malin and Hodder, 1982; Pinheiro et al., 2011], two model inversion approaches were used, both following Equation (4.4.9) but with different terms in the $\mathbf{d}$, $\mathbf{G}$ and $\mathbf{m}$ components. First that of Equation (4.4.13), which assumes a potential field, and then three more inversions, utilising only the X-, Y- or Z-component terms of Equation (4.4.13) and the corresponding data in Equation (4.4.11). This, along with data misfits and model complexity measures, allows comparison of how well the potential field assumption fits the data in any one given component in a more visual manner than considering data misfits alone. Without the assumption of a potential field the SH coefficients simply describe the spatial character of the data being modelled and are not true Gauss coefficients.

An example of such an inversion is shown in Figure 4.8 which also demonstrates an example of the testing and benchmarking procedures used to verify the computations. The inversion procedure was developed and benchmarked by increasingly complex examples, beginning with single harmonics before moving on to snapshots of field models for which there were also example spectra and field component maps in the published literature. Since the final inversion procedure used applies a spatial regularisation, tests involving adding noise to field model component samples and sparse, irregular spatial sampling from instances of field models were also performed. The example in Figure 4.8 is a test case where 500 spatial samples were randomly taken from the X-, Y- and Z-components of the MF of *CHAOS-4*α at 2005.0 at the Earth's surface, expanded to SH degree 13. These samples had a Gaussian noise of 100 nT standard deviation added to them and then the three field components were inverted for a potential, in this case assuming a minimal influence from the spatial regularisation by applying a small damping parameter $\lambda = 1.0\times10^{-10}$. The recovered potential can be seen to compare very favourably in amplitude and spatial pattern and thus also in the three recovered field components (compare Figure 4.8 a, f, g, h

to a', f', g', h', respectively). Upon closer inspection, the effect of the spatial regularisation can be seen in the original and recovered spectra (Figure 4.8b, b'); above degree 8 the spectra begin to diverge as the higher degree terms of the inverted model are damped more severely. This has little effect on this model snapshot as the MF has a much greater relative power at lower degrees. A more stringent test case can be seen in Figure 4.9 which displays the results when the same procedure is applied to *CHAOS-4*α SV at 2005.0 with only one hundred sample points globally, the standard deviation of the Gaussian noise is reduced in this case to 10 nT and the damping parameter adjusted to $\lambda = 1.0\times10^{-4}$. Again there is good visual agreement between the original and recovered models despite the relative increase in power at higher degrees. The spatial regularisation can be seen beginning to damp the recovered spectrum from SH degree 9 onwards.

The damping parameter was fixed for all synthetic jerk inversions for consistency rather than tailor it to each. The value of $\lambda = 1.0\times10^{-4}$ was chosen after a comparison of results from several realisations of synthetic model to trade-off between the level of spatial regularisation and the misfit to jerk amplitudes. An example case depicting the inversion results for a variety of damping parameters is shown in Figures 4.10 and 4.11 along with the corresponding trade-off curve and misfit information in Figure 4.12 from which a balancing value for the damping parameter can be discerned. The corresponding impact of damping parameter choice on the spectrum of the potential is shown in Figure 4.13.

Through the series of plots in Figures 4.10 and 4.11 it can be seen that the effect of a large damping parameter is to enforce the regularisation's preference to damp small spatial scales. This acts to not only decrease the spatial complexity (seen visually and measured by the norm of Equation (4.4.8) as plotted in Figure 4.12a) but also to limit the amplitude of the recovered model. This is demonstrated by the reduced colour scales of Figure 4.10 as the damping parameter increases and, perhaps more intuitively, in Figure 4.11 where the jerk amplitude values which are being modelled can be directly compared. This behaviour is expected, if not entirely desired, and so is minimised by choosing a damping value that sits near the knee of the trade-off curve in Figure 4.12a. It can be seen in Figure 4.12b that this knee area also equates to RMS misfit values, per observation, which lie below the level of the mean input uncertainty on the jerk amplitudes. This informs us that the data are overfit in this case by a factor of $\sim$2.5 with an RMS of $\sim$1.1 nT/yr^2 versus a mean uncertainty of $\sim$2.5 nT/yr^2 at $\lambda = 1.0\times10^{-4}$. However, the spectra in Figure 4.13a show that regardless of damping parameter, the greatest power is always at SH degree 2, unaffected by the spatial regularisation so that even when overfitting the data somewhat

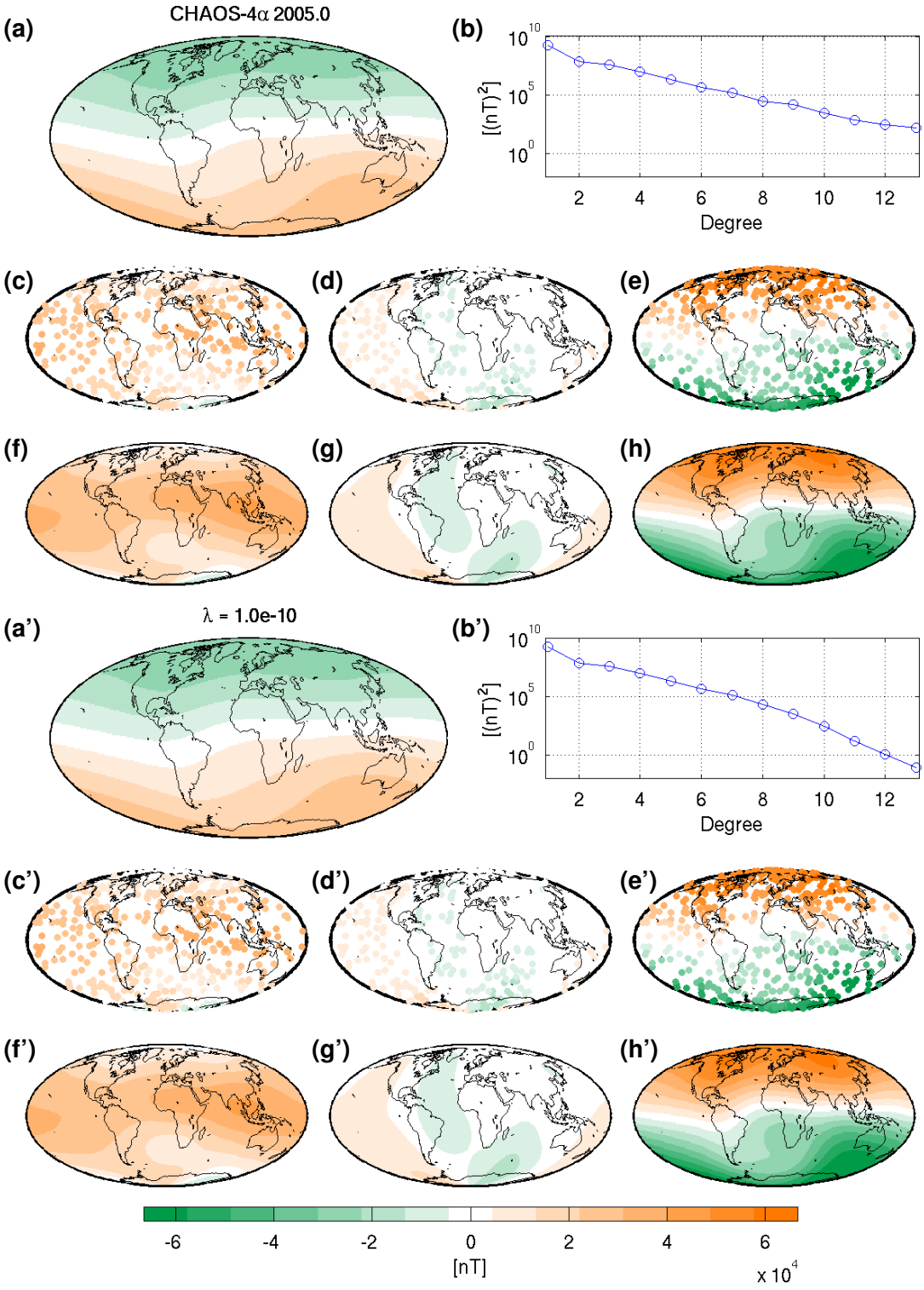

Figure 4.8: Comparison of *CHAOS-4*α MF at 2005.0 (a–h) and an inversion of noisy magnetic field data (a'–h') derived from this model to attempt recovery of the original model. Potential (a) and its spectrum (b) are shown with the derived field components (X (f), Y (g), Z (h)) at Earth's surface with a random sampling of 500 locations from these components (c,d,e,respectively). The random spatial samples were overlaid with noise (c',d',e') then inverted for the potential (a',b') from which each field component was then derived (f',g',h'). The potentials (a,a') are scaled by Earth's radius to fit the same colour scale as all other plots.

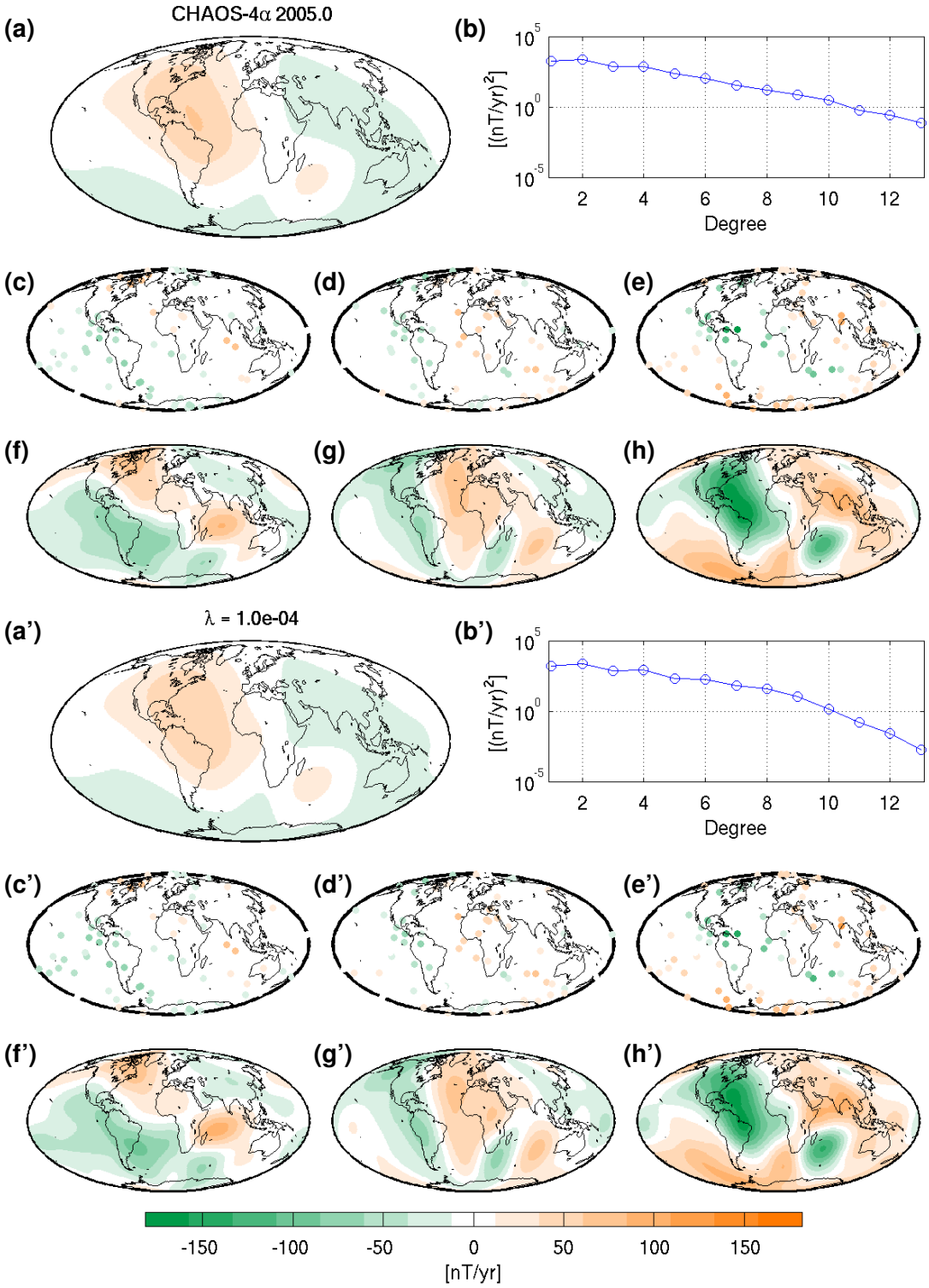

Figure 4.9: Comparison of *CHAOS-4*α SV at 2005.0 (a–h) and an inversion of noisy magnetic field data (a'–h') derived from this model to attempt recovery of the original model. Potential (a) and its spectrum (b) are shown with the derived field components ($\dot{X}$ (f), $\dot{Y}$ (g), $\dot{Z}$ (h)) at Earth's surface with a random sampling of one hundred locations from these components (c,d,e,respectively). The random spatial samples were overlaid with noise (c',d',e') then inverted for the potential (a',b') from which each field component was then derived (f',g',h'). The potentials (a,a') are scaled by Earth's radius to fit the same colour scale as all other plots.

($\lambda \leq 1.0\times10^{-1}$), the result is still a large-scale field with the same dominant degree.

I decided a damping parameter value of $\lambda = 1.0\times10^{-4}$ provided the most spatial detail before a plateau in the misfit to the jerk amplitudes at lower values of λ while avoiding a higher misfit plateau of a spectrum dominated by the spatial regularisation seen for smaller values of λ in Figure 4.12b. Lower values of λ may be reasonable in the case of dense spatial sampling but will become less so when sparser observatory style sampling is used. Still one must be cognisant of Figure 4.13a when interpretting features at higher degrees, it is likely that at $\lambda = 1.0\times10^{-4}$, features above SH degree 6 are poorly resolved. Beyond that one clearly must be wary of underestimating the power in a spectrum by regularising too severely. The impact of the damping parameter can be understood by considering the comparative magnitude of prior model covariance terms shown in Figure 4.13b which step up by degree from 1.4×10^{4} at SH degree 1 to 7.7×10^{11} at SH degree 13. A final note on damping parameter choice is that the inversions were found to be more sensitive (in terms of change in the spectrum of the inverted potential) to the choice of damping parameter than to the PDF cut-off level. Hence it is judged that keeping a constant PDF cut-off level of 0.07 and a damping parameter of $\lambda = 1.0\times10^{-4}$ is a suitable combination. As will be seen in Section 5.2, the patterns described for this example case hold for the range of synthetic cases.

I chose to invert for models expanded up to SH degree 13 as this was the resolution of the synthetic models from which the jerk amplitudes were originally derived. Increasing the truncation above SH degree 13 has little benefit as it has already been seen that the spatial regularisation dominates before that point. As such there is no strong case to increase the maximum degree of the model, but a lower truncation could be considered. Authors such as Malin and Hodder [1982], Le Huy et al. [1998] and De Michelis et al. [2000] all assumed SH model expansions to degree 4 when modelling jerks (Malin and Hodder [1982] also expanded the external field to degree 4 in their models to prove jerks were internally generated). Pinheiro et al. [2011] expanded up to degree 14 and found that the spectrum was essentially zero beyond degree 6. A series of example spectra for inverse models expanded to a variety of truncation degrees is depicted in Figure 4.14. Assuming the original degree 13 model expansion of *CHAOS-4*α to be the true spectrum, it was found that the SH degree of truncation induces ringing (Gibbs) effects in degrees below the truncation level, leading to poor recovery of the spectrum at degrees lower than the truncation degree itself. I decided it was more consistent to keep a higher truncation degree (degree 13) and acknowledge the known impacts of the spatial regularisation at

the higher degrees, than to further alter the recovered models by potentially introducing truncation effects to the resolved low degrees as well. A series of figures in the vein of Figure 4.9 and corresponding to the spectra shown in Figure 4.14, depicting the impacts of varying the truncation degree on a test case of *CHAOS-4*α SV at 2005.0 are given in Appendix E, Figures E.1 through E.4, for completeness.

From each inversion, four sets of coefficients were produced, one set of coefficients describing the potential, and one each describing a SH model of the X-, Y- and Z-components. These SH models were then compared to equivalent models attained by inverting the jerks identified in observatory data in Chapter 2, following the same procedure.

4.5 SUMMARY

The work of this chapter describes the theory and reasoning behind the construction of synthetic stochastic field models to imitate magnetic observatory data on a global scale. The synthetic models are found to be suitable substitutes for observatory data and the jerks in them match the observed characteristics, further parallels can be drawn as to what possible spatial scales of jerk signals are and whether periodicity in jerk amplitudes are a sound observation.

The synthetic models built following Gillet et al. [2013] possess characteristics very similar to our knowledge of the geomagnetic field over the last half-century. To achieve an Earth-like field orientation and allow direct spatial comparisons between synthetic realisations, a rotation to a common dipole location was applied. This is shown to be equivalent to imposing an Earth-like mean value for the dipole g_1^0 coefficient *a priori*. The prior assumptions in the model construction are discussed further in light of results in Chapter 5.

I find the MF temporal spectrum to have a $-4\,\mathrm{nT}^2/\mathrm{yr}$ slope with frequency which fits estimates derived from the catalogue of observatory data describing the MF at periods from 5–100 yrs by Currie [1968] and De Santis et al. [2003] as well as a study of 50 yrs of cleaned observatory monthly means by myself in Section 4.3.1. While the $-4\,\mathrm{nT}^2/\mathrm{yr}$ slope appears to fit well for the periods in question and with the computation procedure used for estimating the frequency spectra, whether this is truly representative of the field at all periods present in monthly observatory SV data remains to be investigated. Additionally the spectral content of the signals removed during the cleaning process is of some interest regarding external field content and further contamination of observatory data.

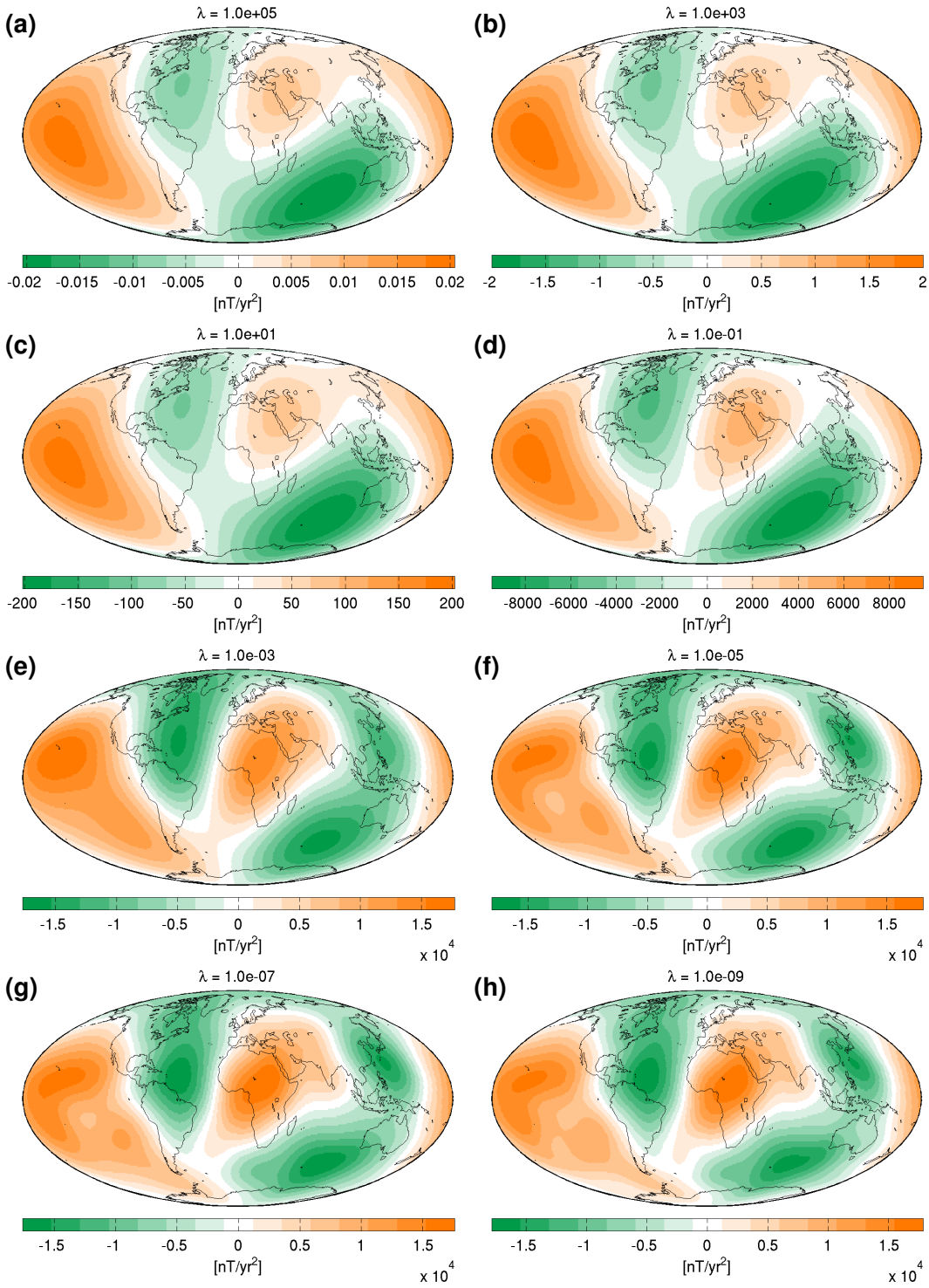

Figure 4.10: Potential of an example SH fit to jerk signal at the Earth's surface in a synthetic realisation for a range of damping parameters (λ). As λ is decreased (from (a) to (h)), higher SH degree spatial variations are penalised less and the resulting fit becomes more complex as well as increasing in magnitude (note colour scale changes).

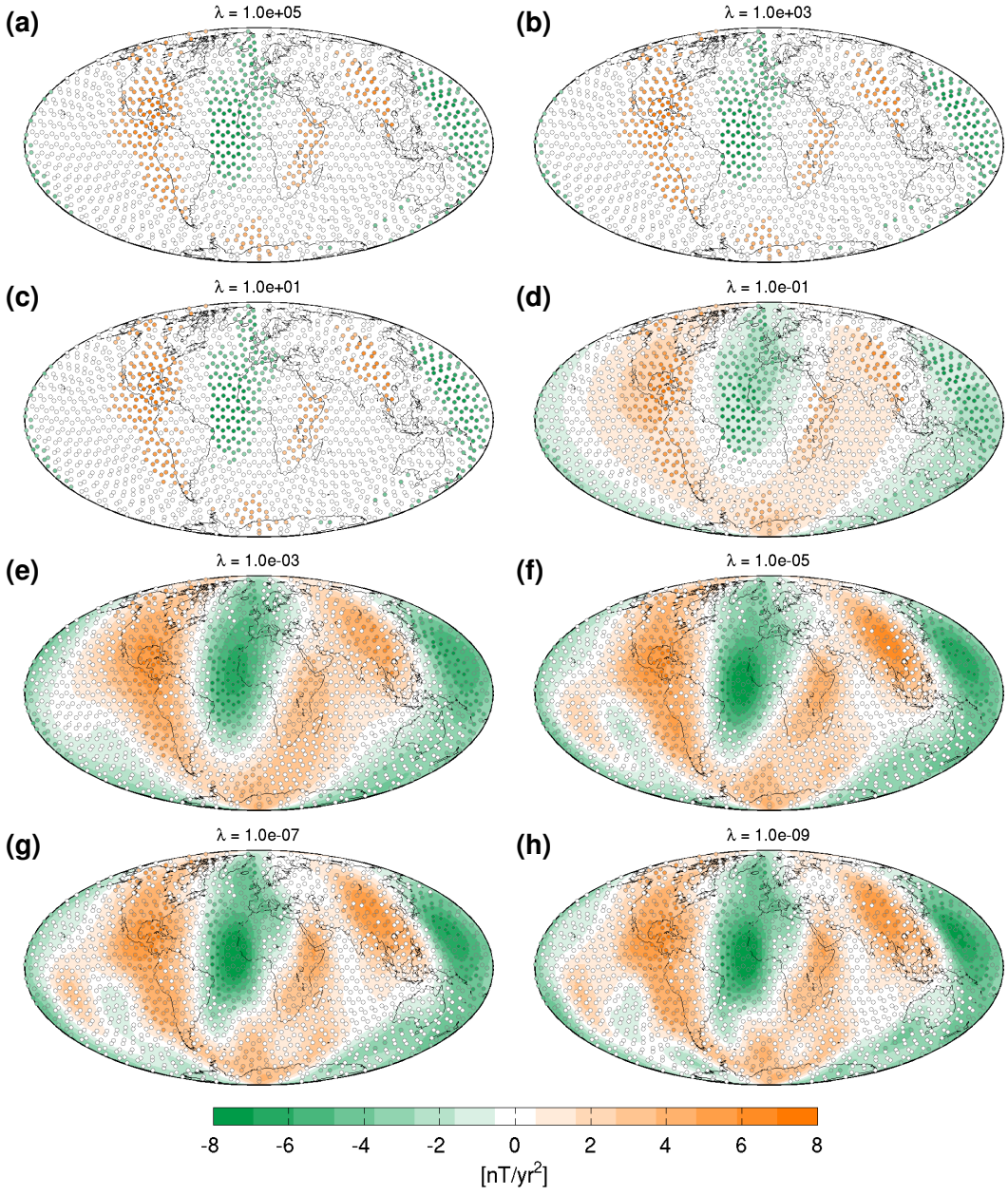

Figure 4.11: Y-component of an example SH fit to synthetic jerk signal at the Earth's surface for a range of damping parameters (λ). As λ is decreased (from (a) to (h)), higher SH degree spatial variations are penalised less and the resulting fit becomes more complex as well as increasing in magnitude. Jerk amplitudes are overlaid on the same colour scale, which is fixed for all plots to show how the misfit to this data is affected by the damping parameter.

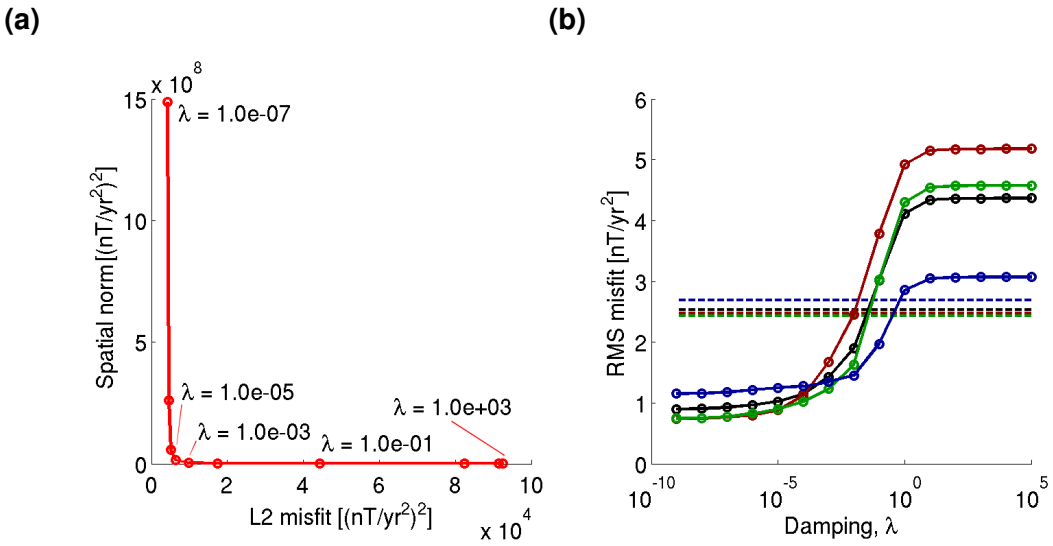

Figure 4.12: Misfit versus spatial norm trade-off curve (a) for an example SH fit to synthetic jerk signal at the Earth's surface (Figures 4.10 and 4.11) and RMS misfit (b) for a range of damping parameters (λ). In (b), RMS misfit overall (black) and for the X- (red), Y- (green) and Z-components (blue) individually are shown with dashed lines corresponding to the mean uncertainty of jerk amplitudes using the same colour coding.

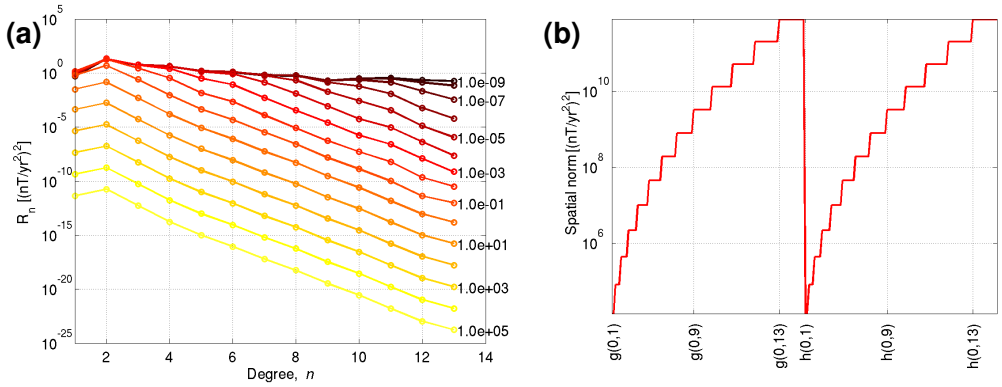

Figure 4.13: Recovered spectra for an example SH fit to synthetic jerk signal at the Earth's surface (Figures 4.10 and 4.11) for a range of damping parameters (λ) (a) and magnitude of spatial regularisation terms for each coefficient (b). The characteristic spectral slope of the spatial regularisation can be seen dominating to an increasingly low degree in (a) as λ is increased, corresponding to the degree at which the magnitude of the diagonal terms of the prior model covariance matrix as depicted in (b) multiplied by a factor of λ overtakes the spectral power of the modelled jerk amplitudes.

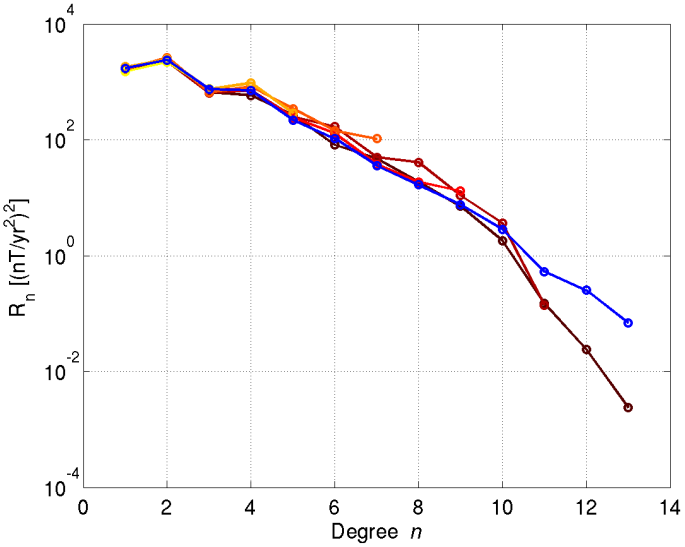

Figure 4.14: Comparison of SH model spectra for inversion of noisy magnetic field data derived from *CHAOS-4*α (SV at 2005.0, expanded to SH degree 13) for a range of SH truncation degrees. The original *CHAOS-4*α spectrum (blue) is shown with inversion spectra truncated at SH degrees 3, 5, 7, 9, 11 and 13. A value of $\lambda = 1.0\times10^{-4}$ was applied in all cases. The truncation at degree 13 (darkest red) can be seen to best track the original spectrum until the spatial regularisation overrides above degree 9.

Spatial spectra for the MF and SV were found that are very close to those of field models. Whilst this spectral agreement to *GRIMM-2* and *COV-OBS* does not persist above SH degree 11 in the MF, the departure is in line with the variations observed between field models built with different constraints and is not expected to significantly impact on the resolution of the SV. Additionally, jerks are not expected to be resolved in the highest SH degrees as will be seen in Chapter 5. The SV spectra matches that of *GRIMM-2* exactly which, consistent with other satellite field models (e.g. *CHAOS-4*α) presents a more powerful mean degree 1 component than is seen over the longer timescale of *COV-OBS*. The SA of the synthetic models is likely the most contentious component as it is not constrained or regularised *a priori* as in most field models, rather left to be described by the derivative of a Wiener process (white noise). As a result the SA is of greater magnitude than in most field models, except at SH degrees 1 and 3. Gillet et al. [2013] argue the additional power is representative of a genuine property of the geomagnetic field, not captured by SA regularised field models. I assume that this argument is valid for the purpose of this work.

Key to the interests of this thesis, the field component timeseries produced from the synthetic models contain rapid SV changes that fit with my definition of jerks and whose spatial and temporal distributions will be analysed and compared to the jerks identified in

observatory data (Chapter 3) in the following chapter. Aside from providing a new tool for field modelling [see Gillet et al., 2013; Hellio et al., 2014], the synthetic models are overall judged to be an excellent tool for synthetic magnetic field studies, not solely limited to the topic of jerks but other spatial or temporal analysis of internal field data. These models are particularly interesting for studies of SV since it is presented in a manner far more similar to observatory data than any field model to date. As Gillet et al. [2013] demonstrated, being a "clean" model of the internal field, the effectiveness of inversion techniques and impacts of procedures such as regularisation can be tested. In Chapter 5 I aim to validate the interpretations of real observations by drawing comparison to these synthetic models. The applicability of prior assumptions to this, and other, topics will also be discussed.

CHAPTER 5

JERKS IN STOCHASTIC SYNTHETIC FIELDS

5.1 OVERVIEW

This chapter presents the results of the modelling and analysis procedures described in Chapter 4, endeavouring to address some of the issues raised by the analysis of observatory data in Chapter 2 regarding the impact of the limited spatial and temporal coverage of geomagnetic measurements.

To reiterate, the aim of this work is to validate the interpretation of jerks as regional and not global scale events at the Earth's surface, as made from observatory data, and to quantify the possible spatial extent of events which resemble jerks as sampled by observatory data. It is also possible to comment on the reliability of the observations of periodic jerk amplitudes and the character of possible jerk properties which fit with the behaviour of the geomagnetic field. This study also raises questions about the interpretation of jerks in global field models and the importance of modelling assumptions.

Section 5.2 presents and discusses the results of the analysis, split into sections describing the applicability of the assumption of jerks as a potential field (Section 5.2.1) and the temporal (Section 5.2.2), spatial (Section 5.2.3) and periodic (Section 5.2.4) characteristics of the synthetic jerks. The synthetic and observed jerks are compared in Section 5.3 at the surface and the CMB before Section 5.4 questions what impact the model assumptions have on such studies. Finally, conclusions are drawn in Section 5.5.

5.2 RESULTS

In the case of the jerk identification procedure using observatory data, described in Chapter 2, a large amount of information was generated, this is truer still for the jerk analysis of synthetic models. Here I will summarise the key general results and discussion points, highlighted by examples that are found to be representative of the many realisations of synthetic models. Additional information of interest but surplus to the presentation and discussion of results here are included in Appendix F and will be referenced where appropriate.

Here I skip ahead slightly to confirm that, as suggested by the similarities observed between observatory data and the synthetic data in Section 4.3, the characteristics of results for jerk identification in the synthetic models greatly resemble those achieved with observatory data and will thus be analysed in detail.

Statistical analysis of results across realisations of synthetic models will be used where possible (e.g. Tables 5.1–5.3). The results for three detection window lengths (5, 15, 25 yr) for twenty five realisations are considered here. Otherwise the results for the jerk which produced the closest spectrum to the overall mean jerk spatial spectrum will be presented (and closest to the median, which was found to approximate the mean, as the Gaussian design of the synthetic model variations imposes). Where applicable the results for the realisation containing this closest-to-mean jerk will be represented.

For all window lengths, the numbers of jerks were found to be approximately equal in each field component, with overall detected numbers decreasing with increasing window length, as with observatory data. As indicated in Figure 4.7, with the selected jerk probability cut-off of 0.07, totals of $\sim$15,000, $\sim$29,000 and $\sim$23,000 individual jerks were detected with the 5, 15, and 25 yr window lengths, respectively. Again the mean and median jerk probability values given by the PDFs increased as expected with window length, with the mean and median values being roughly equal (Table 5.1). As for observatory data, the temporal error bars on jerk detection times in all three field components were found to be roughly symmetrical and increased with window length from $\pm$0.2 yr for 5 yr to $\pm$0.5 yr for 25 yr windows (Table 5.2). This again confirms that the Gaussian error assumption (ensured by additional Gaussian noise in the SV in this case) is reasonable. Interestingly the error bars on jerk amplitude values are seen to decrease with increasing window length (Table 5.3). The amplitude error bars are also symmetric, as for observatory data and vary from a mean value across components of $\pm$2.7 nT/yr^2 for 5 yr to $\pm$1.5 nT/yr^2 for 25 yr

windows. The amplitude error bars on the Z-component were found to be systematically higher than those on the X- and Y-components.

These statistical values are found to be very similar to those found for observatory data, implying that the timeseries analysed possess very similar properties, a promising result for a synthetic data substitute. Generally the results for the 25 yr detection window will be favoured here as describing the large-scale jerk phenomena that resemble features like the 1969 Y-component jerk seen in observatory data. Additionally they are seen to have the smallest amplitude error bars, a useful fact considering the SH modelling procedure to come.

Table 5.1: Mean and median probability values over all jerks detected in twenty five 100 yr synthetic realisations, by field component and window length.

Stat.	Window [yr]	X	Y	Z	Overall
Mean probability	5	0.08	0.08	0.08	0.08
	15	0.12	0.12	0.11	0.12
	25	0.17	0.17	0.13	0.16
Median probability	5	0.08	0.08	0.08	0.08
	15	0.11	0.11	0.10	0.10
	25	0.14	0.14	0.11	0.13

Table 5.2: Mean time uncertainty values over all jerks detected in twenty five 100 yr synthetic realisations, by field component and window length. The negative and positive error bar values are given as well as the mean and mean magnitude of the error bar pairs.

Comp.	Window [yr]	−error [yr]	+error [yr]	Mean error [yr]	Mean |error| [yr]
X	5	−0.19	0.23	0.02	0.21
	15	−0.38	0.40	0.01	0.39
	25	−0.48	0.51	0.01	0.49
Y	5	−0.19	0.23	0.02	0.21
	15	−0.38	0.40	0.01	0.39
	25	−0.48	0.51	0.02	0.50
Z	5	−0.17	0.20	0.02	0.19
	15	−0.36	0.39	0.02	0.37
	25	−0.50	0.53	0.01	0.51

5.2.1 Jerks as a Potential Field

Before any analysis of spatial patterns in the synthetic SH jerk models it is necessary to assess whether the assumption that the jerk signal can be treated as a potential field is sound or whether SH models of individual components are a better representation. It should be stressed that landmasses are plotted in all map figures simply to highlight spatial scales and to give an intuitive reference frame; the functions plotted are synthetic.

As illustrated by the example in Figure 5.1 there is a visual similarity between the SH

Table 5.3: Mean jerk amplitude uncertainty values over all jerks detected in twenty five 100 yr synthetic realisations, by field component and window length. The negative and positive error bar values are given as well as the mean and mean magnitude of the error bar pairs.

Comp.	Window [yr]	−error [nT/yr^2]	+error [nT/yr^2]	Mean error [nT/yr^2]	Mean |error| [nT/yr^2]
X	5	−2.27	2.24	−0.01	2.25
	15	−1.64	1.62	−0.01	1.63
	25	−1.11	1.14	0.02	1.12
Y	5	−2.25	2.25	0.00	2.25
	15	−1.65	1.67	0.01	1.66
	25	−1.12	1.13	0.00	1.12
Z	5	−3.52	3.54	0.01	3.53
	15	−3.08	3.00	−0.04	3.04
	25	−2.39	2.37	−0.01	2.38

models of individual field components and field components derived from a potential. In terms of agreement to data, the models are smoother, as expected given the assumption of a large-scale phenomenon implicitly made with the choice of model prior in the inversion. The models do, however, show good agreement to jerk amplitude estimates, perhaps better illustrating the taper of jerk amplitudes towards zero which is treated as a sharp cut at 3 nT/yr^2 in the jerk detection algorithm. The inversions to produce the maps in Figure 5.1 applied the same damping parameters and data uncertainties, however, the misfit to data that resulted in each case, and the spatial power spectrum of the SH model (Figure 5.2) were found to show differences.

The broad visual agreement in Figure 5.1 is reflected in the similarity of spectra in Figure 5.2 for the lowest degrees. Key differences are seen between the spectrum of the potential and the individual components for degrees greater than 5 and between the potential and X-component at degree 3. The potential can be seen to agree well with the trends of the Y- and Z-components, peaking at degrees 2 and 4, although with less power. The X-component conversely shows lower power at degrees 2 and 4 and a peak at degree 3. It might be expected that these spectral differences at the largest, most powerful scales would lead to starker contrast between the maps in Figure 5.1. However, it seems that the additional power at degree 5 and above in the potential acts to balance the lower power in the potential at degrees below 5.

The additional small scale variability is reflected in the misfit to jerk amplitude data. For the case of individual field component SH models, the sum-of-square misfits (the L2 norm minimised during the inversion) was found to be 2587 (nT/yr^2)^2, 3387 (nT/yr^2)^2 and 4285 (nT/yr^2)^2 for the X-, Y- and Z-components, respectively, which corresponds to root-mean-square (RMS) errors of 1.26 nT/yr^2, 1.45 nT/yr^2 and 1.63 nT/yr^2, respectively. When

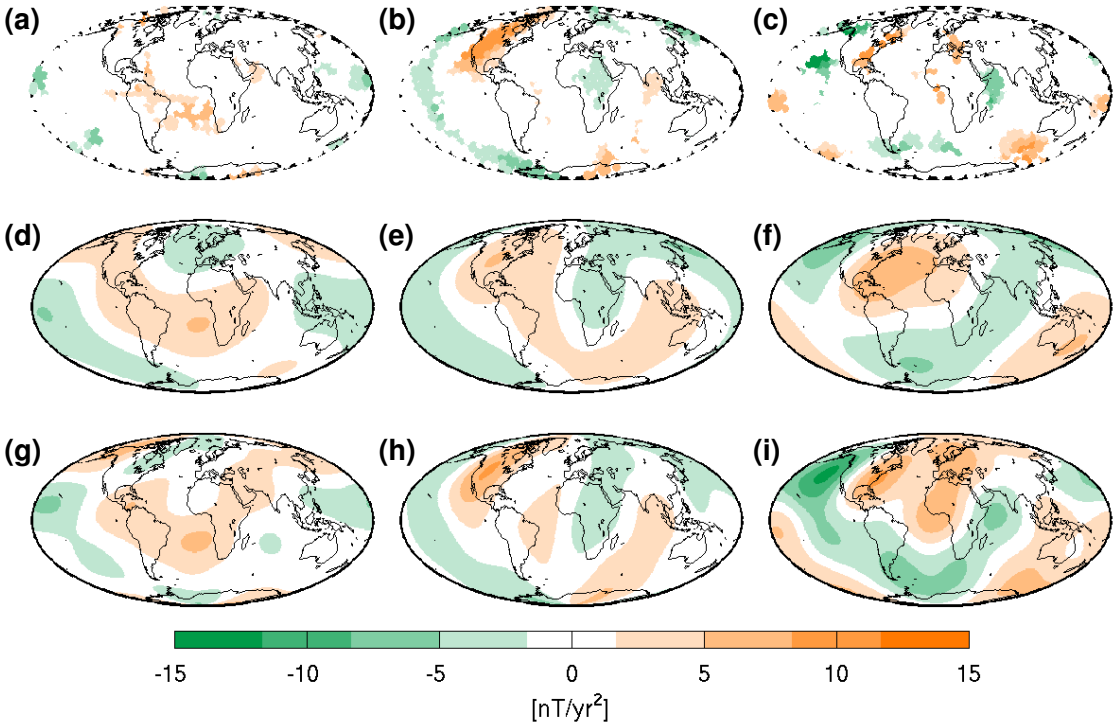

Figure 5.1: Example comparison of potential field model of synthetic jerk amplitudes and SH models of individual X-, Y- and Z-component amplitudes. Columns left to right show X-, Y- and Z-components, respectively, of jerk amplitudes in a 3 yr timespan (a,b,c), individual field component SH models fit to these amplitudes (d,e,f) and the X-, Y- and Z-components derived from a potential fit to the amplitudes of all three components simultaneously (g,h,i).

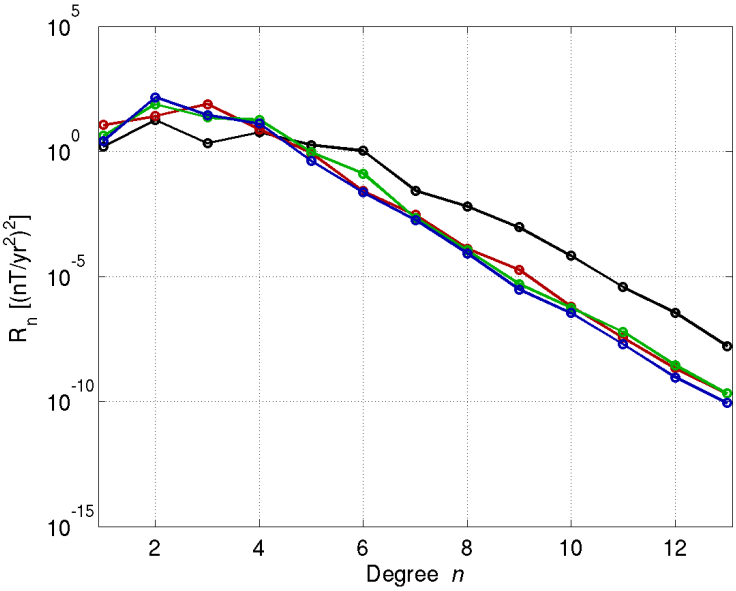

Figure 5.2: Spatial power spectra corresponding to jerk amplitude model inversions in Figure 5.1, comparing inversion of individual field components to inversion of all components for a potential field. Spectrum of jerk potential (black) and X- (red), Y- (green) and Z-component (blue) SH models are shown.

a potential field was assumed, the least-squares misfit was found to be 5606 $(\mathrm{nT/yr^2})^2$ (bear in mind that 3 times as many data points are included since all three components are considered simultaneously) which corresponds to an overall RMS error of 1.07 $\mathrm{nT/yr^2}$, lower than in any of the individual component model cases. This overall RMS error can be broken down into an RMS error for each field component derived from the potential to give 0.87 $\mathrm{nT/yr^2}$, 0.94 $\mathrm{nT/yr^2}$ and 1.35 $\mathrm{nT/yr^2}$ for the X-, Y- and Z-components, respectively. In all synthetic jerk cases, as was seen in Figure 4.12, the small misfit means that despite the spatial regularisation, the data are being overfit. However, despite overfitting, a predominantly large-scale field is achieved in all cases. The greater power in small scale structure in the potential can be seen to better represent the jerk amplitude data than the individual component models do in cases such as the Z-component in Figure 5.1 (compare (c), (f) and (i) around central longitudes in particular).

The assumption of a potential field is judged to be a reasonable one; visually similar results to modelling field components individually are attained but data misfit was found to be lower for the case of a potential field across the majority of synthetic jerk instances. One benefit of this assumption is that a potential field can be upward- or downward-continued to be mapped at other radii away from the source, for example jerk models built at the Earth's surface can be projected to the CMB.

5.2.2 TEMPORAL CHARACTERISTICS OF SYNTHETIC JERKS

Recalling the jerk histograms of Chapter 3 (Figures 3.1–3.4), the temporal distribution of identified jerks in the synthetic time series bears close resemblance to that of observatory data. Since the synthetic timeseries for all locations span the full time period of the synthetic models, there is no need for the histogram weighting procedure used in the previous chapter. Time bins of 1 yr were again used having confirmed that the mean temporal error bars on detection times were 6 months or less.

As Figure 5.3 shows, regardless of the detection window length used, there are time periods of many jerks and few, with detections rarely exceeding 50% of the STT cell locations sampled. This trend is still borne out when only the observatory locations are considered (Figure F.1). This suggests that as observed for jerks in observatory data, there is never a literally global phenomenon. At any given time there are jerk like features present at some locations but rarely the majority, even with full spatial knowledge. Whether these detected synthetic jerks are evenly distributed in space, apropos achieving global coverage in a general sense, will be discussed in Section 5.2.3.

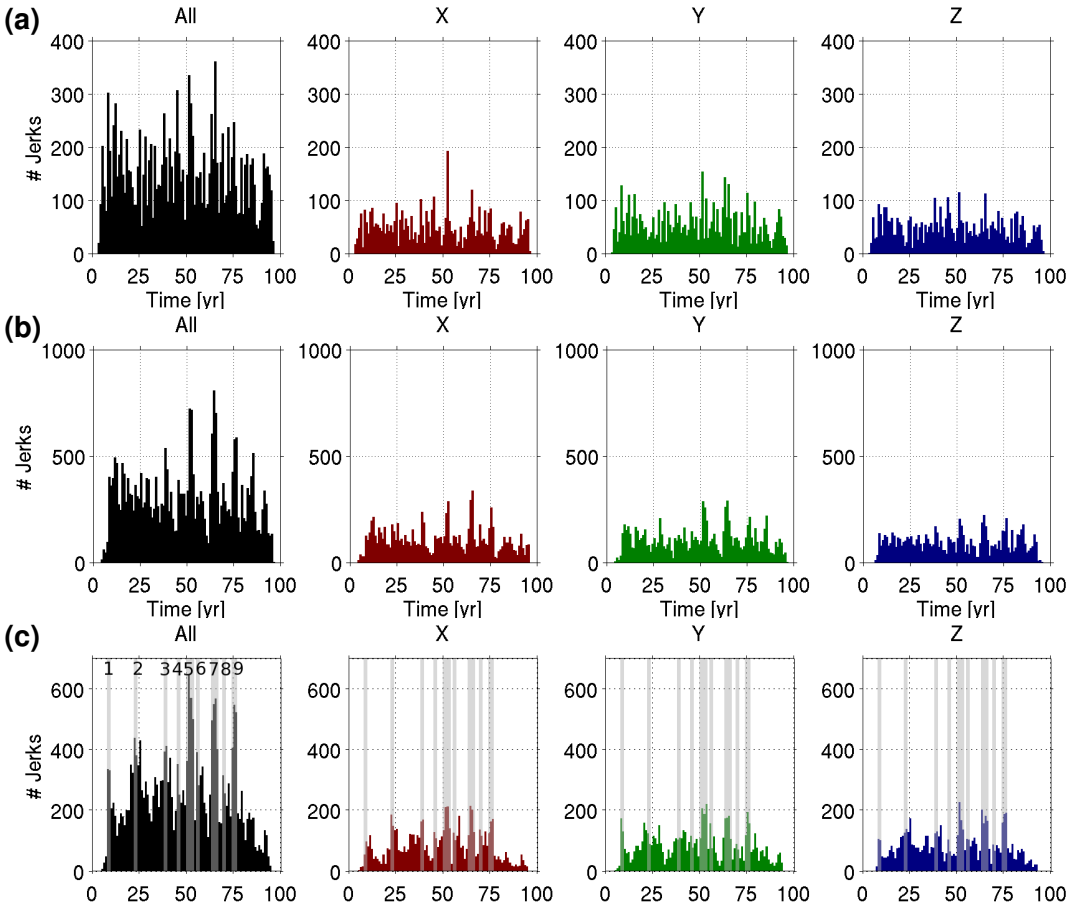

Figure 5.3: Histograms of number of jerks detected in a 100 yr realisation of synthetic model at 1620 STT cell locations, with 1 yr bins. Total count (black) and those for individual X- (red), Y- (green), and Z-components (blue) are shown for results using detection windows of 5 yr (a), 15 yr (b) and 25 yr (c). Grey bars highlight nine histogram peaks considered jerks as defined in the 25 yr window, all-component histogram (black) in (c).

The periods of frequent and limited jerk occurrences vary with detection window length. Evidently there are features at different temporal scales that behave in a jerk-like manner in the SV, much as was seen in observatory data. The times with the highest numbers of jerk detections over 1 to 4 yr spans can be seen to be more consistent between window lengths (e.g. at ∼50 yrs, ∼58 yrs, ∼75 yrs in Figure 5.3). It is these histogram peaks (defined in the all-component histograms) that will be used to select jerk amplitude data for building SH models of synthetic jerks. A simple maxima finding algorithm[1] was applied to each all-component histogram for consistency and efficiency in dealing with the large volume of data. Histogram peaks were defined as local maxima where jerk numbers exceeded the neighbouring local minima on either side by ≥20% of the maximum value for a single

[1] Based on alternating derivative signs, by Nathanael Yoder, available from http://uk.mathworks.com/matlabcentral/fileexchange/25500-peakfinder, 2015-03.

histogram bin. Through this method not all local histogram peaks will be considered jerks, only the peaks which stand out most from the background level of jerk detections per year; shoulders on larger peaks and rapid fluctuations of jerk numbers in particular are discounted by this method.

When considering the combination of components which results in an overall histogram peak, it can be seen that there are differences between the case of full spatial knowledge and observatory style spatial sampling (Figure 5.4). Generally the overall histogram peaks in the STT cell case are more evenly composed of each component than in the case of observatory sampling (compare components at $\sim$75 yrs in Figure 5.4). This is likely due to the location of the highest amplitude parts of the jerk signal relative to the sampling locations. In the case of the STT cells all parts of the signal are observed; when the sampling is degraded, some components may be affected more severely than others if the highest amplitude jerks are located away from an area of dense sampling such as over Europe. Histogram peaks for jerks in observatory data were observed to show a varying trend of component make up. The results from observations suggest two possible inferences: that jerks do not occur equally in all field components, or that they do and the spatial sampling merely disguises this since the regions of high and low amplitude are not coherent between components. Of course there is also a third case where both are true at different times. To the best of my knowledge it has not been quantitatively shown, explicitly or otherwise, in a study of satellite data whether the case for uneven component make up is seen for jerks since 2000. The level of spatial coverage achieved in satellite models should be able to confirm or refute this trend, although whether this is taken to be representative of the entire observatory era SV remains an open question.

With the knowledge that temporal patterns of jerks in the synthetic models closely resemble those found in observatory data, the most significant behaviour to analyse is the impact of the observatory style spatial sampling on the synthetic results, as illustrated in Figure 5.4 (see Figures F.2 and F.3 for 5 yr and 15 yr window equivalent). The periods of frequent jerks seen with full spatial coverage (Figure 5.4a) can generally still be identified when the sampling is reduced to observatory locations (Figure 5.4b), this is found to be true for the majority of all-component histogram peaks across realisations. This is encouraging in terms of the expectations held for interpretation of observatory data, at least in the latter half of the 20st century when the observatory distribution is widest. It is possible, however, that this overall temporal trend masks a more disparate spatial picture in regions such as the Pacific where there is very limited sampling at any point in time.

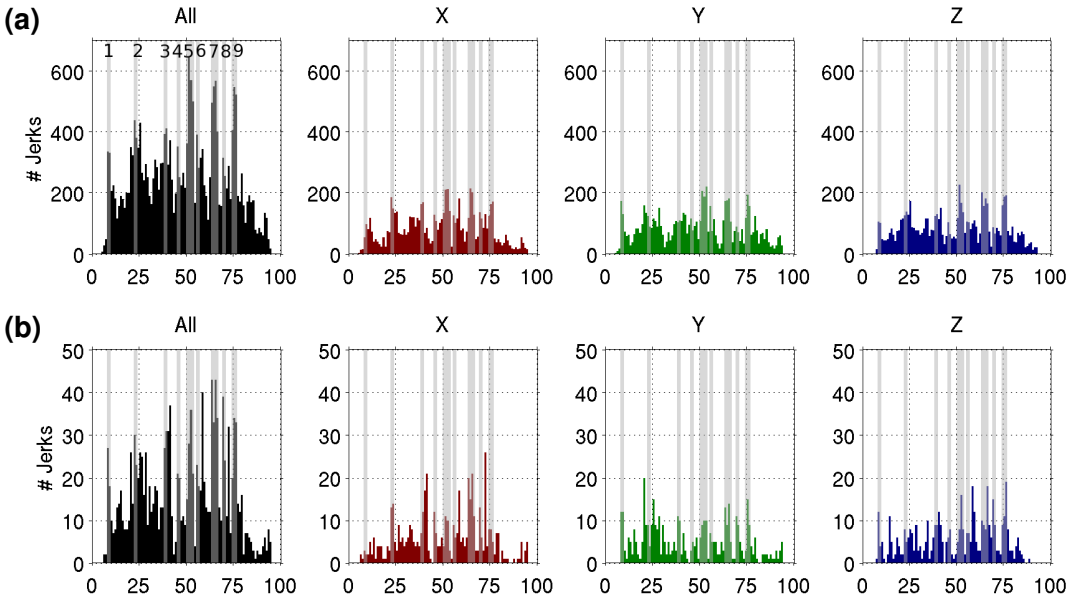

Figure 5.4: Histograms of number of jerks detected in a 100 yr realisation of synthetic model at 1620 STT cell locations (a) and 102 observatory locations (b), with 1 yr bins. Total count (black) and those for individual X- (red), Y- (green), and Z-components (blue) are shown for a 25 yr detection window. Grey bars highlight nine histogram peaks considered jerks as defined in the all-component histogram (black) in (a).

5.2.3 Spatial Characteristics of Synthetic Jerks

Across the twenty five 100 yr realisations of synthetic models analysed[1], 254 instances of relatively high numbers of jerk occurrences were identified from peaks of histograms such as those in Section 5.2.2. These will be the synthetic jerk examples modelled and analysed further. As was seen for observatory data, histogram peaks are relative and can contain greater or fewer numbers of jerks identified in the field components at individual spatial locations. This is illustrated by the example synthetic jerks in Figure 5.5. It can be seen that as in observatory data, jerk amplitudes are indeed consistent in sign across spatial regions. The synthetic jerks appear at clusters of tens to hundreds of spatial locations. As the comparison of Figure 5.5a,c to Figure 5.5b,d shows, the area of the Earth's surface covered by these clusters of positive and negative jerk amplitudes can vary greatly. A very rough estimate can be given by multiplying the number of points in a cluster by the fraction of spherical surface corresponding to a single STT cell, assuming they are evenly distributed in space. This leads to areas on the order of 3×10^6 km^2 for tens of locations to 3×10^7 km^2 for hundreds. A better way to estimate the spatial scale of

[1] While twenty five realisations is not a particularly large number, this constitutes a substantial 2,500 yrs of three-component, monthly resolution timeseries to analyse. Since the model variations are governed by a Gaussian distribution and the mean and median of results approximate each other, I take this as a sign that a suitable and representative distribution of realisations is studied.

the jerk signal can be given by noting the dominant spatial scale of a SH model of the jerk amplitudes.

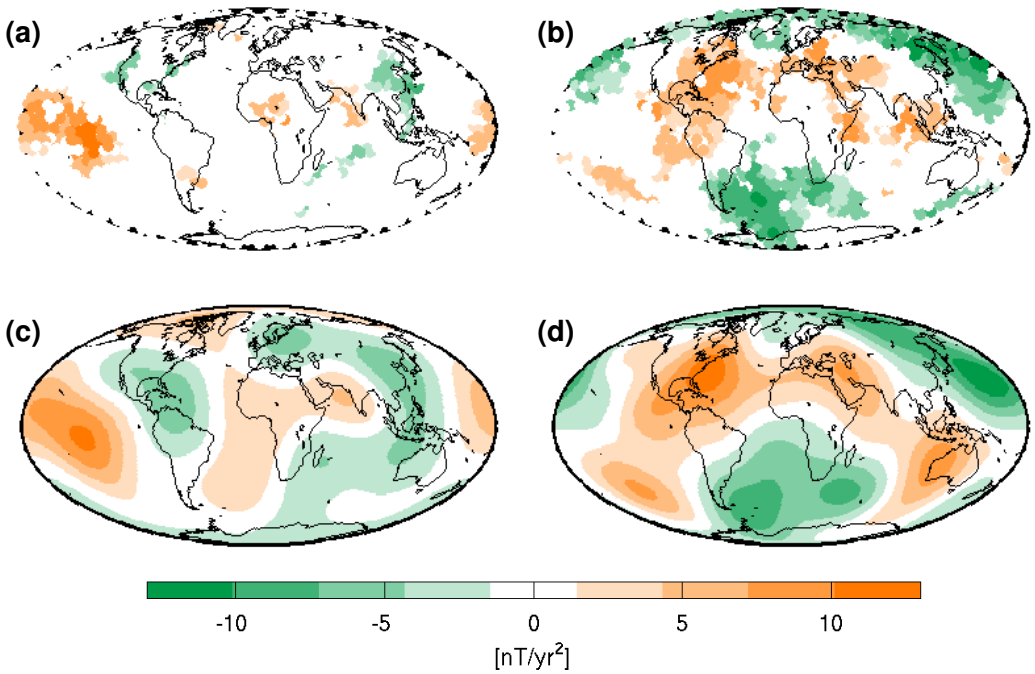

Figure 5.5: Example maps of synthetic jerks refined to peaks of jerk occurrence histograms. Detected jerk amplitudes in the Z-component are shown for the case of a relatively lower ((a), peak 6 in Figure 5.4) and higher ((b), peak 7 in Figure 5.4) number of identified jerk amplitudes and the resultant SH models (c,d), respectively.

Computation of such models for all 254 jerk instances was performed, assuming the jerk can be fit by a potential field at the Earth's surface and with a damping parameter of $\lambda = 1.0 \times 10^{-4}$. Mapped examples of the results can be seen in Figure 5.5 whilst a compilation of all the spectra can be seen in Figure 5.6. The two cases of less and more numerous jerks in Figure 5.5c,d illustrate that the SH inversion produces better representations of larger patches of jerk amplitudes, as is to be expected when a spatial regularisation is applied and the model expansion is truncated. Nevertheless, whilst there is variation from jerk to jerk, a general trend can be identified in the spectra in Figure 5.6. This is well demonstrated by the mean spectrum which shows peaks in power at SH degrees 2 and 4. As was found for test examples, the spatial regularisation appears to be dominant above degree 6. The largest error bar (indicating one standard deviation from the mean) is for degree 1, likely reflecting the large variance assumed in the prior information. Despite the potential for degree 1 terms to be somewhat larger and more variable than other degrees, degree 1 is found to be a relatively weak contribution to the jerk signal. By far the majority of the models computed suggest that the synthetic

jerks can be best described by a predominantly low degree potential field, peaking at degrees 2 and 4. Degree 2 corresponds to a wavelength of ∼10,000 km and degree 4 a wavelength of ∼5,000 km at the Earth's surface.

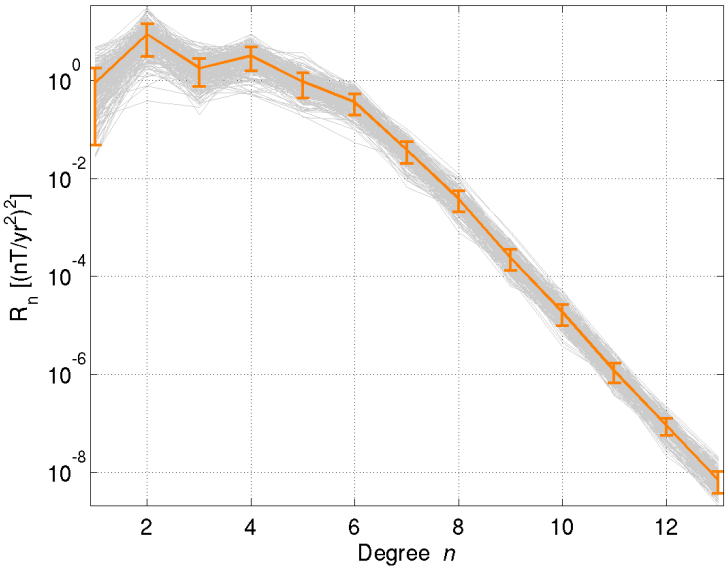

Figure 5.6: Spectra at Earth's surface of synthetic jerks from all realisations as defined by peaks in histograms of jerk occurrences (grey) overlaid with mean of spectra with error bars of one standard deviation (orange).

The spectrum of a SH model does not inform of the spatial locations of any part of the signal directly. As might be expected given the construction of the synthetic models, there is no bias to any particular spatial region when temporal histograms are limited to displaying, for example, jerks detected in a single Hemisphere. Histograms for the Northern (Figure F.4), Southern (Figure F.5), Eastern (Figure F.6) and Western (Figure F.7) Hemispheres also confirm that there is no observed systematic delayed trend in jerk occurrences, as has been suggested for observatory data [e.g. Alexandrescu et al., 1996b; Pinheiro et al., 2011]. Neither can any inference be made about a region of low SV in the Pacific [Holme et al., 2011] from these synthetic models. Naturally, the Northern and Western Hemispheres fair better from the spatial down-sampling to observatory locations due to the higher abundance of observatories (Figures F.4–F.7) but all Hemispheres still, at least in terms of global trends, recover a representative picture of jerk occurrences. This may indicate a lacking on the part of the synthetic models since the Earth is known, at least in recent decades, to have low SV in the Pacific region [Holme et al., 2011]. Throughout the observatory age there is little that can be said about Pacific region SV with coverage only from the very isolated observatory at Hawaii. With 15 yrs of satellite data available it

can be said that there is no notable presence of jerks in the Pacific region as jerks in 2003, 2005, 2007 and 2011 were reported to be localised in the region from just West of Africa to the Indian Ocean [Chulliat and Maus, 2014; Olsen and Mandea, 2007, 2008].

This is highlighted in Figure 5.7 where the results of inversion are compared for jerk amplitudes sampled densely across the globe and for the case when observatory style sampling is used. Encouragingly, the SH models are broadly similar despite the lack of data constraints in the X-component in particular. The large positive jerk patch in the South Atlantic region of the X-component lies away from any observatory locations but the positive lobe is still present, required in the potential by the better constrained variations in the Y- and Z-components. It is clear that assuming a potential field contributes more than convenience to the results of the inversions and provides a means to temper the varying distributions of jerk amplitude data across the field components. These large-scale similarities between the models of dense and sparse spatial sampling cannot be attributed entirely to the spatial regularisation which is seen to dominate the spectra at only the highest (Figure 5.8). This point is reinforced by comparing the individual component SH models in Figure 5.1d,e,f to the models in Figure 5.7. The sparse observatory sampling can be seen to better capture some of the small scale jerk amplitude variations than modelling the field component individually (compare the Z-components of the three cases for example). The large-scale agreement between the results with dense and sparse spatial sampling can be quantified via the spectra of the modelled potentials as in Figure 5.8. The mean spectra for all jerks at both spatial sampling densities show agreement, within error, for the first three degrees with a more spurious agreement at degree 4. The spatial regularisation can be seen to dominate from then onwards in the sparse observatory sampling case while it doesn't overtake the jerk signal until above degree 6 with dense spatial sampling. The dominant spatial scale features are therefore captured in either spatial sampling case.

Globally anticorrelated series of jerk amplitudes have been noted for jerks in observatory data in 1969, 1978, 1991 and 1999 both in my results in Chapter 3 and by authors such as Le Huy et al. [1998] and Sabaka et al. [2004]. The synthetic jerks show complex spatial patterns without global consistency between consecutive jerks. Given that at any given point on the sphere, synthetic jerk amplitudes can be positive, negative or zero in succession through time it is difficult to trace the regional clusters of high jerk amplitudes in all field components of each realisation in a mathematically rigorous manner. What can be done is to investigate whether there is any underlying trend in the distribution of

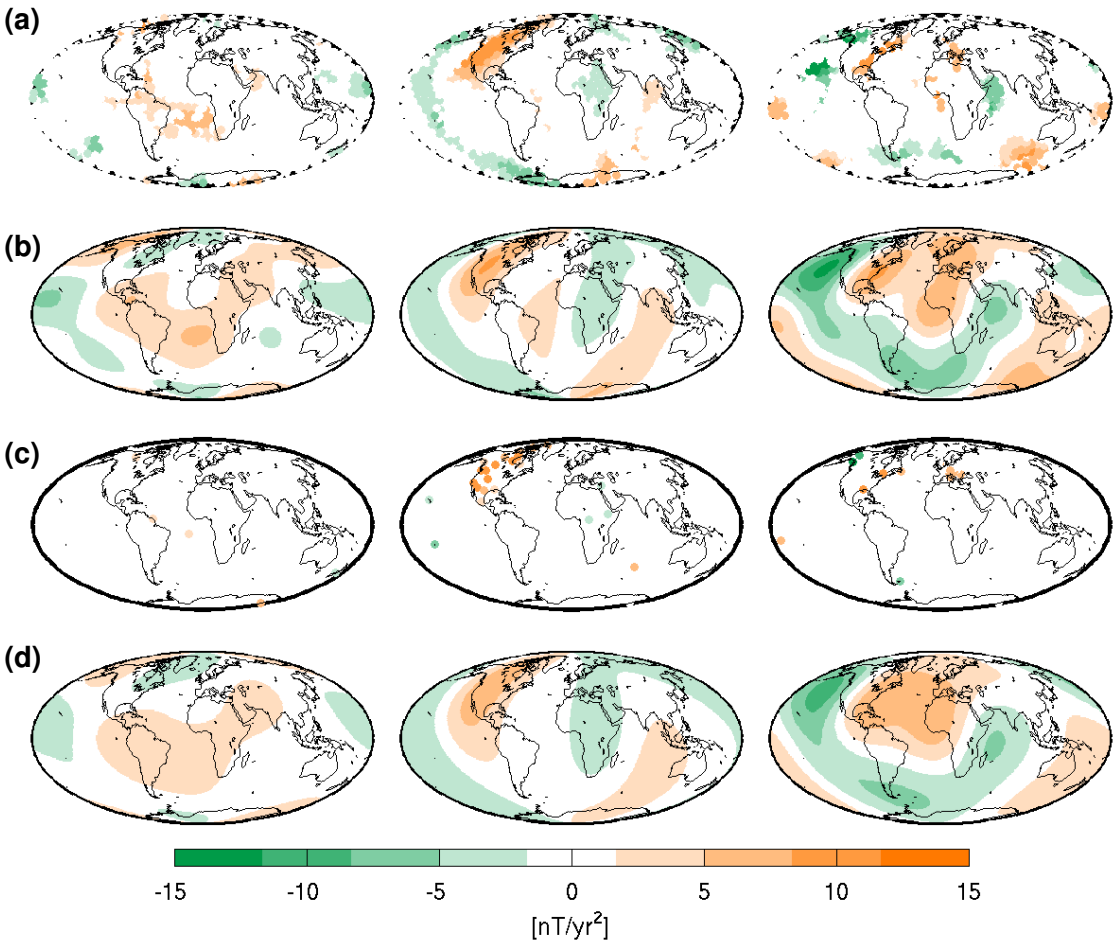

Figure 5.7: Example of jerk amplitudes (peak 1 in Figure 5.4) at all 1620 STT cells (a) and the resulting SH model (b) with the case of observatory style sampling (c) and the resulting SH model (d) for comparison. Columns represent X-, Y- and Z-components from left to right.

power amongst the Gauss coefficients and whether these more simple patterns show such anticorrelated behaviour in successive jerks. The global correlation coefficient for a pair of jerk Gauss coefficient sets, denoted by subscripts 1 and 2, can be calculated by,

$$c_{1,2} = \frac{\int \ddot{\mathbf{B}}_1 \cdot \ddot{\mathbf{B}}_2 \, \mathrm{d}\theta \mathrm{d}\phi}{\sqrt{\int \ddot{\mathbf{B}}_1^2 \, \mathrm{d}\theta \mathrm{d}\phi \int \ddot{\mathbf{B}}_2^2 \, \mathrm{d}\theta \mathrm{d}\phi}}$$
$$= \frac{\sum_{n=1}^{n_{\max}} (n+1) \sum_{m=0}^{n} \left[(g_n^m)_1^2 (g_n^m)_2^2 + (h_n^m)_1^2 (h_n^m)_2^2 \right]}{\sqrt{\left(\sum_{n=1}^{n_{\max}} (n+1) \sum_{m=0}^{n} \left[(g_n^m)_1^2 + (h_n^m)_1^2 \right] \right) \left(\sum_{n=1}^{n_{\max}} (n+1) \sum_{m=0}^{n} \left[(g_n^m)_2^2 + (h_n^m)_2^2 \right] \right)}}, \tag{5.2.1}$$

[McLeod, 1985] where $\int \mathrm{d}\theta \mathrm{d}\phi$ signifies an integral over the surface of the Earth. This correlation coefficient can be calculated for all possible pairs of jerk models, as shown in Figure 5.9, and in the idealised situation of perfectly anticorrelated successive jerks would

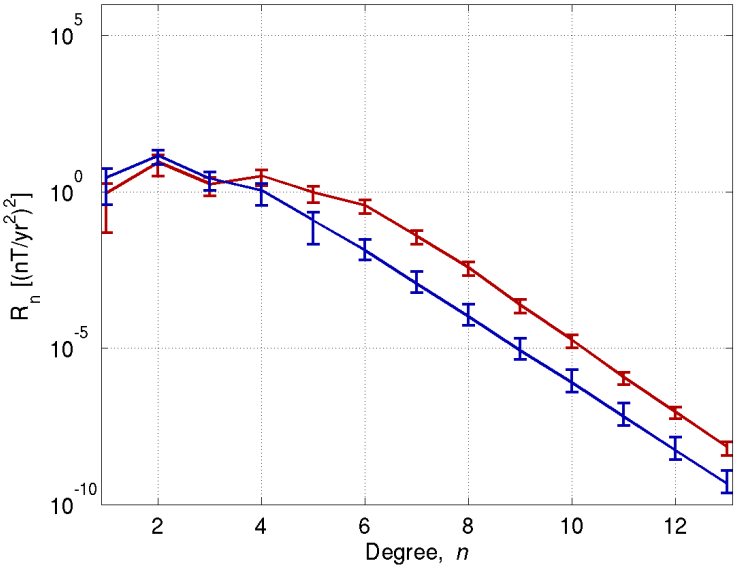

Figure 5.8: Effects of spatial sampling on the spatial power spectrum of synthetic jerks. Mean results across all jerks for all STT cell locations (red) and observatory style sampling (blue) are depicted at the Earth's surface.

show a checkerboard pattern of $+1$, -1 values.

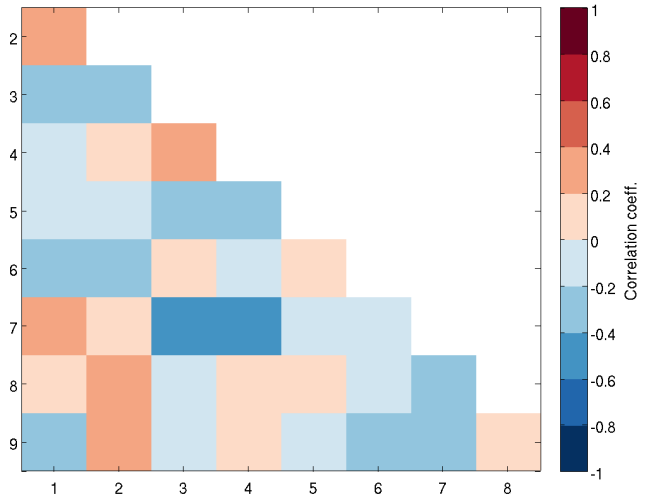

Figure 5.9: Global correlation coefficients [after McLeod, 1985] for the nine jerk histogram peaks in an example synthetic realisation (Figure 5.4).

A pattern of successive anticorrelated pairs of coefficient sets is not seen in Figure 5.9, nor any other distinguishable pattern. The strongest correlation coefficient is found to be -0.5 while 25% of the correlation coefficients (the nine smallest magnitude coefficients) are determined to be statistically insignificant. This was judged by the p-value null

hypothesis test (assuming no correlation) at the 0.05 significance level. These coefficients are included in Figure 5.9 simply to illustrate that no pattern in the sign or strength of the correlation is apparent.

The model coefficients for each jerk were also divided into their equatorially and azimuthally symmetric and anti-symmetric groups, as well as zonal and non-zonal contributions. The correlations of these groups of coefficients are displayed in Figure F.8, the correlation of the zonal parts is seen to be strongest but still no clear pattern is seen through the complete sequence of jerks in any group, only limited example cases. Maps of the coefficient groups are also considered, no consistent preference is found towards stronger field in any one of these groups of coefficients, they are generally evenly proportioned. The degree 2 dominance seen in the spectra of the jerk potentials is evident in the equatorially and azimuthally symmetric and anti-symmetric groups. A sequence of the equatorially symmetric and anti-symmetric parts of four jerks is illustrated in Figure 5.10 and shows jerks 5–8 from Figure 5.9. Figure 5.10 shows in this case an anticorrelated series of degree 2 order 2 patterns for the equatorially symmetric part of the jerk potentials and a series of degree 2 order 1 patterns which alternate polarity every second jerk in the anti-symmetric part. The anti-symmetric part of the field is first strong, then weak in successive jerks. The distinctive degree 2 patterns are not always as clear for every jerk, but are the strongest component on average while the strong then weak behaviour is seen in several of the coefficient groups in realisations of different jerk sequences. For the equatorially symmetric parts in Figure 5.10 correlations (statistically significant at a 0.05 level) are -0.6 between peak 7 (c) and peak 8 (d), 0.2 between peak 5 (a) and peak 6 (b) and -0.2 between peak 6 (b) and peak 7 (c) (Figure F.8).

An example decomposition showing all six coefficient subgroups derived for the example jerk case is shown in Figure F.9 with the observatory style sampling equivalent given in Figure F.10, demonstrating that similar patterns are still recorded with sparser spatial sampling.

Overall the synthetic models imply that any spatial patterns interpreted as characteristic of jerks in observatory data are likely to be representative of the actual patterns, at scales of degree 4 (or $\sim$5,000 km) and greater.

5.2.4 Periodicity of Synthetic Jerks

An alternative way to assess the anticorrelated amplitude patterns in time, as discussed in Section 5.2.3, lies in analysis of jerk amplitude timeseries in a small region over which

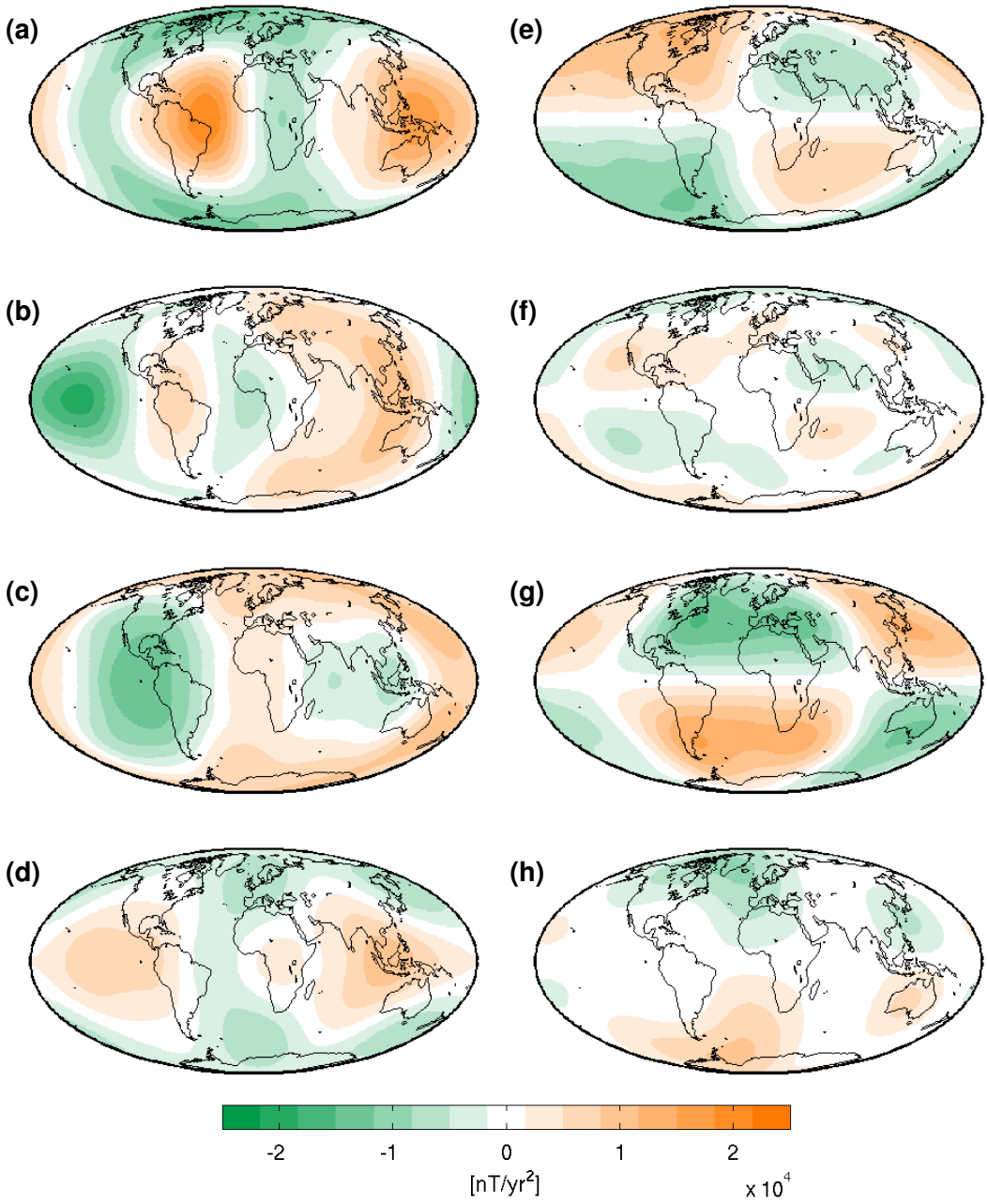

Figure 5.10: Equatorially symmetric ($n+m=$ even) (a–d) and anti-symmetric ($n+m=$ odd) (e–h) parts of jerk potential at Earth's surface for four consecutive synthetic jerks (peaks 5, 6, 7, 8 in Figure 5.4). The general trend of alternating polarity is highlighted by considering only a selection of the Gauss coefficients.

they may be expected to show consistent polarity. This analysis was performed with observatory data from Europe and North America in Chapter 3 with the lack of dense spatial sampling outside of Europe leaving the open question of whether the periodic trends were significant geodynamic tracers or not. While I cannot directly corroborate the interpretations of the observatory data, I can test whether the synthetic data show similar trends. Under the assumption that the synthetic models represent the typical spatial and temporal variations of the Earth's field, I can assess whether it is reasonable to interpret such periodic signals as robust findings or not. Testing whether any detected periodicity in the synthetic jerk amplitudes is consistent across the globe and whether it varies with the sampling density in space or the observed timeseries length may provide insight with which to temper the view of the observatory data analysis. The synthetic jerk amplitudes are found to show similar trends with statistically significant periodic components in a manner similar to the observatory data (Figure 5.11). Before considering interpretation of these periods there are three basic hurdles to clear.

First, are the periods detected unique to a particular synthetic realisation or consistent in all models? The periodic trends are found to be unique to the realisation, confirming that there is no forcing from the build of the models or from the detection and analysis techniques used. This can be viewed as both positive and negative for my investigation. It means that while the analysis imposes no periodicity on the jerk amplitudes and thus implies periodicity in observatory data results is a genuine feature, neither does the model acquire any from the *a priori* information derived from real observations.

Second, are the detected periodicities influenced by the timeseries length used? Comparison of the Lomb periodograms for jerk amplitudes in a given region over timeseries of 50, 75 or 100 yr were compared and found to indicate that for periods longer than approximately 5 yrs, the periodic trends were consistently detected (see Figures F.13–F.11). There is however a trend of reducing power with reducing timeseries length, a factor of decreasing data constraints. Naturally there is an upper limit to the periodic trends that can be detected with reasonable confidence in a given timeseries length (half the series length as a rule of thumb). This leads to the third question.

Third, does the jerk detection window length alter the periods detected? While the periodic trends detected are shown to be unrelated to the detection window length (for example, periods of 12.5, 25 or 50 yrs are not consistently found with a 25 yr detection window), there is some variation of the resolved periods with detection window length. This can also be seen in Figures F.13–F.11. The significant periodic content detected tends

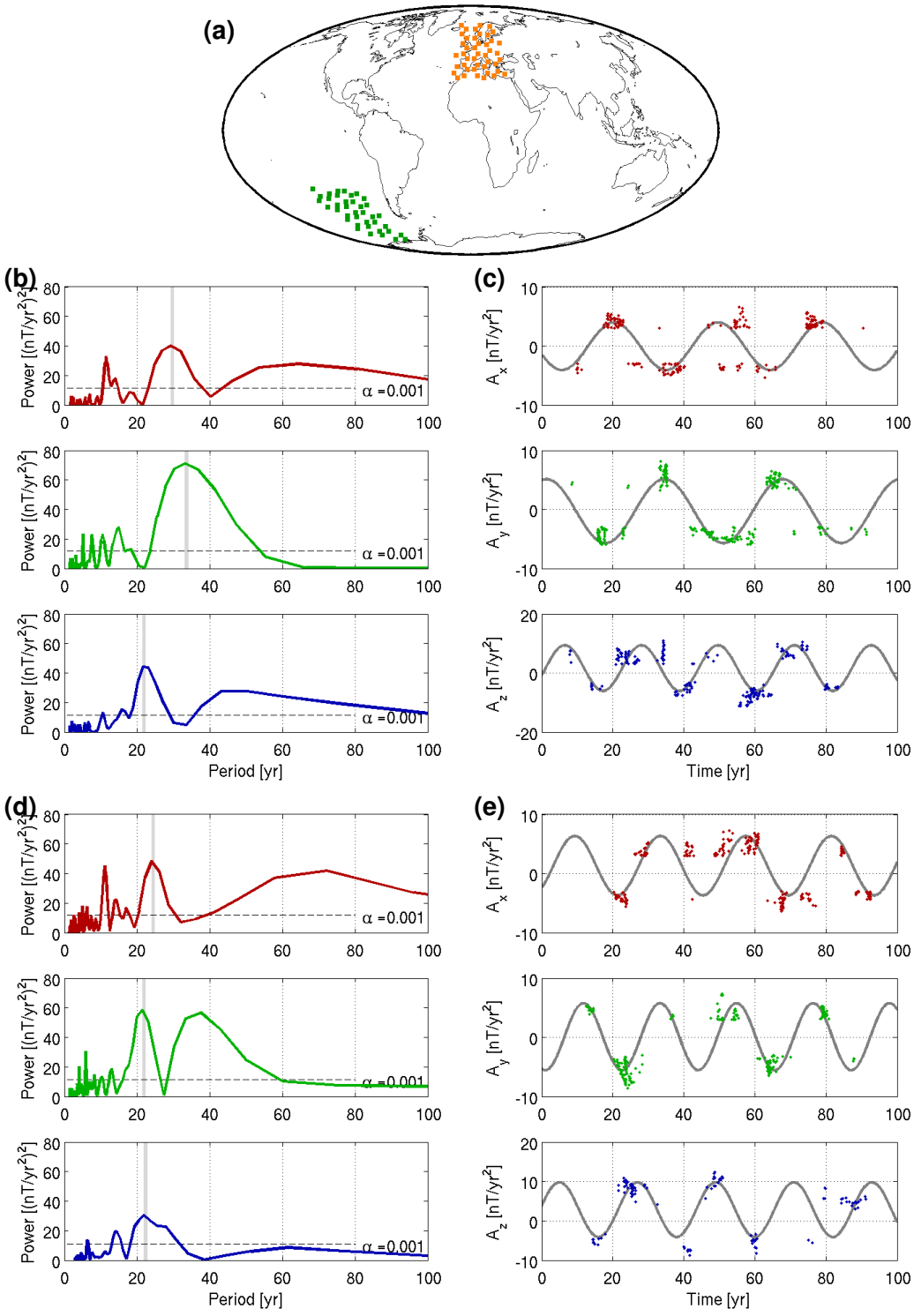

Figure 5.11: Periodicity of synthetic jerk amplitudes detected with a 25 yr window compared between clustered observation points in two discrete regions. Regions are marked on map (a), orange region corresponds to (b,c), green region to (d,e). The normalised Lomb periodogram for jerk amplitudes in each region over 100 yrs is shown for the X- (red), Y- (green) and Z-components (blue) (b,d) while the estimated jerk amplitudes are shown in (c,e), respectively. Best fitting periods (grey) are marked on all plots, α is the statistical significance criteria.

to decrease in power (and therefore significance) as the detection window is decreased in length. For example, the periodic content below 15 yrs in the Y-component for all timeseries lengths are present at all window lengths, but decrease in power from the 25 yr detection window to the 5 yr window (Figures F.13–F.11). Similarly the periodogram peak at ∼30 yrs in the X-component is seen for all timeseries lengths and window lengths but with progressively less power as the detection window length and timeseries length are decreased. The decrease in power with decreasing timeseries length is likely an effect of the timeseries analysis technique.

Having satisfactorily answered the proceeding questions it is deemed that the synthetic models do contain periodic jerk amplitudes, that these do exhibit behaviour much like that of observatory data and that these trends can be resolved reliably by my analysis. I can therefore assess the question of most interest with respect to periodic content of observatory data: does the periodic content of jerk amplitudes vary spatially within each synthetic realisation? This is asked since whether or not this is the case for a model field, behaving in an assumed Earth-like manner, may imply whether or not this is possible for the real Earth. A lack of consistency in periodicities was found between Europe and North American observatory data, but the North American observatories cover a larger area in a more sparse manner so this could simply be a reflection of the difference in spatial sampling.

In Figure 5.11 the periodicity of jerk amplitudes in two regions of the same realisation are compared. No consistency in periodic trends of jerk amplitudes is found between spatial regions when clusters of equal numbers of sample points (equal areas) are considered. This reinforces the view that the synthetic jerk signals are spatially complex and that while periodic content is always seen, it need not be globally consistent, reflecting a SA that varies rapidly to account for the rapid spatial SV changes (that is the small clusters of jerk amplitudes). The synthetic models do not show any spatial pattern in the variations of periodic content of jerk amplitudes for example, dependence on latitude or longitude to suggest the inherent geometry of the magnetic field is an influential factor.

Synthetic jerk amplitudes are seen to display a consistent magnitude range in all field components and are approximately zero mean in a series through time as well as zero mean globally for the duration of the 100 yr synthetic model realisations. There is no tendency for the amplitudes to sum to zero during a jerk histogram peak or sum to zero when successive jerks are considered. It is only over several decades that amplitudes average out to zero. This implies the synthetic SA is zero mean in the long term but very

variable at any given instant to account for the allowed rapid SV changes of jerks. At a single point on the surface, amplitudes do not always alternate polarity with successive jerks and do not consistently wax and wane in amplitude of the same polarity before a polarity change occurs.

Whether the noted synthetic model properties hold true for the geomagnetic field cannot be concluded so easily but I suggest that it is likely given that any signal emanating from the core will be shaped by interaction with a spatially variable MF and potentially by months of transit through a heterogeneously electrically conducting mantle [e.g. Pinheiro and Jackson, 2008]. Indeed the localised nature of jerk signals at the Earth's surface in general may be a result of these influences on a global jerk signal as suggested by Olsen and Mandea [2007]. If the source of jerks is indeed globally distributed but the surface effects are localised, it would suggest that any periodicity detected at the surface is a reflection of the interactions of the jerk signal with the MF and mantle in that region. Variations in the periodicity spatially, as well as the jerk amplitudes, may then provide useful information about the properties involved in the interaction.

5.3 SYNTHETIC VERSUS OBSERVED JERKS AND IMPLICATIONS

The results in the previous section show that the synthetic models do more than simply resemble the statistical properties of observatory timeseries. They contain jerks which fit with the interpretations made in the observatory data study in Chapter 3, namely: that jerks are very frequent but more abundant spatially for some 1–5 yrs spans and less abundant at other times; that high jerk amplitudes are spatially localised, to a greater or lesser degree but never globally observed; that the spatial pattern of jerk amplitudes is not consistent but that a general trend follows amplitude sign variations from negative to positive and back; that this trend of amplitudes is periodic when considered over a small spatial region.

The synthetic models are consistent with our knowledge of the recent temporal and spatial variations of the geomagnetic field. Comparative analyses of synthetic models with dense STT cell or sparse observatory style spatial sampling suggests that observatory distributions are sufficient to capture the large-scale (SH degree 4 and below) features of jerks. For the synthetic models this was a spatial pattern dominated by a SH degree 2 pattern. An obvious next step is to apply the same SH modelling procedure to the real observatory jerk cases which were identified in Chapter 3.

5.3.1 Spherical Harmonic Models of Jerks in Observatory Data

The inversion procedure described in Section 4.4.2 was applied to the peak jerk occurrence intervals identified in Chapter 3: 1968–71; 1973–74; 1977–79; 1983–85; 1989–93; 1995–98; 2002–03. A damping parameter of $\lambda = 1.0 \times 10^{-4}$ was applied as before and will likely play a strong role due to the very low number of spatial data points. The models for the 1968–71 and 2002–03 jerks are displayed in Figures 5.12 and 5.13, equivalent figures for the remaining models can be found in Figures F.14–F.16. The power spectra for each jerk model, at both the Earth's surface and at the CMB, are shown in Figure F.17.

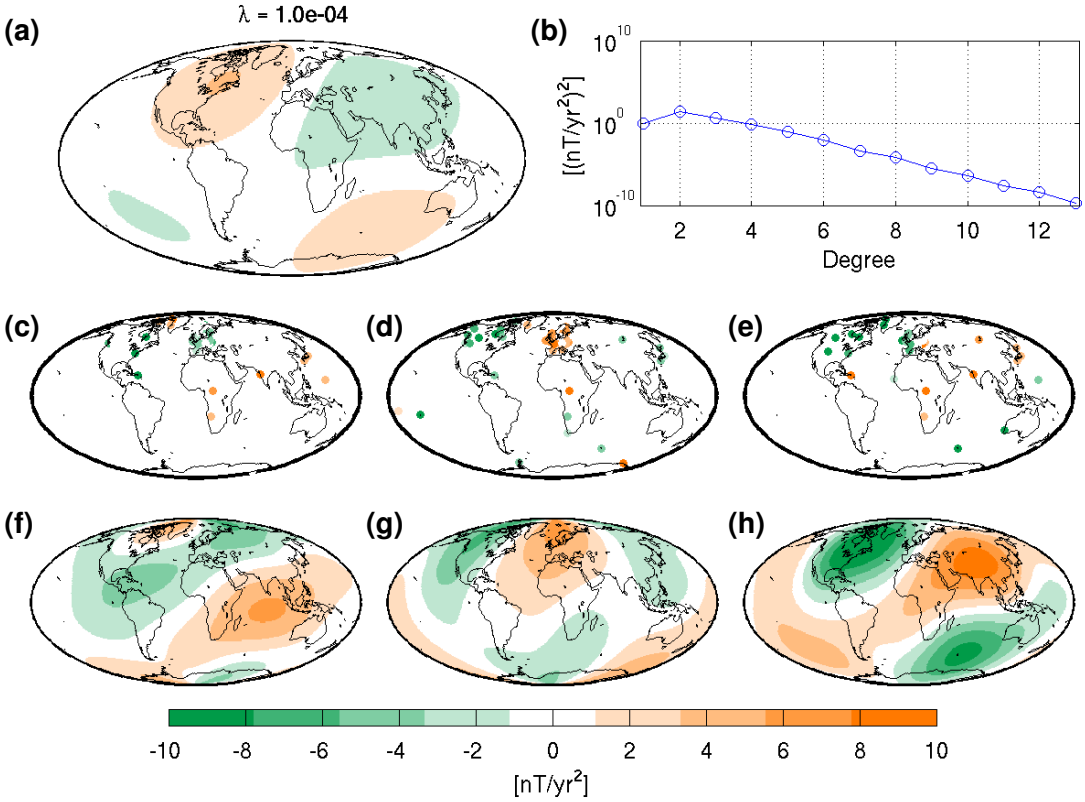

Figure 5.12: SH model of the 1968–71 peak in jerk occurrences detected in observatory data. The potential (a) and its spatial power spectrum (b) are shown with the derived X-, Y- and Z-component models (f,g,h), respectively, and the X-, Y- and Z-component jerk amplitude data being modelled (c,d,e), respectively.

The results of these inversions are varied: those times with more observatories available and more jerks detected such as 1989–93 (Figure F.15) produce spatially complex jerk patterns much like those seen in the synthetic models. Times when the observatory distribution is more sparse produce largely zero amplitude models such as that of 1973–74 (Figure F.14) where jerks are only detected in the Northern Hemisphere. The RMS misfits were found to be as follows: 1.6 nT/yr^2 (1968–71); 0.9 nT/yr^2 (1973–74); 1.3 nT/yr^2

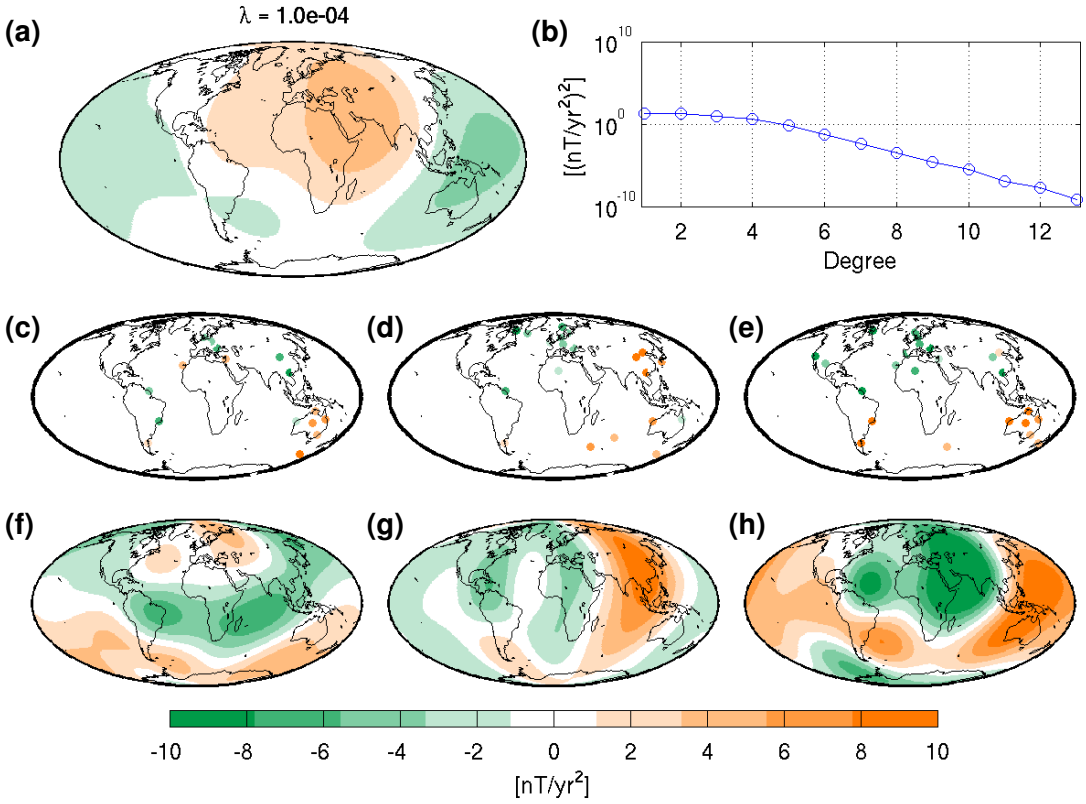

Figure 5.13: SH model of the 2002–03 peak in jerk occurrences detected in observatory data. The potential (a) and its spatial power spectrum (b) are shown with the derived X-, Y- and Z-component models (f,g,h), respectively, and the X-, Y- and Z-component jerk amplitude data being modelled (c,d,e), respectively.

(1977–79); 1.4 nT/yr^2 (1983–85); 2.3 nT/yr^2 (1989–93); 1.9 nT/yr^2 (1995–98); 1.7 nT/yr^2 (2002–03). All RMS error values are within the uncertainty bounds of modelled jerk amplitudes, used as prior data constraints and so the inversion procedure performs well despite the dearth of data.

The SH models can be compared to previous examples of SHA of jerk amplitudes or changes in SA at the time of jerks for the 1968–71, 1977–79, 1989–93 and 2002–03 events. It should be noted that the "jerk amplitudes" modelled here and by Pinheiro et al. [2011] and the "$\Delta\ddot{g}_n^m$" or "$\Delta\ddot{B}$" properties of other authors mentioned below are all a measure of the step change of SA across a jerk and are equivalent.

For 1968–71 my model (Figure 5.12) broadly agrees with the analysis of McLeod [1985], Malin and Hodder [1982], Le Huy et al. [1998] and Pinheiro et al. [2011]. Differences stem primarily from greater spatial constraints in South America with jerks detected in annual mean observatory data that I do not detect in cleaned monthly data in Chapter 2. Amplitude values lie in a similar range for all models with similar corresponding spectral power overall. While Malin and Hodder [1982] suggest that power decreases with degree,

Le Huy et al. [1998] and Pinheiro et al. [2011] find their spectra peak at degree 2, as do my models.

For 1977–79 Le Huy et al. [1998] and Pinheiro et al. [2011] again found degree 2 dominated patterns, with secondary peaks at degree 3 or degree 4, respectively. My model (Figure F.14) shows stronger degree 1 and 2 terms but generally matches the Y- and Z-component features and amplitude ranges over all. The X-components present a greater contrast. This is again due to a lack of South American, but also Southern African jerks not detected in the cleaned monthly data, that Le Huy et al. [1998] and Pinheiro et al. [2011] found in annual observatory means.

For 1989–93 the starkest contrast between my model (Figure F.15) and those of Le Huy et al. [1998], De Michelis et al. [2000] and Pinheiro et al. [2011] is the recurring theme of a lack of constraint over South America. The largely sectoral Y-components are most similar between models in this region and prove a better match than the X- and Z-components. This time Le Huy et al. [1998], De Michelis et al. [2000] and Pinheiro et al. [2011] find strong degree 2, 3 and 4, degree 2 and 3 and degree 1 and 3 components, respectively. My models possess a flat spectrum across degrees 1 to 3 before rapidly losing power at higher degrees. The visual appearance in all cases is similar for the well constrained regions, differences arising from single, spatially isolated observatory results that sway a significant region in the models. This likely explains the large-scale spectral differences although generally all coefficients are relatively small once portions of the SA are being considered.

For 2002–03 comparison can be drawn with models by Olsen and Mandea [2007] which represent the best constrained spatial observations of any jerk event. While they do not publish a spectrum or quote values for all coefficients modelled, Olsen and Mandea [2007] state that the jerk behaviour of the $\ddot{h}_2^2$ coefficient is the most notable, with other degree 1 to 4 terms contributing significantly also, degree 1 contributing the most power overall. For my model (Figure 5.13) degree 1 is also the dominant component, with a strong degree 2 portion also before degree 3 weakens further. The models of Olsen and Mandea [2007], built from dense satellite observations capture far more spatial complexity than my models but nevertheless, the cleaned monthly mean data produce a remarkably similar result. The strong variation in the form of a positive and negative patch in the Z-component over the Indian Ocean can be seen, as can a distinctive degree 2 sectoral pattern in the Y-component. A similar weak positive over Europe in the X-component is found in both models but the lack of resolution over the high latitudes of East Asia in

the observatory data is evident. Although spatial patterns are similar, unlike the previous three cases, my model shows significantly weaker amplitudes ($\sim$5 nT/yr^2 less) than the peaks of the Olsen and Mandea [2007] model. Whether this is a real signal or a result of different modelling techniques is unknown. It is certainly more reasonable to believe high peaks of power in localised regions when dense spatial knowledge of the field is available as in the model of Olsen and Mandea [2007]. Such behaviour is intentionally limited by spatially smoothing of the sparse data in my models to cope with the general lack of spatial coverage.

While there are subtle differences in the spectra of each of the seven jerk periods from observatory data, they all show a general trend of power predominantly in the first four degrees. On the one hand this is unsurprising, the data are sparse and the inversion favours large-scale models. However, given that this behaviour was predicted by the synthetic models when sampling was reduced to the observatory distribution, it is not unreasonable behaviour either. As Figure 5.14 shows the observatory style sampled synthetic models possess a very similar spectrum to the average behaviour of the observed jerks, with the exception of degree 1 which is stronger in the observed jerk models. This similarity suggests that the jerks in the geomagnetic field appear to behave in a similar manner to those in the synthetic models. While a similarity between observatory data and synthetic models built with the same spatial sampling of course does not unequivocally mean the synthetic models are exactly realistic, it does suggest that the behaviour observed with full spatial knowledge of the synthetic models is a good potential candidate for what geomagnetic jerks over the past half century might look like. The synthetics behave in a quantifiably similar manner to the geomagnetic field by the measures used in this work and suggest that jerks, on average, possess a spectrum dominated by degrees $\leq$4 with a preference to degree 2 patterns. The synthetics also suggest that this observation is a robust one, unlikely to be a result simply of the spatial sampling or of the analysis technique used since my results tally well with those of previous authors. It can be speculated that the synthetic models built from dense STT cell spatial sampling are consistent with our knowledge of the geomagnetic field and that the spectrum up to degree 6 is most likely also a robust inference.

On the question of anticorrelated sequences of jerk amplitudes, no convincingly consistent trend was found in the synthetics although some short sequences of jerks were found to show stronger anticorrelations in subgroups of coefficients (see Figures 5.9 and F.8). Anticorrelation of successive jerks has been noted by Golovkov et al. [1989] for 1947,

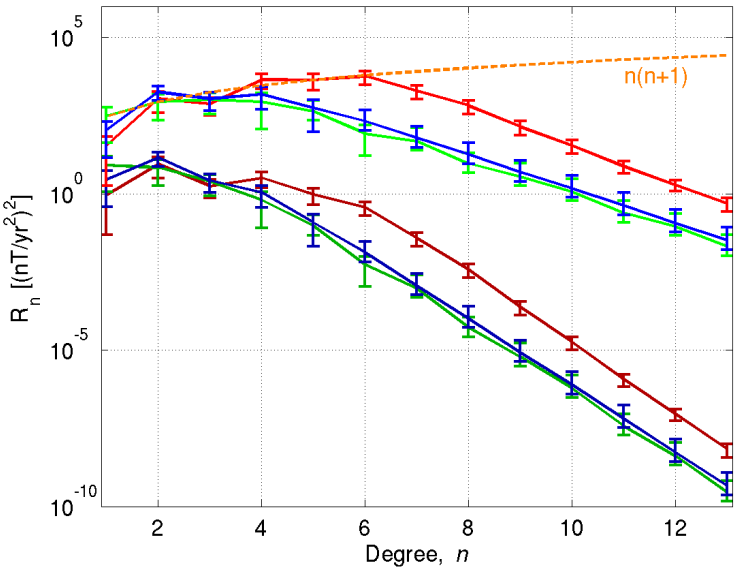

Figure 5.14: Effects of spatial sampling on the spatial power spectrum of synthetic jerks and comparison to observed jerks. Mean results for all STT cell locations (red), observatory style sampling (blue) and observatory data (green) are depicted at the Earth's surface (lower spectra) and at the CMB (upper spectra).

1958, 1969, by Alexandrescu et al. [1996b] for 1969, 1978, by Le Huy et al. [1998] for 1969, 1978, 1991 and by Sabaka et al. [2004] for 1969, 1979, 1992, 1997, 2000. The jerk models described by Sabaka et al. [2004] were consciously omitted from detailed discussion previously as they are derived from *CM4* rather than directly from data. These models are similar in character to those of Le Huy et al. [1998] for jerks in 1969, 1979 and 1991 and also include models for possible jerks in 1997 and 2000. The smooth nature of the regularised internal field model from which the jerk models of Sabaka et al. [2004] are derived differs from the data driven ethos of this study but is interesting for the remarkably clear anticorrelation sequence of jerk models that is produced.

Figure 5.15 illustrates the correlation of models of jerks in observatory data with the equivalent plots for the subgroups of coefficients shown in Figure F.18. It can be seen that there is indeed a case to be made for sequences of anticorrelation of successive jerks although the pattern is less definitive than in the results of Le Huy et al. [1998] or Sabaka et al. [2004] and correlation coefficients do not exceed values of ± 0.6. Results for the best studied events agree with the sign of the correlation but differ in magnitude with correlation coefficients: between 1969 and 1978 found to be -0.9 by Le Huy et al. [1998], -0.49 by Sabaka et al. [2004] and -0.15 here; between 1978 and 1992 (1989–93 by my study) -0.6 by Le Huy et al. [1998], -0.57 by Sabaka et al. [2004] and -0.01

here; and between 1969 and 1992 (1989–93 by my study) 0.7 by Le Huy et al. [1998], 0.18 by Sabaka et al. [2004] and 0.37 here. The discrepancies in magnitude are likely to reflect several differences between the data and analysis in each work. Firstly, each author defines the time of the jerk, and for how long signals prior to and post this time are considered part of the same jerk, differently. Furthermore, Le Huy et al. [1998] derive their models from observatory annual means giving a different spatial constraint and temporal resolution and apply Equation (5.2.1) to poloidal and toroidal coefficients at the CMB rather than the Gauss coefficients for the SA of the potential at the Earth's surface. Sabaka et al. [2004] calculate the correlation coefficients as I do here but from the Gauss coefficients of a smoothed internal field model, *CM4*. Such differences are emphasised by comparing the correlation of the 2000 jerk of Sabaka et al. [2004] and my 1994–98 jerk with each jerk prior to this time. Correlation coefficients are found to be: -0.47 and 0.26 between 1969 and 2000; 0.11 and -0.40 between 1978 and 2000; -0.51 and 0.17 between 1992 (1989–93 by my study) and 2000, for my results and those of Sabaka et al. [2004], respectively. This opposite polarity suggests that the 2000 jerk of Sabaka et al. [2004] is not resolved properly so close to the model end in 2002. Much better agreement is found if the 1997 jerk of Sabaka et al. [2004] is considered to be contemporary to my 1994–98 jerk and the 2000 jerk of Sabaka et al. [2004] is considered to be contemporary to my 2002-03 jerk. This is likely a coincidence stemming from end effects in *CM4* in the latter case since *CM4* only covers the period 1960–2002 so does not contain the later jerk.

The anticorrelation trend is somewhat muddled by combinations of jerks which show no significant correlation at all. Part of this may be down to the generally sparse models and is not notably altered by only considering a SH degree truncated version of the correlation coefficients. I do not find the strong correlation between the 1977–79 jerk and others as noted by Le Huy et al. [1998], finding correlation coefficients that, while successively anticorrelated, are statistically insignificant. I do find the series of all jerks to show successive anticorrelation to the 2002–03 jerk, perhaps helped by the localised nature of this jerk signal. It may be more relevant to design a criteria to assess correlations in a more localised manner rather than globally in light of the conclusion from Chapter 3 that jerks tend to be localised features.

5.3.2 JERKS AT THE CMB

It has been shown here that SH models can be built with jerk amplitude data derived from observatory monthly means and confirmed through synthetic modelling that these models

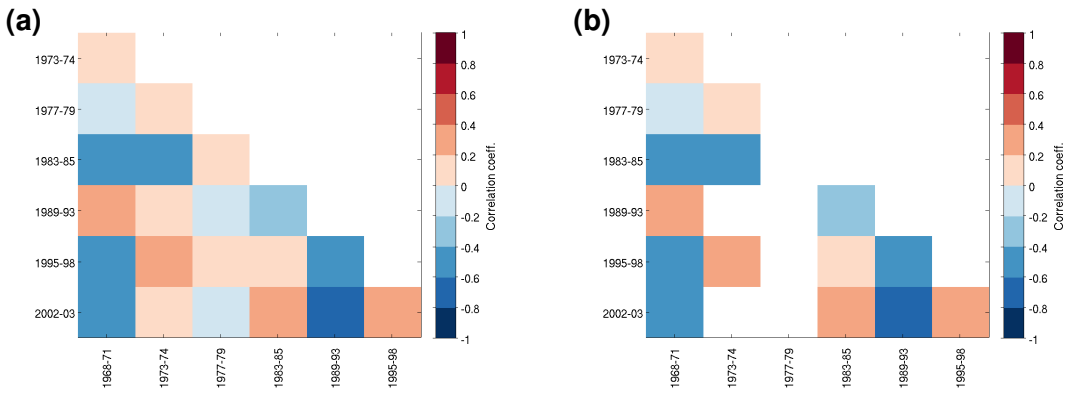

Figure 5.15: Global correlation coefficients [after McLeod, 1985] for the seven jerk histogram peaks in observatory data (a). Only those coefficients judged to be statistically significant at a 0.05 p-value level are shown in (b).

are capable of representing jerks at the largest spatial scales. Bearing in mind the ultimate goal of a better understanding of jerks at their source in the outer core, I ask what these models might represent at the CMB. Knowledge of the geomagnetic field at the CMB is key to understanding the dynamical features that can explain jerks through techniques such as core flow inversion [e.g Shen et al., 2012]. In order to downward continue the jerk signal from the surface where my models are built, to the CMB through the r_E/r factor of Equation (1.5.3), assumptions must be made. First the model must represent a potential field for this equation to be valid, which it has been designed to do and which I have validated as an appropriate assumption in Section 5.2.1. Secondly that the mantle is an electrical insulator, a more debatable assumption. A mantle that is transparent to all magnetic signals that pass through it is a very common assumption in studies of core dynamics [see for example Silva and Hulot, 2012; Wardinski et al., 2008] although it may not be negligible in all situations. Electrical conductivity is believed to be low in the upper mantle, increasing with depth, and for realistic lower mantle ranges of 1–10 S/m is expected to result in transit times of $<$3 months for magnetic signals to reach the Earth's surface [Olsen and Mandea, 2008]. This would likely lead to limited distortion of jerk signals, particularly if the conductivity was laterally homogeneous [Pinheiro and Jackson, 2008] and make assuming an insulator reasonable. However jerk delay times on the order of 1.5 yrs were reported by Pinheiro et al. [2011] and by applying the mantle filter theory of Backus [1983], Pinheiro and Jackson [2008] related such delays to higher and more widespread mantle conductivity, as did Nagao et al. [2003]. Pinheiro et al. [2015] recently re-assessed the applicability of mantle filter theory, discussing the situations in which it

is and is not applicable, concluding that its assumptions hold for many jerk cases. Jault [2015], for example, question the applicability of the mantle filter theory of Backus [1983], arguing that the electrical conductivity structure of the mantle may effect magnetic signals in a different manner and that the screening properties of the mantle may be overstated.

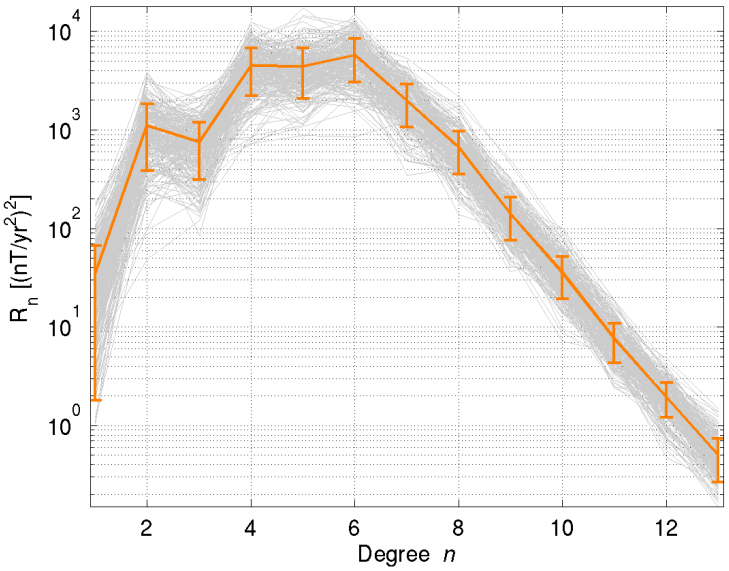

Figure 5.16: Spectra at CMB of all synthetic jerks (grey) at full STT cell sampling as defined by peaks in histograms of jerk occurrences overlaid with mean spectra with error bars of one standard deviation (orange).

I will consider the models built at the surface to be directly related to the jerk signal at the CMB and will downward continue both the synthetic jerk models and the models built from observatory data. A comparison of the mean spectra in these two cases and for the case of synthetic models derived from observatory style sampling is depicted in Figure 5.14. A more detailed view of the spectra of the 254 synthetic jerk models that contributed to this mean is depicted in Figure 5.16. The most obvious differences from the spectrum at the surface are that there is more power with reduced distance to the source and that the shape has altered. Now the spectrum peaks at SH degrees 4 to 6 with a smaller peak at degree 2. As at the Earth's surface, the degree 1 contribution is the smallest of the low degrees, but the most variable from model to model. The models of observatory data are similar to the synthetic results, particularly for the observatory style sampled models, with power increasing from degree 1 to a relatively flat trend between degrees 2 and 4 before a steep drop off. The mean synthetic spectrum at the CMB for degrees 1 to 6 is found to be well fit by a trend of $n(n+1)$ as described by Voorhies [2004] and Holme et al. [2011] which correspondingly fits the observatory model spectrum within

tolerance for the first four degrees. This trend can be seen plotted in Figure 5.14 as fit to the first six degrees via the same parameter modelling procedure as the temporal spectra in Section 4.3.1. Beyond degree 6 at the surface, the spectrum of the synthetic models is not resolved (the spatial regularisation dominates), therefore the rapid decrease in power seen from degree 6 at the CMB and the resultant misfit to the $n(n+1)$ law is attributed to this. According to Voorhies [2004] such a spectral trend may be related to partially resolved eddies in the core surface flow $<$90 km below the CMB generating the SV and may also be an indicator of laterally heterogeneous electrical conductivity in the lowermost mantle.

The models of observatory data continued to the CMB can be compared to similar efforts by other authors. Le Huy et al. [1998] gave the spectra of their models at the CMB up to SH degree 4 for the 1969, 1978 and 1991 jerks. They found that power is enhanced for lower degrees relative to at the surface, as is seen in my synthetic and observatory based results. Peaks were found at degrees 2 and 4 for 1969, degrees 4 and 3 for 1978 and degrees 2 and 3 for 1991. These trends, and the magnitude of the coefficients Le Huy et al. [1998] calculated, agree well with my results. Ballani et al. [2010] reported a degree 2, order 1 pattern for the 1991 jerk, which again tallies with the results presented here.

With these models, key questions are: what do observations of jerks tell us about the geomagnetic field at the CMB, and how might the dynamics of the core reflect this behaviour. One point to be wary of is that when inverting magnetic field observation for core flow, only the radial component ($-$Z-component) is considered to penetrate the boundary and therefore trace the flow. I have found that the uncertainties on Z-component jerk amplitudes tend to be larger in absolute terms than in either of the horizontal components, reflecting the greater amplitudes in the Z-component generally. Another potential concern is the limit to which my models resolve the SA. Works such as Gillet et al. [2009] have shown that large-scale ($n \leq$10) flow in the core can explain much of the signal of jerks but not all of this is contributed by the large-scale field. As Silva and Hulot [2012] for example discuss in their study of the dynamics of the 2003 jerk, there will be contributions to the large-scale flow by small scale fields. While the models of observatory data do provide constraints on the large-scale field, they cannot improve on the small scale resolution of existing field models, and certainly not that of models built from satellite data. This is an aspect where the synthetic models could improve the existing knowledge, by providing small scale field information that I have shown describes the behaviour of geomagnetic

observations to the best of our knowledge. A study of the flows which are compatible with jerk instances in the synthetic models would be beneficial.

Recent studies concerning the field behaviour at the CMB during jerks have suggested that the SA spectra of the first 6 to 8 degrees behave in a pulse-like manner through time, with jerks related to the peaks in this trend [Chulliat and Maus, 2014; Chulliat et al., 2010; Olsen et al., 2014]. The study of satellite measurements developed through Chulliat et al. [2010] and Chulliat and Maus [2014] suggests that large-scale SA pulses seen in degrees 5 and 6 at the CMB or degrees 2 and 3 at the Earth's surface are responsible for the 2003, 2007 and a possible 2011 jerk. These pulses are seen to be localised and anticorrelated in time forming a standing wave with a period of 6 yrs. In the analysis of the *CHAOS-4* model by Olsen et al. [2014], similar smooth, large-scale pulses are observed. While the spectral content at both the CMB and Earth's surface documented in these works and the timings of the 2003 jerk (the 2007 and 2011 jerks are not studied here) correspond well to the analysis and implications in this thesis, there is one fundamental difference.

The SA of *CHAOS-4* and the SA model constructed by Chulliat and Maus [2014] although not spatially regularised still have some temporal constraints. Olsen et al. [2014] used order 6 B-splines to regularise time variations, while Chulliat and Maus [2014] expand their time variations as a 2^{nd} order Taylor series of the MF, SV and SA coefficients and then smooth the SA with a 3 year running mean. Although both models make efforts to minimise regularisation, the time variations produced are much smoother than those of the synthetic models. The mean SA that provides the smooth pulses of power in time and correlates to jerk times cannot be reproduced with the synthetic models of this thesis. The instantaneous SA of the synthetic models is not constrained and acts as a discontinuous process to allow the SV to make rapid changes. Even when smoothed with running averages in the same manner as Chulliat and Maus [2014], no correlation can be found between the jerk histograms and the SA power series in time summed over the first 6 SH degrees. If the synthetic model SA is visualised at any given instance during a peak in the jerk detection histograms, or otherwise, it does not bear a resemblance to the portion of SA modelled from the jerk amplitudes. Neither is there a resemblance to the mean SA through the time window of the jerk. The jerk amplitude maps are found to show greatest resemblance to ΔSA, that is the difference in SA before and after the discontinuity of a jerk, a time window I define by the width of the peak in the jerk detection histogram. An example of this comparison is shown in Figure 5.17 with corresponding spatial spectra

shown in Figure 5.18. The agreement between the X- and Z-components of ΔSA and the jerk model is obvious while the Y-component shows more variation (e.g. compare at central longitudes in Figure 5.17g, g'). Despite this the spectra, plotted together in Figure 5.18 show a very similar trend for the first 5 SH degrees, degree 6 being relatively more powerful in the jerk spectrum. The jerk spectrum is found to be roughly one third of the magnitude of the ΔSA and becomes increasingly weak once the spatial regularisation begins to dominate past degree 6. The difference at higher degrees also hints at the reason for the magnitude difference at low degrees — the more linear parts of the SV are more harshly treated as zero SA by the jerk detection algorithm and the inversion method further leaks energy by smearing the intense localised jerk patches to fit a larger scale field. The jerk detection and modelling essentially highlights the peak amplitudes of the ΔSA and masks the weaker parts but otherwise, the two spectra show similar behaviour.

A timeseries of ΔSA summed over SH degrees 1 to 6 at the CMB [as in Chulliat and Maus, 2014; Olsen et al., 2014] can be compared to histograms of jerk detection numbers for the synthetic models, this is shown in Figure 5.19. This aims to determine whether SA pulses are seen at times of jerks in the synthetic models which do not have a forced large spatial scale SA or smooth temporal constraints. A value of Δ=3 yrs was chosen to represent the average width of jerk histogram peaks. As Figure 5.19 shows there is no consistent correlation between high ΔSA and high numbers of jerk occurrences. While the two peaks in jerk occurrences around 64 yrs and 75 yrs correspond to high ΔSA, those at 53 yrs and 57 yrs correspond to low ΔSA. When instantaneous SA spectra, temporal mean SA spectra or ΔSA spectra are compared between the times of numerous jerks and few, no consistent difference is found. All show that the same general spectral behaviour occurs throughout the synthetic models. It was found for the case of the synthetic models that varying the time difference used in ΔSA had a profound effect on the timeseries of spectral power in the lower degrees. This indicates that the instantaneous SA is, as was already shown, highly variable on short timescales to account for the rapid SV changes. No temporal smoothing was found to produce a correlation with jerk times for the examples studied.

5.3.3 Implications of Jerk Analyses

Having come from a synthetic study some of the information in this chapter cannot inform directly of the way the geomagnetic field operates but by combining and comparing the synthetic and observation based analysis, insights can be gained. I can suggest that

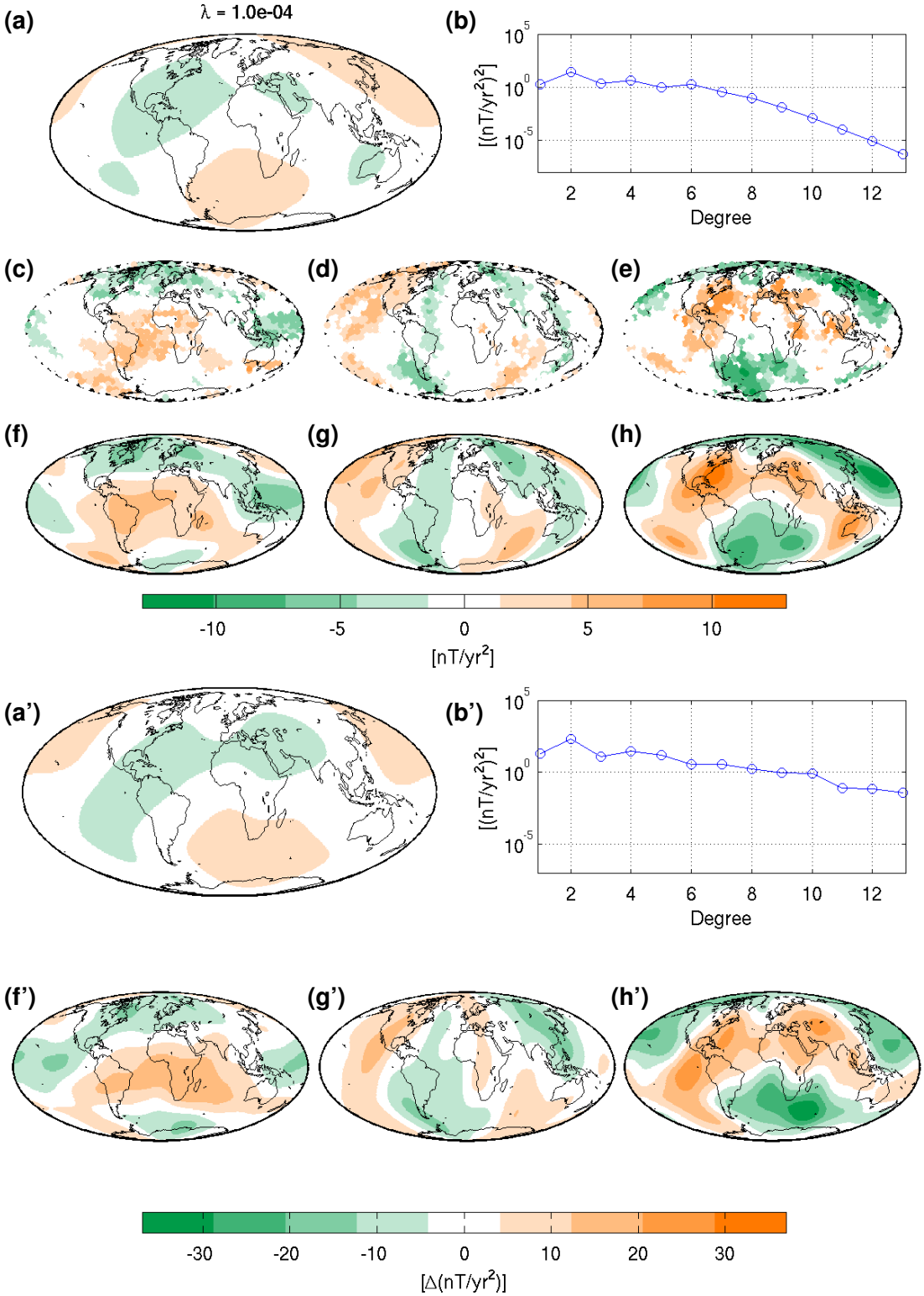

Figure 5.17: Example of synthetic jerk data and SH model at the Earth's surface at full STT cell sampling density and the synthetic ΔSA for the equivalent time window of the model these jerk amplitudes are derived from (peak 7 in Figure 5.4). Depicted are the modelled jerk potential (a), its spectrum (b) and derived X- (f), Y- (g) and Z-components (h) with the detected jerk amplitude data in the X- (c), Y- (d) and Z-components (e). Also shown are the ΔSA potential (a'), its spectrum (b') and its derived X- (f'), Y- (g') and Z-components (h'). Note the change in scales.

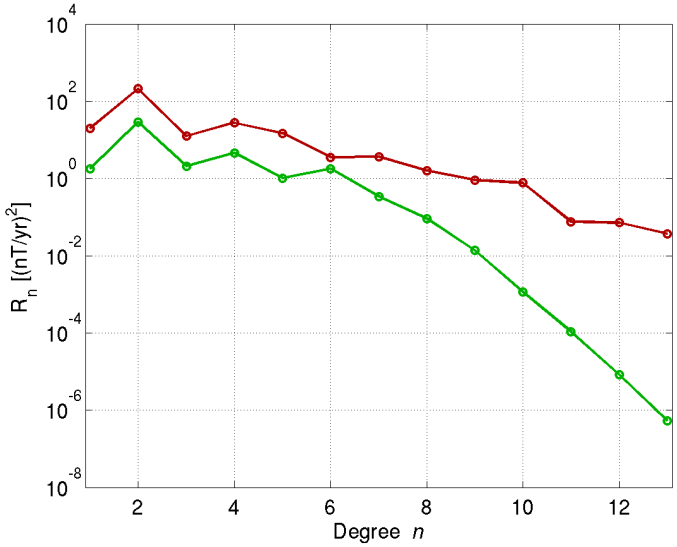

Figure 5.18: Comparison of spectrum of the synthetic ΔSA spectra (red) and jerk model spectrum (green) at the Earth's surface corresponding to the example jerk mapped in Figure 5.17 (peak 7 in Figure 5.4).

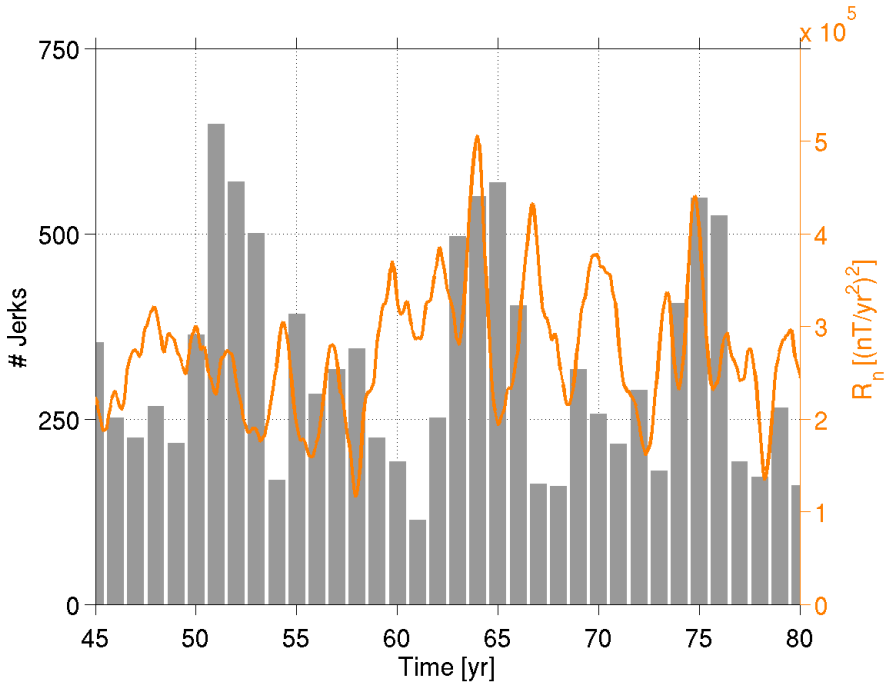

Figure 5.19: Histogram of synthetic jerk detections in all field components with full STT cell sampling and time series of the summation of the first 6 SH degrees of the ΔSA spectrum at the CMB with $\Delta = 3$ yrs (histogram is section of Figure 5.4).

large-scale temporally coherent SA pulses are not a requirement to fit jerk features. The jerks modelled do require a predominantly large-scale ΔSA across a jerk but not so for the SA at any given instance in time or as a mean field over the duration of the jerk occurrence. This touches on two views that have been discussed in recent literature. Gillet et al. [2013] demonstrate with synthetic tests that the choice of temporal and spatial regularisation for a field model and the damping that balances these terms will greatly affect the SA spectrum that is recovered from that model, implying that one should be cautious reading anything from the instantaneous SA, even at large-scales. Chulliat and Maus [2014] on the other hand found that a large-scale coherent SA can be extracted during the satellite observation era even without spatial regularisation, although filtering is applied. Given the analysis of Gillet et al. [2013] however, it must be considered whether it is in fact the temporal regularisation that is forcing large-scale, smooth temporal variations to be found in the SA.

The synthetic models also tell us there is no significant difference between the spectrum of the SA at times of many jerks or few jerks in the synthetic models. Either the SA provides little coherent information at all, which is entirely possible given the design of the synthetic models, or the required field changes for jerk-like SV features are fundamentally no different to the behaviour of the SV at other times. I would suggest that this is true regardless of the model choices here and that jerks in the synthetic models and by inference (and agreeing with my observations in Chapter 3) jerks in observatory data are a continuation of the known spectral behaviour of the geomagnetic field. The only difference between a period with many jerks and one with few jerks is a greater deviation further from the average spectral behaviour of the field. Essentially while SV is considered to be linear between times of jerks, this assumption is only reasonable on certain timescales. As has been shown by varying detection window lengths, zoom temporally closer in or further out and you will observe jerk-like changes of SV on timescales between months and centuries, a continuum of similar behaviour which sometimes (less frequently with larger scale) manifest as large, near globally observed periods of jerks. That is not to say that jerks are unimportant, they still inform us of core dynamics and hint at constraints on these processes, but do not represent the rare unusual phenomena originally suggested by authors such as Courtillot et al. [1978]. In fact I would argue that viewing jerks as ordinary behaviour of the geomagnetic field gives them more importance than as curiosities — any field model or dynamo simulation which does not produce jerks is lacking a known and significant part of the SV.

As for inferring core flow dynamics for periods of jerks, it is clear that $\triangle$SA contains some information analysed here in the form of jerk amplitudes and not the instantaneous SA before and after, or the mean SA across, the time of jerks. This is a similar conclusion to the work of Silva and Hulot [2012] who investigated core flows compatible with the 2003 jerk as seen in the *x-CHAOS* model [Olsen and Mandea, 2008]. It was found that flow acceleration, constrained by the MF, SV and SA and not just the flow constrained by the MF and SV, was required to explain the jerk. Silva and Hulot [2012] found the most appropriate method to estimate this flow acceleration was a joint inversion of the field before and after the jerk, minimising the flow acceleration required to fit the SA change between epochs either side of the jerk. Both the flow and the flow acceleration were assumed to be tangentially geostrophic, the flow acceleration was also assumed to be equatorially symmetric. The 2003 jerk was found to be explained by a predominantly non-zonal flow acceleration change. Initial tests applying this inversion method to the synthetic models (not documented here) suggest that it can provide a suitable way to determine the lower bound of required flow and flow acceleration change at the times of jerks. Additionally, by considering sequential pairs of epochs of the models at a constant time separation, a sliding window inversion can be used to quantify the changes of the flow at times of few jerks and many. This may be a useful tool to apply to, for example, the *COV-OBS* model, with its corresponding SV uncertainty information, to assess what dynamics can explain the jerks in the observatory era and how this compares to the analysis of jerks in satellite data by authors such as Silva and Hulot [2012] and Chulliat and Maus [2014].

JERKS AND LENGTH-OF-DAY

Correlation of jerks to LOD changes can be considered to relate variations in the flow dynamics during and outside of times of jerks. Holme and de Viron [2013] investigated intradecadal LOD associated with core processes and found that a decomposition was possible, into a decadal variation, an oscillation of 5.9 yr period and instances of deviations away from this smooth oscillation which appear correlated with reported jerk times in the period of 1960 to 2010. It was suggested that jerks at the CMB temporarily couple a region of the fluid outer core and electrically conducting mantle as the expression of the expulsion across the boundary of toroidal field, the unobservable internal component of the geomagnetic field. This expelled toroidal flux could then, invoking Taylor-Proudman theorem, excite an axially concentric cylinder of fluid inside the outer core, leading to a measureable amount of angular momentum exchange by the coupling of toroidal zonal

flows to the mantle [see e.g. Jackson et al., 1993]. A comparison of the 5.9 yr oscillation to previously reported jerk times and the findings of this thesis is depicted in Figure 5.20.

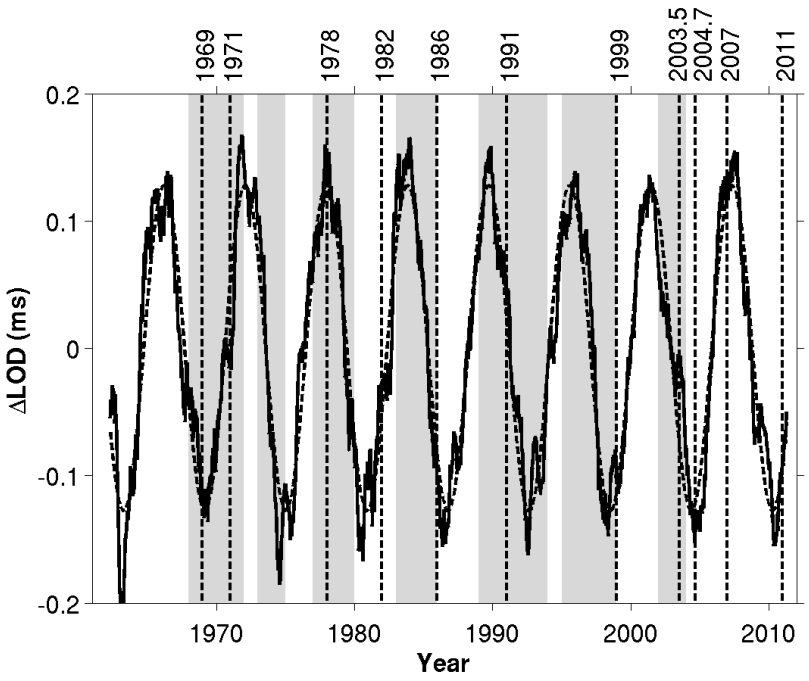

Figure 5.20: Six month running average of LOD data, de-trended on a decadal scale (solid curve), fit with a 5.9 yr period sinusoid (dashed curve) and displayed with marking of jerk occurrence times from other authors (vertical dashed lines, see Table 2.1) and from this thesis (grey boxes). Figure adapted and data from Holme and de Viron [2013].

For the relation between jerks and LOD to be borne out, one would expect the majority of documented jerk instances to correlate to the deviations in LOD. With the few previously reported jerk instances plotted at the mean year of their detection, there is good agreement. When considering the results of this thesis, the patterns considered are more complex and the waters are muddied somewhat. Here it is considered that each of these jerk events is in fact not instantaneous but occurs over a span of several years about the indicated times, and these are merely the periods of most intense jerk activity, there are fewer jerks at other times but still some occurring. The indicated peak jerk periods do still correlate quite well to the LOD deviations but there is not a detected jerk for every deviation and there seems to be little relation to the 5.9 yr oscillation itself. A cross correlation of the all field component histogram of jerks in observatory data (Figure 3.1a) with the timeseries of residual deviations, once the smooth 5.9 yr oscillation is removed, was found to show a correlation (0.24, statistically significant at a 0.01 level) at a lag time of roughly 6 months. It appears that the observations of this work are compatible with the LOD trends of Holme and de Viron [2013] although as always correlation does not imply causation necessarily.

Assuming this causative link is true and following the calculations of Holme and de Viron [2013], the lag time between LOD signals and the proposed responsible jerk signals can be approximated as,

$$T = \mu_0 h G, \tag{5.3.1}$$

where μ_0 is the permeability of free space, h is the height above the CMB of the centre of a thin (thickness $<2h$), electrically conducting layer responsible for the electromagnetic coupling of the core and mantle, and G is the conductance of the layer. Assuming that a conductance of $G = 10 \times 10^8$ S is necessary for significant coupling to occur [Holme and de Viron, 2013], a lag time of 6 months suggests a layer of material up to $\sim$130 km above the CMB is required. Alternately, if particularly non-uniform in structure, the conducting material could be present over a wider, less homogeneous layer closer to the CMB. This implies the opposite conclusion to that of Holme and de Viron [2013] who found a zero lag correlation time between the LOD series and the 1969 and 1978 jerks identified by Alexandrescu et al. [1996b]. This zero lag time suggested that a conducting layer in the mantle was $<$50 km above the CMB and therefore could not be associated with the mineralogical phase transition to post-perovskite occurring higher in the mantle and linked with increased conductivity [Holme and de Viron, 2013]. The lag time of 6 months that I find here suggests that a conducting layer would lie higher in the mantle than the suggested post-perovskite stability zone roughly 100–200 km above the CMB, or 50–300 km above the CMB in cool regions associated with slab subduction [Hernlund et al., 2005]. Since this work does not have the scope (or frankly the space by this point) to further the understanding of the dynamic of the flows responsible for jerks or of the method of coupling between the core and mantle on intradecadal periods, it is difficult to develop on this topic further for now.

A suitable expansion might be to assess the flows compatible with the jerk signals as discussed above and to search for common dynamics at times of jerks that contribute to the toroidal flow and so could transfer angular momentum. If the results of Silva and Hulot [2012] are to be believed, the 2003 jerk required a non-zonal flow primarily but did also demonstrate some zonal motions which could produce LOD changes of the correct magnitude ($\sim$0.1 ms) to tally with the observations of Holme and de Viron [2013]. What effects a proposed stably stratified layer at the top of the outer core [e.g. Buffett, 2014] might have on the situation is another interesting challenge, certainly it would be expected to alter radial motions near the CMB which may impact the effectiveness of flux expulsion.

It would however allow toroidal motions and wave oscillations, torsional oscillations being previously shown to contribute partially to jerk signals [Bloxham et al., 2002]. Early works such as Malin and Hodder [1982] attributed the low SH degree signal associated with jerks (confirmed to be the case in this chapter) with a source deep inside the core and not at the CMB. In recent years, work by for example Bloxham et al. [2002], Olsen and Mandea [2008] and Silva and Hulot [2012] has treated the source of jerks as being located in the core surface flow, at the top of the free stream of motion in the outer core. There is certainly a related signal of intense SA patches at the CMB as the expression of jerks and portions of this can be explained by core surface flows although no convincing mechanism has yet been found. The presence of a stably stratified layer would act to mask deep geomagnetic variations [Buffett, 2014] and would likely be host to, potentially many, types of oscillatory wave motion. This may be further evidence for a shallow source for jerks and an opportunity to further explore generation dynamics.

5.4 ALTERNATIVE SYNTHETIC MODELS

A final point of discussion is required on the topic of the synthetic models and their suitability for geomagnetic studies, regarding the *a priori* mean and variance of the SH degree 1 terms.

The method used in this thesis is that of Gillet et al. [2013], which assumes that all Gauss coefficients in the synthetic model have a mean value of zero and a variance equal to the variance of the coefficients of a satelite field model, per SH degree (hereafter called the variable dipole models). Using *GRIMM-2* at 2005.0, this gave a variance for degree 1 terms of 3×10^8 nT^2. An alternative treatment of the stochastic synthetic modelling procedure in Hellio et al. [2014] assumes that all synthetic model coefficients have a mean of zero except for the dipole term (g_1^0) which has a mean of $-35{,}000$ nT and that variances are taken from a satellite field model except for that of the SH degree 1 terms for which a value of 5×10^6 nT^2 is used (hereafter called the fixed dipole models). This acts to ensure that g_1^0 has an Earth-like magnitude and that g_1^1 and h_1^1 are smaller than g_1^0 with a mean of zero. These parameters were chosen based on findings from models of the past 4000 yrs by Korte and Constable [2011] to represent a steady background MF at these timescales. The period of interest for this thesis has been the observatory era, focussing on the last 50 yrs and so it raises the question of which degree 1 variance and mean g_1^0 value are most appropriate. Given that the satellite models and palaeomagnetic field models represent

end member cases for observational model periods, it is not clear whether my choice of prior information should be tailored to either or should lie somewhere in between. The primary concern here is to gauge what effect this choice may have on my analysis, if any. Additional synthetic models were built following the procedure in Section 4.2 but using the prior information of Hellio et al. [2014] and the jerk detection analysis and SH modelling procedure was then performed for the dense STT cell spatial sampling. The examples and calculation given here are preliminary only, taken across a set of five realisations of synthetic models (except where stated) and assumed to be representative of the general characteristics of a larger set.

A comparison of the mean spatial spectra and the spectral variation with realisation for the fixed and variable synthetic models is shown in Figure 5.21. Predictably the only difference between the two sets of models is in the power and variance of the degree 1 terms, however the impact of the choices for the MF can be seen to filter through to the SV and SA. Naturally the variations in the MF degree 1 terms are reduced in the fixed dipole case compared to the variable case but the mean overall power is equivalent (see degree 1 in Figure 5.21a,b). The wider variation of the power in degree 1 in the variable dipole model case comes from the fact that all degree 1 coefficients can have a large magnitude comparable to that of the g_1^0 term in the fixed dipole case where g_1^0 is likely to be largest. By rotating all variable dipole synthetic model coefficients to an approximately axial dipole orientation, I ensure that g_1^0 is the largest magnitude term and that g_1^1 and h_1^1 are reduced, but this does not account for the possibility that g_1^0 is now allowed to be no ticably larger or smaller than the observed magnitude of g_1^0 in recent satellite field models ($\sim$-29,000 nT). This can be seen in the larger standard deviation of the degree 1 term in Figure 5.21b compared to Figure 5.21a. Hence one can see that fixing the mean g_1^0 value is not the primary concern with respect to synthetic model behaviour, the same mean power can be achieved in either case. Doing so will ensure a similar dipole orientation for all realisations which is desirable if comparisons of spatial patterns are being made, as they were in this chapter, but not essential. Rotating the MF coefficients to a consistent mean orientation has an identical effect. Assigning a larger or smaller magnitude variance will however alter the behaviour of the spectra of individual MF realisations.

More importantly for this work, the alteration of the MF variance will impact on the spectra of the SV and SA as Figure 5.21c,d and Figure 5.21e,f show, respectively. As noted by Hellio et al. [2014], altering the variance of any degree coefficients of the MF does not impact on the variance of the SV coefficients. While the variance of the SV is

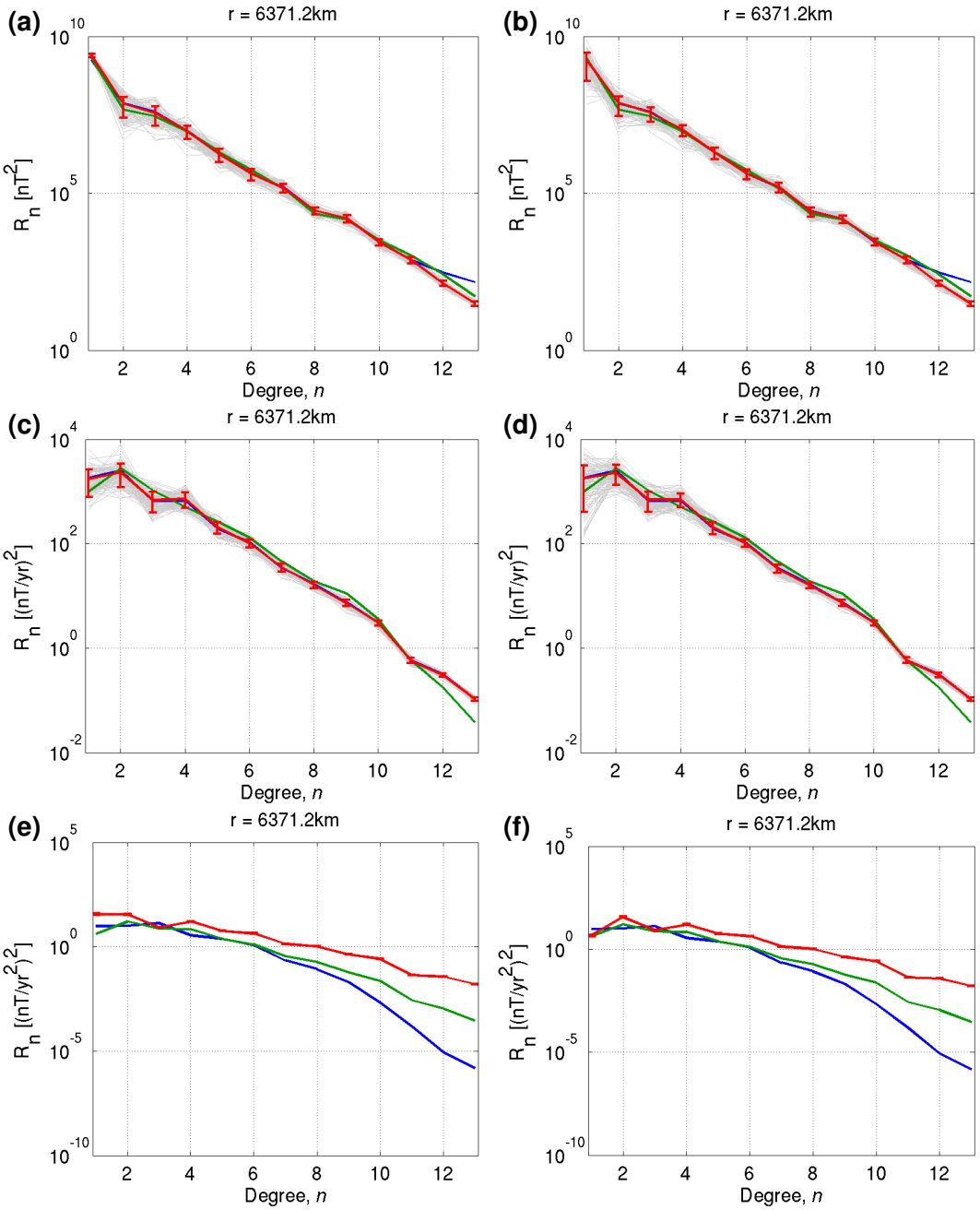

Figure 5.21: Comparison of spatial power spectra for both fixed (a,c,e) and variable (b,d,f) dipole synthetic models. One hundred spectral realisations (grey) and mean spectra with one standard deviation error bars (red) are shown for the MF (a,b), SV (c,d) and SA (e,d). The equivalent spectra of *GRIMM-2* (blue) and *COV-OBS* (green) are shown for reference.

the same in both fixed and variable dipole models (and the SA variances are not directly controlled *a prior*), the correlation time $\tau_c(n)$ for degree 1 given by Equation (4.2.9) will alter depending on the MF variance choice. This is reflected by the decreased variation of degree 1 power between realisations (a wider spread of realisations) in the fixed dipole versus the variable dipole case (Figure 5.21c,d), while the mean power at degree 1 is the same in both cases.

Another gauge of how variable the dipole is in the fixed scenario, the dipole wander over a century can be calculated as before. This calculation was performed for one hundred 100 yr model realisations sampled monthly. An average drift rate of $0.03\pm0.01^\circ$/yr was found: lower than the $0.05\pm0.03^\circ$/yr for the variable dipole models but still greater than the *IGRF-12* value of 0.02°/yr. Again, this is within tolerance of the *IGRF-12* value. Naturally, the tolerance was found to reflect the tighter constraints with little variation from this mean figure compared to the variable dipole case.

The variance assumed in this thesis of $\sigma_g^2(1) = 3\times10^8$ nT^2 leads to a value of $\tau_c(1) = 1800$ yrs while a variance of $\sigma_g^2(1) = 5\times10^6$ nT^2 leads to a value of $\tau_c(1) = 200$ yrs. Hence assuming a lower variance equates to assuming a degree 1 component with a shorter correlation time and a reduced variation of degree 1 in the SV as a result. This also corresponds to an increase in the degree 1 SA power that is unnecessary in the variable dipole case since the SV can accommodate the variable MF. This difference between the synthetic SA spectra is entirely dependent on the *a priori* choice of variances and impacts on the jerk models that result.

In terms of the jerk content of the models, the field component timeseries produced from the fixed dipole models bear a great resemblance to those from the variable dipole models because the formulation of the spectral character is not altered by the change in timescale. The spectral slope of -4 nT^2/yr will always hold for values of $\tau \ll \tau_c$, which with a g_1^0 value of $\tau_c(1) = 200$ yrs in the fixed dipole case, is still longer than the periods being studied. Hence jerks appear as before and can be shown to have similar distributions and properties as in the case of a more variable dipole component. By again creating histograms in time for numbers of jerks detected, peaks of numerous jerk occurrences can be seen. These epochs of intense jerk activity were inverted for a series of SH models, a comparison of model jerk spectra for fixed and variable dipole models is shown in Figure 5.22. Example jerk identification histograms and amplitude maps are given in Figures F.19 and F.20, respectively, and can be compared to the previous result in Figures 5.3 and 5.5 or 5.7. The same inversion parameters were, encouragingly, found to

be appropriate for the fixed dipole model case and so were re-used.

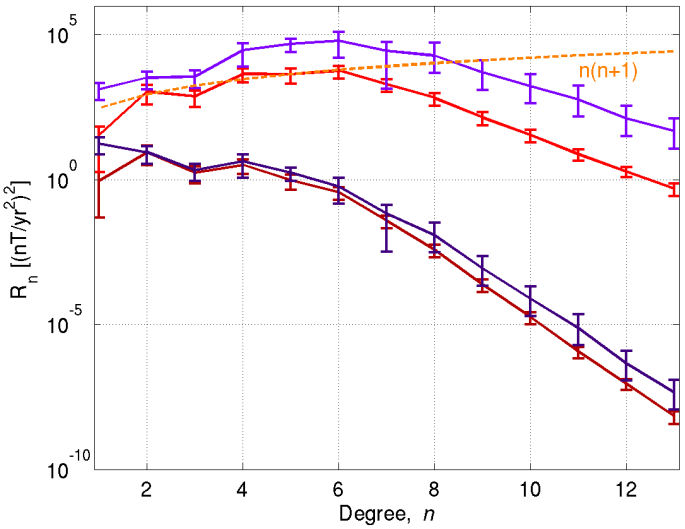

Figure 5.22: Comparison of jerk model spectra at the Earth's surface (lower spectra) and at the CMB (upper spectra) for the variable and fixed dipole synthetic models. Mean spectra are shown for the dense STT cell sampling of jerks in one hundred 100 yr realisation of variable dipole models (red) and five 100 yr fixed dipole model realisations (purple). An $n(n+1)$ law is fit to degrees 1 to 6 of the variable dipole model (orange).

It can be seen in Figure 5.22 that at the Earth's surface, the primary difference is at degree 1 with the fixed dipole models showing greater SA power than the variable dipole models. This is taken to be an indication of the role of the variation of the dipole and the degree 1 SV in the variable dipole case, where a longer timescale and thus greater MF and SV degree 1 power are seen versus the fixed dipole with a shorter timescale and more rapid variations accounted for by SA changes. While there is more power in the fixed dipole models at degrees $>$4 also, these differences may well be a sign that, with so few events analysed, trends may not yet have converged to be representative of the mean model behaviour. This is reflected in the greater error bars for the fixed dipole models, it is likely that were more realisations processed, small uncertainties and a superior agreement at all degrees except degree 1 could be achieved. The differences seen in the surface spectra are similarly evident at the CMB. The increase in power is more noticeable here but the same general trend as the variable dipole case is seen, apart from for degree 1. With the increased degree 1 power in the fixed dipole model, the $n(n+1)$ spectral law fit is improved from the variable dipole case. The interpretation of jerks as able to be represented by a large-scale SH model still holds true for the fixed dipole models. At the Earth's surface, the spectra still peak at degrees 2 and 4 and at the CMB there is a build

up to degree 6 as before. At both radii, degree 3 is notably weaker than the general trend of degrees ≤ 6. An additional strong degree 1 component for jerk fields at the Earth's surface would be a new interpretation however, not in line with the results from variable dipole models.

At this juncture it can be asked, if I find the jerk spectral signature to be dependent on the prior assumptions, is any interpretation made a robust one? Additionally, which prior is more suitable and is there a better choice than either? The agreement for all degrees except degree 1 in both of the synthetic model cases presented here is proof that the coefficients are independent and uncorrelated between degrees but the impact seen from altering a single parameter is marked. The assumption of zero mean coefficient values seems to hold unquestionably well for higher degree components and has been used in this manner by Hulot and Le Mouël [1994], Gillet et al. [2013] and Hellio et al. [2014]. For both sets of models the MF and SV spatial and temporal spectra agree well with our best knowledge of the geomagnetic field in the form of observatory data and satellite field models. It is the SA where differences are observed — unfortunately the component associated with the jerk signal. The SA, as noted by Gillet et al. [2013], is the least well known time derivative of the three, and often at the mercy of the modelling techniques. It can clearly be said that both prior variance assumptions lead to models which resemble the Earth's field in many ways and contain jerks which match our best observational knowledge. The dipole wander in the fixed dipole case is more in line with values from the *IGRF*, but the SA from the variable dipole case agrees more closely with the values given by satellite field models at degree 1. While the satellite field models may be representative of sub-decadal variations, they may not be representative of the past century of SV. The *IGRF-10* model provides a degree 1 variance of $4\times10^5\,\mathrm{nT}^2$ if the spread of coefficient magnitudes at each 5 yr snapshot from 1900 to 2010 are considered. This representation of decadal scale SV provides an even tighter constraint than the fixed dipole case of Hellio et al. [2014] does, corresponding to a correlation time of only $\tau_c(1) = 20$ yrs. This would work to generate even more powerful degree 1 SA, at which point the jerks may no longer be as compatible with the observational result of work such as Le Huy et al. [1998] and those in this chapter. The largest scale spatial variations would be expected to be captured most effectively, even with the sparse observatory network, although an underestimation of the power is possible. Clearly this case highlights the importance and difficulties of modelling assumptions in geophysical research. This sidenote does add an additional inference about jerk behaviour that would not have been obvious from the variable dipole

models alone. It has been seen now for the case of variable dipole synthetic models, fixed dipole synthetic models and observatory data models that the spectra of jerks appears to be a somewhat weaker version of the general trend in the long term SA, best judged in specific jerk cases by ΔSA, the change in instantaneous SA before the jerk to that after the jerk.

5.5 SUMMARY

The work in this chapter set out to answer several questions. Primarily whether the interpretation of jerks in observatory data could be considered robust enough to represent large-scale signals and whether regional jerks were simply a factor of poor spatial sampling. Similarly whether the temporal variations of jerk occurrences were an effect of convenient positioning at the dense observatory networks of Europe or North America and likewise if spatial patterns and trends were simply factors of this setup.

I found the synthetic models described in Chapter 4 to closely imitate the known temporal and spatial properties of the geomagnetic field and have shown in this chapter that these models contain jerks which mimic those in observatory data. I proceeded to combine the ability to vary synthetic model spatial sampling with the jerk analysis techniques of Chapter 2 to attempt to validate the interpretations of real observations.

The fact that stochastic synthetic models can be shown to imitate geomagnetic observations, particularly those of jerks, is of interest in its own right. The stochastic construction implies that the modelled process, here the SV on sub-decadal to centennial timescales, is random in nature. This may contradict the assumption that jerks are coherent large-scale geomagnetic variations that can be related to coherent large-scale variations in the core flow and a predictable and identifiable dynamic in the outer core. Concurrent works such as Buffett et al. [2013] and Buffett et al. [2014] consider the poorly constrained behaviour of the geomagnetic field on palaeomagnetic timescales as a stochastic process; it may be that the entire geomagnetic spectrum of behaviour (and thus geodynamo behaviour) can be considered a stochastic process with jerks as the most rapid observed phenomena and magnetic reversals as the slowest.

Despite the positive view I present for the synthetic models used here, there are of course caveats to their use. The questions of *a priori* choices of Gauss coefficient variances and mean values are found to impact on the resultant models. This has been demonstrated by comparison of models produced after the methods of Gillet et al. [2013]

and Hellio et al. [2014]. The coefficient for which the assumption of a mean value of zero is least likely to be representative at the sub-century timescales of interest is that which describes the dipole, g_1^0. This can be corrected via a post-calculation rotation of the spherical harmonic model. The assumed variances of the Gauss coefficients of a satellite field model also appear to be suitable constraints for all coefficients except possibly the degree 1 terms. Based on comparison of spatial spectra and the dipolar wander rate of the synthetic models to that of the *IGRF*, assuming a higher variance calculated from a satellite model leads to a more variable MF and SV degree 1 component between model realisations. This impacts the SA, leading to a weak degree 1 variation and a similar trend in the spectrum associated with the synthetic jerks. Assuming a lower variance, calculated from the *CALS3k.4* model of Korte and Constable [2011] representing the geomagnetic field over the past 3,000 yrs leads to a more stable MF and SV but a stronger degree 1 SA, with this trend again being reflected in the jerk signal. Both of these assumptions lead to models which strongly resemble known MF and SV of the geomagnetic field and both contain jerk features which match the observed properties of jerks. Observations suggest that jerks have occurred in the past 50 yrs that are best described by a signal with a spectral peak at degree 1, more compatible with the models when a lower variance is assumed and also that jerks with a degree 2 peak have occurred, more compatible with the higher assumed variance models. Both assumptions come from field models, one at short sub-decadal timescales, one at long millennial timescales and both can produce SA signals which resemble jerks. Neither model version clearly represents a more realistic geomagnetic model than the other and both meet our knowledge of jerks equally. This highlights the lack of understanding of both jerks and the SA in general.

Accepting this behaviour I summarise what these synthetic models can tell us about geomagnetic jerks. The observations of jerks as frequently occurring regions of high SA are replicated by the synthetic models suggesting that this disparate and not necessarily globally observed signal is an accurate picture of the signal of jerks at the Earth's surface. This does not require high SA evenly spread across the globe and it can be localised into one main region (and naturally there will also be regions of zero SA between the positive and negative amplitude regions). The signals are highly variable from jerk to jerk and persist for 1–5 yrs. The ΔSA across this period can be convincingly fit by a potential field suggesting that jerk models should always be considered in all field components, even though the rapid SV changes will almost certainly not be present in all components simultaneously. Despite the appearance of jerks as regional patches of SA, this potential

field model has most power at SH degree 4 and below, implying a large-scale signal underlies the small scale variations, to some extent this is to be expected for signals that must travel from the CMB. One possible implication of this is that jerks are a large-scale phenomenon at the CMB and the detailed spatial variations seen at the surface reflect the complexity of the source and/or the electrical properties of the mantle and crust that this signal must pass through. On average, a strong degree 2 and 4 component are seen with the possibility of a degree 1 component being present although this was found to depend on the model assumption. Synthetic signals that therefore appear to fit the observational criteria do not appear to be affected by the spatial sampling of the observatory distribution, other than reducing the maximum degree to which the signal can be resolved. This is a promising result for considering future comparisons of jerks in the satellite era to those of the past century.

This result can be extended further to provide a possible view of jerks at the CMB. Here I find that the models, regardless of the prior coefficient variance assumptions can be fit by an $n(n+1)$ law, for the degrees which are resolved (degrees 1 to 4 with observatory sampling). As Voorhies [2004] states, this may represent partially resolved eddies in the core surface flow generating the SV associated with jerks and may also be an indicator of lateral variations of lower mantle electrical conductivity. This would imply that jerks are indeed generated by core surface flows, as their short time scale also points to, and do not stem from deep within the core as suggested by Malin and Hodder [1982] and would agree with the random nature of a source which can be modelled stochastically.

Considering the relation of jerks and LOD changes as two observable effects of outer core motions; a cross correlation of the residuals to a 5.9 yr ΔLOD oscillation [Holme and de Viron, 2013] with the histogram of jerks detected in observatory data suggests a strong positive correlation with a lag time of 6 months. If jerks are indeed the magnetic signature of intradecadal LOD variations caused by electromagnetic coupling between the core and mantle, this lag time is compatible with a homogeneous layer of enhanced electrically conducting material below $\sim$130 km above the CMB. This may be related the presence of significant amounts of post-perovskite and related to observed seismic discontinuities [e.g. Hernlund et al., 2005].

It has been suggested that jerks are magnetic manifestations of wave motion in the outer core [e.g. Bloxham et al., 2002], possible in a stably stratifed layer below the CMB [Buffett, 2014]. In Chapter 3 I associated these ideas with observations that suggested jerks detected in Europe showed periodic amplitude variations. These periodicities varied

by field component with different periodicities seen over North America. The synthetic models show similar behaviour indicating that such spatial variations in periodicity are described by the temporal and spatial spectra of the geomagnetic field and are likely not a factor of data sampling. Indeed these trends are believed to be real but a complex pattern and not a single periodic trend that can be linked to a single example of a wave motion. On this note the periods of observations in one region (i.e. Europe) should not be taken to be representative of the entire globe, all regions should be considered where possible. Nevertheless further investigation into these signals is encouraged, particularly in light of recent developments in the study of torsional oscillations and magnetic-Archimedes-Coriolis (MAC) waves. The complex patterns and frequent occurrences of jerks may represent a complex mixture of wave signals reverberating throughout the outer core resulting in intense regions of core-surface flow variations. Such a source may be more easily modelled as a stochastic process while the dynamics are not known. Investigating whether it is possible to achieve such rapid SV though either single or combined wave generation forward models and whether these signals are global or localised would be a logical subject for future research. It may be the case that it is the interaction with a spatially variable MF [Olsen and Mandea, 2007] and/or several months transit through an electrically conducting mantle [Pinheiro and Jackson, 2008; Pinheiro et al., 2015] that can make a regular wave source appear to be a more complex signal at the surface, both temporally and spatially.

Despite the arguments for stable stratification at the top of the outer core, jerks have been related to local maxima of mean dynamic pressure at the CMB when tangentially geostrophic flows are assumed [Olsen and Mandea, 2008; Silva and Hulot, 2012]. This implies that up- and down-welling motion is present. The ability to build synthetic models to test the flow dynamics compatible with a wider array of jerk features than is possible with limited satellite based observations could be a key tool to investigate these possibilities further. If vertical motions or horizontal flows in a stable layer can be shown to best explain jerks in the synthetic models it may reinforce equivalent interpretations made from real observations.

CHAPTER 6

CONCLUSIONS

6.1 OVERVIEW

The broad aim of this thesis has been to further knowledge of the rapid SV changes known as geomagnetic jerks. This has been achieved through the analysis of half a century of global observatory data and comparison of this data to stochastic synthetic field models designed to imitate them. Having presented this work in detail in the preceding chapters, I now briefly summarise the main results and implications, in Section 6.2, followed by discussion of outstanding questions that remain and possible avenues of future research to tackle these, in Section 6.3.

6.2 SUMMARY

6.2.1 JERKS IN OBSERVATORY DATA, 1957–2008

In Chapter 2, to address the aim of cataloguing observations of jerks and quantifying their properties, I propose that three aspects are key to studying jerks:

1. Use of monthly observatory data in order to resolve such rapid SV features, rather than annual data or field models which introduce a greater temporal smoothing of jerks. In order to best assess occurrence times and spatial patterns and extents, all field components should be used rather than just the Y-component. With the higher temporal resolution also comes a relative increase in external field contamination of variations with periods less than 1 yr.

2. Removal of external noise to improve the signal to noise ratio of the internal field. This is achieved by focussing on one of the most significant components, the external field aligned in a North-South direction, associated with the equatorial ring current in the magnetosphere, using the technique of Wardinski and Holme [2011]. This method leads to reduced SV standard deviations and a more accurate representation of the core field, increasing the accuracy of jerk identification.

3. A jerk detection method which considers entire timeseries so as to avoid data selection bias, and that can provide quantitative uncertainties. The uncertainty analysis of Pinheiro et al. [2011] is adapted for use with a new algorithm which performs a two-part linear regression of SV in a sliding window, solving for jerk amplitudes at all possible times in the window. The misfit of this simple jerk model to the data is converted to a PDF to indicate the likely occurrence times of jerks within a timeseries and allows jerk time and amplitude uncertainties to be calculated. This method requires minimal prior information about jerk times and properties and allows the robust identification of all features which fit the defined jerk model given basic selection criteria, which can be varied to gauge sensitivity.

This method is applied in Chapter 3. I find that published global and local jerk times do not fully characterise jerks in observatory data between 1957 and 2008. Jerks are found to occur frequently across the globe in all field components but as localised patches of high SA, never observed at more than 30% of the observatories studied in a given year and not globally contemporaneous. Previously reported jerks represent those most isolated in time and of widest spatial extent. Relative peaks are seen in the number of jerk occurrences in 1968–71, 1973–74, 1977–79, 1983–85, 1989–93, 1995–98 and 2002–03. No consistent distributions or patterns in occurrence times, spatially or between field components, are found. This does not favour regular delay times between regions and therefore is suggestive of a complex physical source and/or laterally variable electrical conductivity structure in the mantle. However, without a clear understanding of the physical source of jerks or the effects of a conducting mantle on the jerk signal, further confidence here is not possible. To be consistent with the results here, the source and mantle interaction must be more complex than the simple case discussed by, for example, Pinheiro and Jackson [2008]. Jerk amplitudes at European observatories are shown to display periodic variations. Regularity in the timing and amplitudes of successive jerks suggests that the source mechanism operates in a similarly repetetive manner and suggests oscillatory

wave motion such as torsional oscillations on decadal to sub-decadal timescales [as in e.g. Bloxham et al., 2002]. With the sparse observatory distribution outside of Europe, similar claims cannot confidently be made for other regions of the globe.

6.2.2 Synthetic Field Modelling of Jerks

In order to investigate the spatial resolution of jerks given the distribution of observatories and the validity of the proposed periodic jerk amplitudes, I chose to utilise synthetic field models. In Chapter 4 I describe the synthetic stochastic field modelling technique of Gillet et al. [2013] and how it can be applied here. Such synthetic models are found to imitate observatory data well, possessing a similar temporal spectral slope and spatial spectral trend. Of particular importance to this study, and the primary reason for choosing the synthetic models over existing data based field models, are the rapid SV variations and jerk features which the synthetic models contain. A method for the SHA of estimated jerk amplitudes, from the application of the jerk detection algorithm presented in Chapter 2, is also described. This can be used to assess whether the distribution of observatories is sufficient to resolve the spatial extent of jerk occurrences.

In Chapter 5 I apply the methods described in Chapter 4 and discuss the results with regard to the aims of assessing how representative my observations of jerks are, what the likely characteristics of jerks are, and what implications these results have for the nature of the source of jerks. The synthetic models agree with the observations of jerks as localised patches of high SA which occur frequently in any field component, but are not globally contemporaneous. Brief periods in which large numbers of jerks occur and periods in which few are detected are seen as in observatory data. The intense SA patches are not seen to be evenly distributed and can be localised into a single region of high positive and negative amplitudes (separated by bands of zero SA by necessity) [as with the 2003 jerk in Olsen and Mandea, 2007]. The jerk signals in the synthetic models are found to be best represented by a SH fit of a potential field to the ΔSA across the temporal peaks in jerk occurrences. Comparing full spatial knowledge of the synthetic jerk models to models of the same durations sampled only at observatory locations, and models fit to the observed jerk amplitudes from Chapter 3, suggests that both synthetic jerks and observed jerks are dominated by a large-scale signal. The models show highest power below SH degree 4 with peaks at degrees 2 and 4. This analysis suggests that direct comparison of SH jerk models can be made with confidence between observatory and satellite eras to SH degree 4, and core flow estimates derived from these models could thus also be

resolved to a similar degree. This resolution will likely be reduced prior to 1957.

6.2.3 IMPLICATIONS OF JERK ANALYSES

Downward continuation of the models to the CMB shows that the jerk spatial spectra are compatible with an $n(n+1)$ law [Holme et al., 2011] for the resolved SH degrees. Voorhies [2004] related such a spectrum to products of core-surface flows and possibly an indicator of partially resolved eddies and/or lateral variations of mantle electrical conductivity. The synthetic models confirm that observations of jerk periodicity are likely not a factor of data sampling and that spatially variable periodicities are possible. From this I infer that the European view of these periodicities may not be representative of any global patterns and that this signal is likely from a complex combination of core-surface motions and not a single distinguishable wave period, at least if not in conjunction with a heterogeneous arrangement of mantle electrical conductivity. A view of jerks as a complex superposition of signals at several periods is not new and has been recently been discussed by e.g. Demetrescu and Dobrica [2014]. On the topic of mantle electrical conductivity, a lag time of 6 months is found between a histogram of observed jerk occurrence times and deviations from a 5.9 yr oscillation in ΔLOD. A thin layer of material with enhanced electrical conductivity relative to the rest of the lower mantle, at a height of up to $\sim$130 km above the CMB, is inferred if the relationship holds that the magnetic signals of jerks are the result of outer core motions which couple to the mantle to produce the sub-decadal ΔLOD. It is possible that this thin layer of conductive material is related to the phase transitions to and from post-perovskite but it is also possible to explain the lag time with a more diffuse and expansive layer or more concentrated regions of an unknown, even more highly conductive material. Lateral variations of electrical conductivity seem likely since, while the properties of the lower mantle are poorly known, it is known that large low shear velocity provinces (LLSVP) [e.g. Garnero and McNamara, 2008] and ultra low velocity zones (ULVZ) [e.g. Rost et al., 2005] are present and likely demonstrate at least some component of compositional distinction, likely to include iron. Despite this likely lateral heterogeneity, seismic wave speeds are seen to vary by $<$5% which may indicate a rather small relative variation in properties overall compared to vertical variations.

The fact that stochastic models effectively imitate the SV is suggestive that the causative processes of the geodynamo behave in a random nature. This could be of particular significance when considering estimation of core surface flows from SV, and in works attempting prediction of the geomagnetic field, since the fundamental assumption is made

that the SV reflects a large-scale, coherent flow. It may be the case that the magnetic picture we see is the result of a complex combination of chaotic flow features on a range of scales, the smallest of which are masked from our observations. The stochastic models show that jerks can be effectively modelled by a SA that is random in nature and uncorrelated with SA at other time instances, contrary to suggestions from works such as Chulliat and Maus [2014] that invoke large-scale, coherent SA variations as the underlying jerk signal. Indeed both methods seem to explain the jerk signals, highlighting a lack of understanding that still exists regarding the operation of the core on rapid timescales.

My study suggests that there is a spectrum of geomagnetic behaviour which at the rapid end consists of frequent rearrangements of core fluid, the magnetic signatures of which combine over a period of several months travel through the mantle to produce a complex behaviour at the surface. This is not to say that these events are not still important, jerks can be features in the SA on the order of 15 nT/yr^2; simply put, these are large signals, if a field model or numerical simulation does not represent such features at the appropriate timescales, then it does not accurately describe a known property of the geomagnetic field. The links to independent observables such as sub-decadal LOD, while still unclear themselves in terms of a causative mechanism, reinforce the important role that rapid SV plays as an indicator of behaviour of the Earth system.

The remarkable consistency between jerks in this study and previous published works regarding the magnitude of jerk amplitudes and the spatial scale of the jerk signal, despite great variations in spatial patterns, could be a key point. I suggest that the varying spatial patterns of jerks and localised nature of the signals imply the source of jerks is also localised (although given the effect of downward continuation, still large scale) and variable in the core. The consistency of jerk amplitude magnitudes may signify that the effect of mantle electrical conductivity on magnetic signals and screening by the lithospheric field are similar globally, and act as a threshold; the flow features which produce jerks occurring frequently on a range of scales but only those over a certain spatial scale or magnitude surviving the attenuation and masking to be observed at the surface. This range of behaviour, the demonstrated slope of the temporal spectrum and the fit to an $n(n+1)$ spatial spectrum at the CMB suggest the source may thus be a chaotic regime of turbulent flow in the core, operating on a range of length scales rather than a coherent large-scale feature. Turbulence is associated with chaotic variations of diffusion, convection, pressure and flow velocity, all of which are possible factors in the behaviour of the geodynamo and are not yet fully understood.

6.3 OUTSTANDING QUESTIONS AND FURTHER WORK

There are naturally many questions on the topic of jerks which are unanswered by this thesis and several more which it provokes. This is of course not an exhaustive survey of future directions or open questions, there is plenty more intrigue yet hidden in the understanding of jerks and the workings of the geomagnetic field in general.

6.3.1 IMPROVING JERK DETECTION

Firstly, can we do a better job of identifying instances of jerks — are we tackling the problem in the correct way? As I have discussed there have been numerous techniques applied in previous studies of jerks with varied results. A possible issue is that we have not found the optimal approach to limit subjective assumptions. One currently untested path would be to utilise a full Bayesian approach such as the transdimensional Markov chain Monte Carlo method of Gallagher et al. [2009] and Gallagher et al. [2011]. This method brings the requirement of *a priori* constraints to a bare minimum, gauging tolerances from estimates of noise content and allowing considerable flexibility in the definitions of jerks and inter-jerk characteristics. Such a technique could consider the MF, SV, SA or a simultaneous combination of these data sets as well as definitively addressing the question of contemporaneous jerk occurrences though simultaneous co-estimation of jerks in all observatory series.

6.3.2 EXTERNAL FIELD REMOVAL

Studies of the SV in general could benefit from further improvements in external field removal techniques. The ability to achieve this may be provided in part by the RC-index [Olsen et al., 2014], as noted in Chapter 2. Initial tests (see Appendix B) suggest that for the period of 1998–2008, correction of monthly observatory data with predictions of the RC-index can provide enhanced cleaning of the X-component (closely associated with the orientation of ring current signals) compared to the method of Wardinski and Holme [2011] that I use in this thesis. Larger magnitude corrections to the Y-component and particularly the Z-component are also achieved compared to the Wardinski and Holme [2011] method. Any studies of jerks during the satellite era should certainly consider making such a correction for the external field. The design of a similar method focussing on auroral zone corrections may be of additional benefit but with limited numbers of observatories at high latitudes, the scope of any improvements may also be limited for the observatory era.

Methods which focus on the ability to constrain external signals with satellite constellations such as *Swarm* might be of greatest benefit, particularly at high latitudes. While such methods are in development, a simple improvement to studies of internal SV during the observatory era could be to employ the method of Wardinski and Holme [2011] using the recent *COV-OBS* model, allowing extension of corrections back to 1840.

6.3.3 A Robust Definition for Jerks

It must be noted that perhaps the main unanswered question in jerk studies and reason for discrepancies in published results is the lack of a strict definition of jerks, both in terms of the source and in terms of the magnetic expression seen at (or above) the Earth's surface. Are jerks infrequent, singular global scale events or are they expressions of frequent, ordinary behaviour, and localised? The work in this thesis suggests that the latter is true but a far more strict definition would be to single out a particular core flow dynamic which creates such signals. One approach to this question is to consider inversion of observations for core surface flow both at times of abundant jerks and times of few jerks to distinguish any differences. A possible task could be to consider inversion of the ensemble *COV-OBS* model of Gillet et al. [2013] and its covariance information for core surface flows, focussing on the jerks identified in this thesis. Progress towards a definition could stem from associating a particular flow feature or component with the signals of multiple jerks over a span of decades. Considering jerks in the satellite era and the information they can provide for core flow studies, an improvement on the spatial resolution of jerk studies might be made if the external field reduction procedures for the virtual observatory technique of Olsen and Mandea [2007] can be improved on through the possibilities of the *Swarm* constellation. A benefit of a better understanding of the core flow associated with jerks also extends to an improved view of the link to LOD as estimates can be calculated from a given flow model. If a consistent jerk producing flow dynamic can be found, the relationship can be validated by comparing model predictions to the independent LOD measurements. The flow dynamic problem can also be tackled through forward modelling, as the theoretical knowledge of wave motion in the core develops.

A problem not considered in depth here is an assessment of the distinction between rapid SV fluctuations and geomagnetic jerks as suggested by Mandea and Olsen [2009]. There is no clear evidence in this thesis for a distinct boundary or cut-off scale between two such phenomena but a behaviour dependent on scale is certainly observed. While it may seem obvious to state; shorter period SV changes are observed to occur more

frequently than jerks which separate spans of linear SV several years in length — these two features may not be results of the same process. The jerk detection algorithm I use does not restrict or impose detection of jerks at any time so there is no requirement for more jerks to be identified with a shorter time window than with a longer one. There are far more 5 yr window jerks post-1985 than pre-1985. Whether this represents a shift in SV behaviour or simply that we are able to identify more sub-decadal variations when the SV is generally smaller in magnitude remains to be seen. Partly a differentiation of two phenomena might be linked to the assumption made here of linear SV between jerks. At a certain scale this assumption is true but there may be a limit where an even more rapid step on the geomagnetic spectrum can be resolved. There is evidence in this thesis and elsewhere [e.g. Silva et al., 2012] for periodicity in SV at sub-decadal scales which cannot entirely be explained by jerks and that merits investigation. The quest for a strict definition may be hindered by the possibility that jerks are a result of a combination of processes, each difficult to separate

6.3.4 PROPERTIES OF THE GEOMAGNETIC SPECTRUM

Two other studies have been touched on in this thesis. The first, to reassess the properties of the temporal spectrum of observatory data. The analyses considered in Chapter 4 of Currie [1968], De Santis et al. [2003] and the corresponding assumption of a temporal spectral slope of $-4\,\mathrm{nT}^2/\mathrm{yr}$ by Gillet et al. [2013], on which the synthetic models I use are based, indicate that such a linear trend is likely limited to a particular frequency range. There may be other laws rather than this power law relation which can more accurately fit a greater range of periods, particularly when monthly observatory data are considered. A proviso of this and the reason the previous studies have considered annual rather than monthly means as I have here, is that an effective external noise removal technique is required to be confident that the shorter end of the internal spectrum is considered and not external field contamination. Hence there is also interest in analysing the content of the removed external signal from the application of the Wardinski and Holme [2011] method (and/or other cleaning methods) as this too may contain information which could benefit future parameterisation of external fields for modelling purposes (see Appendix D).

6.3.5 FINER RESOLUTION OF JERK EXTENT

A second prospect, mentioned briefly, would be to study the size and the balance of the spatial extent of jerks between each field component in satellite observations where

uniform global spatial coverage is available. Such an assessment would be simple with a virtual observatory type technique [e.g. Olsen and Mandea, 2007]. The observatory study in Chapter 3 and synthetic study in Chapter 5 cannot attest to whether the spatial extent (numbers of detections for evenly distributed observation sites) of jerks is uniform in all field components or quantify the exact size of each patch of high SA with the large-scale focussed SHA I applied. It may be the case that the spatial extent of jerks is misrepresented in observatory data because spatial regions of jerks in each component are not congruent and the distribution of observatories is spatially biased. If the localised SA jerk patches observed at the Earth's surface are equally distributed between field components through the satellite era, this would suggest the generation mechanism does not favour a particular orientation of operation. If these SA patches are found to be equivalent in size (or in total size between the field components through time) and evenly distributed across the globe, as this thesis suggests for the largest scale parts of the jerk signal, then no specific source region at the CMB is preferred. Both of these factors would be indicative of jerks being the result of a random process as the effectiveness of stochastic modelling and the spectral character of my jerk models suggest.

APPENDIX A

OBSERVATORY DETAILS

Table A.1: Details of *IAGA* and *INTERMAGNET* affiliated geomagnetic observatories from which data between 1957 and 2008 were used in this thesis. All observatories with a minimum of 5 yrs continuous monthly mean data are included, records are split when data gaps >6 months exist and a section number added to the *IAGA* code accordingly.

IAGA	Location	Lat. [°]	Lon. [°]	Alt. [m]	Start	End
AAE1	Addis Ababa	9.04	38.77	2441.0	2001.1	2008.3
ABG1	Alibag	18.64	72.87	7.0	1957.0	2008.3
ABK1	Abisko	68.36	18.82	380.0	1966.0	2008.3
AIA1	Faraday Islands	−65.25	295.74	10.0	1957.2	1985.0
AIA2	Faraday Islands	−65.25	295.74	10.0	1986.4	2008.3
AMS1	Martin de Vivies	−37.80	77.57	48.0	1981.3	2008.3
API1	Apia	−13.82	188.22	4.0	1965.0	1990.0
API2	Apia	−13.82	188.22	4.0	1992.0	2004.9
AQU1	L'Aquila	42.38	13.32	682.0	1960.0	2008.3
ASC1	Ascension Island	−7.95	345.62	177.0	1993.0	2001.0
ASC2	Ascension Island	−7.95	345.62	177.0	2003.0	2008.3
ASP1	Alice Springs	−23.76	133.83	557.0	1992.5	2008.3
BDV1	Budkov	49.08	14.02	496.0	1980.0	2008.3
BEL1	Belsk	51.84	20.79	180.0	1966.0	2008.3
BFE1	Brorfelde	55.63	11.67	80.0	1981.1	2008.3
BLC1	Baker Lake	64.33	263.97	30.0	1957.0	2007.5
BMT1	Beijing Ming Tombs	40.30	116.20	183.0	1996.0	2008.3
BNG1	Bangui	4.33	18.57	395.0	1957.0	2004.0
BOU1	Boulder	40.14	254.77	1682.0	1967.0	1978.3
BOU2	Boulder	40.14	254.77	1682.0	1979.0	2008.3
BOX1	Borok	58.07	38.23	115.0	1980.6	2001.0
BRW1	Barrow	71.30	203.38	12.0	1964.7	2008.3

Continued on next page.

Table A.1 — continued from previous page.

IAGA	Location	Lat. [°]	Lon. [°]	Alt. [m]	Start	End
BSL1	Stennis Space Centre	30.35	270.36	8.0	1987.0	2005.6
CBB1	Cambridge Bay	69.12	254.97	20.0	1972.5	2008.3
CLF1	Chambon-la-Foret	48.03	2.26	145.0	1957.0	2008.3
CMO1	College	64.87	212.14	197.0	1960.0	2008.3
CNB1	Canberra	−35.32	149.36	859.0	1980.0	2008.3
CTA1	Charters Tower	−20.10	146.26	370.0	1990.0	2008.3
CZT1	Port Alfred	−46.43	51.87	155.0	1974.0	2008.3
DLR1	Del Rio	29.49	259.08	355.0	1984.0	2007.5
DOB1	Dombas	62.07	9.12	660.0	1999.0	2006.9
DOU1	Dourbes	50.10	4.60	225.0	1957.5	2008.3
DRV1	Dumont d'Urville	−66.67	140.01	30.0	1962.1	2008.3
EBR1	Ebro	40.82	0.49	46.0	1957.5	1981.0
EBR2	Ebro	40.82	0.49	46.0	1995.0	2008.3
ESK1	Eskdalemuir	55.31	356.79	245.0	1957.0	2008.3
EYR1	Eyrewell	−43.42	172.36	120.0	1979.9	2008.3
FCC1	Fort Churchill	58.79	265.91	15.0	1964.0	2008.3
FRD1	Fredericksburg	38.21	282.63	69.0	1957.0	2008.3
FRN1	Fresno	37.09	240.28	331.0	1983.2	2008.3
FUR1	Furstenfeldbruck	48.17	11.28	572.0	1957.0	2006.0
GDH1	Qegertarsuaq (Godhavn)	69.25	306.47	24.0	1957.0	2006.9
GNA1	Gnangara	−31.78	115.95	60.0	1959.0	1991.0
GNA2	Gnangara	−31.78	115.95	60.0	1992.0	2008.3
GUA1	Guam	13.59	144.87	140.0	1957.5	1964.0
GUA2	Guam	13.59	144.87	140.0	1964.7	1980.3
GUA3	Guam	13.59	144.87	140.0	1981.0	2008.3
GUI1	Guimar	28.32	343.56	868.2	1993.6	2008.3
GWC1	Great Whale River	55.27	282.22	0.0	1965.7	1984.5
GZH1	Guangzhou	23.09	113.34	11.0	1980.0	1998.0
HAD1	Hartland	51.00	355.52	95.0	1957.0	2008.3
HBK1	Hartebeesthoek	−25.88	27.71	1555.0	1972.9	2007.9
HER1	Hermanus	−34.43	19.23	26.0	1957.0	2008.3
HLP1	Hel	54.61	18.82	1.0	1966.0	2008.3
HON1	Honolulu	21.32	202.00	4.0	1957.8	1976.3
HON2	Honolulu	21.32	202.00	4.0	1981.0	2008.3
HRB1	Hurbanovo	47.87	18.19	120.0	1957.0	2008.3
HRN1	Hornsund	77.00	15.55	15.0	1978.8	2008.3
HUA1	Huancavo	−12.05	284.67	3313.0	1979.7	1991.0
HUA2	Huancavo	−12.05	284.67	3313.0	1997.0	2008.3
IQA1	Iqaluit	63.75	291.48	67.0	1995.0	2006.0
IRT1	Irkutsk (Patrony)	52.17	104.45	465.0	1957.8	2008.3
KAK1	Kakioka	36.23	140.19	36.0	1957.0	2008.3
KDU1	Kakadu	−12.69	132.47	14.6	1996.5	2008.3

Continued on next page.

Table A.1 — continued from previous page.

IAGA	Location	Lat. [°]	Lon. [°]	Alt. [m]	Start	End
KNY1	Kanoya	31.42	130.88	107.0	1958.0	2008.3
KOU1	Kourou	5.21	307.27	10.0	1996.0	2008.3
LER1	Lerwick	60.14	358.82	85.0	1957.0	2008.3
LOV1	Lovo	59.34	17.82	25.0	1957.0	1978.0
LOV2	Lovo	59.34	17.82	25.0	1980.0	2004.2
LRM1	Learmonth	−22.22	114.10	4.0	1999.0	2008.3
LVV1	Lvov	49.90	23.75	400.0	1957.5	2002.0
LZH1	Lanzhou	36.09	103.85	1560.0	1997.0	2007.4
MBO1	MBour	14.39	343.04	7.0	1957.0	2008.3
MCQ1	Macquarie Island	−54.50	158.95	8.0	1993.0	2008.3
MEA1	Meanook	54.62	246.65	700.0	1957.0	2008.3
MMB1	Memambetsu	43.91	144.19	42.0	1957.5	2008.3
NAQ1	Narsarsuaq	61.17	314.57	4.0	1980.5	2008.3
NCK1	Nagycenk	47.63	16.72	160.0	1980.0	2008.3
NEW1	Newport	48.27	242.88	770.0	1966.3	2008.3
NGK1	Niemegk	52.07	12.68	78.0	1957.0	2008.3
NUR1	Nurmijarvi	60.51	24.66	105.0	1957.0	2008.3
NVS1	Novosibirsk (Klyuchi)	54.85	83.23	130.0	1967.0	2008.3
OTT1	Ottowa	45.40	284.45	75.0	1968.5	2008.3
PAF1	Port-aux-Francais	−49.35	70.26	15.0	1960.2	2008.3
PBQ1	Post-de-la-Baleine	55.28	282.26	40.0	1984.7	2007.4
PHU1	Phuthuy	21.03	105.96	5.0	1999.1	2008.3
PPT1	Pamatai (Papeete)	−17.57	210.43	357.0	1968.0	2008.3
PST1	Port Stanley	−51.70	302.11	135.0	1994.1	2001.0
QSB1	Qsaybeh	33.87	35.64	525.0	2001.1	2007.8
RES1	Resolute Bay	74.69	265.11	30.0	1957.0	2008.3
RSV1	Rude Skov	55.85	12.45	48.0	1957.0	1980.9
SBA1	Scott Base	−77.85	166.76	16.0	1964.1	2006.0
SIT1	Sitka	57.07	224.67	24.0	1957.0	2008.3
SJG1	San Juan	18.12	293.85	424.0	1957.0	1984.0
SJG2	San Juan	18.12	293.85	424.0	1984.9	2008.3
SOD1	Sodankyla	67.37	26.63	178.0	1957.0	2008.3
SPT1	San Pablo-Toledo	39.55	355.65	922.0	1981.0	2008.3
STJ1	Saint Johns	47.60	307.32	100.0	1968.6	2008.3
SUA1	Surlari	44.68	26.25	84.0	1995.0	2005.4
TAM1	Tamanrasset	22.79	5.53	1373.0	1993.0	2008.3
TAN1	Antananarivo	−18.92	47.55	1375.0	1992.0	2006.0
TEN1	Las Mesas (Tenerife)	28.48	343.74	310.0	1975.0	1992.9
TEO1	Teoloyucan	19.75	260.82	2280.0	1980.0	2000.0
TEO2	Teoloyucan	19.75	260.82	2280.0	2002.6	2008.3
THL1	Tihany	77.48	290.83	57.0	1957.0	2008.3
THY1	Toolangi	46.90	17.90	187.0	1957.0	2008.3

Continued on next page.

Table A.1 — continued from previous page.

IAGA	Location	Lat. [°]	Lon. [°]	Alt. [m]	Start	End
TRO1	Tromso	69.66	18.95	105.0	1966.0	2006.9
TRW1	Trelew	−43.27	294.62	15.0	1998.1	2008.3
TSU1	Tsumeb	−19.20	17.55	1273.0	1964.7	1989.9
TSU2	Tsumeb	−19.20	17.55	1273.0	1992.2	2008.1
TUC1	Tucson	32.17	249.27	946.0	1957.0	1969.1
TUC2	Tucson	32.17	249.27	946.0	1970.2	2008.3
UPS1	Uppsala (Fiby)	59.90	17.35	50.0	2003.0	2008.3
VAL1	Valentia	51.93	349.75	14.0	1961.0	1990.0
VAL2	Valentia	51.93	349.75	14.0	1994.0	2008.3
VIC1	Victoria	48.52	236.58	197.0	1957.5	2008.3
VSS1	Vassouras	−22.40	316.35	457.0	1999.0	2008.3
WNG1	Wingst	53.74	9.07	50.0	1957.0	2004.0
YKC1	Yellowknife	62.48	245.52	198.0	1975.0	2008.3

APPENDIX B

EXTERNAL SIGNAL REMOVAL WITH THE RC-INDEX

The RC-index, initially proposed by [Olsen, 2002] and most recently updated in [Olsen et al., 2014] has been developed as part of the *CHAOS* series of internal field models. The index intends to describe ring current activity, including accounting for night-side, quiet-time variations of the symmetric and asymmetric ring current and is aimed at benefitting field modelling of satellite data. It was developed to address issues of unrepresented asymmetric ring current activity and a questionably stable baseline in the D_{st}-index, as well as allowing much faster production of definitive values [Olsen, 2002].

The RC-index is derived from hourly mean observatory data at up to twenty one locations on the night-side between $\pm 60^{\circ}$ magnetic latitude. First an internal MF model (a preliminary iteration of *CHAOS*) is subtracted from each field component at each observatory location and a crustal field bias removed [Olsen et al., 2014]. The horizontal component is then rotated to geomagnetic coordinates (i.e. X and Y are rotated from geographic North and East to geomagnetic North and East). The geomagnetic North component each hour is then fit with a degree 1 spherical harmonic (SH) expression,

$$\frac{\partial P_1^0}{\partial \theta} = -\sin\theta_{\text{dip}}, \tag{B.0.1}$$

[Olsen, 2002] where P_1^0 is a degree 1 order 0 associated Schmidt semi-normalised associated Legendre function and θ_{dip} is the geomagnetic dipole co-latitude of the observatory. This SH model is decomposed into external and internal induced components using a 1D mantle electrical conductivity model following Olsen et al. [2005]. The amplitude of the

remaining external model expression then provides the RC-index value at that location. Index values are further weighted by their proximity to local midnight (weighted 1), with minimum weightings found closest to the associated dawn and dusk regions.

A comparison of the internal signal enhancement when observatory SV is cleaned with the RC-index and my results of the application of the Wardinski and Holme [2011] method from Chapter 2 is shown in Figures B.1 and B.2. It can be seen that, as expected, the RC-index leads to an improvement in the resolution of internal signal in the X-component of the SV. Figure B.1d shows that at several observatories, the RC-index achieves a greater reduction in the standard deviation of the data compared to the method of Wardinski and Holme [2011] (Figure B.1a). Due to the allowance for partial ring currents in the calculation of the RC-index, some improvement over Wardinski and Holme [2011] is also seen in the Y- and Z-components. The Z-component is the most improved relative to the Wardinski and Holme [2011] method.

The trend of noise level changes with geographic latitude is displayed in Figure B.2. The improvements in the X-components with both techniques can be seen to be greatest at low latitudes, the region most effected by the ring current. The Z-component conversely shows greatest change at high latitudes with both methods. In the Y-component, the difference between the methods is more obvious. While the Wardinski and Holme [2011] correction is approximately equal at all latitudes, the RC-index correction is greatest in equatorial regions. This likely indicates resolution of longitudinal variations in the ring current (partial ring currents). The significance of positive changes to the standard deviation of data timeseries at several observatory locations in all field components with the RC-index correction remains to be investigated.

Future studies of the SV could benefit from application of the RC-index correction, currently this is only possible for the satellite era (1999–(2015)). In theory, provided a suitable internal field model and distribution of hourly mean observatory data can be found, the index could be calculated for a greater historical span.

I would like to acknowledge the work of undergraduate intern Dinko Sindija for whom I supervised a more in depth study comparing my results of the Wardinski and Holme [2011] method from Chapter 2 to those with a set of observations and corresponding RC-index values from Olsen et al. [2014], kindly provided by Nils Olsen. This internship study inspired the comparison in this appendix and the same data set was used however the calculations and results presented here are entirely my own.

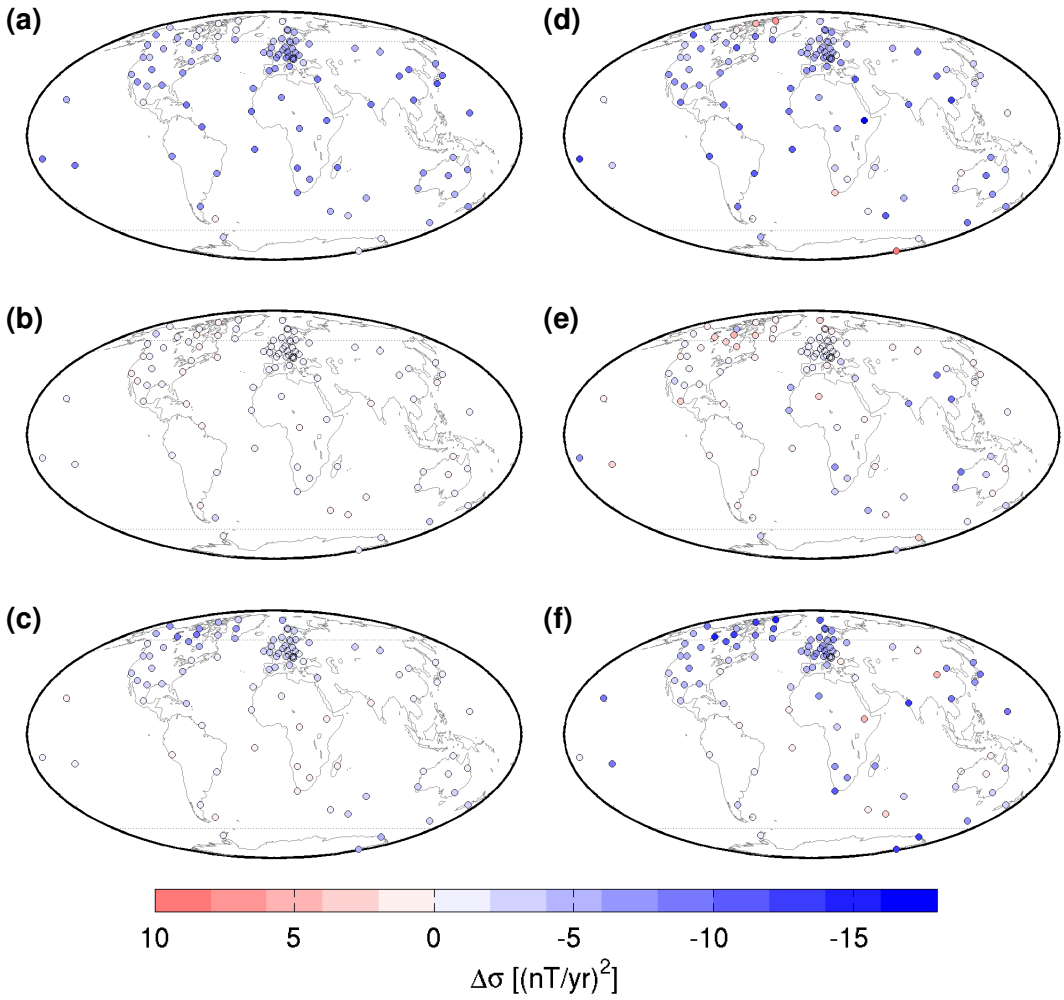

Figure B.1: Comparison of change in standard deviation ($\Delta\sigma$) of observatory SV timeseries with external field correction applied after the method of Wardinski and Holme [2011] (a–c) and using the RC-index of Olsen et al. [2014] (d–f). The change in the X- (a,d), Y- (b,e) and Z-component (c,f) are shown for each observatory between 1998 and 2008. Negative change signifies a smaller standard deviation after cleaning and thus a reduced noise content. Parallels are marked at $\pm 60°$.

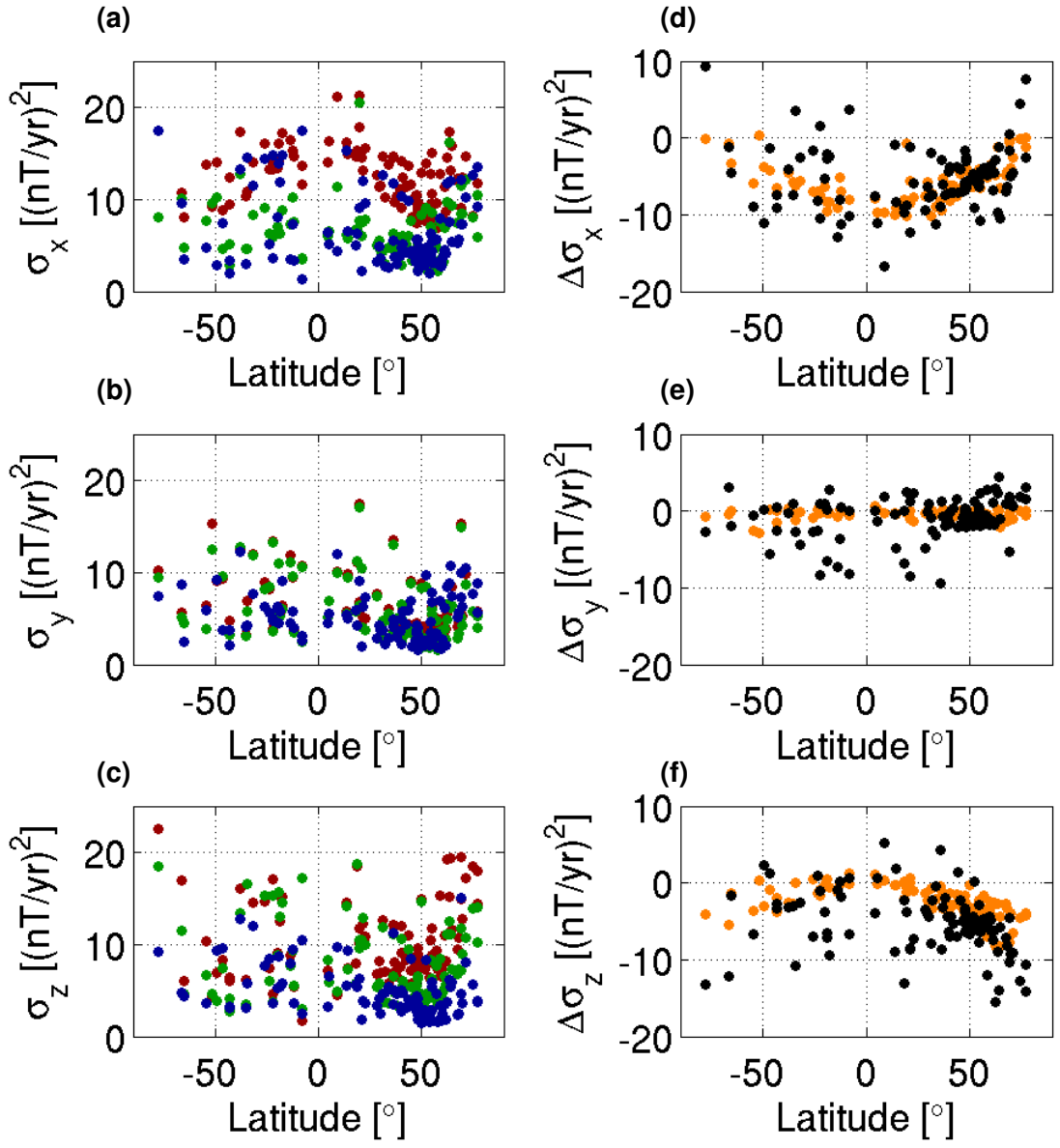

Figure B.2: Comparison of noise levels in observatory timeseries (observatories used in Chapter 2) with application of two external field removal techniques, by latitude of observatory in the X-, Y- and Z-components, from top to bottom. Standard deviations of original observatory data (red), series cleaned after the method of Wardinski and Holme [2011] (green) and cleaned using the RC-index of Olsen et al. [2014] (blue) are displayed (a–c). The change in the standard deviation of the data after the Wardinski and Holme [2011] (orange) and RC-index (black) corrections are made are also displayed (d–f), where negative values indicate a reduction in noise level with cleaning.

APPENDIX C

OBSERVATORY JERK ANALYSIS RESULTS

This appendix contains extra figures, referenced in the text but surplus to the main discussion points of Chapter 3, they are nonetheless informative and necessary for completeness.

Figures C.1–C.3 show jerk occurrence histograms for the results with detection window lengths of 5, 15 and 20 yrs, respectively.

Figures C.4–C.7 display jerk probability and amplitude maps for the 1973–74, 1977–79, 1983–85, and 2002–03 peaks in number of jerk occurrences, using a 10 yr detection window. Figure C.8 again displays maps of the 2002–03 jerk but in this case for the results with a 5 yr detection window to highlight the rapid nature of the 2002–03 jerk. The jerk is well established in the literature, having been the first widely documented in the satellite era, but is poorly resolved so close to the end of the timeseries with detection windows longer than 5 yrs.

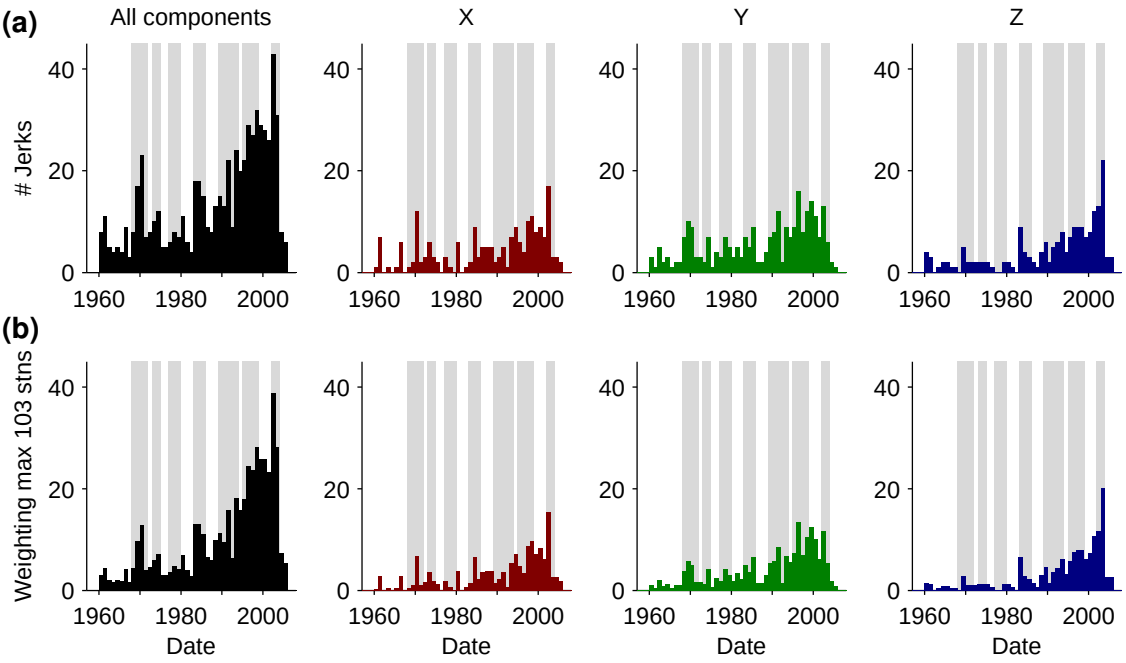

Figure C.1: Histograms of detected jerks in 1 yr time bins between 1957 and 2008, (a) shows straight counts for a 5 yr window, (b) shows 5 yr window counts weighted by the number of operating observatories during any given time bin. Columns represent from left to right: the collation of all components, X-component only, Y-component only, Z-component only. The maximum possible weighting value is indicated by the maximum number of observatories (stns) on the y-axis label; this maximum represents a jerk detected at every observatory. Detections at all observatories worldwide are included, grey bands indicate times of peaks in combined histogram for all window lengths. From Brown et al. [2013] supplement.

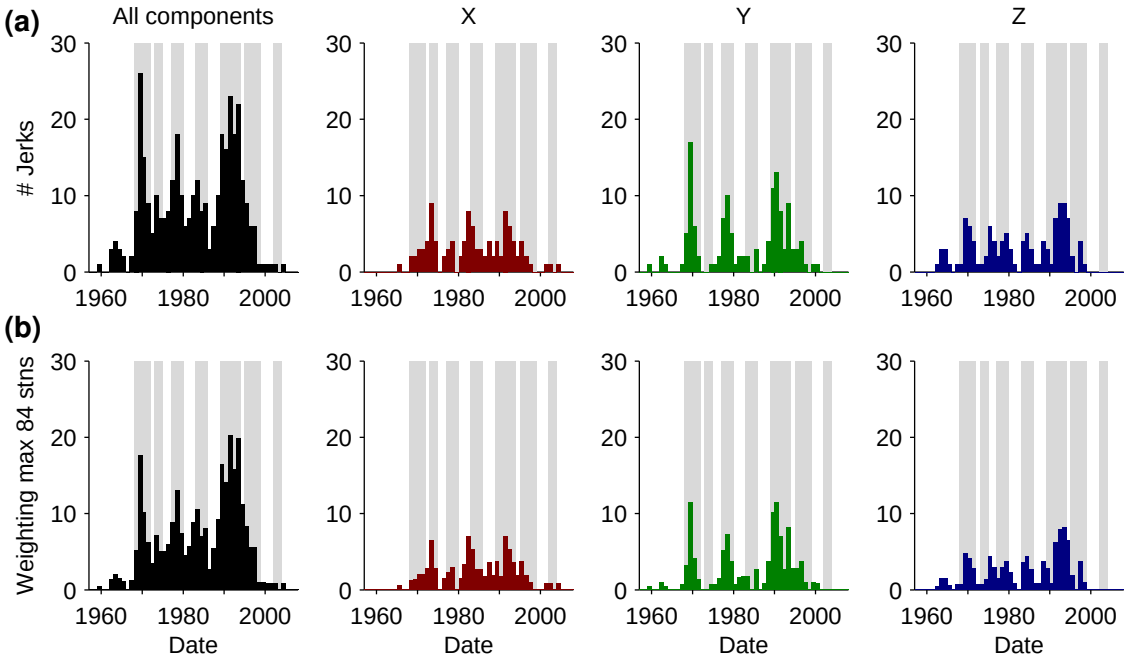

Figure C.2: Histograms of detected jerks in 1 yr time bins between 1957 and 2008, (a) shows straight counts for a 15 yr window, (b) shows 15 yr window counts weighted by the number of operating observatories during any given time bin. Layout as in Figure C.1. From Brown et al. [2013] supplement.

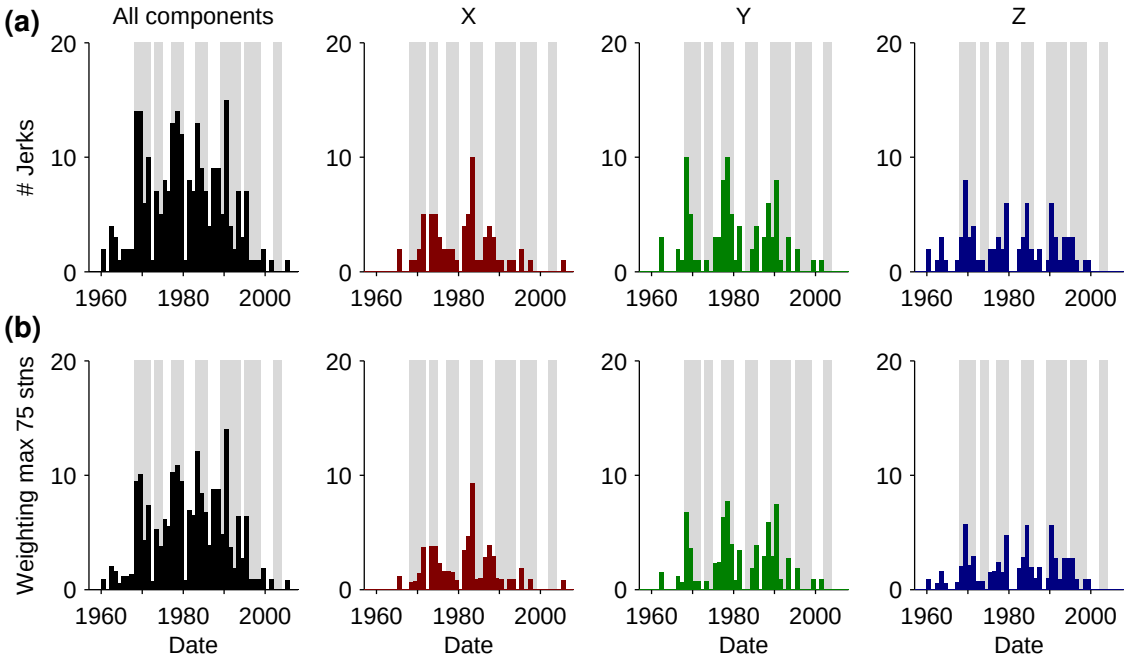

Figure C.3: Histograms of detected jerks in 1 yr time bins between 1957 and 2008, (a) shows straight counts for a 20 yr window, (b) shows 20 yr window counts weighted by the number of operating observatories during any given time bin. Layout as in Figure C.1. From Brown et al. [2013] supplement.

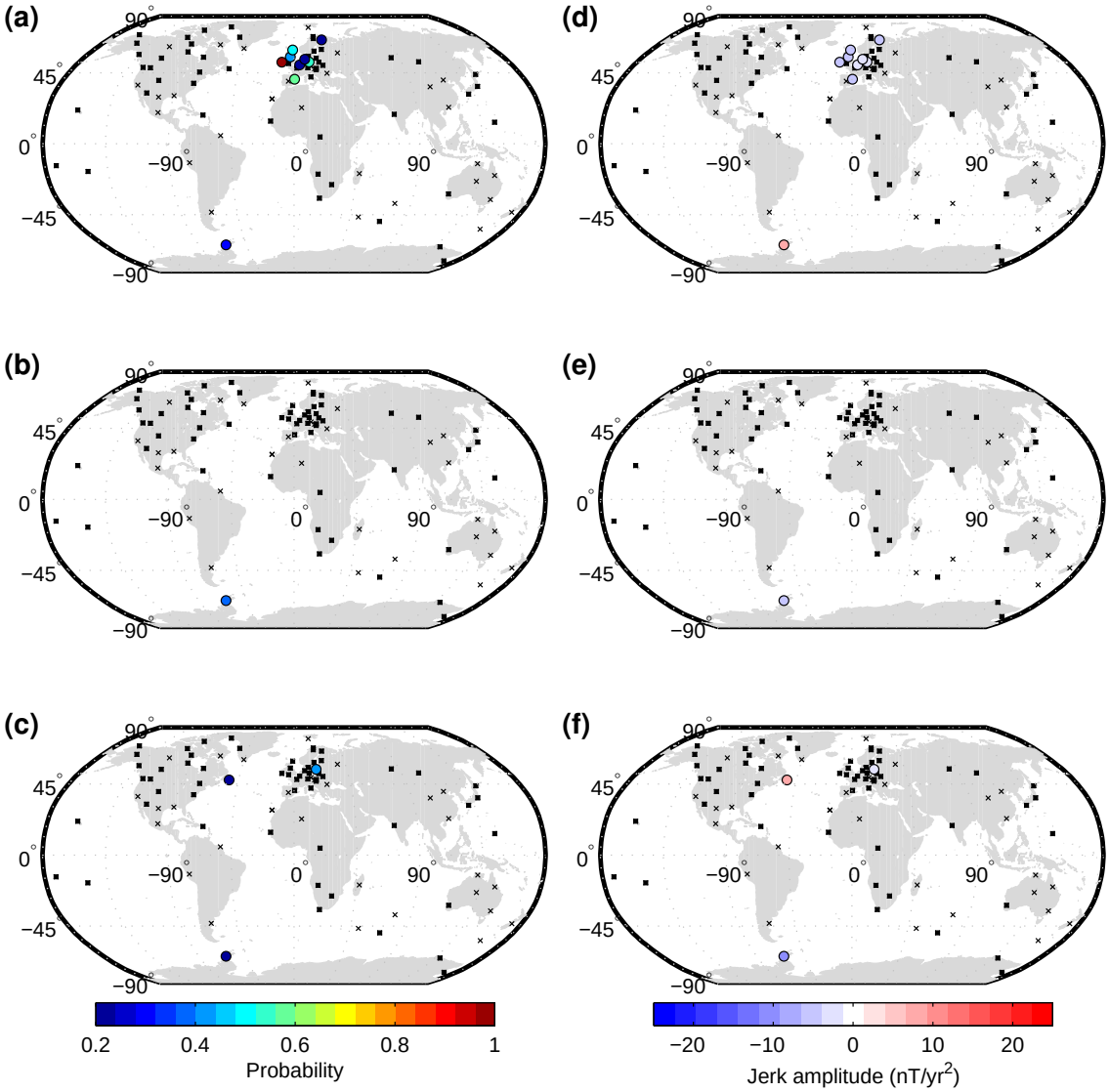

Figure C.4: Jerk probability (a–c) and amplitudes (d–f) for the period of 1973–74. Top to bottom are the X-, Y- and Z-components respectively. Black crosses represent inactive observatory locations, black squares represent active observatory locations which did not detect a jerk and coloured circles represent identified jerks. Results from 10 yr window. From Brown et al. [2013] supplement.

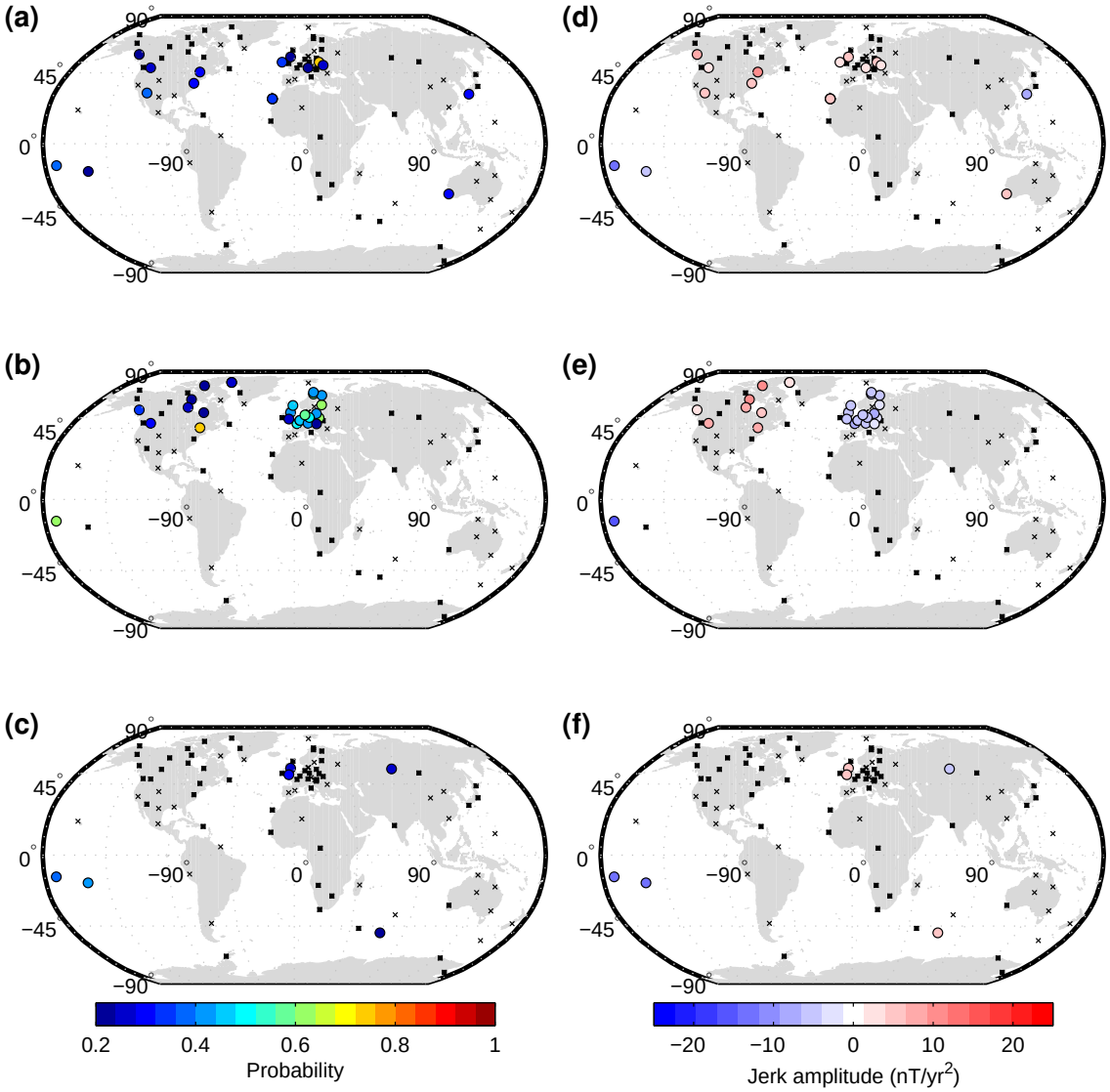

Figure C.5: Jerk probability (a–c) and amplitudes (d–f) for the period of 1977–79. Top to bottom are the X-, Y- and Z-components respectively. Black crosses represent inactive observatory locations, black squares represent active observatory locations which did not detect a jerk and coloured circles represent identified jerks. Results from 10 yr window. From Brown et al. [2013] supplement.

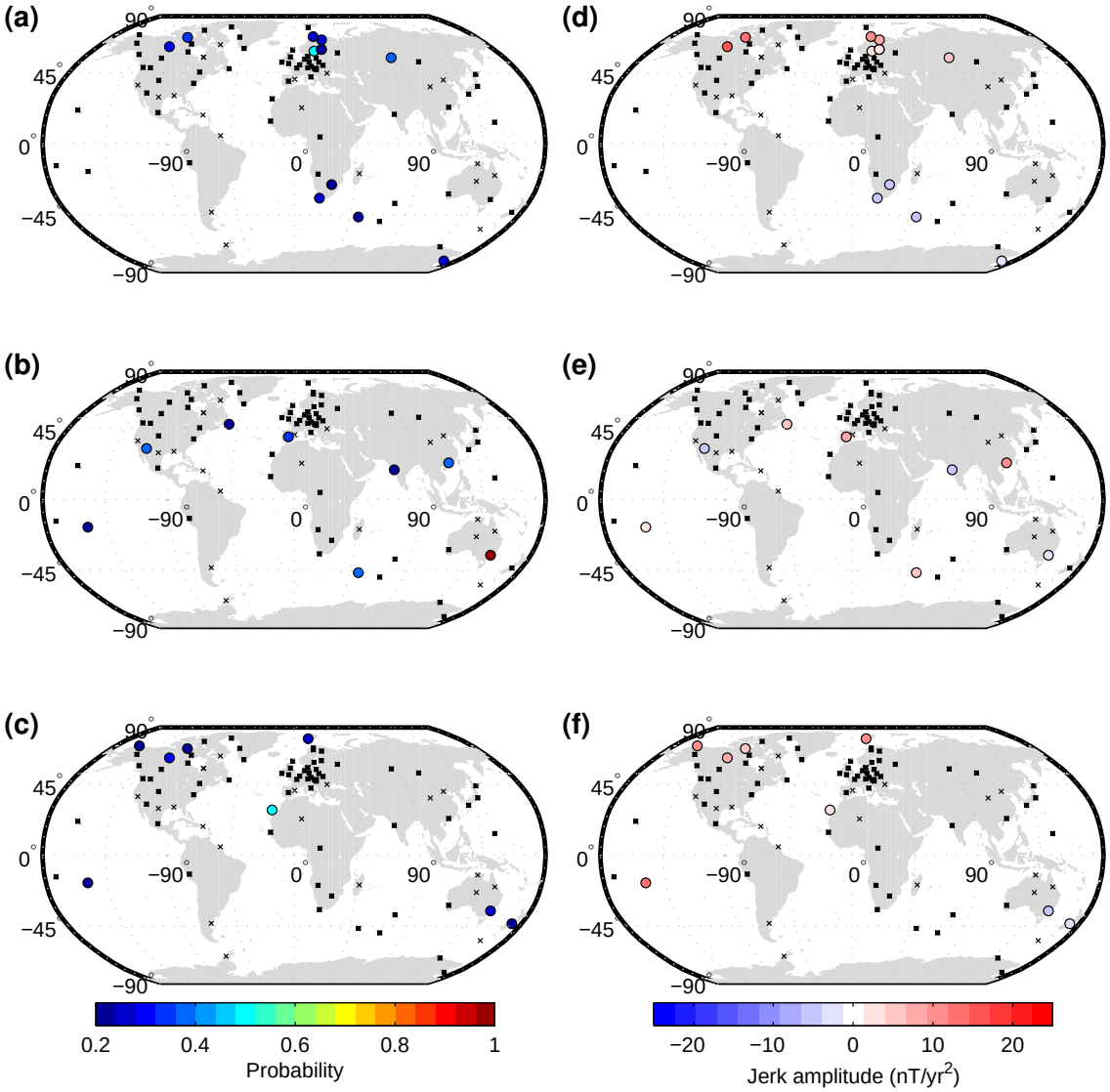

Figure C.6: Jerk probability (a–c) and amplitudes (d–f) for the period of 1983–85. Top to bottom are the X-, Y- and Z-components respectively. Black crosses represent inactive observatory locations, black squares represent active observatory locations which did not detect a jerk and coloured circles represent identified jerks. Results from 10 yr window. From Brown et al. [2013] supplement.

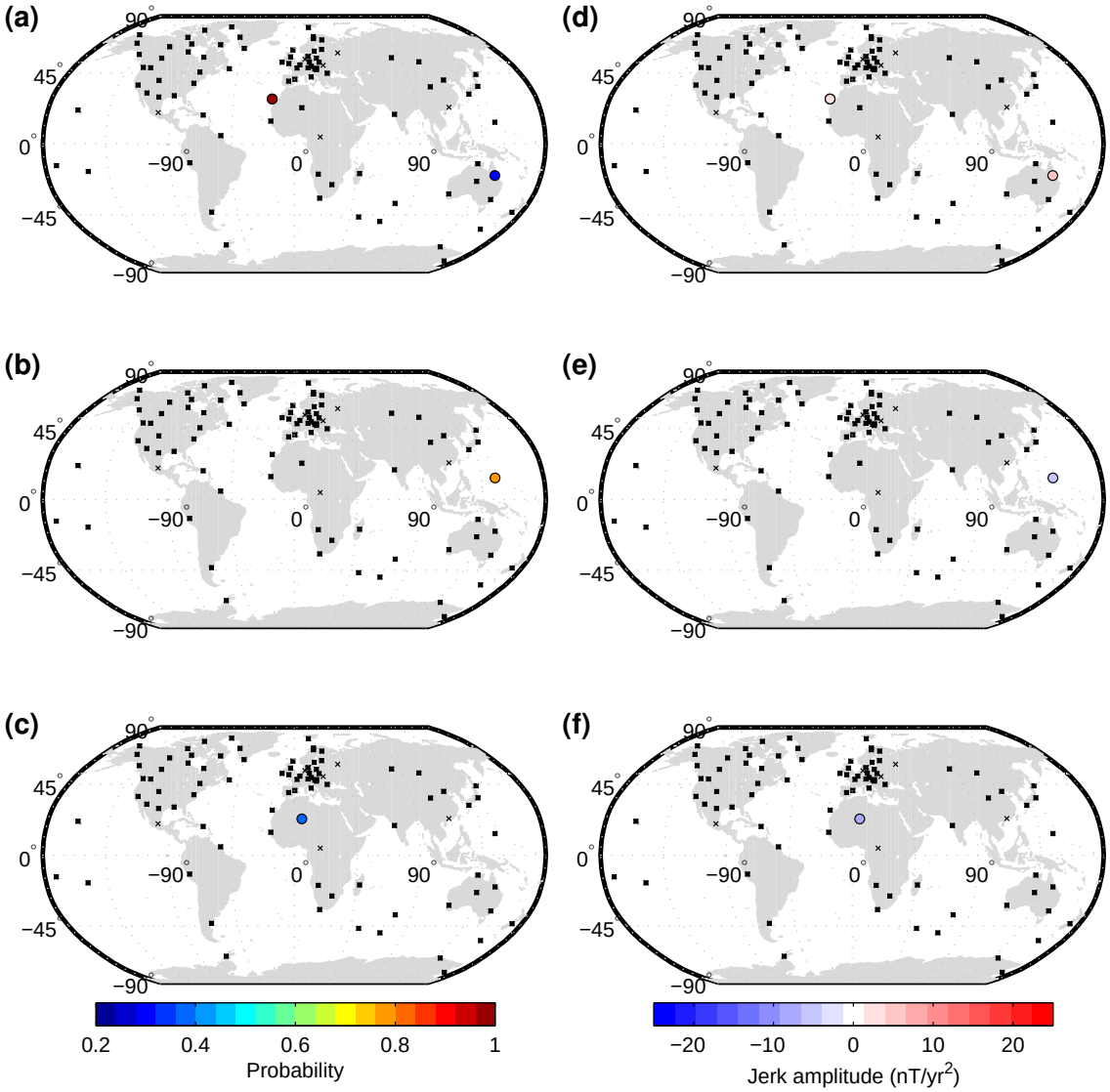

Figure C.7: Jerk probability (a–c) and amplitudes (d–f) for the period of 2002–03. Top to bottom are the X-, Y- and Z-components respectively. Black crosses represent inactive observatory locations, black squares represent active observatory locations which did not detect a jerk and coloured circles represent identified jerks. Results from 10 yr window. From Brown et al. [2013] supplement.

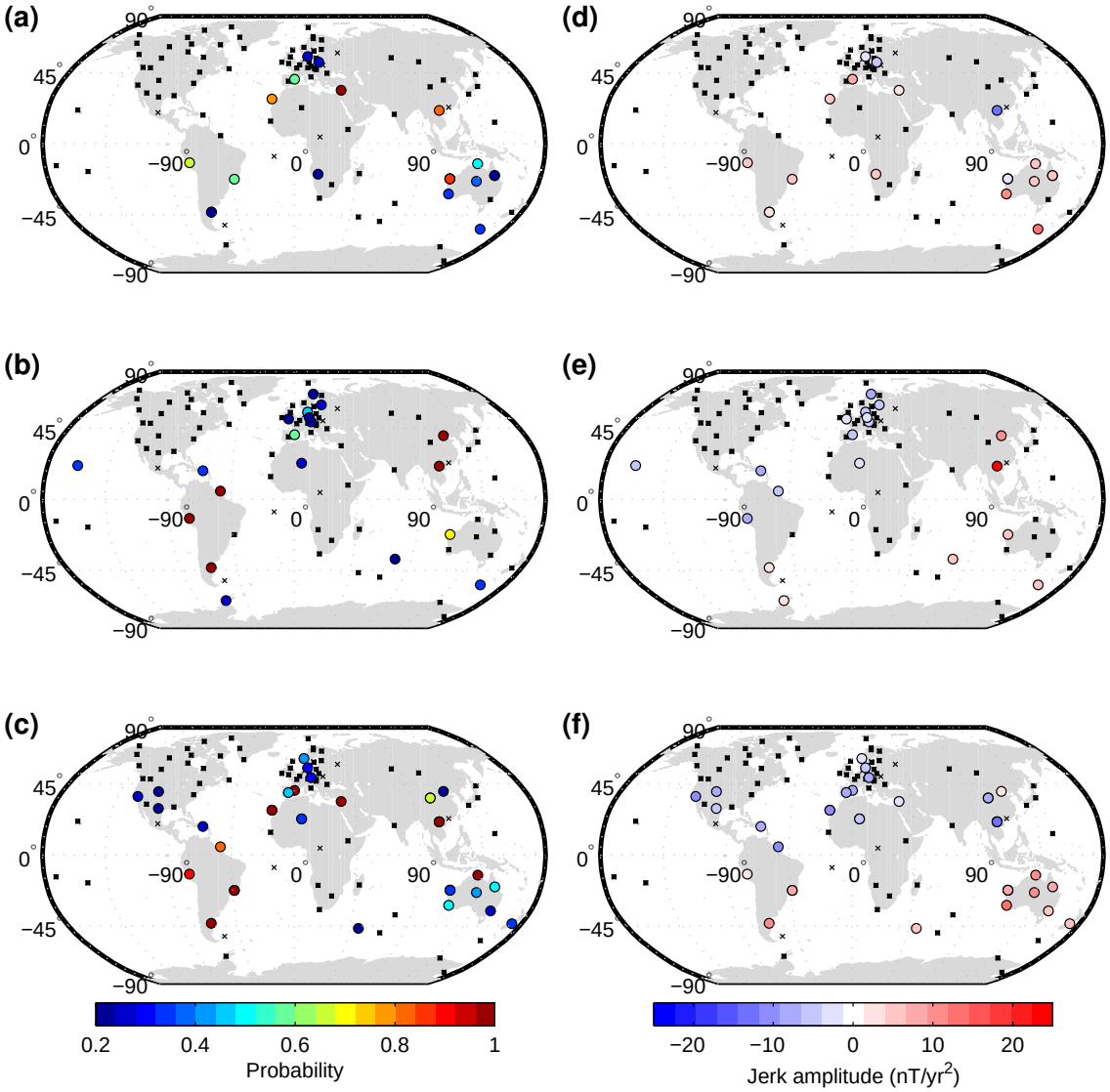

Figure C.8: Jerk probability (a–c) and amplitudes (d–f) for the period of 2002–03. Top to bottom are the X-, Y- and Z-components respectively. Black crosses represent inactive observatory locations, black squares represent active observatory locations which did not detect a jerk and coloured circles represent identified jerks. Results from 5 yr window. From Brown et al. [2013] supplement.

APPENDIX D

TEMPORAL SPECTRUM OF GEOMAGNETIC OBSERVATIONS

In Chapter 4, the global mean MF temporal spectrum of monthly observatory data was calculated to compare to that of the stochastic synthetic field models. This was in order to validate the realism of the synthetic models. It raises two questions, outside of the primary aim of this test and the narrative of this thesis, but related to the study of rapid SV and therefore of more general interest.

Firstly, since the spectral behaviour of the geomagnetic field at short periods is unknown, whether a reassessment of the global temporal spectrum similar to the work of Currie [1968] and De Santis et al. [2003] should be attempted with monthly or hourly observatory data. This would be worthwhile since in Chapter 2 I have demonstrated that effective cleaning of external signals from observatory data can be achieved, which may allow insight into a more rapid part of the geomagnetic spectrum as yet unobserved. A sensible approach to this investigation may be to apply an external field cleaning technique to annual, monthly and hourly observatory data from as wide a spatial distribution and as long a time period as is available, and then to calculate the global temporal spectrum as in Chapter 4. While in Chapter 4 I used only observatory data from the location which provided a continuous record from 1957–2008, an updated data set should be gathered and all length of record combined to enhance the reliability, particularly at the high frequency end of the spectrum, and to extend the frequency band with longer records. Continuous data from 1840–2015 is available for some limited locations, and provided an internal field model such as *COV-OBS* or *gufm1* proves suitable for use in the external signal cleaning method of Wardinski and Holme [2011] as used Chapter 2, corrections

can be made troughout the observatory era.

As noted by De Santis et al. [2003], there are other possible spatial spectrum models for the geomagnetic field which relate to different temporal spectrum laws than the discussed power law which may describe the observed geomagnetic temporal spectrum (De Santis et al. [2003] find an exponential law to be suitable also). Since in Chapter 4 I observe that the frequency band considered has a large impact on the slope of the power law fit to the MF spectrum, it seems sensible to assess if the existing proposed models or a new model can best account for a wider frequency band, particularly extended to higher frequencies.

The second question raised is that of the spectral content of the external signals removed from the observatory data and of the assumed internal SV signal that remains. An equivalent plot to Figure 4.3 for the SV and SA is given in Figure D.1. There is clear structure to the spectrum of observations below periods of 10 yrs, in both the SV and SA, how much of this can be confidently described as internal remains to be seen. It is at these periods also that the observed spectrum and that of the synthetic models diverge most, perhaps indicating an unexplained behaviour of the internal field or that significant external contamination remains. Works such as Silva et al. [2012] have shown that the SA contains a $\sim$6 yr periodicity of internal origin and that field models such as *CHAOS-3* and *CM4* show SA periodic content on subdecadal scales also. A better understanding of this signal content or relation of specific periods to internal or external features could benefit future parameterisation techniques for modelling purposes.

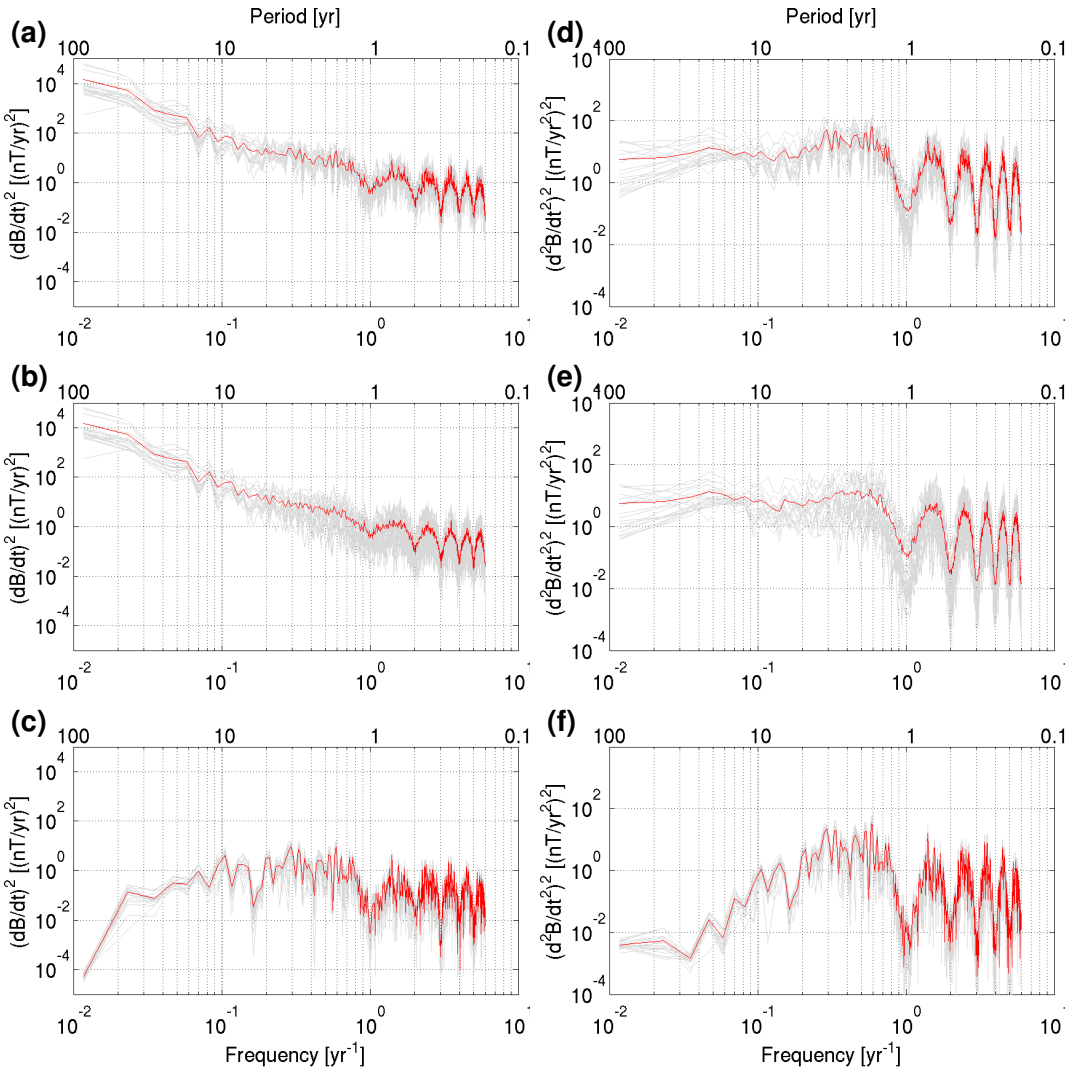

Figure D.1: Global mean temporal power spectra from observatory SV and SA data. Shown are spectra of observatory monthly mean SV series (a–c, grey) with global mean (a–c, red) and spectra of observatory monthly mean SA series (d–f, grey) with global mean (d–f, red). Top "clean" row for cleaned observatory data (a,d). Middle "noisy" row for raw observatory data (b,e). Bottom row for differences between "clean" and "noisy" rows.

APPENDIX E

SPHERICAL HARMONIC INVERSION TRUNCATION DEGREE

This appendix contains a series of SH inversion cases corresponding to the power spectra shown in Figure 4.14, depicting the impacts of varying the truncation degree on a test case of *CHAOS-4*α SV at 2005.0. The model snapshot is shown in Figure E.1 with the inverted models of sub-sampled data from this snapshot, at progressively lower truncation degrees, shown in Figures E.2–E.4.

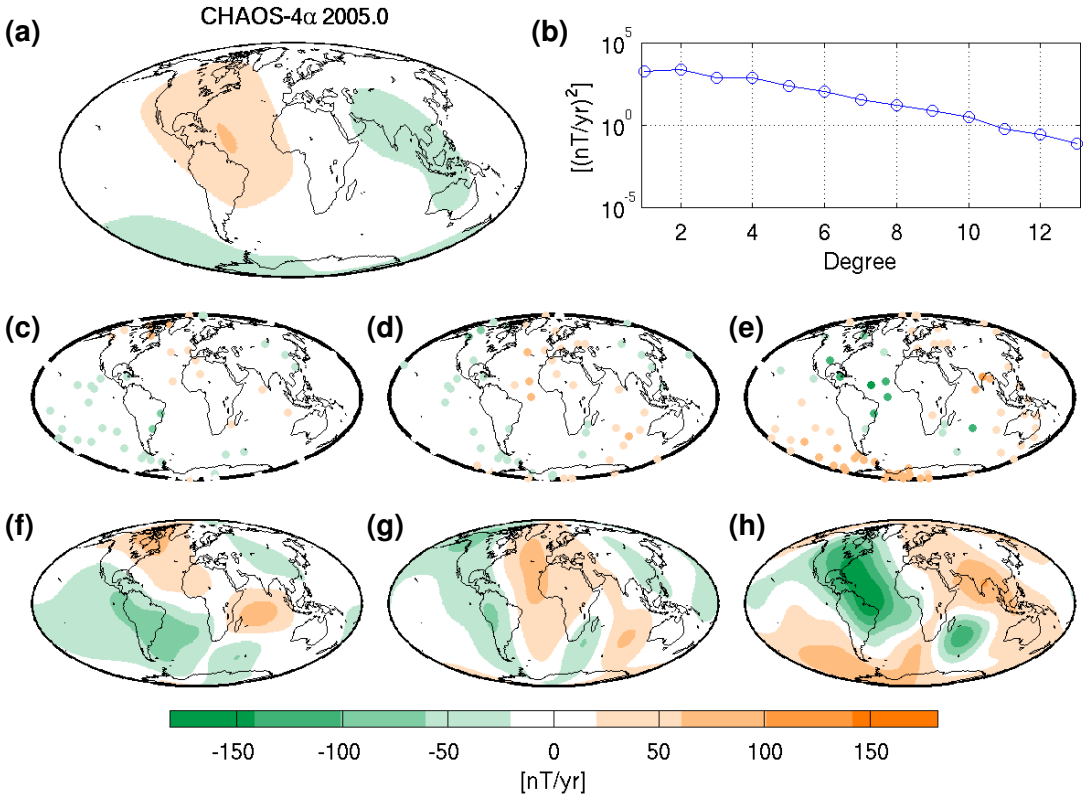

Figure E.1: Example snapshot of *CHAOS-4*α SV at 2005.0 to SH degree 13 for benchmark of SH model inversion dependence on SH truncation degree. The potential scaled by r_E (a), the spectrum of the potential (b), one hundred randomly positioned spatial samples of X- (c), Y- (d) and Z-components (e) and full X- (f), Y- (g) and Z-component (h) field derivatives are shown. All plots are at the Earth's surface.

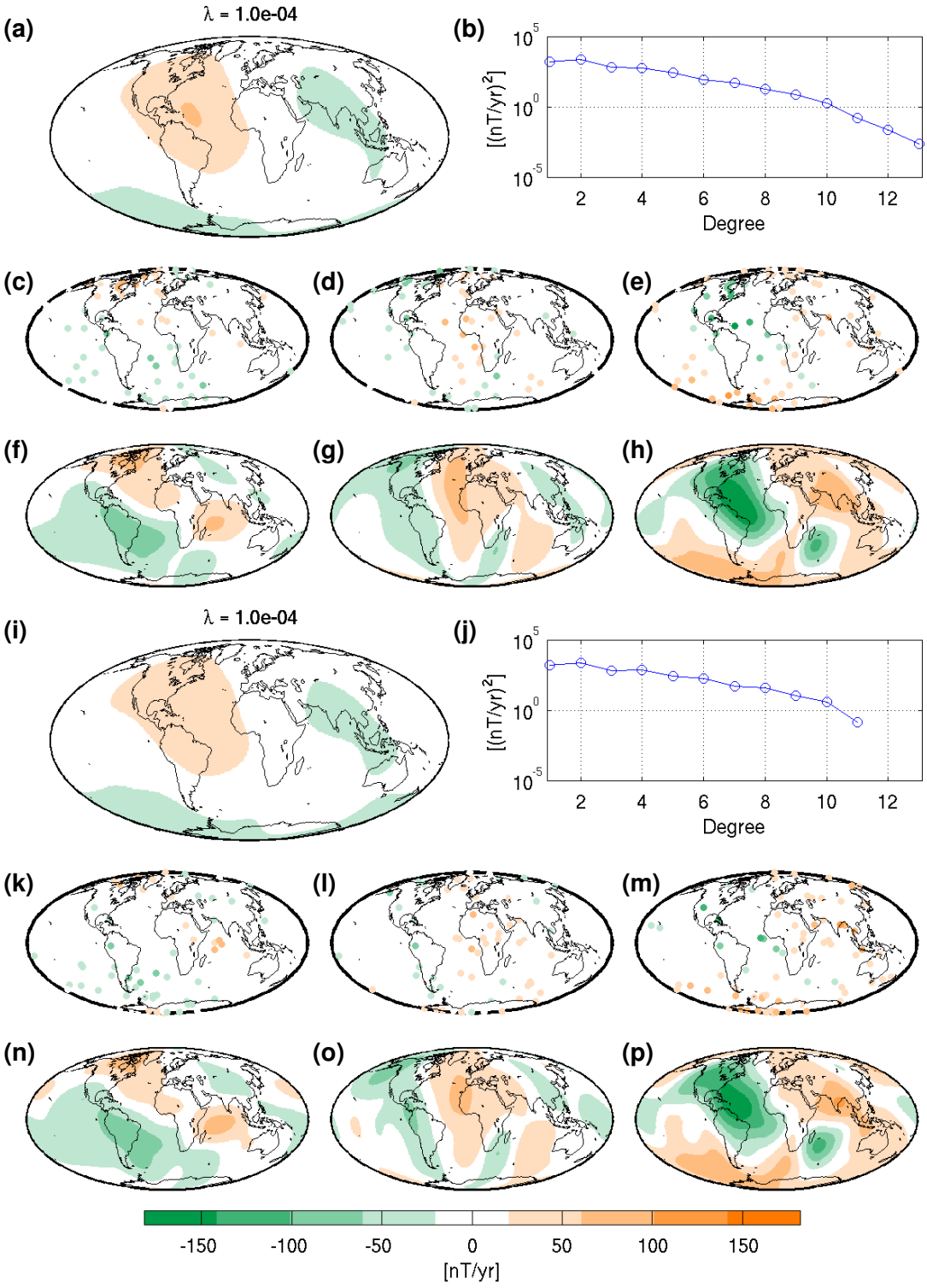

Figure E.2: Example snapshots of inverted SH model recovered from one hundred random spatial samples of *CHAOS-4*α SV at 2005.0 (Figure E.1) with model expansion truncated at SH degree 13 (a–h) and 11 (i–p). Plots are arranged as in Figure E.1. Gaussian noise was added to one hundred randomly located samples of the X- (c,k), Y- (d,i) and Z-components (e,m) of Figure E.1 and then inverted for the potential from which the remaining plots are derived. Corresponds to spectra shown in Figure 4.14.

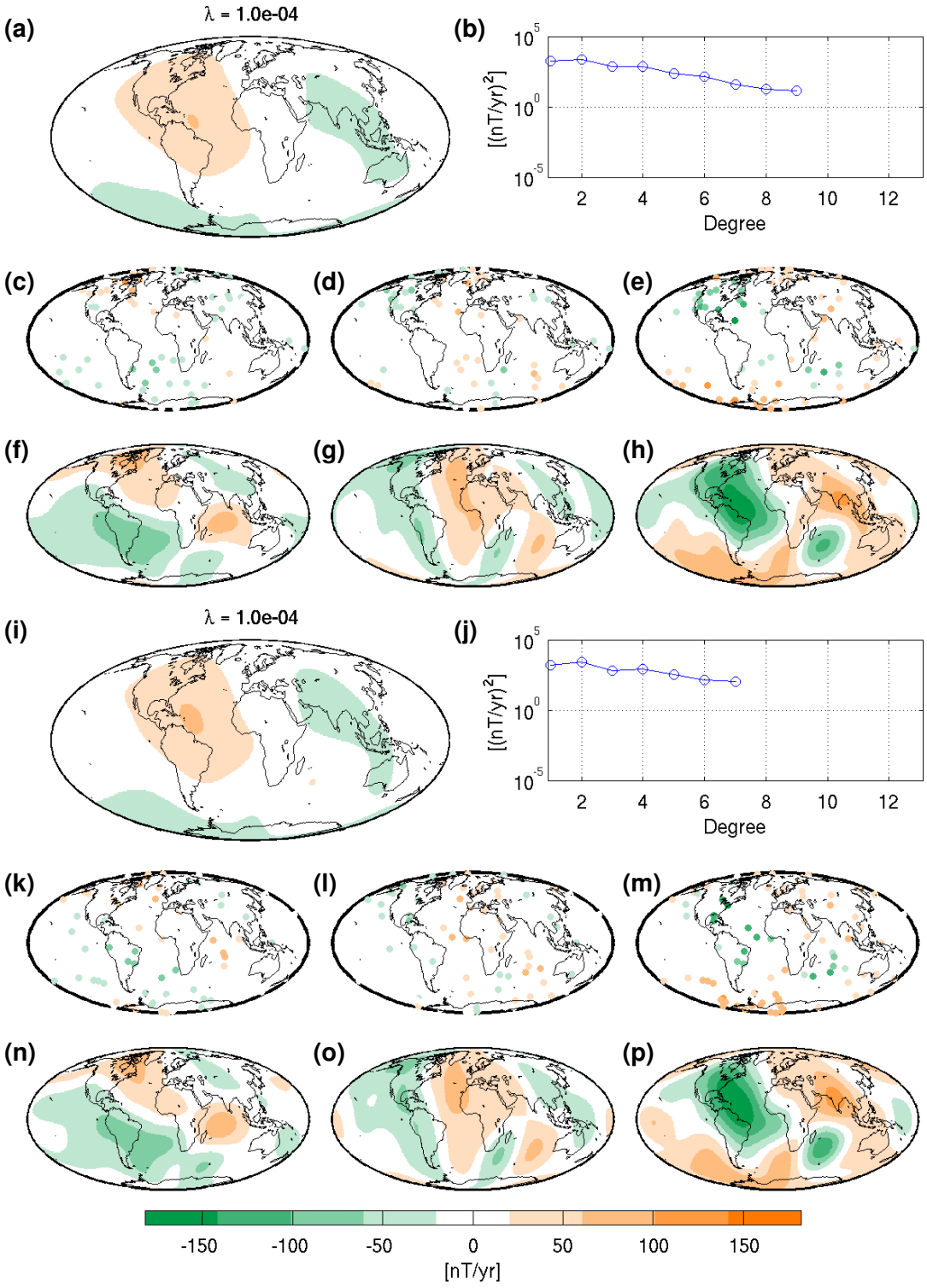

Figure E.3: Example snapshots of inverted SH model recovered from one hundred random spatial samples of *CHAOS-4*α SV at 2005.0 (Figure E.1) with model expansion truncated at SH degree 9 (a–h) and 7 (i–p). Plots are arranged as in Figure E.1. Gaussian noise was added to one hundred randomly located samples of the X- (c,k), Y- (d,i) and Z-components (e,m) of Figure E.1 and then inverted for the potential from which the remaining plots are derived. Corresponds to spectra shown in Figure 4.14.

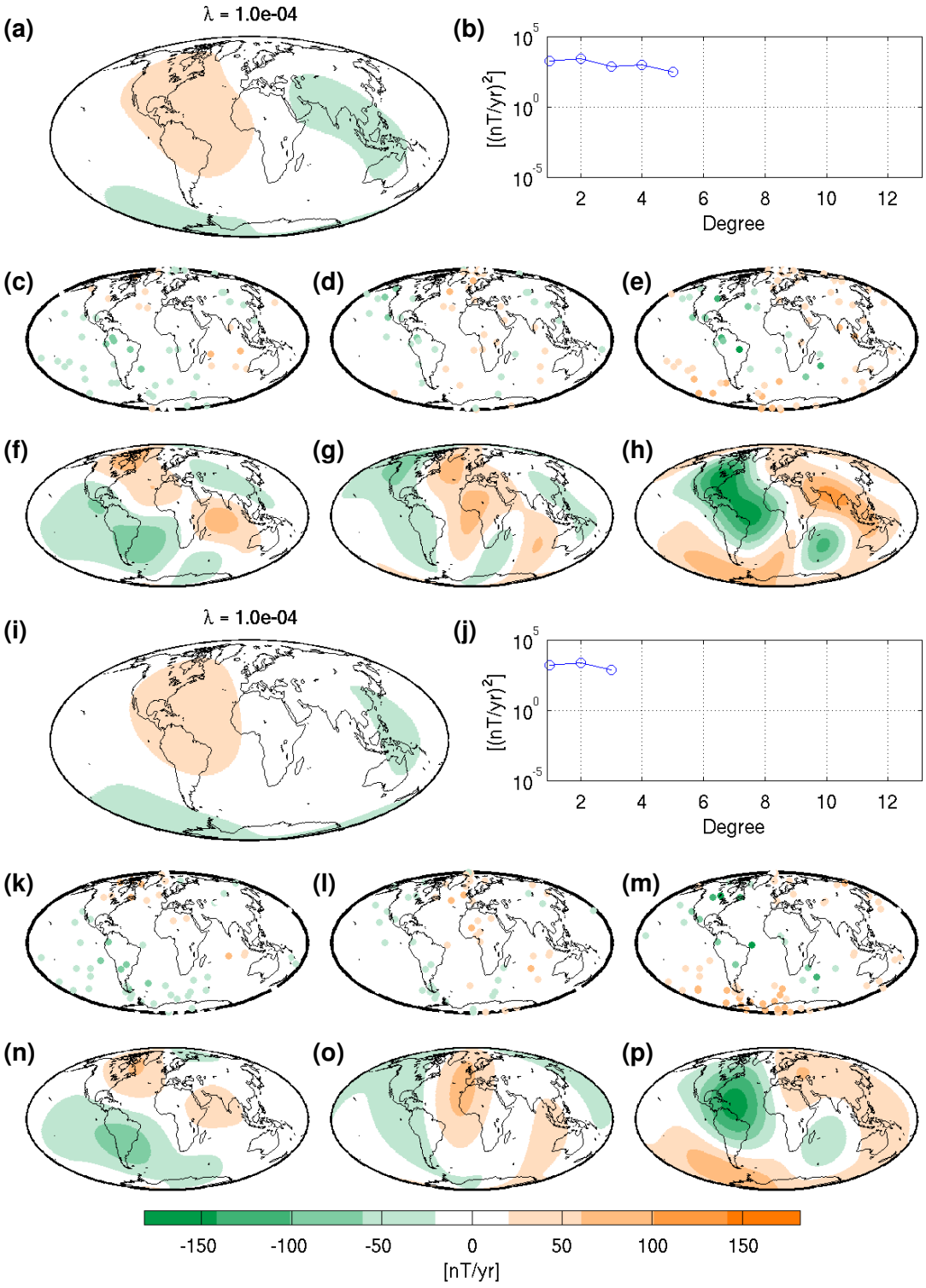

Figure E.4: Example snapshots of inverted SH model recovered from one hundred random spatial samples of *CHAOS-4*α SV at 2005.0 (Figure E.1) with model expansion truncated at SH degree 5 (a–h) and 3 (i–p). Plots are arranged as in Figure E.1. Gaussian noise was added to one hundred randomly located samples of the X- (c,k), Y- (d,i) and Z-components (e,m) of Figure E.1 and then inverted for the potential from which the remaining plots are derived. Corresponds to spectra shown in Figure 4.14.

APPENDIX F

SYNTHETIC JERK ANALYSIS RESULTS

This appendix contains extra figures, referenced in the text but surplus to the main discussion points of Chapter 5, they are nonetheless informative and necessary for completeness.

Figure F.1 shows a comparison of histograms of jerk occurrences detected in a synthetic model for observatory style sampling of a realisation with 5, 15 and 25 yr detection windows. Histograms which compare the jerks identified when either STT cell or observatory style spatial sampling are used are displayed in Figure F.2 and Figure F.3 for 5 yr and 15 yr detection windows, respectively. Figures F.4–F.7 show a similar comparison for results with a 25 yr detection window when only the Northern, Southern, Eastern or Western Hemisphere is considered, respectively.

Global correlation coefficients for the synthetic jerk models from an example synthetic model realisation are shown in Figure F.8. Examples of the coefficient symmetry subgroups for a synthetic jerk model from STT cell and observatory style sampling, demonstrating their similarity are shown Figures F.9 and F.10, respectively.

Test cases to demonstrate the consistency of jerk amplitude periodicity in the synthetic field models, for detection window lengths of 5 yrs, 15 yrs and 25 yrs, are shown in Figures F.11–F.13, respectively.

Spherical harmonic models of the jerks detected in observatory data in Chapter 3, in 1973–74, 1977–79, 1983–85, 1989–93 and 1995–98 are displayed in Figures F.14–F.16, respectively. Global correlation coefficients for the coefficient symmetry subgroups of these models can be seen in Figure F.18.

Figure F.19 illustrates a comparison of histograms of jerk occurrences detected in a

synthetic model with an alternative prior constraint, limiting the variation of the degree 1 term. STT cell sampling of a realisation is used with 5, 15 and 25 yr detection windows. Figure F.20 shows an example of a SH jerk model inverted from jerks detected in this alternative, fixed dipole model.

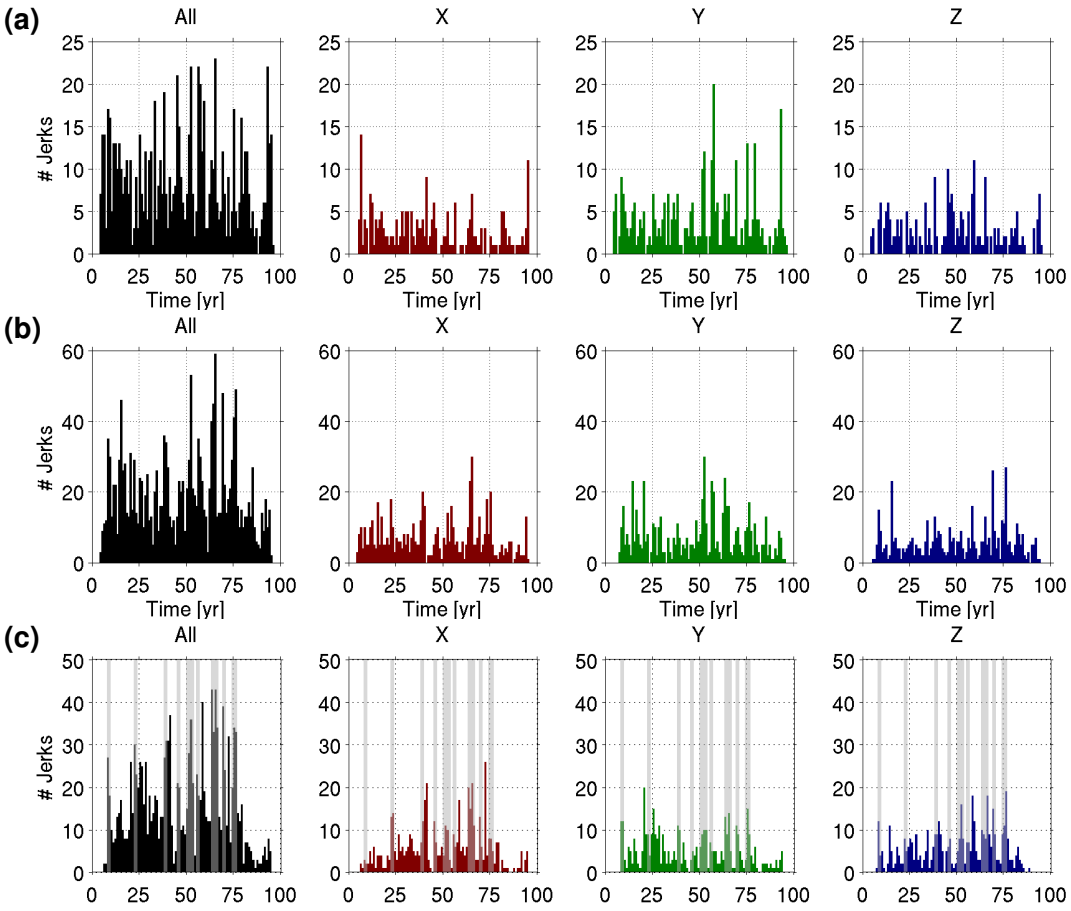

Figure F.1: Histograms of number of jerks detected in a 100 yr realisation of synthetic model at 102 observatory locations, with 1 yr bins. Total count (black) and those for individual X- (red), Y- (green), and Z-components (blue) are shown for results using detection windows of 5 yr (a), 15 yr (b) and 25 yr (c). Grey bands in (c) highlight the peaks of the all-component (black) histogram, taken to represent major jerks as assessed in Chapter 5.

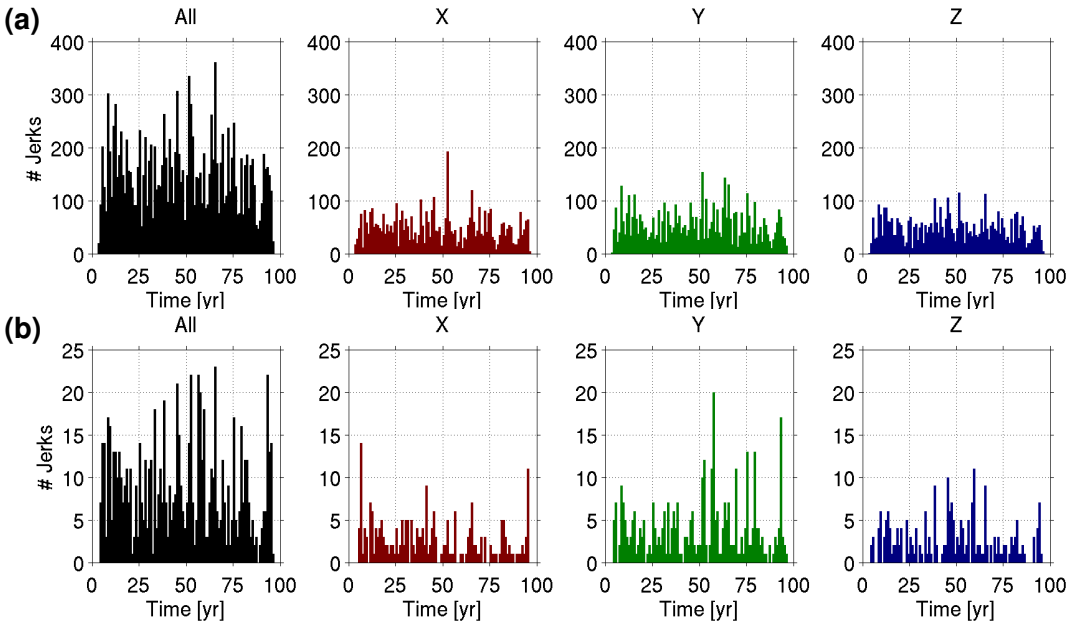

Figure F.2: Histograms of number of jerks detected in a 100 yr realisation of synthetic model at 1620 STT cell locations (a) and 102 observatory locations (b), with 1 yr bins. Total count (black) and those for individual X- (red), Y- (green), and Z-components (blue) are shown for a 5 yr detection window.

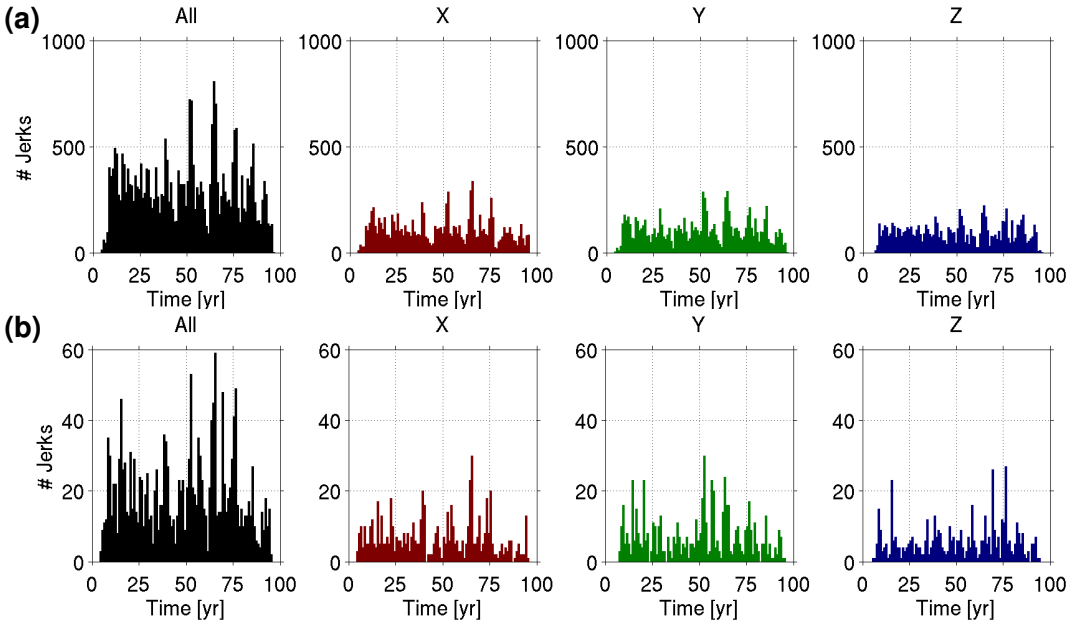

Figure F.3: Histograms of number of jerks detected in a 100 yr realisation of synthetic model at 1620 STT cell locations (a) and 102 observatory locations (b), with 1 yr bins. Total count (black) and those for individual X- (red), Y- (green), and Z-components (blue) are shown for a 15 yr detection window.

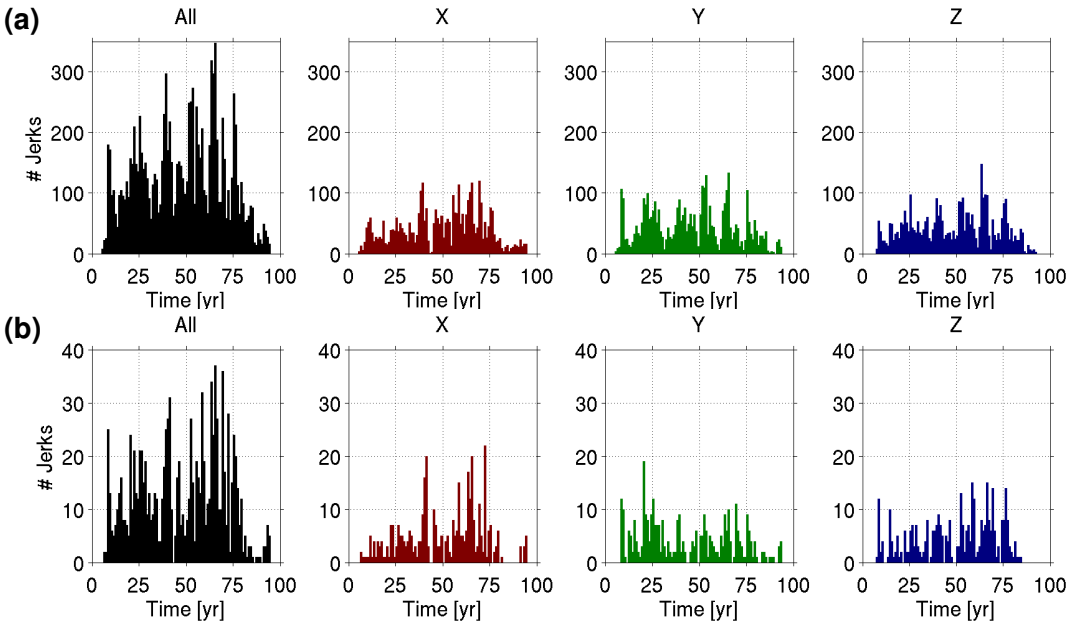

Figure F.4: Histograms of number of jerks detected in a 100 yr realisation of synthetic model at STT cell (a) and observatory locations (b) in the Northern hemisphere, with 1 yr bins. Total count (black) and those for individual X- (red), Y- (green), and Z-components (blue) are shown for a 25 yr detection window.

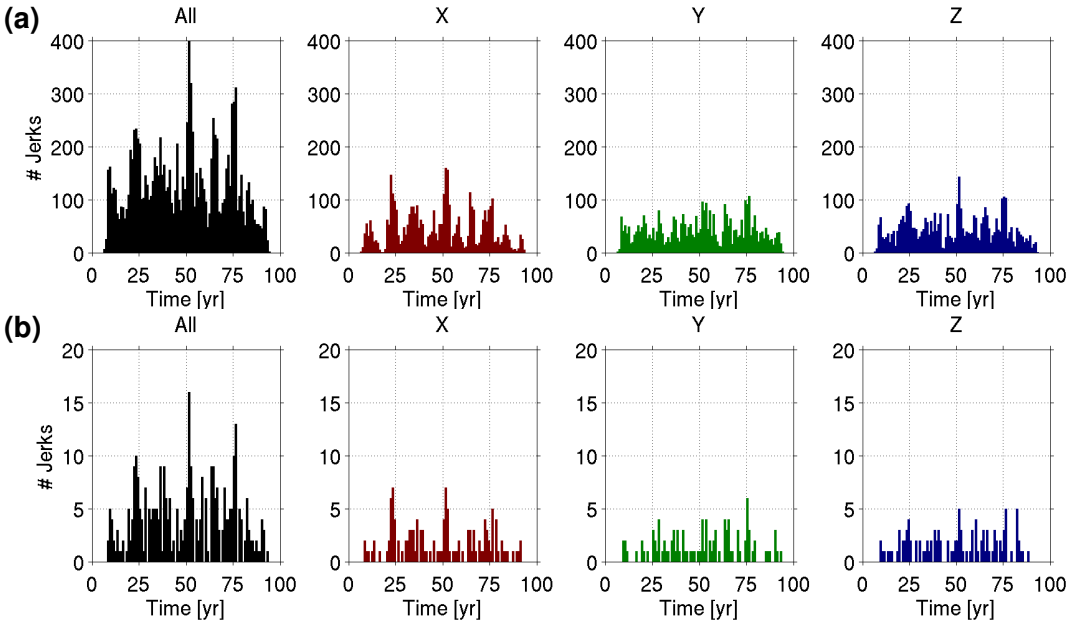

Figure F.5: Histograms of number of jerks detected in a 100 yr realisation of synthetic model at STT cell (a) and observatory locations (b) in the Southern hemisphere, with 1 yr bins. Total count (black) and those for individual X- (red), Y- (green), and Z-components (blue) are shown for a 25 yr detection window.

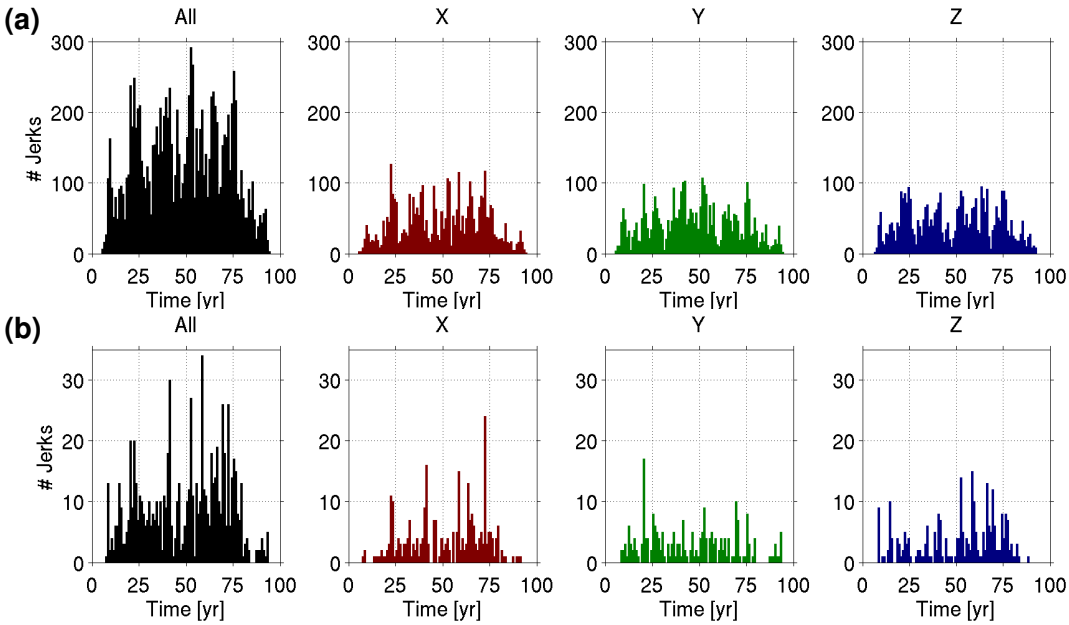

Figure F.6: Histograms of number of jerks detected in a 100 yr realisation of synthetic model at STT cell (a) and observatory locations (b) in the Eastern hemisphere, with 1 yr bins. Total count (black) and those for individual X- (red), Y- (green), and Z-components (blue) are shown for a 25 yr detection window.

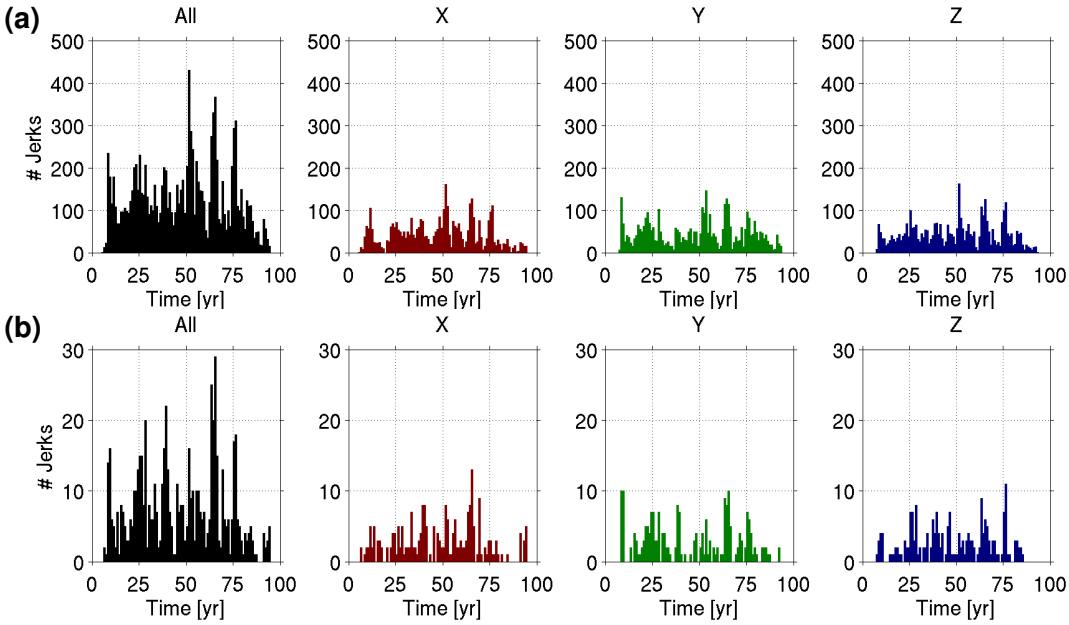

Figure F.7: Histograms of number of jerks detected in a 100 yr realisation of synthetic model at STT cell (a) and observatory locations (b) in the Western hemisphere, with 1 yr bins. Total count (black) and those for individual X- (red), Y- (green), and Z-components (blue) are shown for a 25 yr detection window.

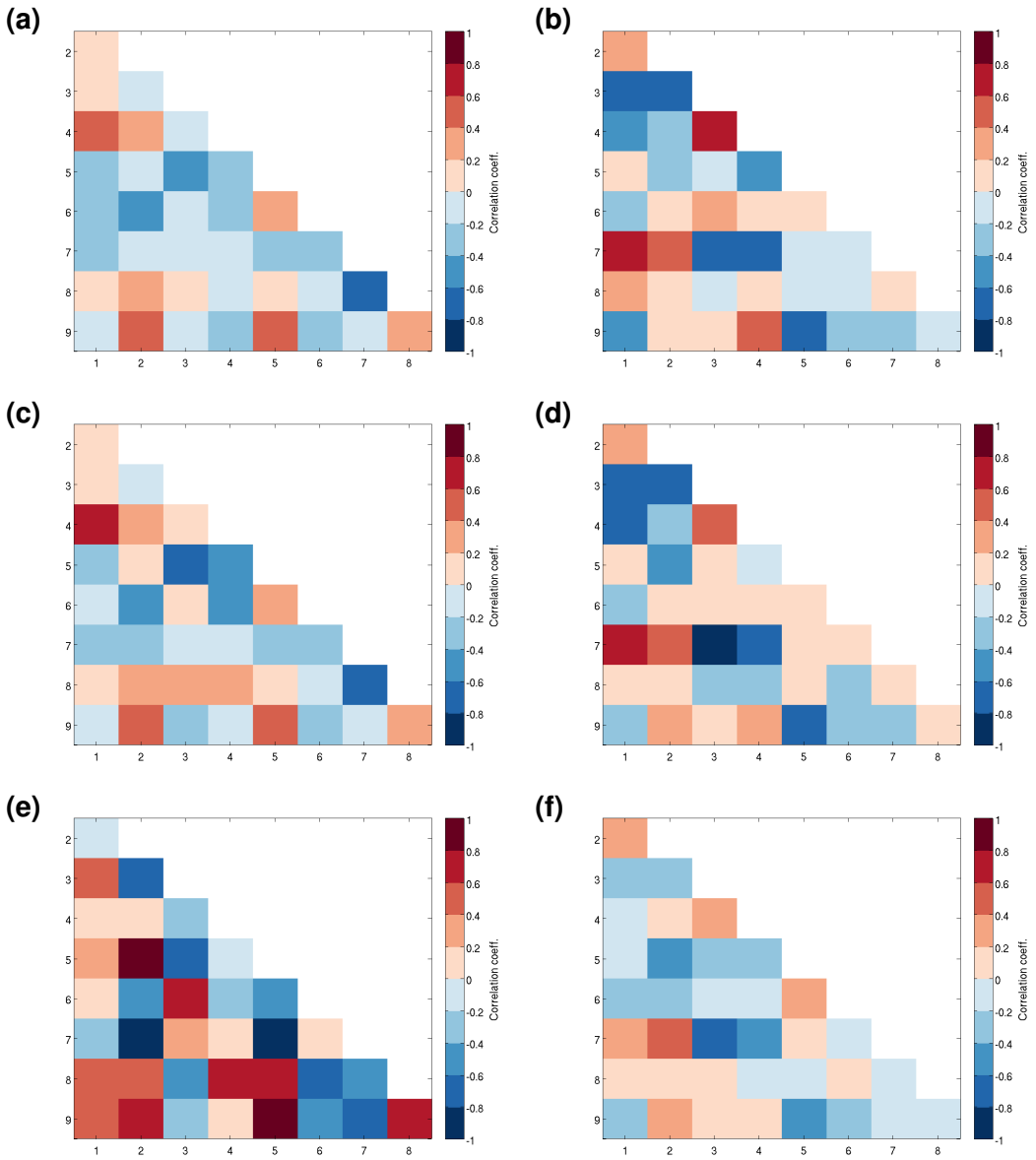

Figure F.8: Global correlation coefficients [after McLeod, 1985] for various coefficient subgroups of the nine jerk histogram peaks in an example synthetic realisation (Figure 5.4). Correlation for the equatorially symmetric (a) and anti-symmetric (b), azimuthally symmetric (c) and anti-symmetric (d), zonal (e) and non-zonal (f) coefficient subgroups are shown.

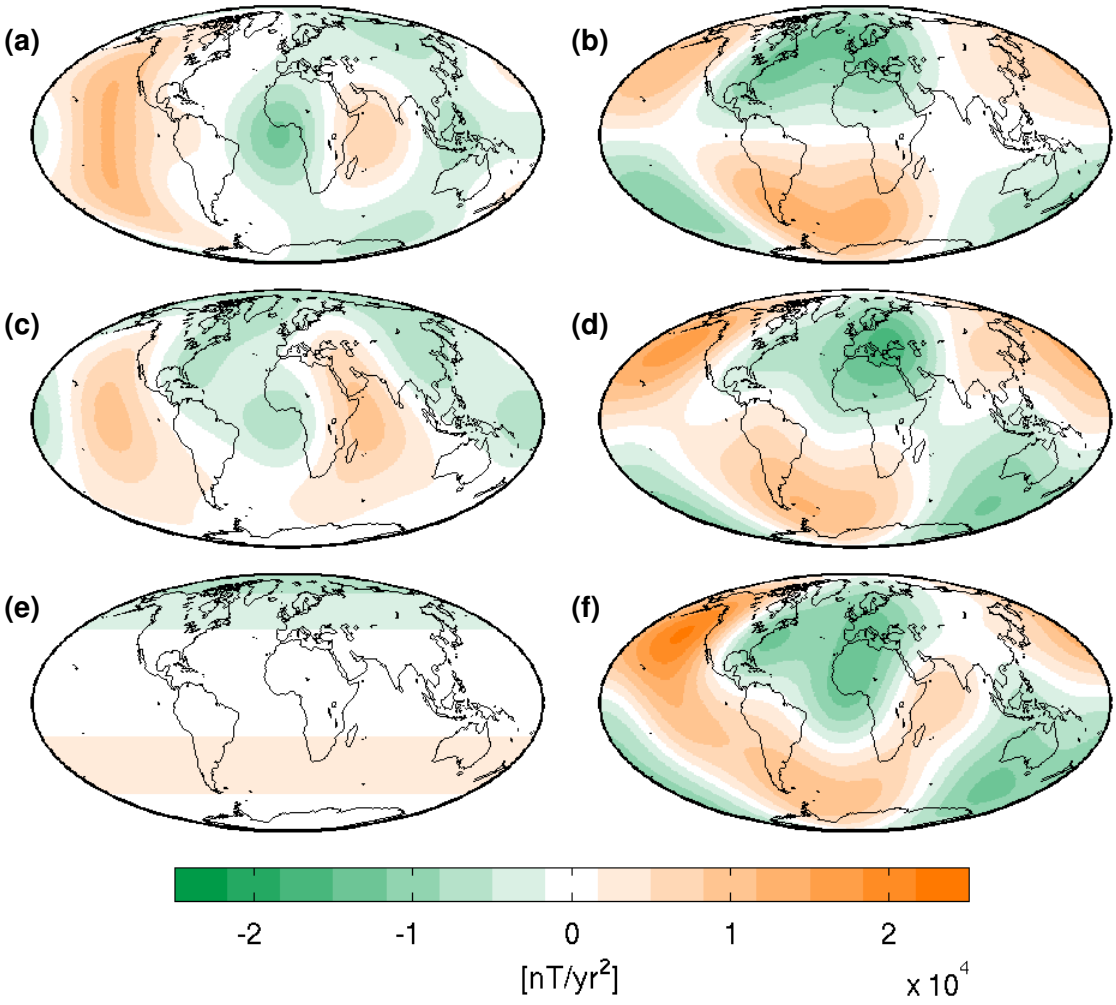

Figure F.9: Equatorially symmetric (a), equatorially anti-symmetric (b), azimuthally symmetric (c), azimuthally anti-symmetric (d), zonal (e) and non-zonal (f) parts of a synthetic jerk potential inverted from STT cell sampling of jerk amplitudes (peak 1 in Figure 5.4).

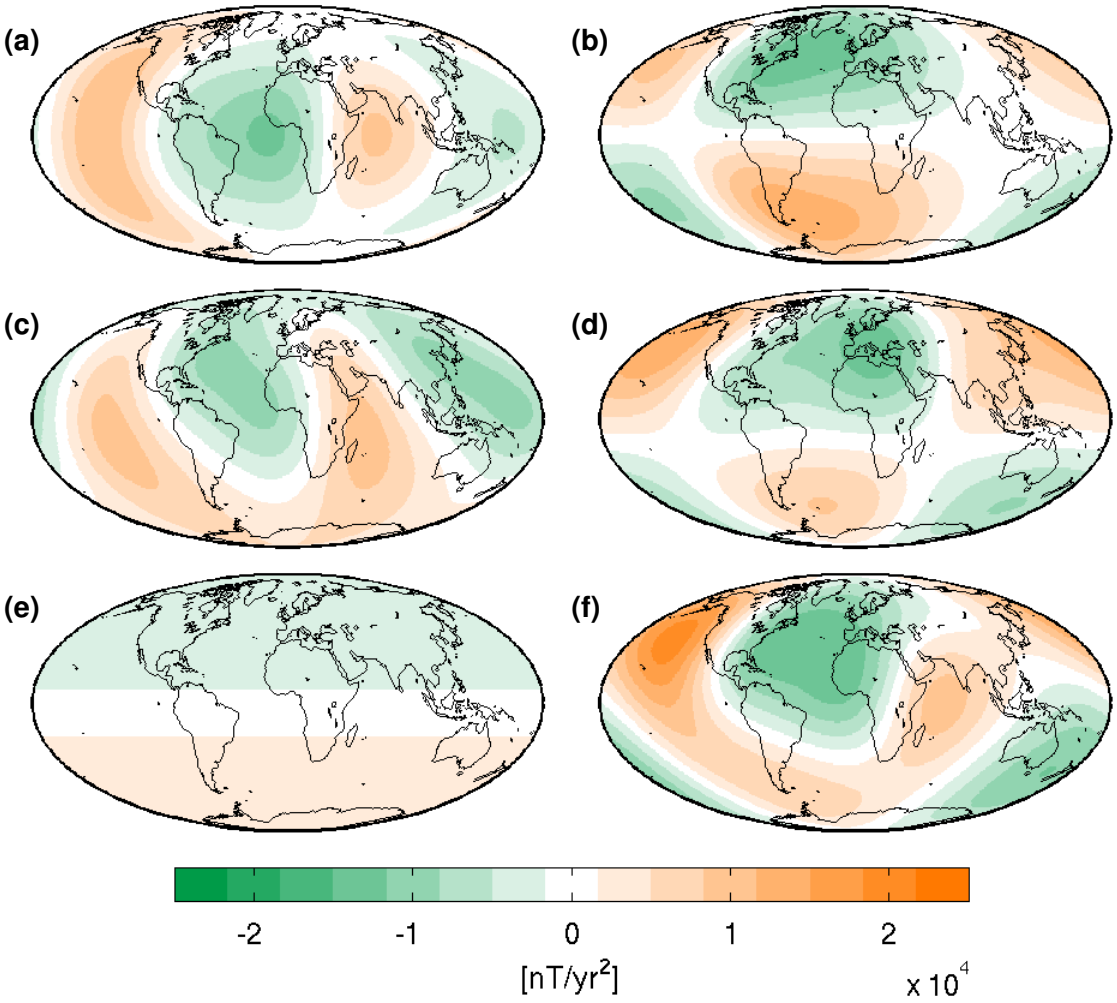

Figure F.10: Equatorially symmetric (a), equatorially anti-symmetric (b), azimuthally symmetric (c), azimuthally anti-symmetric (d), zonal (e) and non-zonal (f) parts of a synthetic jerk potential inverted from observatory style sampling of jerk amplitudes (peak 1 in Figure 5.4).

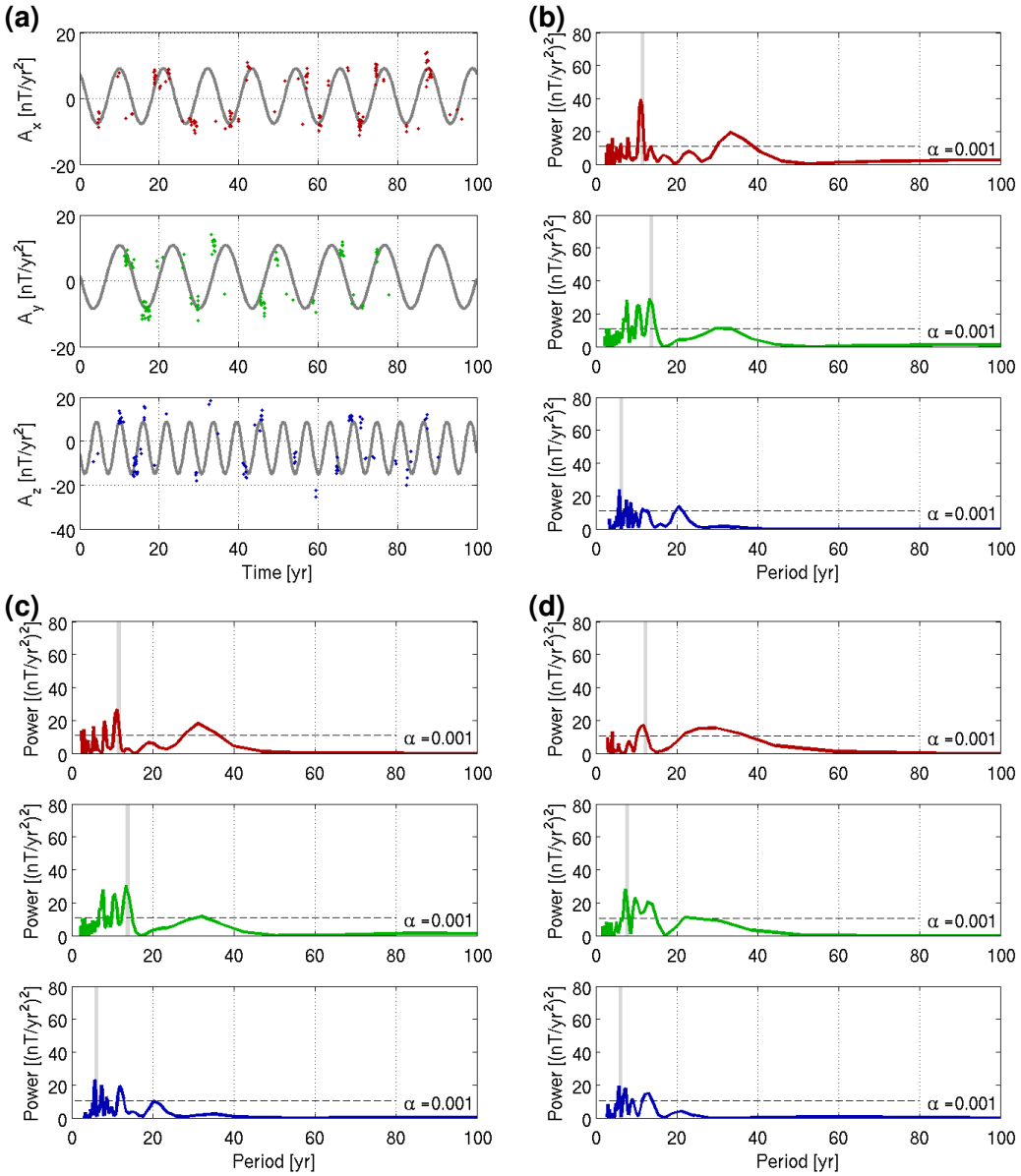

Figure F.11: Periodicity of synthetic jerk amplitudes detected with a 5 yr at spatially clustered observation points (orange region from Figure 5.11). The estimated jerk amplitudes are shown (a) along with the normalised Lomb periodogram for jerk amplitudes over 100 yrs (b), the first 75 yrs (c) and the first 50 yrs (d) for the X- (red), Y- (green) and Z-component (blue). Best fitting periods (grey) are marked on all plots, α is the statistical significance criteria, the sinusoids in (a) correspond to the marked periods in the 100 yr periodogram in (b).

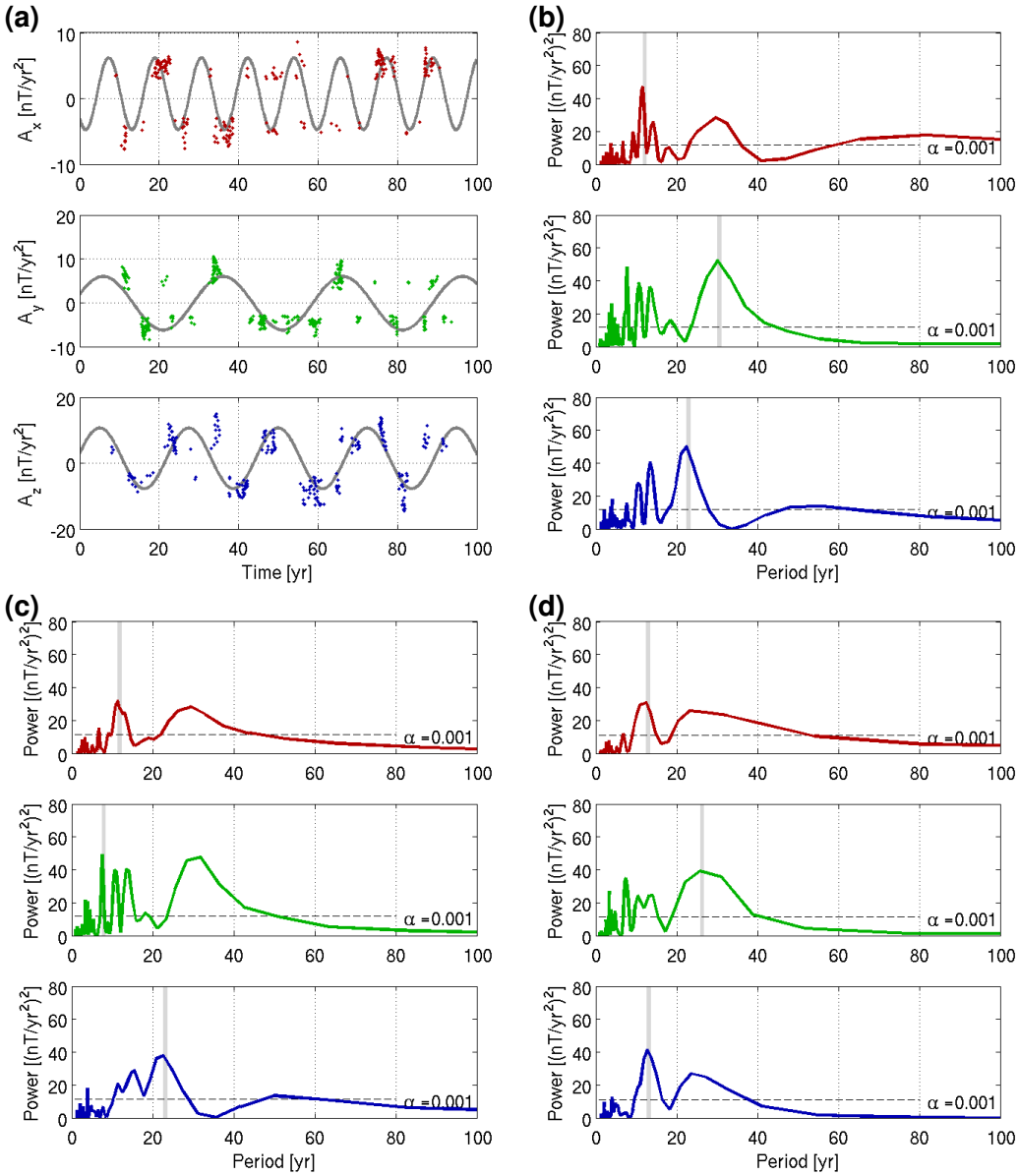

Figure F.12: Periodicity of synthetic jerk amplitudes detected with a 15 yr window at spatially clustered observation points (orange region from Figure 5.11). The estimated jerk amplitudes are shown (a) along with the normalised Lomb periodogram for jerk amplitudes over 100 yrs (b), the first 75 yrs (c) and the first 50 yrs (d) for the X- (red), Y- (green) and Z-component (blue). Best fitting periods (grey) are marked on all plots, α is the statistical significance criteria, the sinusoids in (a) correspond to the marked periods in the 100 yr periodogram in (b).

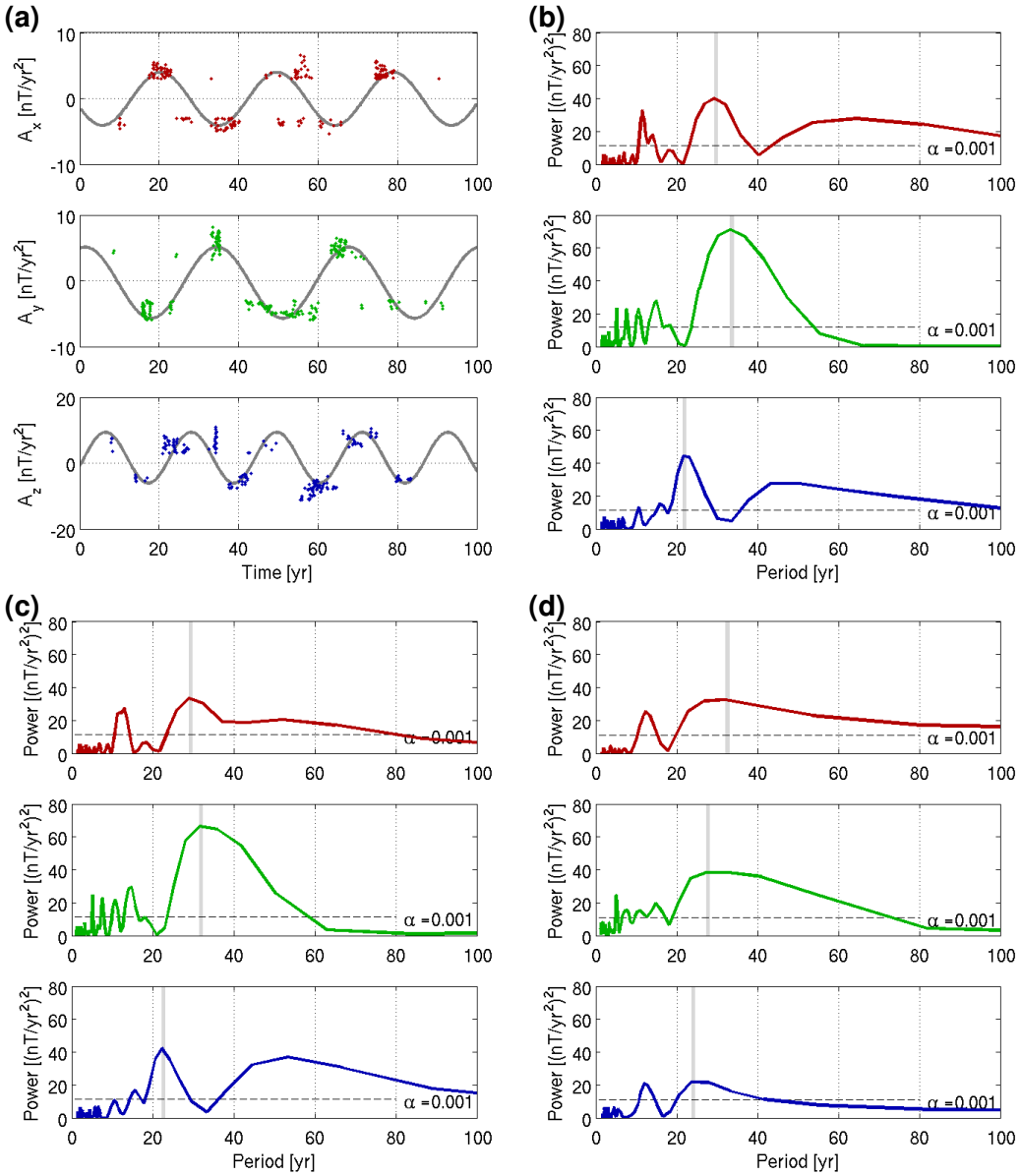

Figure F.13: Periodicity of synthetic jerk amplitudes detected with a 25 yr window at spatially clustered observation points (orange region from Figure 5.11). The estimated jerk amplitudes are shown (a) along with the normalised Lomb periodogram for jerk amplitudes over 100 yrs (b), the first 75 yrs (c) and the first 50 yrs (d) for the X- (red), Y- (green) and Z-component (blue). Best fitting periods (grey) are marked on all plots, α is the statistical significance criteria, the sinusoids in (a) correspond to the marked periods in the 100 yr periodogram in (b).

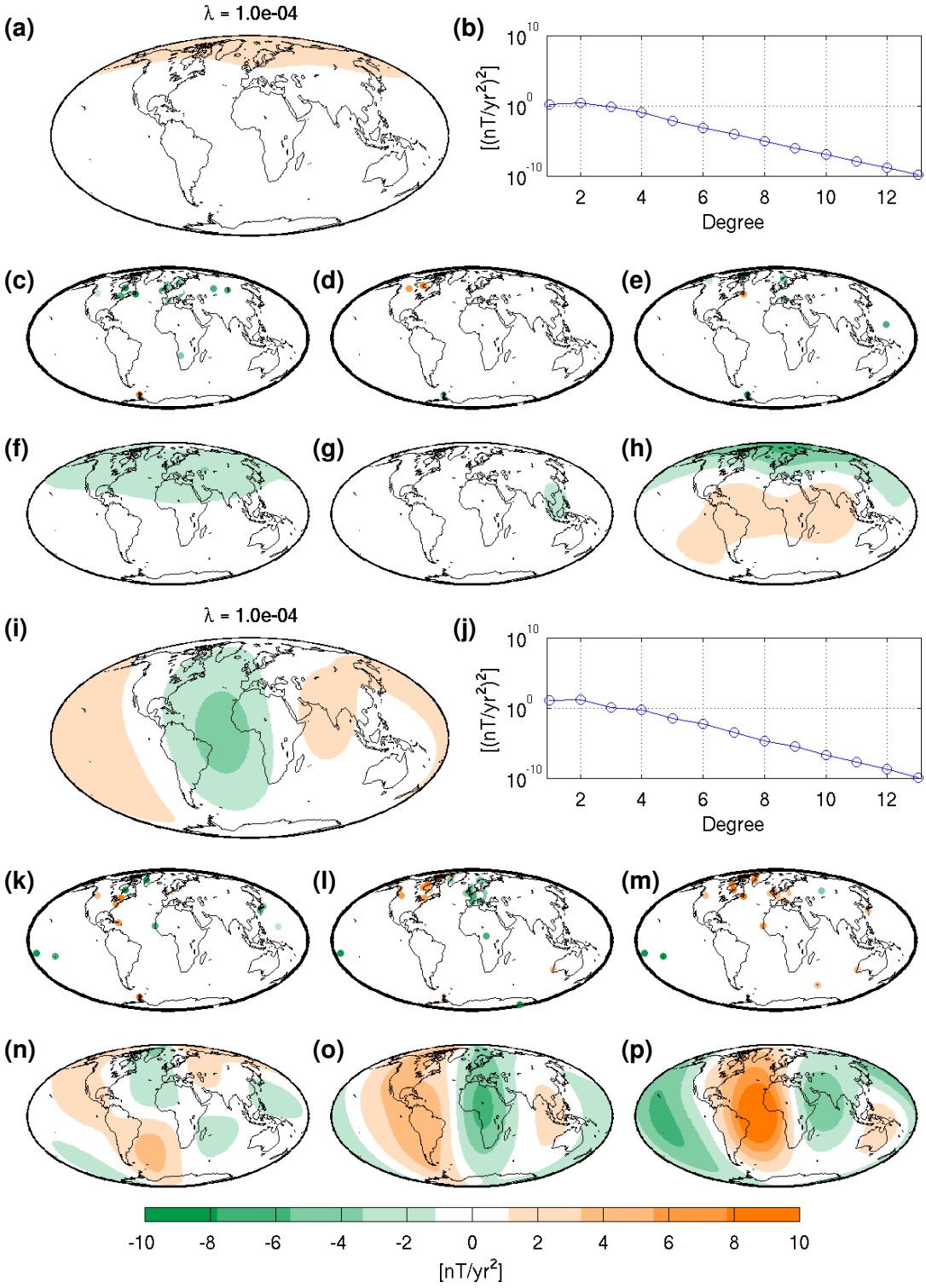

Figure F.14: SH model of the 1973–74 (a–h) and 1977–79 (i–p) peaks in jerk occurrences detected in observatory data. The potential (a,i) and its spatial power spectrum (b,j) are shown with the derived X-, Y- and Z-component models (f,g,h and k,l,m), respectively, and the X-, Y- and Z-component jerk amplitude data being modelled (c,d,e and n,o,p), respectively.

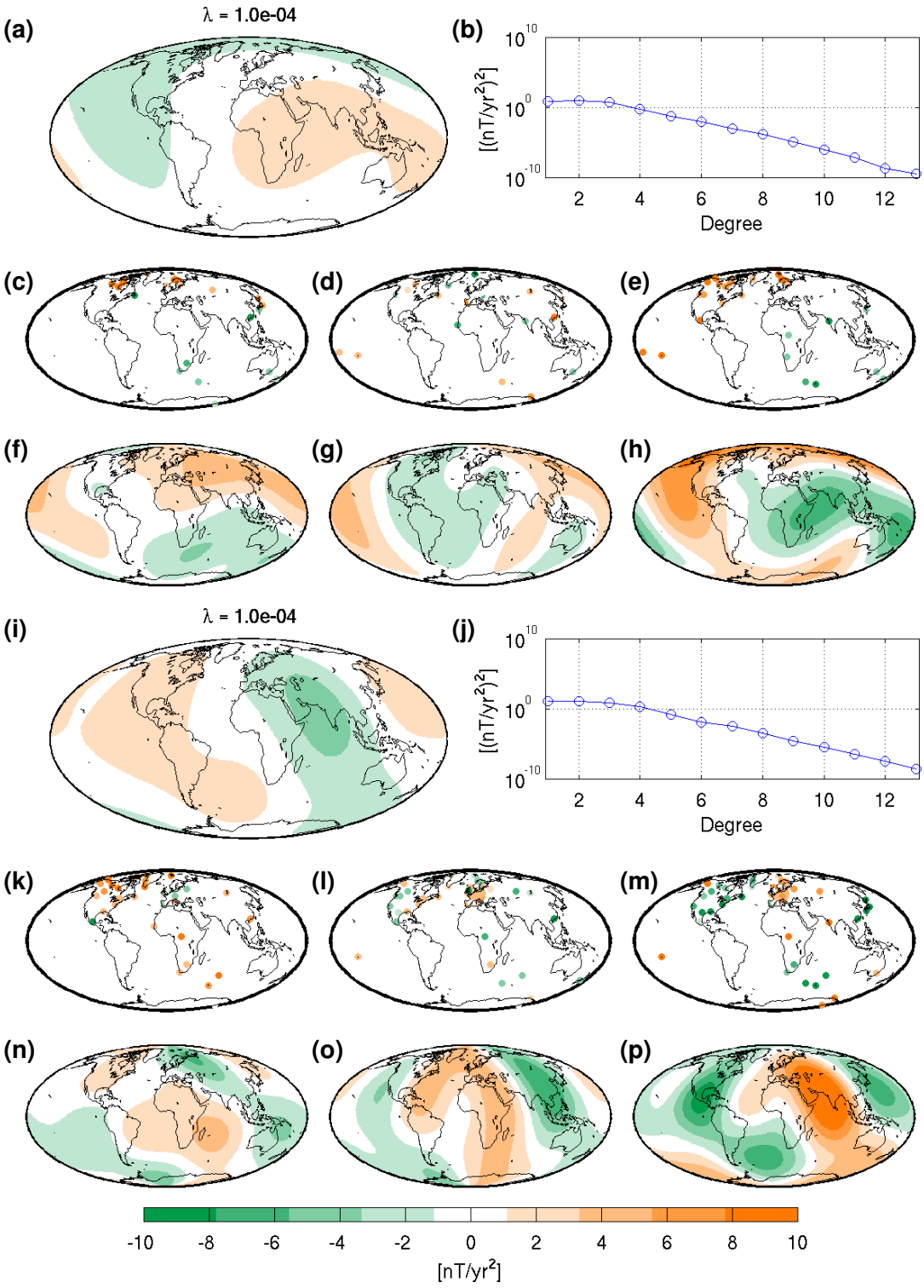

Figure F.15: SH model of the 1983–85 (a–h) and 1989–93 (i–p) peaks in jerk occurrences detected in observatory data. The potential (a,i) and its spatial power spectrum (b,j) are shown with the derived X-, Y- and Z-component models (f,g,h and k,l,m), respectively, and the X-, Y- and Z-component jerk amplitude data being modelled (c,d,e and n,o,p), respectively.

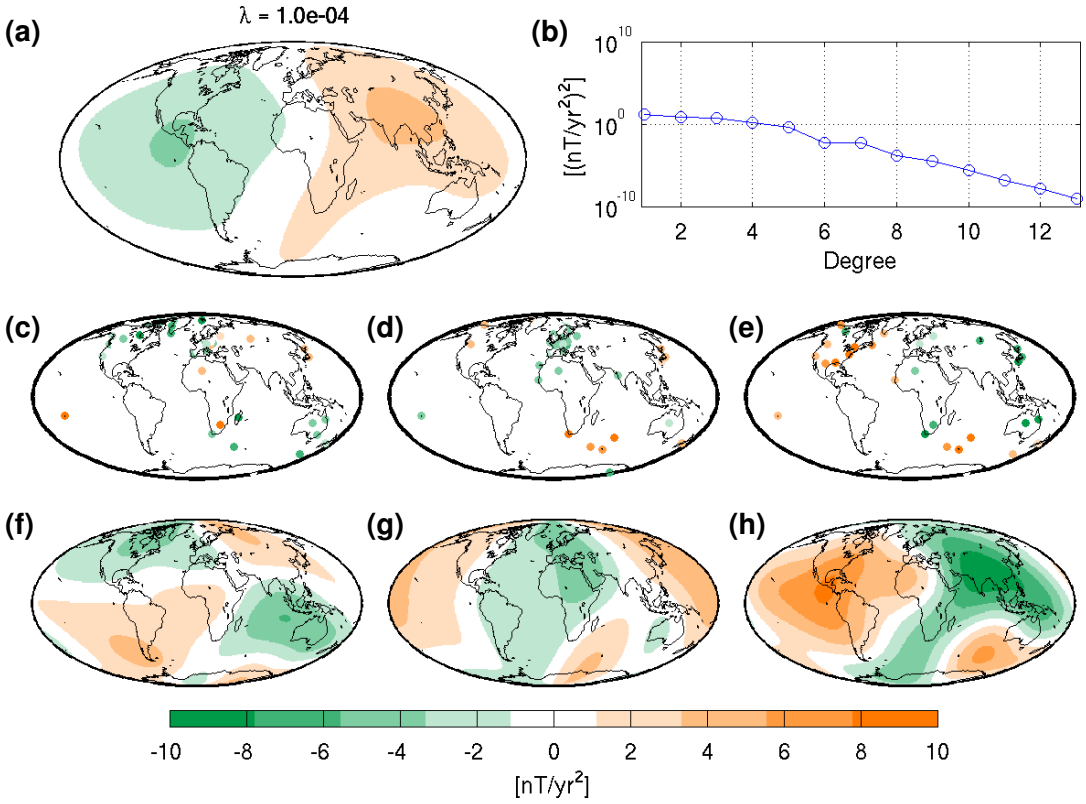

Figure F.16: SH model of the 1995–98 peak in jerk occurrences detected in observatory data. The potential (a) and its spatial power spectrum (b) are shown with the derived X-, Y- and Z-component models (f,g,h), respectively, and the X-, Y- and Z-component jerk amplitude data being modelled (c,d,e), respectively.

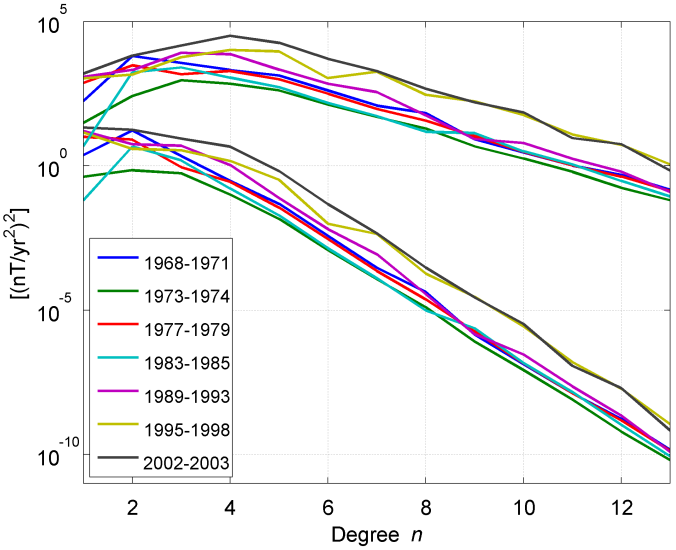

Figure F.17: Power spectra of SH models of jerk occurrences detected in observatory data. The upper group of spectra are for the models at the CMB, the lower group of spectra, for the models at the Earth's surface.

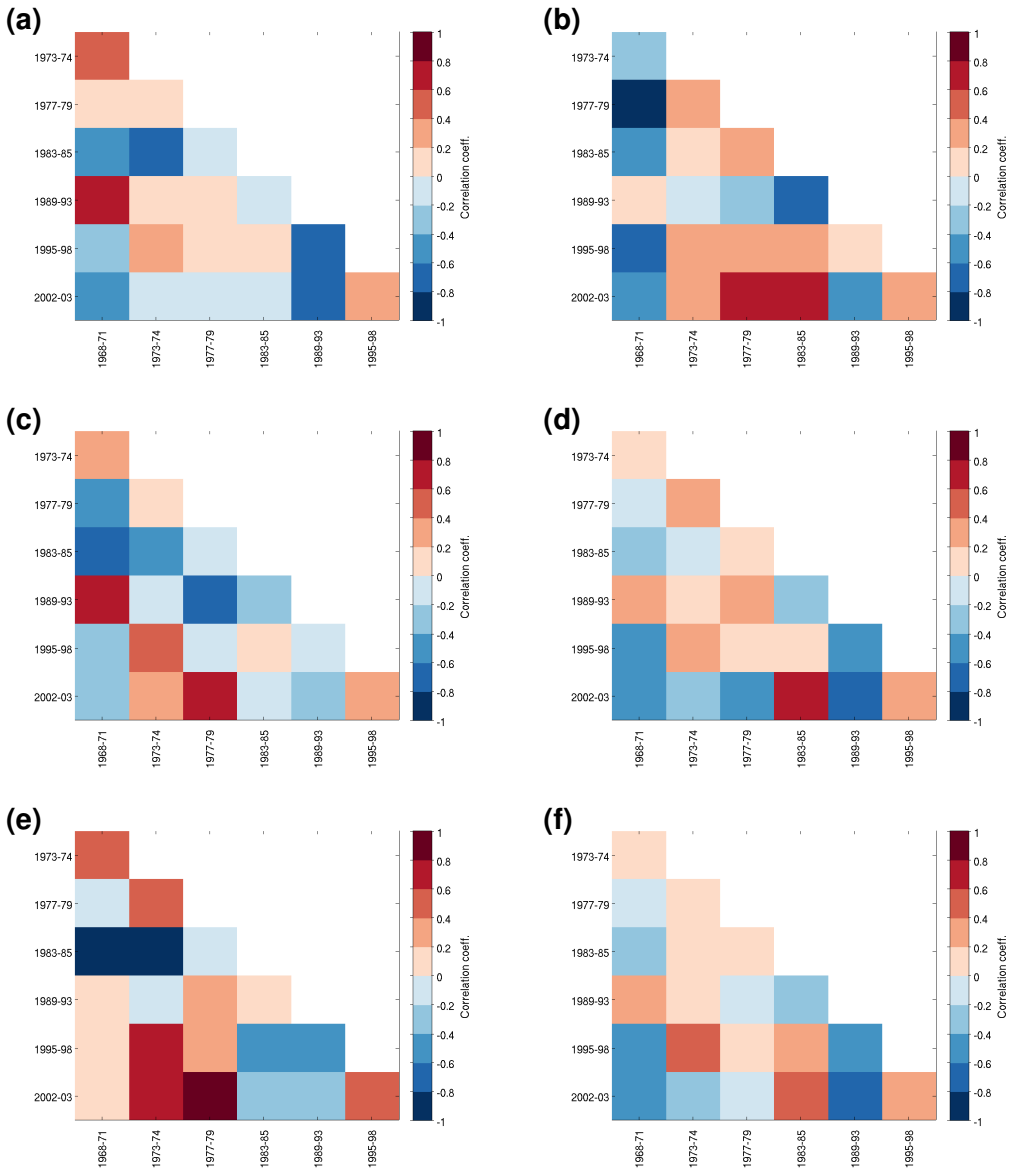

Figure F.18: Global correlation coefficients [after McLeod, 1985] for various coefficient subgroups of the seven jerk histogram peaks in observatory data. Correlation for the equatorially symmetric (a) and anti-symmetric (b), azimuthally symmetric (c) and anti-symmetric (d), zonal (e) and non-zonal (f) coefficient subgroups are shown.

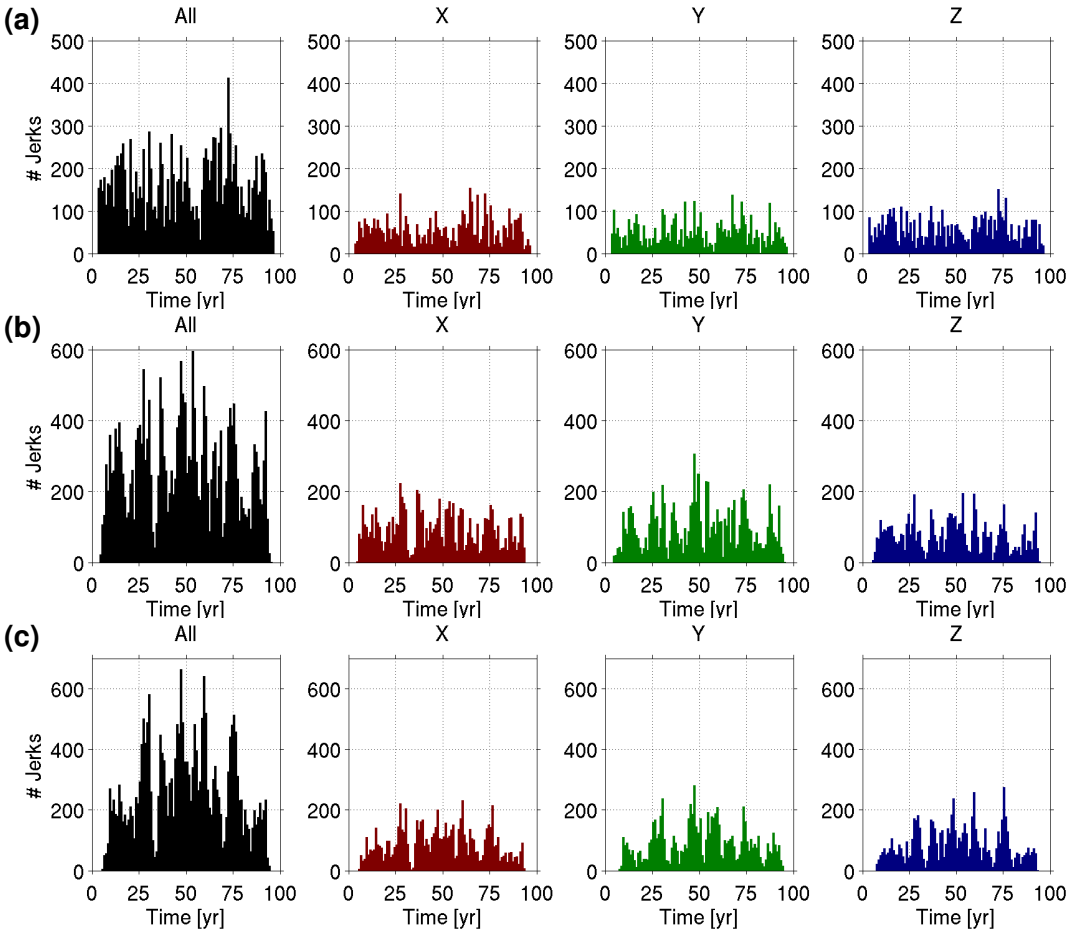

Figure F.19: Histograms of number of jerks detected in a 100 yr realisation of synthetic model, with a fixed dipole component, at 1620 STT cell locations, with 1 yr bins. Total count (black) and those for individual X- (red), Y- (green), and Z-components (blue) are shown for results using detection windows of 5 yr (a), 15 yr (b) and 25 yr (c).

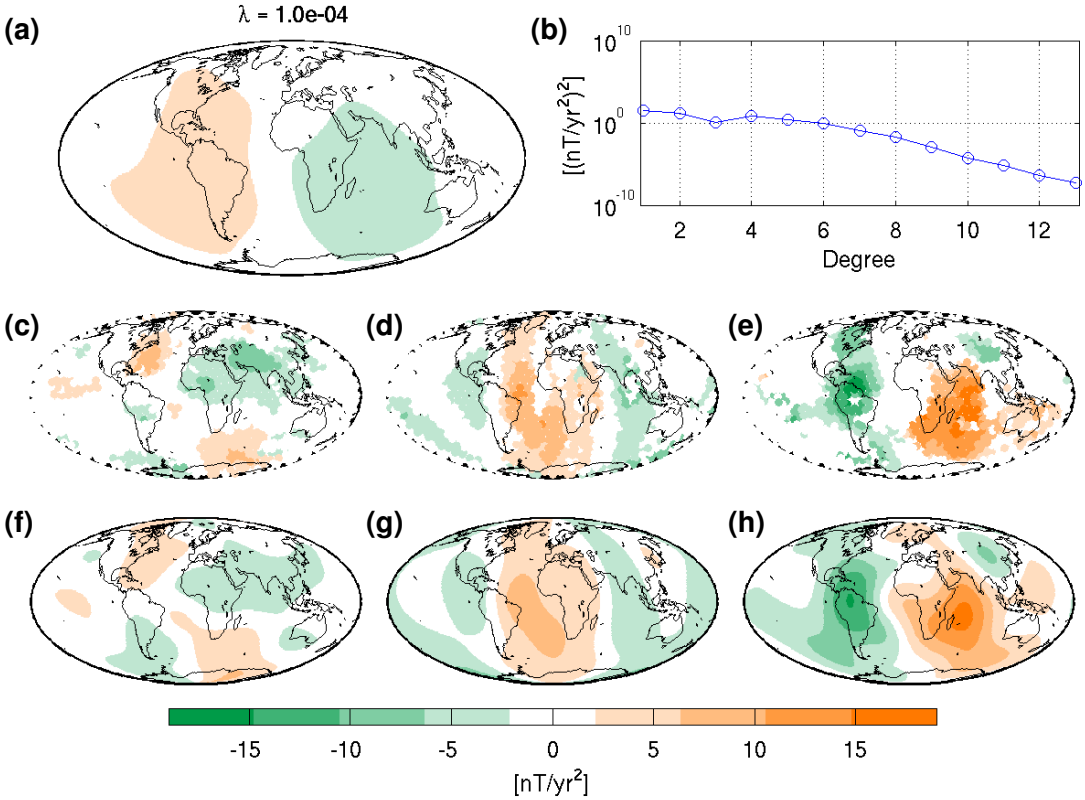

Figure F.20: SH model of the 45–49 yr peak in jerk occurrences detected in the fixed dipole model also depicted in Figure F.19. The potential (a) and its spatial power spectrum (b) are shown with the derived X, Y and Z component models (f,g,h), respectively, and the X-, Y- and Z-component jerk amplitude data being modelled (c,d,e), respectively.

REFERENCES

Abarco del Rio, R., D. Gambis, and D. A. Salstein (2000), Interannual signals in length of day and atmospheric angular momentum, *Ann. Geophys.*, *18*(3), 347–364, doi:10.1007/s00585-000-0347-9. 80

Alexandrescu, M., D. Gibert, G. Hulot, J.-L. Le Mouël, and G. Saracco (1995), Detection of geomagnetic jerks using wavelet analysis, *J. Geophys. Res.*, *100*(B7), 12,557–12,572, doi:10.1029/95JB00314. 22, 37

Alexandrescu, M., V. Courtillot, and J.-L. Le Mouël (1996a), Geomagnetic field direction in Paris since the mid-sixteenth century, *Phys. Earth Planet. Inter.*, *98*(3-4), 321–360, doi:10.1016/S0031-9201(96)03194-9. 36

Alexandrescu, M., D. Gibert, G. Hulot, J.-L. Le Mouël, and G. Saracco (1996b), Worldwide wavelet analysis of geomagnetic jerks, *J. Geophys. Res.*, *101*(B10), 21,975–21,994, doi:10.1029/96JB01648. 37, 38, 47, 67, 78, 85, 133, 147, 159

Alexandrescu, M., V. Courtillot, and J.-L. Le Mouël (1997), High-resolution secular variation of the geomagnetic field in western Europe over the last 4 centuries: Comparison and integration of historical data from Paris and London, *J. Geophys. Res.*, *102*(B9), 20,245–20,258, doi:10.1029/97JB01423. 38

Alldredge, L. (1984), A discussion of impulses and jerks in the geomagnetic-field, *J. Geophys. Res.*, *89*(NB6), 4403–4412, doi:10.1029/JB089iB06p04403. 22

Backus, G. (1983), Application of mantle filter theory to the magnetic jerk of 1969, *Geophys. J. Roy. Astr. S.*, *74*(3), 713–746. 22, 149, 150

Backus, G. E. (1968), Kinematics of geomagnetic secular variation in a perfectly conducting core, *Philos. T. R. Soc. S.-A*, *263*(1141), 239–266. 19

Backus, G. E. (1988), Bayesian inference in geomagnetism, *92*(1), 125–142, doi:10.1111/j.1365-246X.1988.tb01127.x. 87

Ballani, L., J. M. Hagedoorn, I. Wardinski, D. Stromeyer, and H. Greiner-Mai (2010), The 1991 geomagnetic jerk as seen at the Earth's surface and the core-mantle boundary, *Geophys. J. Int.*, *183*(2), 659–680, doi:10.1111/j.1365-246X.2010.04787.x. 151

Barraclough, D. (1995), Observations of the earth magnetic-field made in Edinburgh from 1670 to the present-day, *T. Roy. Soc. Edin.-Earth*, *85*(Part 4), 239–252. 36

Baumjohann, W., and R. Nakamura (2007), 5.03 - Magnetospheric Contributions to the Terrestrial Magnetic Field, in *Treatise on Geophysics*, edited by Kono, M. and Schubert, G., pp. 77–92, Elsevier, Amsterdam, doi:10.1016/B978-044452748-6.00088-2. 4, 7, 31

Beggan, C. D., and K. A. Whaler (2009), Forecasting change of the magnetic field using core surface flows and ensemble Kalman filtering, *Geophys. Res. Lett.*, *36*(18), doi:10.1029/2009GL039927. 25

Blanco, M. A., M. Flórez, and M. Bermejo (1997), Evaluation of the rotation matrices in the basis of real spherical harmonics, *J. Mol. Struc.-TheoChem*, *419*(1), 19–27. 105

Bloxham, J., and D. Gubbins (1985), The secular variation of earth's magnetic field, *Nature*, *317*, 777–781. 19

Bloxham, J., and A. Jackson (1991), Fluid-flow near the surface of earths outer core, *Rev. Geophys.*, *29*(1), 97–120, doi:10.1029/90RG02470. 19

Bloxham, J., S. Zatman, and M. Dumberry (2002), The origin of geomagnetic jerks, *Nature*, *420*(6911), 65–68, doi:10.1038/nature01131. 22, 77, 160, 168, 173

Brown, W., J. Mound, and P. Livermore (2013), Jerks abound: An analysis of geomagnetic observatory data from 1957 to 2008, *Phys. Earth Planet. Inter.*, *223*(0), 62–76, doi:10.1016/j.pepi.2013.06.001, SI:13th SEDI Conference. 38, 43, 48, 55, 57, 68, 69, 71, 72, 74, 75, 76, 77, 79, 82, 190, 191, 192, 193, 194, 195, 196

Buffett, B. (2014), Geomagnetic fluctuations reveal stable stratification at the top of the earth's core, *Nature*, *507*, 484–487, doi:10.1038/nature13122. 19, 159, 160, 168

Buffett, B. A., L. Ziegler, and C. G. Constable (2013), A stochastic model for palaeomagnetic field variations, *Geophys. J. Int.*, *195*(1), 86–97, doi:10.1093/gji/ggt218. 166

Buffett, B. A., E. M. King, and H. Matsui (2014), A physical interpretation of stochastic models for fluctuations in the earth's dipole field, *Geophys. J. Int.*, *198*(1), 597–608, doi:10.1093/gji/ggu153. 166

Cafarella, L., A. De Santis, and A. Meloni (1992), Secular variation in italy from hisorical geomagnetic-field measurements, *Phys. Earth Planet. Inter.*, *73*(3-4), 206–221, doi:10.1016/0031-9201(92)90091-9. 36

Chambodut, A., and M. Mandea (2005), Evidence for geomagnetic jerks in comprehensive models, *Earth Planets Space*, *57*(2), 139–149. 38, 72, 83

Chambodut, A., C. Eymin, and M. Mandea (2007), Geomagnetic jerks from the earth's surface to the top of the core, *Earth Planets Space*, *59*(7), 675–684, doi:10.1186/BF03352730. 38, 39, 85

Chulliat, A., and S. Maus (2014), Geomagnetic secular acceleration, jerks, and a localized standing wave at the core surface from 2000 to 2010, *J. Geophys. Res.-Sol. Ea.*, *119*(3), 1531–1543, doi:10.1002/2013JB010604. 23, 38, 134, 152, 153, 156, 157, 175

Chulliat, A., and K. Telali (2007), World Monthly Means DataBase Project, *Publ. Inst. Geophys. Pol. Acad. Sci.*, *C-99*(398). 56

Chulliat, A., S. Macmillan, P. Alken, C. Beggan, M. Nair, B. Hamilton, A. Woods, V. Ridley, S. Maus, and A. Thomson (2015), The US/UK World Magnetic Model for 2015-2020: Technical report, doi:10.7289/V5TB14V7. 13

Chulliat, A., E. Thébault, and G. Hulot (2010), Core field acceleration pulse as a common cause of the 2003 and 2007 geomagnetic jerks, *Geophys. Res. Lett.*, *37*, doi:10.1029/2009GL042019. 22, 38, 39, 68, 73, 78, 152

Constable, C. G., and S. C. Constable (2013), *Satellite Magnetic Field Measurements: Applications in Studying the Deep Earth*, pp. 147–159, American Geophysical Union, doi:10.1029/150GM13. 6

Courtillot, V., and J.-L. Le Mouël (1976), On the long-period variations of the earth's magnetic field from 2 months to 20 years, *J. Geophys. Res.*, *81*(17), 2941–2950. 30

Courtillot, V., J. Ducruix, and J.-L. Le Mouël (1978), Sur une acceleration recente de la variation seculaire du champ magnetique terrestre, *C. R. Acad. Sci.*, *D*(287), 1095–1098. 21, 156

Cowling, T. G. (1933), The magnetic field of sunspots, *Mon. Not. R. Astron. Soc.*, *94*, 39–48. 100

Cox, G., and W. Brown (2013), Rapid dynamics of the earth's core, *Astron. Geophys.*, *54*(5), 5.32–5.37, doi:10.1093/astrogeo/att167. 21, 24

Currie, R. G. (1968), Geomagnetic spectrum of internal origin and lower mantle conductivity, *J. Geophys. Res.*, *73*(8), 2779–2786, doi:10.1029/JB073i008p02779. 89, 95, 96, 97, 116, 178, 197

Currie, R. G. (1976), Long period magnetic activity - 2 to 100 years, *Astrophysics and Space Science*, *39*(1), 251–254, doi:10.1007/BF00640525. 80

Daglis, I. A., R. M. Thorne, W. Baumjohann, and S. Orsini (1999), The Terrestrial Ring Current: Origin, Formation, and Decay, *Rev. Geophys.*, *34*(7), 407–438, doi:8755-1209/99/1999RG900009. 31

De Boor, C. (2001), *A practical guide to splines*, *Mathematics of Computation*, vol. 27, Springer-Verlag, New York. 15

De Michelis, P., and R. Tozzi (2005), A Local Intermittency Measure (LIM) approach to the detection of geomagnetic jerks, *Earth Planet. Sci. Lett.*, *235*(1-2), 261–272, doi:10.1016/j.espl.2005.04.001. 37, 38, 47, 70, 72, 73, 85

De Michelis, P., L. Cafarella, and A. Meloni (1998), Worldwide character of the 1991 geomagnetic jerk, *Geophys. Res. Lett.*, *25*(3), 377–380. 34, 35, 38, 73

De Michelis, P., L. Cafarella, and A. Meloni (2000), A global analysis of the 1991 geomagnetic jerk, *Geophys. J. Int.*, *143*(3), 545–556, doi:10.1046/j.1365-246X.2000.00208.x. 34, 37, 38, 71, 73, 82, 115, 145

De Santis, A., D. Barraclough, and R. Tozzi (2003), Spatial and temporal spectra of the geomagnetic field and their scaling properties, *Phys. Earth Planet. Inter.*, *135*(2-3), 125–134, doi:10.1016/S0031-9201(02)00211-X. 89, 93, 95, 96, 97, 116, 178, 197, 198

Demetrescu, C., and V. Dobrica (2014), Multi-decadal ingredients of the secular variation of the geomagnetic field. Insights from long time series of observatory data, *Phys. Earth Planet. Inter.*, (0), –, doi:10.1016/j.pepi.2014.03.001, in press. 22, 174

Ducruix, J., V. Courtillot, and J.-L. Le Mouël (1980), The late 1960s secular variation impulse, the eleven year magnetic variation and the electrical conductivity of the deep mantle, *Geophys. J. Int.*, *61*(1), 73–94, doi:10.1111/j.1365-246X.1980.tb04305.x. 30

Dziewonski, A. M., and D. L. Anderson (1981), Preliminary reference Earth model, *Phys. Earth Planet. Inter.*, *25*(4), 297–356. 2

Eymin, C., and G. Hulot (2005), On core surface flows inferred from satellite magnetic data, *Phys. Earth Planet. Inter.*, *152*(3), 200 – 220, doi:10.1016/j.pepi.2005.06.009. 19

Finlay, C., M. Dumberry, A. Chulliat, and M. Pais (2010), Short timescale core dynamics: theory and observations, *Space Sci. Rev.*, *155*(1-4), 177–218, doi:10.1007/s11214-010-9691-6. 18

Finlay, C., N. Olsen, and L. Tøffner-Clausen (2014), Use of SWARM data in an update of the CHAOS-4 field model, 3rd SWARM Science Meeting. 12

Finlay, C. C., A. Jackson, N. Gillet, and N. Olsen (2012), Core surface magnetic field evolution 2000-2010, *Geophys. J. Int.*, *189*(2), 761–781, doi:10.1111/j.1365-246X.2012.05395.x. 90, 99

Fournier, A., G. Hulot, D. Jault, W. Kuang, A. Tangborn, N. Gillet, E. Canet, J. Aubert, and F. Lhuillier (2010), An introduction to data assimilation and predictability in geomagnetism, *Space Sci. Rev.*, *155*(1-4), 247–291. 25

Gallagher, K., K. Charvin, S. Nielsen, M. Sambridge, and J. Stephenson (2009), Markov chain Monte Carlo (MCMC) sampling methods to determine optimal models, model resolution and model choice for Earth Science problems, *Mar. Petrol. Geol.*, *26*(4), 525–535, doi:10.1016/j.marpetgeo.2009.01.003, Thematic Set on Basin Modeling Perspectives. 176

Gallagher, K., T. Bodin, M. Sambridge, D. Weiss, M. Kylander, and D. Large (2011), Inference of abrupt changes in noisy geochemical records using transdimensional changepoint models, *Earth Planet. Sci. Lett.*, *311*(1-2), 182–194, doi:10.1016/j.epsl.2011.09.015. 176

Garnero, E. J., and A. K. McNamara (2008), Structure and dynamics of Earth's lower mantle, *Science*, *320*(5876), 626–628, doi:10.1126/science.1148028. 174

Gavoret, J., D. Gibert, M. Menvielle, and J. Le Mouël (1986), Long-term variations of the external and internal components of the Earth's magnetic field, *J. Geophys. Res.*, *91*, 4787–4796. 34, 35

Gibert, D., and J.-L. Le Mouël (2008), Inversion of polar motion data: Chandler wobble, phase jumps, and geomagnetic jerks, *J. Geophys. Res.*, *113*(B10), doi:10.1029/2008JB005700. 23

Gillet, N., D. Jault, C. C. Finlay, and N. Olsen (2013), Stochastic modelling of the earth's magnetic field: Inversion for covariances over the observatory era, *Geochem. Geophys. Geosys.*, *14*(4), 766–786, doi:10.1002/ggge.20041. 15, 16, 17, 86, 87, 88, 89, 90, 91, 99, 100, 102, 116, 120, 121, 156, 160, 165, 166, 173, 177, 178

Gillet, N., M. A. Pais, and D. Jault (2009), Ensemble inversion of time-dependent core flow models, *Geochem. Geophys. Geosys.*, *10*, doi:10.1029/2008GC002290. 19, 20, 22, 87, 151

Gillet, N., D. Jault, E. Canet, and A. Fournier (2010), Fast torsional waves and strong magnetic field within the Earth's core, *Nature*, *465*, 74–77, doi:10.1038/nature09010. 80, 83

Golovkov, V., S. Yakovleva, and A. Simonyan (2003), Relation between geomagnetic jerks and the earth's rotation pole wander, *Izv. Phys. Solid Earth*, *39*(9), 741–748. 23

Golovkov, V. P., T. I. Zvereva, and A. O. Simonyan (1989), Common features and differences between "jerks" of 1947, 1958 and 1969, *Geophys. Astrophys. Fluid Dyn.*, *49*(1-4), 81–96, doi:10.1080/03091928908243465. 146

Gubbins, D. (1975), Can the earth's magnetic field be sustained by core oscillations?, *Geophys. Res. Lett.*, *2*(9), 409–412, doi:10.1029/GL002i009p00409. 109

Gubbins, D. (1983), Geomagnetic field analysis - i. stochastic inversion, *Geophys. J. Roy. Astr. S.*, *73*(3), 641–652, doi:10.1111/j.1365-246X.1983.tb03336.x. 15

Gubbins, D., and J. Bloxham (1985), Geomagnetic field analysis - iii. magnetic fields on the core-mantle boundary, *Geophys. J. Roy. Astr. S.*, *80*(3), 695–713, doi:10.1111/j.1365-246X.1985.tb05119.x. 87, 109

Gubbins, D., and L. Tomlinson (1986), Secular variation from monthly means from Apia and Amberley magnetic observatories, *Geophys. J. Int.*, *86*(2), 603–615, doi:10.1111/j.1365-246X.1986.tb03846.x. 34

Hagedoorn, J. M., and Z. Martinec (2015), The adjoint-state method for the downward continuation of the geomagnetic field, *Geophys. J. Int.*, *201*(2), 724–740, doi:10.1093/gji/ggv049. 19

Hellio, G., N. Gillet, C. Bouligand, and D. Jault (2014), Stochastic modelling of regional archaeomagnetic series, *Geophys. J. Int.*, *199*(2), 931–943, doi:10.1093/gji/ggu303. 15, 86, 87, 89, 91, 102, 121, 160, 161, 165, 167

Hernlund, J. W., C. Thomas, and P. J. Tackley (2005), A doubling of the post-perovskite phase boundary and structure of the Earth's lowermost mantle, *Nature*, *434*, 882–886, doi:10.1038/nature03472. 159, 168

Holme, R. (2007), 8.04 - Large-Scale Flow in the Core, in *Treatise on Geophysics*, edited by Olsen, P. and Schubert, G., pp. 107 – 130, Elsevier, Amsterdam, doi:10.1016/B978-044452748-6.00127-9. 18, 19

Holme, R., and O. de Viron (2005), Geomagnetic jerks and a high-resolution length-of-day profile for core studies, *Geophys. J. Int.*, *160*(2), 435–439, doi:10.1111/j.1365-246X.2004.02510.x. 23

Holme, R., and O. de Viron (2013), Characterization and implications of intradecadal variations in length of day, *Nature*, *499*, 202–204, doi:10.1038/nature12282. 23, 80, 157, 158, 159, 168

Holme, R., and K. Whaler (2001), Steady core flow in an azimuthally drifting reference frame, *Geophys. J. Int.*, *145*(2), 560–569, doi:10.1046/j.1365-246x.2001.01436.x. 22

Holme, R., N. Olsen, and F. L. Bairstow (2011), Mapping geomagnetic secular variation at the core-mantle boundary, *Geophys. J. Int.*, *186*(2), 521–528, doi:10.1111/j.1365-246X.2011.05066.x. 133, 150, 174

Horn, S. D., R. A. Horn, and D. B. Duncan (1975), Estimating heteroscedastic variances in linear models, *J. Am. Stat. Assoc.*, *70*(350), pp. 380–385. 95

Hulot, G., and J. Le Mouël (1994), A statistical approach to the Earth's main magnetic field, *Phys. Earth Planet. Inter.*, *82*(3-4), 167–183, doi:10.1016/0031-9201(94)90070-1. 90, 165

Isenberg, P. (1991), *Geomagnetism*, vol. 4, chap. The Solar Wind, pp. 1–85, Academic Press, London. 4

Jackson, A., and P. Livermore (2009), On Ohmic heating in the Earth's core I: Nutation constraints, *Geophys. J. Int.*, *177*(2), 367–382, doi:10.1111/j.1365-246X.2008.04008.x. 87

Jackson, A., J. Bloxham, and D. Gubbins (1993), *Time-Dependent Flow at the Core Surface and Conservation of Angular Momentum in The Coupled Core-Mantle System*, pp. 97–107, American Geophysical Union, Washington D.C., doi:10.1029/GM072p0097. 20, 158

Jackson, A., P. W. Livermore, and G. Ierley (2011), On Ohmic heating in the Earth's core II: Poloidal magnetic fields obeying Taylor's constraint, *Phys. Earth Planet. Inter.*, *187*(3 - 4), 322 – 327, doi:10.1016/j.pepi.2011.06.003, SI: Planetary Magnetism, Dynamo and Dynamics. 87

Jackson, A., A. Jonkers, and M. Walker (2000), Four centuries of geomagnetic secular variation from historical records, *Philos. T. R. Soc. S.-A*, *358*(1768), 957–990, doi:10.1098/rsta.2000.0569. 8, 15, 17, 86, 87, 109

Jault, D. (1988), Westward drift, core motions and exchanges of angular momentum between core and mantle, *Nature*, *333*, 353–356. 20

Jault, D. (2015), Illuminating the electrical conductivity of the lowermost mantle from below, *Geophys. J. Int.*, *202*(1), 482–496, doi:10.1093/gji/ggv152. 150

Karinen, A., and K. Mursula (2005), A new reconstruction of the D-st index for 1932-2002, *Ann. Geophys.*, *23*(2), 475–485. 33, 35

Karinen, A., and K. Mursula (2006), Correcting the Dst index: Consequences for absolute level and correlations, *J. Geophys. Res.-Space*, *111*(A8), doi:10.1029/2005JA011299. 33

Kennett, B., E. Engdahl, and R. Buland (1995), Constraints on seismic velocities in the earth from traveltimes, *Geophys. J. Int.*, *122*(1), 108–124. 2, 3

Kivelson, M. G., and C. T. Russell (1995), *Introduction to Space Physics*, Cambridge University Press. 5, 31, 32

Korte, M., and C. Constable (2011), Improving geomagnetic field reconstructions for 0–3ka, *Phys. Earth Planet. Inter.*, *188*(3), 247–259. 17, 160, 167

Korte, M., M. Mandea, and J. Matzka (2009), A historical declination curve for Munich from different data sources, *Phys. Earth Planet. Inter.*, *177*(3-4), 161–172, doi:10.1016/j.pepi.2009.08.005. 36, 38

Kuang, W., A. Tangborn, W. Jiang, D. Liu, Z. Sun, J. Bloxham, and Z. Wei (2008), MoSST-DAS: the first generation geomagnetic data assimilation framework, *Commun. Comput. Phys*, *3*(1), 85–108. 25

Lagarias, J., J. A. Reeds, M. H. Wright, and P. E. Wright (1998), Convergence properties of the Nelder-Mead simplex method in low dimensions, *SIAM J. Optimiz.*, *9*(1), 112–147. 95

Langel, R., J. Ridgway, M. Sugiura, and K. Maezawa (1988), The geomagnetic field at 1982 from DE-2 and other magnetic field data., *J. Geomag. Geoelec.*, *40*(9), 1103–1127. 12

Langel, R. A. (1989), *Geomagnetism*, vol. 1, chap. The Main Geomagnetic Feld, Academic Press, London. 13, 33, 80

Langel, R. A., and R. H. Estes (1985), The near-Earth magnetic field at 1980 determined from Magsat data, *J. Geophys. Res.-Sol. Ea.*, *90*(B3), 2495–2509, doi:10.1029/JB090iB03p02495. 12

Langel, R. A., and W. J. Hinze (1998), *The magnetic field of the Earth's lithosphere: the satellite perspective*, Cambridge University Press. 12

Le Huy, M., M. Alexandrescu, G. Hulot, and J.-L. Le Mouël (1998), On the characteristics of successive geomagnetic jerks, *Earth Planets Space*, *50*(9), 723–732. 22, 37, 38, 71, 72, 73, 78, 82, 111, 115, 134, 144, 145, 147, 148, 151, 165

Le Mouël, J.-L., J. Ducruix, and C. Duyen (1982), The worldwide character of the 1969-1970 impulse of the secular acceleration rate, *Phys. Earth Planet. Inter.*, *28*(4), 337–350, doi:10.1016/0031-9201(82)90090-5. 37, 38, 71

Lesur, V., I. Wardinski, M. Rother, and M. Mandea (2008), GRIMM: the GFZ Reference Internal Magnetic Model based on vector satellite and observatory data, *Geophys. J. Int.*, *173*(2), 382–394, doi:10.1111/j.1365-246X.2008.03724.x. 15

Lesur, V., I. Wardinski, M. Hamoudi, and M. Rother (2010), The second generation of the GFZ Reference Internal Magnetic Model: GRIMM-2, *Earth Planets Space*, *62*, 765–773, doi:10.5047/eps.2010.07.007. 15, 17, 90, 99

Lomb, N. R. (1976), Least-squares frequency analysis of unequally spaced data, *Astrophys. Space Sci.*, *39*(2), 447–462. 78

Love, J. J., and J. L. Gannon (2009), Revised D_{st} and the epicycles of magnetic disturbance: 1958–2007, *Ann. Geofis.*, *27*(8), 3101–3131, doi:10.5194/angeo-27-3101-2009. 33

Love, J. J., and K. J. Remick (2007), *Encyclopedia of Geomagnetism and Paleomagnetism*, chap. Magnetic Indices, Springer. 31

Lowes, F. J. (1966), Mean-square values on sphere of spherical harmonic vector fields, *J. Geophys. Res.*, *71*, 2179. 16

Malin, S., and E. Bullard (1981), The direction of the Earth's magnetic-field at London, 1570–1975, *Philos. T. R. Soc. A*, *299*(1450), 357–&, doi:10.1098/rsta.1981.0026. 36

Malin, S., and B. Hodder (1982), Was the 1970 geomagnetic jerk of internal or external origin?, *Geophys. J. Int.*, *69*(1), 289. 22, 111, 115, 144, 160, 168

Mandea, M., and N. Olsen (2009), Geomagnetic and Archeomagnetic Jerks: Where Do We Stand?, *EOS Trans. AGU*, *90*(24), 208, doi:10.1029/2009EO240004. 20, 177

Mandea, M., E. Bellanger, and J.-L. Le Mouël (2000), A geomagnetic jerk for the end of the 20th century?, *Earth Planet. Sci. Lett.*, *183*(3-4), 369–373, doi:10.1016/S0012-821X(00)00284-3. 38, 73

Mandea, M., R. Holme, A. Pais, K. Pinheiro, A. Jackson, and G. Verbanac (2010), Geomagnetic Jerks: Rapid Core Field Variations and Core Dynamics, *Space Sci. Rev.*, *155*(1-4), 147–175, doi:10.1007/s11214-010-9663-x. 23, 36

Manhes, G., C. J. Allègre, B. Dupré, and B. Hamelin (1980), Lead isotope study of basic-ultrabasic layered complexes: Speculations about the age of the Earth and primitive mantle characteristics, *Earth Planet. Sci. Lett.*, *47*(3), 370–382, doi:10.1016/0012-821X(80)90024-2. 4

Manoj, C., A. Kuvshinov, S. Maus, and H. Lühr (2006), Ocean circulation generated magnetic signals, *Earth Planets Space*, *58*(4), 429–437. 7

Masters, G., and K. Richards-Dinger (1998), On the efficient calculation of ordinary and generalized spherical harmonics, *Geophys. J. Int.*, *135*(1), 307–309, doi:10.1046/j.1365-246X.1998.00622.x. 105

Matérn, B. (1960), *Spatial variation: Stochastic models and their application to some problems in forest surveys and other sampling investigations*, *Medd. Statens Skogsforskningsinst*, vol. 49, Almaenna Foerlaget, Stockholm. Second edition (1986), Springer-Verlag, Berlin. 88

Mauersberger, P. (1956), Das Mittel der Energiedichte des geomagnetischen Hauptfeldes an der Erdoberflache und seine sakulare Anderung, *Gerlands Beitr. Geophys.*, *65*, 207–215. 16

Maus, S., M. Rother, C. Stolle, W. Mai, S. Choi, H. Lühr, D. Cooke, and C. Roth (2006), Third generation of the Potsdam Magnetic Model of the Earth (POMME), *Geochem. Geophys. Geosys.*, *7*(7), doi:10.1029/2006GC001269. 15

Maus, S., H. Lühr, M. Rother, K. Hemant, G. Balasis, P. Ritter, and C. Stolle (2007), Fifth-generation lithospheric magnetic field model from champ satellite measurements, *Geochem. Geophys. Geosys.*, *8*(5), doi:10.1029/2006GC001521. 13

Maus, S., F. Yin, H. Lühr, C. Manoj, M. Rother, J. Rauberg, I. Michaelis, C. Stolle, and R. D. Müller (2008), Resolution of direction of oceanic magnetic lineations by the sixth-generation lithospheric magnetic field model from CHAMP satellite magnetic measurements, *Geochem. Geophys. Geosys.*, *9*(7), doi:10.1029/2008GC001949. 6

Mayaud, P. N. (1980), *Derivation, Meaning, and Use of Geomagnetic Indices*, no. 22 in Geophysical Monograph, American Geophysical Union, Washington D.C. 30, 31, 32, 33, 34

McElhinny, M. W., and W. E. Senanayake (1980), Paleomagnetic evidence for the existence of the geomagnetic field 3.5 ga ago, *J. Geophys. Res.-Sol. Ea.*, *85*(B7), 3523–3528, doi:10.1029/JB085iB07p03523. 4

McEwen, J. D., M. P. Hobson, and A. N. Lasenby (2006), A directional continuous wavelet transform on the sphere, *ArXiv*. 104, 105

McLeod, M. G. (1985), On the geomagnetic jerk of 1969, *J. Geophys. Res.-Sol. Ea.*, *90*(B6), 4597–4610. 135, 136, 144, 149, 212, 221

Mursula, K., and A. Karinen (2005), Explaining and correcting the excessive semiannual variation in the Dst index, *Geophys. Res. Lett.*, *32*(14), doi:10.1029/2005GL023132. 33

Mursula, K., L. Holappa, A. Karinen, and T. Leikanger (2011), *Dcx Server Info and Manual*, University of Oulu, http://soteria-space.eu/docs_tools/Dcx_server_manual_28.10.2011.pdf, 2015-03. 33

Nagao, H., T. Iyemori, T. Higuchi, S. Nakano, and T. Araki (2002a), Local time features of geomagnetic jerks, *Earth Planets Space*, *54*(2), 119–131. 22, 37

Nagao, H., T. Higuchi, T. Iyemori, and T. Araki (2002b), Automatic detection of geomagnetic jerks by applying a statistical time series model to geomagnetic monthly means, in *Progress in Discovery Science*, *Lecture Notes in Computer Science*, vol. 2281, edited by S. Arikawa and A. Shinohara, pp. 360–371, Springer Berlin Heidelberg, doi:10.1007/3-540-45884-0_26. 37

Nagao, H., T. Iyemori, T. Higuchi, and T. Araki (2003), Lower mantle conductivity anomalies estimated from geomagnetic jerks, *J. Geophys. Res.*, *108*(B5), doi:10.1029/2002JB001786. 24, 38, 39, 149

Nakada, M. (2009), Earth's rotational variations by electromagnetic coupling due to core surface flow on a timescale of similar to 1 yr for geomagnetic jerk, *Geophys. J. Int.*, *179*(1), 521–535, doi:10.1111/j.1365-246X.2009.04256.x. 23

Nakada, M. (2011), Earth's rotational variations due to rapid surface flows at both boundaries of the outer core, *Geophys. J. Int.*, *184*(1), 235–246, doi:10.1111/j.1365-246X.2010.04862.x. 23

Neubert, T., M. Mandea, G. Hulot, R. von Frese, F. Primdahl, J. L. Jrgensen, E. Friis-Christensen, P. Stauning, N. Olsen, and T. Risbo (2001), Ørsted satellite captures high-precision geomagnetic field data, *EOS Trans. AGU*, *82*(7), 81–88, doi:10.1029/01EO00043. 12

Nevanlinna, H. (1985), On external and internal parts of the geomagnetic jerk of 1970, *Phys. Earth Planet. Inter.*, *39*(4), 265–269, doi:10.1016/0031-9201(85)90139-6. 22

Olsen, N. (2002), A model of the geomagnetic field and its secular variation for epoch 2000 estimated from Ørsted data, *Geophys. J. Int.*, *149*(2), 454–462. 35, 185

Olsen, N., and M. Mandea (2007), Investigation of a secular variation impulse using satellite data: The 2003 geomagnetic jerk, *Earth Planet. Sci. Lett.*, *255*(1-2), 94–105, doi:10.1016/j.epsl.2006.12.008. 37, 38, 39, 73, 108, 134, 142, 145, 146, 169, 173, 177, 179

Olsen, N., and M. Mandea (2008), Rapidly changing flows in the Earth's core, *Nature Geosci.*, *1*(6), 390–394, doi:10.1038/ngeo203. 17, 22, 38, 39, 68, 73, 134, 149, 157, 160, 169

Olsen, N., T. J. Sabaka, and F. Lowes (2005), New parameterization of external and induced fields in geomagnetic field modeling, and a candidate model for IGRF 2005, *Earth, Planets and Space*, *57*(12), 1141–1149, doi:10.1186/BF03351897. 185

Olsen, N., H. Lühr, T. J. Sabaka, M. Mandea, M. Rother, L. Tøffner-Clausen, and S. Choi (2006), CHAOS – a model of the Earth's magnetic field derived from CHAMP, Ørsted, and SAC-C magnetic satellite data, *Geophys. J. Int.*, *166*(1), 67–75, doi:10.1111/j.1365-246X.2006.02959.x. 12, 17

Olsen, N., G. Hulot, and T. Sabaka (2007), 5.02 - The Present Field, in *Treatise on Geophysics*, edited by M. Kono and G. Schubert, pp. 33–75, Elsevier, Amsterdam, doi:10.1016/B978-044452748-6.00087-0. 6, 7, 10

Olsen, N., H. Lühr, C. C. Finlay, T. J. Sabaka, I. Michaelis, J. Rauberg, and L. Tøffner-Clausen (2014), The CHAOS-4 geomagnetic field model, *Geophys. J. Int.*, *197*(2), 815–827. 15, 17, 18, 35, 152, 153, 176, 185, 186, 187, 188

Olsen, N., G. Hulot, V. Lesur, C. C. Finlay, C. Beggan, A. Chulliat, T. J. Sabaka, R. Floberghagen, E. Friis-Christensen, R. Haagmans, S. Kotsiaros, H. Lühr, L. Tøffner-Clausen, and P. Vigneron (2015), The Swarm Initial Field Model for the 2014 geomagnetic field, *Geophys. Res. Lett.*, doi:10.1002/2014GL062659. 10, 12, 13

Olsen, N., M. Mandea, T. J. Sabaka, and L. Tøffner-Clausen (2009), CHAOS-2-a geomagnetic field model derived from one decade of continuous satellite data, *Geophys. J. Int.*, *179*(3), 1477–1487, doi:10.1111/j.1365-246X.2009.04386.x. 35, 38, 39, 68, 73, 85

Olson, P., and H. Amit (2006), Changes in Earth's dipole, *Naturwissenschaften*, *93*(11), 519–542, doi:10.1007/s00114-006-0138-6. 104

Pinheiro, K., and A. Jackson (2008), Can a 1-D mantle electrical conductivity model generate magnetic jerk differential time delays?, *Geophys. J. Int.*, *173*(3), 781–792, doi:10.1111/j.1365-246X.2008.03762.x. 22, 81, 142, 149, 169, 172

Pinheiro, K. J., A. Jackson, and H. Amit (2015), On the applicability of Backus' mantle filter theory, *Geophys. J. Int.*, *200*(3), 1336–1346, doi:10.1093/gji/ggu477. 149, 169

Pinheiro, K. J., A. Jackson, and C. C. Finlay (2011), Measurements and uncertainties of the occurrence time of the 1969, 1978, 1991, and 1999 geomagnetic jerks, *Geochem. Geophys. Geosys.*, *12*, doi:10.1029/2011GC003706. 30, 38, 39, 40, 45, 46, 47, 58, 60, 62, 64, 70, 71, 73, 81, 82, 83, 111, 115, 133, 144, 145, 149, 172

Pozzo, M., C. Davies, D. Gubbins, and D. Alfè (2012), Thermal and electrical conductivity of iron at Earth's core conditions, *Nature*, *485*(7398), 355–358, doi:10.1038/nature11031. 19

Press, W. H., S. A. Teukolsky, W. T. Vetterling, and B. P. Flannery (2007), *Numerical Recipes: The Art of Scientific Computing*, chap. 13.8, pp. 685–692, third ed., Cambridge University Press. 80

Prestes, A., N. Rigozo, E. Echer, and L. Vieira (2006), Spectral analysis of sunspot number and geomagnetic indices (1868–2001), *J. Atmos. Sol.-Terr. Phy.*, *68*(2), 182–190, doi:10.1016/j.jastp.2005.10.010. 80

Qamili, E., A. De Santis, A. Isac, M. Mandea, B. Duka, and A. Simonyan (2013), Geomagnetic jerks as chaotic fluctuations of the Earth's magnetic field, *Geochem. Geophys. Geosys.*, *14*(4), 839–850, doi:10.1029/2012GC004398. 23, 38, 39

Rangarajan, G. K. (1987), *Geomagnetism*, vol. 3, chap. Indices of Geomagnetic Activity, pp. 323–384, Academic Press, London. 31, 33, 34

Rasmussen, C., and C. Williams (2006), *Gaussian Processes for Machine Learning*, MIT Press, Cambridge. 89

Reigber, Ch., H. Lühr, and P. Schwintzer (2002), CHAMP mission status, *Adv. Space Res.*, *30*(2), 129 – 134, doi:10.1016/S0273-1177(02)00276-4. 12

Roberts, P. H., and S. Scott (1965), On analysis of the secular variation, *J. Geomag. Geoelec.*, *17*(2), 137–151. 18, 19

Rost, S., E. J. Garnero, Q. Williams, and M. Manga (2005), Seismological constraints on a possible plume root at the core-mantle boundary, *Nature*, *435*, 666–669, doi:10.1038/nature03620. 174

Sabaka, T., N. Olsen, and R. Langel (2002), A comprehensive model of the quiet-time, near-Earth magnetic field: phase 3, *Geophys. J. Int.*, *151*(1), 32–68, doi:10.1046/j.1365-246X.2002.01774.x. 13, 35

Sabaka, T., N. Olsen, and M. Purucker (2004), Extending comprehensive models of the Earth's magnetic field with Ørsted and CHAMP data, *Geophys. J. Int.*, *159*(2), 521–547, doi:10.1111/j.1365-246X.2004.02421.x. 13, 17, 35, 58, 134, 147, 148

Sabaka, T. J., N. Olsen, R. H. Tyler, and A. Kuvshinov (2015), CM5, a pre-Swarm comprehensive geomagnetic field model derived from over 12 yr of CHAMP, rsted, SAC-C and observatory data, *Geophys. J. Int.*, *200*(3), 1596–1626, doi:10.1093/gji/ggu493. 13, 35

Scargle, J. D. (1982), Studies in astronomical time series analysis II. Statistical aspects of spectral analysis of unevenly sampled data, *Astrophys. J.*, *263*, 835–853. 78

Shen, C., Z. J. Rong, M. W. Dunlop, Y. H. Ma, X. Li, G. Zeng, G. Q. Yan, W. X. Wan, Z. X. Liu, C. M. Carr, and H. Rme (2012), Spatial gradients from irregular, multiple-point spacecraft configurations, *J. Geophys. Res.-Space*, *117*(A11), doi:10.1029/2012JA018075. 36, 149

Shore, R., K. Whaler, S. Macmillan, C. Beggan, N. Olsen, T. Spain, and A. Aruliah (2013), Ionospheric midlatitude electric current density inferred from multiple magnetic satellites, *J. Geophys. Res.-Space*, *118*(9), 5813–5829. 36

Silva, L., and G. Hulot (2012), Investigating the 2003 geomagnetic jerk by simultaneous inversion of the secular variation and acceleration for both the core flow and its acceleration, *Phys. Earth Planet. Inter.*, *198*(0), 28–50, doi:10.1016/j.pepi.2012.03.002. 22, 149, 151, 157, 159, 160, 169

Silva, L., L. Jackson, and J. Mound (2012), Assessing the importance and expression of the 6-year geomagnetic oscillation, *J. Geophys. Res.*, *117*(B10101), doi:10.1029/2012JB009405. 80, 83, 178, 198

Sivia, D., and J. Skilling (2006), *Data analysis: a Bayesian tutorial*, Oxford science publications, Oxford University Press. 46

Soare, A., G. Cucu, and M. Alexandrescu (1998), Historical geomagnetic measurements in Romania, *Ann. Geofis.*, *41*(4), 539–554. 36

Stein, M. (1999), *Interpolation of spatial data: some theory for kriging*, Springer Series in Statistics, Springer-Verlag, New York. 88

Stewart, D., and K. Whaler (1992), Geomagnetic disturbance fields - an analysis of observatory monthly means, *Geophys. J. Int.*, *108*(1), 215–223, doi:10.1111/j.1365-246X.1992.tb00851.x. 30, 34, 49

Stewart, D., and K. Whaler (1995), Optimal piecewise regression-analysis and its application to geomagnetic time-series, *Geophys. J. Int.*, *121*(3), 710–724, doi:10.1111/j.1365-246X.1995.tb06433.x. 35, 37, 47

Tarduno, J. A., R. D. Cottrell, M. K. Watkeys, A. Hofmann, P. V. Doubrovine, E. E. Mamajek, D. Liu, D. G. Sibeck, L. P. Neukirch, and Y. Usui (2010), Geodynamo, solar wind, and magnetopause 3.4 to 3.45 billion years ago, *Science*, *327*(5970), 1238–1240, doi:10.1126/science.1183445. 4

Thébault, E., M. Purucker, K. A. Whaler, B. Langlais, and T. J. Sabaka (2010), The magnetic field of the Earth's lithosphere, *Space Sci. Rev.*, *155*(1-4), 95–127. 5

Thébault, E., C. Finlay, P. Alken, C. Beggan, A. Du, G. Hulot, V. Lesur, F. Lowes, S. Maus, N. Olsen, V. Petrov, and T. Sabaka (2015), IGRF-12, *Earth Planets Space*. 13, 17, 100, 101

Verbanac, G., H. Lühr, M. Rother, M. Korte, and M. Mandea (2007), Contributions of the external field to the observatory annual means and a proposal for their corrections, *Earth Planets Space*, *59*(4), 251–257. 35

Voorhies, C. V. (2004), Narrow-scale flow and a weak field by the top of Earth's core: Evidence from Ørsted, Magsat, and secular variation, *J. Geophys. Res.-Sol. Ea.*, *109*(B3), doi:10.1029/2003JB002833. 150, 151, 168, 174

Waddington, R., D. Gubbins, and N. Barber (1995), Geomagnetic-field analysis determining steady core-surface flows directly from geomagnetic observations, *Geophys. J. Int.*, *122*(1), 326–350, doi:10.1111/j.1365-246X.1995.tb03556.x. 22

Wardinski, I., and R. Holme (2006), A time-dependent model of the Earth's magnetic field and its secular variation for the period 1980-2000, *J. Geophys. Res.*, *111*(B12), doi:10.1029/2006JB004401. 13, 15, 17

Wardinski, I., and R. Holme (2011), Signal from noise in geomagnetic field modelling: denoising data for secular variation studies, *Geophys. J. Int.*, *185*(2), 653–662, doi:10.1111/j.1365-246X.2011.04988.x. 30, 33, 35, 40, 41, 42, 43, 61, 62, 63, 172, 176, 177, 178, 186, 187, 188, 197

Wardinski, I., and V. Lesur (2012), An extended version of the C3FM geomagnetic field model: application of a continuous frozen-flux constraint, *Geophys. J. Int.*, *189*(3), 1409–1429, doi:10.1111/j.1365-246X.2012.05384.x. 17, 57

Wardinski, I., R. Holme, S. Asari, and M. Mandea (2008), The 2003 geomagnetic jerk and its relation to the core surface flows, *Earth Planet. Sci. Lett.*, *267*(3-4), 468–481, doi:10.1016/j.epsl.2007.12.008. 22, 149

Whaler, K. (1987), A new method for analyzing geomagnetic impulses, *Phys. Earth Planet. Inter.*, *48*(3-4), 221–240, doi:10.1016/0031-9201(87)90147-6. 37

Yaglom, A. (1962), *An introduction to the theory of stationary random functions*, Prentice-Hall, translated and edited by R.A. Silverman. 89